Antonella Guagliardi

Structure – Property Investigations of Nanomaterials by Debye Function Analysis

Structure – Property Investigations of Nanomaterials by Debye Function Analysis

By
Antonietta Guagliardi

A dissertation submitted in partial satisfaction
of the requirements for the Degree
of Doctor of Philosophy in Chemistry

Università degli Studi dell'Insubria
Dipartimento di Scienza e Alta Tecnologia - Como

XXVII Ciclo di Dottorato di Ricerca in Scienze Chimiche

Supervisor: Prof. Ettore Fois

Acknowledgments

For most of the PhD students, the drafting time of their Thesis means having reached the goal after an exciting and stimulating experience lasting three (or more) years. In my case, the story is not very different, except for the fact that I can also say that a dream came true after more than 20 years in Science!

Therefore, before starting to thank all the friends and colleagues who have made this possible, I want to express my sincere gratitude to Ettore Fois, my supervisor, and to University of Insubria, for giving me such a great opportunity.

Here, I want to continue by thanking many others. First of all, Norbert and Antonio, that I admire and respect for their high scientific level and their superior ability to having simple conversations on complex things; they have been for me a continuous source of knowledge, intellectual stimuli, exciting debates… and some lively quarrels!

I want also to thank Ruggero and Federica for their help in performing experiments and for their enthusiasm in joining the larger-scale project on total scattering and DFA methods for nanomaterials.

I want also to thank José Manuel, Giuseppe and Angelo, for their contribution in synthesizing appealing nanoparticles and in performing additional characterization otherwise inaccessible for this Thesis.

I want to thank them again for the exciting, although always exhausting, time spent together at the material science beamline at the SLS, sharing overnight measurements, difficult moments, as well as food and drinks (or the lack thereof...)!

I also want to extend my gratitude to all the inhabitants of “via Lucini” who made my daily work pleasant.

I want to thank my mother and my family, for having in all my life supported my scientific carrier, and Helga, for her being always positive and for her moral and practical help.

I want to thank Fabio and Gabriella, simply for their friendship.

Table of Contents

List of Abbreviations and Symbols..... p. 5

Chapter 1. Investigating Nanomaterials by Total Scattering Techniques: an Introduction……... p. 7

1.1 Motivations……... p. 8

1.2 Objectives……..…… p. 17

References…….…..... p. 20

Chapter 2. Fundamentals of the Debye Function Analysis…….…… p. 25

2.1 Introduction to Total Scattering Techniques ……... p. 26

2.2 The Debye Scattering Equation……..... p. 33

2.3 Debye Equation *vs* Pair Distribution Function…….…… p. 37

References…….…..... p. 41

Chapter 3. Experimental and Computational Aspects of the Debye Function Analysis……..... p. 43

3.1 Introduction…….…….. p. 44

3.2 Experimental Aspects……..…..... p. 46

3.2.1 Experimental effects and corrections in DSE..... p. 47

3.2.2 Data collection strategy at the Material Science beamline X04SA@SLS and data reduction procedure... p. 53

3.3 Computational Aspects…….…… p. 60

3.3.1 Turning DSE into an efficient computational tool..…… p. 61

3.3.2 DFA implementation in the DebUsSy Suite…….…….. p. 63

References……..... p. 71

Cases of Study

Chapter 4. Iron Oxide Nanoparticles…….. p. 73

4.1 Introduction…….……. p. 74

4.2 Experimentals……... p. 78

4.2.1 Synchrotron and laboratory X-ray measurements…….. p. 78

4.2.2 Magnetic measurements……. p. 79

4.3 Modelling and DFA of magnetic IONPs……. p. 80

4.4 DFA *vs* magnetic properties……...…….. p. 87

4.5 Lattice parameters and iron vacancies: a critical study..... p. 94

4.6 Predicting size effects on lattice parameters in IONPs…... p. 100

4.7 Synchrotron *vs* laboratory data……..... p. 103

4.8 Conclusions……...……..... p. 106

References…….. p. 108

Chapter 5. Biomimetic Hydroxyapatite Nanoparticles……... p. 113

5.1 Introduction…….……. p. 114

5.2 Experimentals…….…….. p. 117

5.2.1 Materials and synthesis……..... p. 117

5.2.2 Synchrotron X-rays Total Scattering measurements..... p. 118

5.2.3 AFM measurements..……..... p. 120

5.3 Effects of CO_3^{2-}/PO_4^{3-} substitution on lattice parameters and structural interpretation in carbonated apatite..……... p. 121

5.4 DFA modelling of apatite platelets…….…….. p. 124

5.5 DFA characterization: structure, composition, size and morphology of biomimetic apatites..…….…… p. 130

5.6 Radial Distribution Function characterization…….…… p. 137

5.7 AFM characterization of apatite NPs ……... p. 138

5.8 DFA *vs* AFM: a plausible mechanism forming platelets …. p. 140

5.9 Conclusions…….…… p. 146

References……... p. 147

Chapter 6. Defective Coordination Polymers: From Paracrystalline $[Ru(CO)_4]_n$ 1D Polymer to Nanosized Rhutenium Metal.. p. 153

6.1 Introduction……. p. 154

6.2 Experimentals……... p. 157

6.2.1 Materials.…….……... p. 157

6.2.2 Synchrotron X-rays scattering measurements…… p. 157

6.3 Facing a complex microstructure problem……... p. 158

6.4 Including 2D anisotropic paracrystalline effects in the Debye Function Analysis…… p. 161

6.5 The paracrystalline DFA modeling of $[Ru(CO)_4]_n$ …….. p. 163

6.6 Chemical interpretation of the paracrystalline $[Ru(CO)_4]_n$ model……..... p. 167

6.7 Thermal evolution study of $[Ru(CO)_4]_n$ ……..... p. 171

6.8 Conclusions……...……..... p. 175

References……..... p. 176

Chapter 7. Defective Molecular Crystals: A Multiple Scale Study of Copper and Silver Nitropyralozates..……...….... p. 181

7.1 Introduction…….. p. 182

7.2 Experimentals…… p. 184

7.2.1 X-ray Total Scattering measurements……. p. 185

7.2.2 Scanning Electric Microscopy…...…….. p. 186

7.2.3 Electric properties measurements……...……. p. 186

7.3 Determining the average crystal structure through a*b-initio* conventional XRPD methods…… p. 186

7.3.1 The a*b-initio* structure solution process…..……... p. 186

7.3.2 The average crystal and molecular structures…....…… p. 189

7.4 Identifying the defectiveness of Ag/Cu nitropyrazolates..... p. 190

7.5 Modelling the faulted structures within the DFA approach.. p. 192

7.6 Investigating additional local features by PDF analysis..... p. 197

7.7 Bending by Faulting: the morphological SEM characterization.....…....….....…....….....….....…..... p. 200

7.8 Structure-property relationships: the dielectric behaviour of Ag(I) 4-NO_2-pyrazolate…….……. p. 202

7.9 Conclusions……..……..... p. 204

References……..... p. 207

Chapter 8. General Conclusions …….. p. 213

Annex 1. Details of the Syntheses and Laboratory Experiments……. p. 217

Annex 2. Algebraic Details of the 2D Anisotropic Paracrystalline Model……..... p. 229

Annex 3. Publications……..... p. 235

List of Abbreviations

NPs	Nanoparticles
NCs	Nanocrystals
QDs	Quantum Dots
2D	Two-dimensional
3D	Three-dimensional
TEM	Transmission Electron Microscopy
HRTEM	High Resolution Transmission Electron Microscopy
XRPD	X-ray Powder Diffraction
NPD	Neutron Powder Diffraction
FPA	Fundamentals Parameters Approach
SAXS	Small Angle X-ray Scattering
SANS	Small Angle Neutron Scattering
WAXS	Wide Angle X-ray Scattering
WAXTS	Wide Angle Total Scattering Techniques
NMR	Nuclear Magnetic Resonance
AFM	Atomic Force Microscopy
SEM	Scanning Electron Microscopy
ICP-OES	Inductively Coupled Plasma-Optical Emission Spectroscopy
DFA	Debye Function Analysis
DSE	Debye Scattering Equation
PDF	Pair Distribution Function
RDF	Radial Distribution Function
TDS	Thermal Diffuse Scattering
MS	Material Science
SLS	Swiss Light Source
DR	Data Reduction
IONPs	Iron oxide NPs
GoF	Goodness of Fit
ACS	Apparent crystal size
λ	X-ray beam wavelength
q	Scattering vector length
2θ	Scattering or diffraction or Bragg angle
b	Atomic scattering length
$f(q)$	Atomic scattering form factor
σ	Atomic cross section
$\partial\sigma/\partial\Omega$	Differential cross section
$T(q)$	Atomic Debye-Waller factor

B_{iso}	Atomic Debye-Waller parameter
o	Atomic site occupancy factor
sof	Atomic site occupancy factor
d	glass capillary diameter
D	NP diameter
R	NP radius
$\langle D \rangle_N$	number-based NPs average diameter
$\langle D \rangle_M$	mass-based NPs average diameter
σ_N	standard deviation of number-based logn size distribution
σ_M	standard deviation of mass-based logn size distribution
$\langle D \rangle_{Mag}$	volume-based average diameter of magnetic domains
σ_M	standard deviation of magnetic domains size distribution
β	integral breadth
R_{core}	core radius in core-shell NPs
R_{shell}	shell thickness in core-shell NPs
M_s	saturation magnetization
M_{sB}	saturation magnetization of bulk material
H	applied magnetic field
H_C	sample magnetic coercivity
χ	sample magnetic susceptibility
ZFC	Zero field cooled
FC	Field cooled
T_B	blocking temperature
K_M	magnetic anisotropy constant
K'_M	magnetic anisotropy constant
ε	linear strain
B	bulk modulus
AC	Alternate Current
DC	Direct Current
κ	dielectric constant
σ	electrical conductivity

Chapter 1

Investigating Nanomaterials by Total Scattering Techniques: an Introduction

1.1 Motivations

Since the inspiring concepts of R. P. Feynman, back in 1959 [1], Nanoscience (the study of materials on the nanometer scale) and Nanotechnology (the manipulation of matter on the atomic, molecular and supramolecular scale, with the specific goal of fabricating innovative products) have undergone tremendous advances. In the last two decades, the scientific and technological interest of fields as diverse as Chemistry, Physics, Biology, Medicine, Materials and Environmental Science, has enormously increased the knowledge on the 'nano' world and made the range of applications extremely vast [2-5]. On the application side, despite important concerns about the (still rather unknown) toxicological and environmental implications of nanomaterials, the potential impact of new materials and innovative devices on the society is presently seen as a concrete opportunity (on a global scale), fostering new economical and societal development. Such a vision has elected Nanoscience and Nanotechnolgy as a Key Enabling Technology (KET) by the European Commission.

Various synthetic approaches have been successfully addressed over the years to control the properties of metals, oxides, semiconductors, nanodrugs or nano-biomaterials, as a function of the atomic structure and of the NPs size and shape distribution [6-9]. Nowadays, the forefront scientific investigations and many advanced industrial or biomedical applications are addressed towards complex, multi-functional nano-objects able to synergistically combining different properties (hybrid NCs, core-shell NPs and 2D or 3D superlattices of self-assembled nanoparticles) [10-15]. Control over formation mechanisms and functionalities is required at the molecular and supramolecular levels on

large volumes. This control calls for the deep understanding and the quantitative determination of many structural and microstructural properties, such as crystal structure, stoichiometry and defects, size and shape distributions and surface relaxation effects, phase composition and supramolecular organization, on which material functionality strongly depend.

Despite this exciting scenario, characterizing these complex systems is still a challenging task, usually achieved through the application of different techniques, which typically combine microscopic, spectroscopic, scattering and diffraction methods. Among these, Transmission Electron Microscopy (TEM), particularly in High Resolution mode, has been playing, by far, the leading role. Worth of note, HRTEM describes local features, with limited statistical significance, which makes the technique rather unsuitable in scale-up processes. At the same time, materials production at large scale and the control of properties over large volumes is necessary for industrial applications. Within this context, there is presently a urgent need of new, robust physico-chemical characterization tools.

Most of the advanced engineered nanomaterials have an ordered or a partially ordered structure. In the abovementioned conditions, it is important determining the *distribution* of structural and microstructural features, as typically achieved by X-ray or Neutron Powder Diffraction (XRPD or NPD) techniques. These techniques have reached a high degree of maturity for the characterization of polycrystalline materials at the *micrometer* length scale. At this length scale of the coherent domains, popular approaches as the pristine Rietveld method [16,17] or the Fundamental Parameters Approach (FPA) [18], have been developed

under the hypothesis of a *long-range order* of the atomic arrangement, which is the peculiar feature of the crystalline state, and rely uniquely on the Bragg-based modeling of the diffracted peaks intensity, as determined from the unit cell content for an ideal crystal of infinite extension.

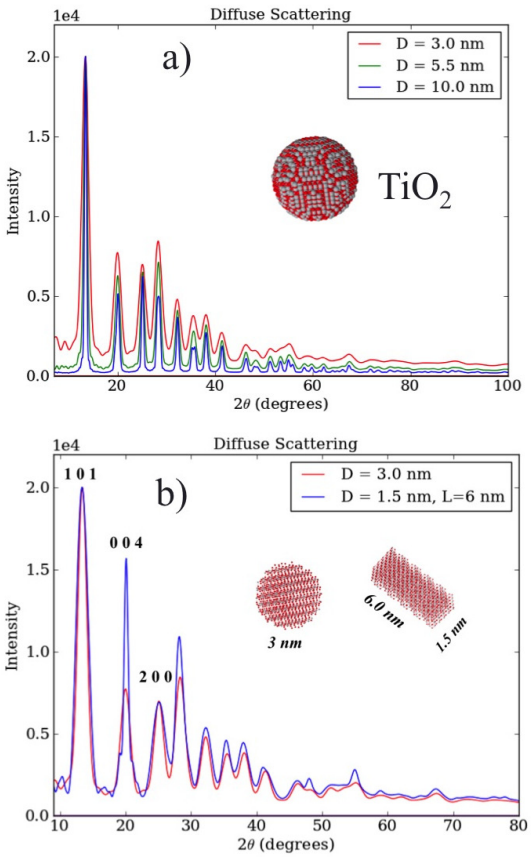

Figure 1.1 a) X-ray total scattering simulations of TiO_2 anatase nanocrystals of spherical shape and growing size. The diffuse scattering below and between the Bragg peaks clearly raises up upon decreasing the particle diameter (patterns are normalized to the same maximum intensity). b) Effects on Bragg and diffuse scattering from elongated nanocrystals are compared to the case of isotropic spheres of similar equivalent volume.

In this view, reducing the extension of the coherent domain down to few (or few tens of) nanometers can be seen, within a first approximation,

as a ‘defective’ reproduction of the corresponding bulk material, preserving the *short-range order* of its atomic arrangement. However, this kind of ‘defect’ (the nanometer size of the crystal) causes, in reciprocal space, very broad Bragg peaks and the appearance of a *diffuse scattering* between and below them. This point is of utmost importance and can be easily caught through Figure 1.1, showing the effects on the (simulated) total scattering patterns of small anatase TiO_2 nanoparticles, upon varying their size and shape. Simulations in the Figure, as well as in the other ones present in this chapter, are all obtained using the Debye Scattering Equation (*vide infra*). TiO_2 nanoparticles have been extensively studied because of their excellent photocatalytic properties, which have important applications in energy-related and environmental fields [19, 20]; NPs size and morphology seem to have a large influence on these properties [21]. The example shows how (Figure 1.1a) a larger amount of diffuse scattering occurs upon decreasing the size of isotropic, spherically shaped NCs. In the case of anisotropically shaped NCs (Figure 1.1b), with the longest size parallel to the crystallographic *c*-axis of the tetragonal anatase structure, the crystal morphology induces anisotropic peak broadening (as expected according to the diffraction theory), but also affects the distribution of intensity between Bragg and diffuse scattering. Therefore, the information on the size and on the shape of the nanocrystals is encoded in the total scattering pattern, which includes both Bragg and diffuse scattering. However, Rietveld-based methods completely disregard the information from the diffuse scattering, which may jeopardize the correct characterization of nanomaterials by XRPD.

On a similar side, real samples are typically made of populations of NCs of different sizes and assessing their distribution of sizes within the

sample may be of high relevance, both for addressing the synthesis process and for improving the material performances. An additional limit of conventional XRPD methods is that they can estimate only the *average size* of coherent domains (from the peak width, through the Scherrer equation [22,23], or using more complex phenomenological models [24,25]), not being able to rescue any information about the size distribution within the sample. For these reasons, when applicable, this kind of characterization is often performed using Small Angle (X-ray or Neutron) Scattering (SAXS/SANS) techniques, providing both average size and size distributions.

However, SAXS/SANS do not reach atomic scale resolution, which remains, within the Scattering techniques, the peculiar feature of the "Wide Angle" approach. Therefore, despite the known limitations, size characterization by conventional WAXS (XRPD) methods are sometimes reported, as they allow simultaneous check of the crystal structure. How much these size estimations are reliable is difficult to say. There are no reports in which a comparison of size values from different techniques is systematically investigated. To have an idea, an example is depicted in Figure 1.2. Here, two pattern simulations have been fitted using the highly performing FPA program TOPAS [26]. The simulations were obtained using populations of spherical TiO_2 NPs having similar average size but rather different size distributions, as shown in the two insets. TOPAS provides average sizes that are slightly overestimated (~19% in the top case and ~14% in the bottom case), the wider size dispersion turning into a major error on the estimated size.

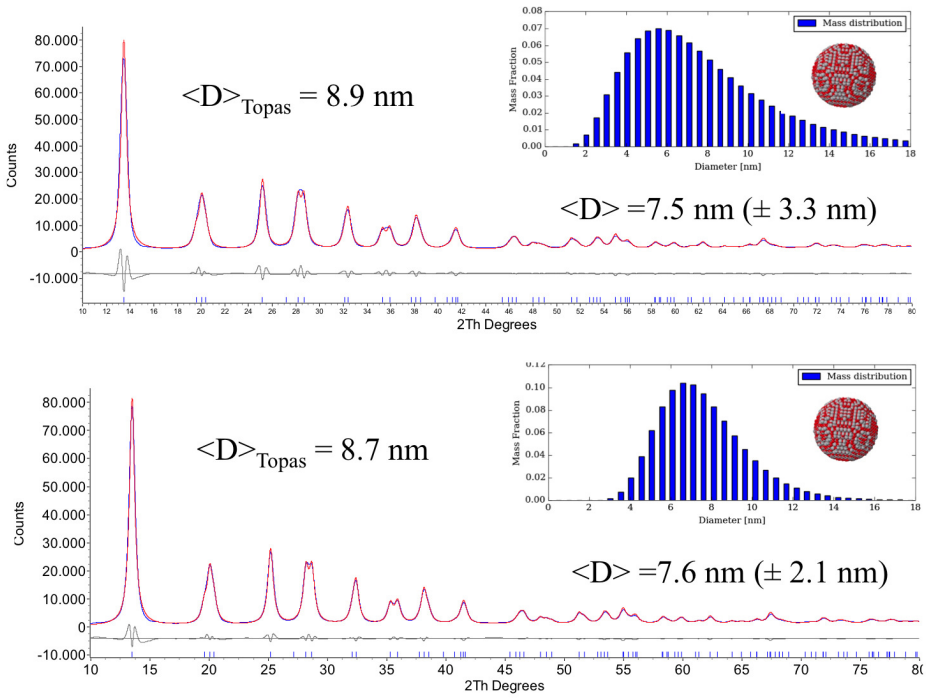

Figure 1.2 Best fit and average size estimation as provided by the TOPAS program on pattern simulations obtained from size dispersed populations of TiO_2 nanocrystals.

To complete this overview on the main limitations of conventional XRPD when used to characterize nanosized materials, it is important to highlight that size and shape effects are not the only ones in determining such a limitation. Many others, of structural nature, may occur. Nanoparticles feature a high surface/volume ratio and the number of atoms in the surface layers may account for more than 80% of the total number. As a consequence of the minimization of the surface energy, atoms can undergo lattice reconstruction processes that can significantly affect the overall structure. Therefore, important structural modifications, surface relaxations or other kinds of defectiveness may be induced. The consequence is that considering a nanocrystal as a small portion of the

corresponding bulk material may be a rather simplified approach. The accurate determination of the atomic arrangement and the existence of local distortion are a fundamental issue in NCs, often accounting for properties not fully explained by finite-size effects. However, all these phenomena further complicate the characterization process, as they cause additional diffuse scattering effects to the diffraction patterns and unpredictable peak shifts, no longer interpretable by standard crystallographic laws. A striking example is provided by noble metal NPs, which show an fcc structure in the bulk material and non crystallographic structure types (icosahedra and decahedra), resulting from a very complex twinning, in NPs below 10 nm [27-29]. For fcc and hcp closed packed structures, which differ only in the stacking sequence of the atomic planes, faulting of the regular sequence can occur due to the low activation energy of the fault formation, as often found in metals and in many semiconductors (CdS, CdSe, ZnO) [30,31].

Surface relaxation effects are shown in Figure 1.3 for very small and narrowly distributed PbSe QDs (average diameter of 3 nm and size dipersion of ~10%). Due to their opto-electronic properties, lead chalcolgenides are another highly appealing class of nanomaterials extensively investigated for applications in energy-related fields [32- 34]. In Figure 1.3 the blue trace describes the scattering pattern corresponding to the case of an "undistorted" crystal lattice (*i.e.* the unit cell parameter of the corresponding bulk structure, a_0 = 4.34164 Å, is assumed). To simulate the surface relaxation effects, a core-shell model was used, having a core diameter of 2.5 nm and a shell thickness of 0.5 nm. The interatomic distances in the external shell have been expanded by 5% with respect to those inside the core. The effects in terms of peak shift and

peak broadening can be observed in the green pattern, and further compared to the case of a simple uniform lattice expansion of ~2% corresponding to the "weighted" contributions of core and shell and to a lattice parameter a_1=4.42847 Å. The red trace is the only one that can be correctly modeled by standard crystallographic methods.

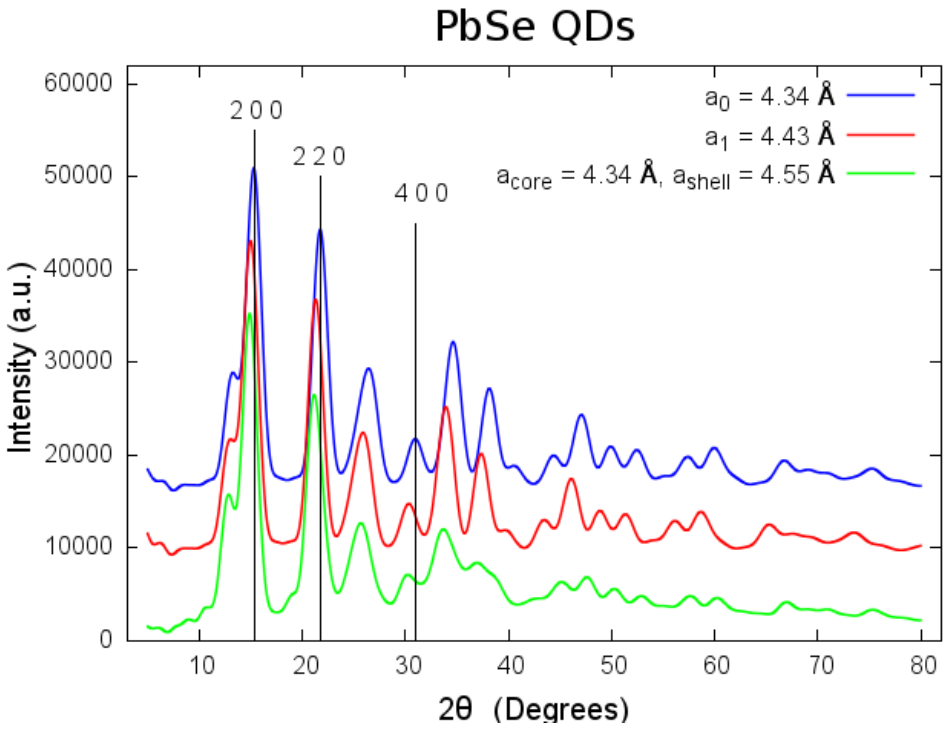

Figure 1.3 Surface relaxation effects simulated on a core-shell NPs of PbSe, in which the interatomic distance of the external shell underwent an expansion of 5% compared to the core distances (green trace); the red and the blue traces correspond to NPs with a uniform (2%) expansion of distances and to NPs without any relaxation, respectively.

Despite the limits of conventional XRPD modeling, in the last years new *Wide Angle X-ray Total Scattering Techniques* (WAXTS) have emerged as suitable characterization tools for nanomaterials, thanks to their ability to simultaneously modeling both Bragg and diffuse scattering

and therefore accounting for the entire information encoded in the powder diffraction pattern. Contrary to standard crystallographic methods, total scattering approaches can be applied *regardless of any periodicity and order*. Such a feature, which has traditionally limited their use for studying amorphous and liquids, makes them the ideal techniques for dealing with crystalline, partially ordered and even disordered nanomaterials.

Two different and complementary total scattering approaches can be used: the Pair (or Radial) Distribution Function (PDF) [35] and the Debye Function Analysis (DFA) [36]. The basics of the total scattering approach are extensively presented in the next chapters. Here is important to anticipate the main difference between the two: PDF is a real-space technique working on the sine-Fourier transformed scattering pattern; DFA uses the opposite approach, as it constructs an atomistic model of the material in real space and then, through the Debye Scattering Equation (DSE), provides a model of the experimental pattern in reciprocal space. In this Thesis, the focus will be mainly on the DFA method. The intrinsic advantage, compared to PDF, of avoiding numerical transformation of the measured data and of not requiring high-energy beams, has recently gained new consideration to DFA. However, despite its potential, few cases of applications are found in the literature (mainly to treat defects in small NPs) and the method is still rather unknown to the nanotechnology community [27,37-39]. Reasonably, this is likely due to the fact that the experimental requirements make laboratory equipment not the best choice, and that presently available computational tools need further improvement and specialization to the different classes of nanomaterials.

1.2 Objectives

The objectives of this Thesis can be summarized in three main goals:

1) Developing and applying reciprocal space Total Scattering Techniques, through the Debye Function Analysis (DFA) method, on different classes of advanced nanomaterials;

2) Assessing the DFA versatility in dealing with the different nature of the structural and microstructural problems occurring in nanosized systems, and the DFA ability in extracting reliable *quantitative* information about NPs structure and defectiveness, size and shape distribution, stoichiometry and phase composition, all within a unique coherent framework;

3) Using the analytical, structural and microstructural characterization assessed by DFA to interpret the material functional properties.

To accomplish these goals, four different classes of nanomaterials have been investigated: iron oxide super-paramagnetic nanoparticles, biomimetic apatite NPs, and two highly defective materials: the 1D $Ru(CO)_4$ polymer (a potential metal nanowire precursor), showing a structural disorder of *paracrystalline* nature, and the Ag/Cu nitropyrazolates, possessing a very complex defectiveness in which faulting and paracrystalline phenomena are simultaneously present.

Each one of the investigated systems presents its own peculiar structural and microstructural issues, which have required specific modelling approaches. All the models developed and applied during this

Thesis have been implemented in the (recently developed) Suite of programs DebUsSy [40], by contributing to preparing a new release, expected to be ready in 2015.

In all cases, the characterization aimed at extracting *quantitative* structural properties, to be correlated, when applicable, to the different functional properties, as in the case of iron oxide NPs (magnetic properties) and Ag/Cu nitropyrazolates (dielectric properties); or to interpret formation and growth mechanisms (as in the case of biomimetic NPs); or to be addressed to the comprehension of a complex defectiveness and its possible causes, which is still a conundrum for many appealing materials (as in the cases of the polymeric metal carbonyl and of metal nitropyrazolates).

Finally, the work of this Thesis was also a great opportunity to enhance the knowledge and the skill on the experimental side. In fact, all the materials here investigated have been characterized through synchrotron X-rays diffraction data, which were collected during several and exciting beamtime shifts at the Material Science X04SA beamline of the Swiss Light Source. The data collected within this Thesis contributed to developing and optimizing the data reduction procedure applied to the materials under study, providing a stable and robust protocol for data treatment, now available to the scientific community.

The work presented in this Thesis is organized in eight chapters. Chapter 1 describes the general motivations that have inspired this work and its main objectives. Chapter 2 and 3 are dedicated to the fundamentals of total scattering techniques and Debye Functional Analysis, and present the most relevant theoretical, experimental and computational aspects. In

chapters 4, 5, 6, and 7, the four cases of study previously mentioned are extensively discussed, each chapter being dedicated to the specific material. Genral vonclusions are given in chapter 8. The Annexes contain further details (mostly – but not uniquely - of the experimental type) and the lists of the papers published during this Thesis.

References

1. R. P. Feynman, *There is plenty of room at the bottom, an invitation to enter a new field of physics*, **1960**, Engineering Science Magazine, *23*, 143.

2. C. Binns, *Introduction to Nanoscience and Nanotechnology*, **2010**, John Wiley & Sons, Inc., Hoboken, New Jersey

3. G. Schmid, *Nanoparticles*: *From Theory to Application*, **2003**, Wiley-VCH Verlag GmbH & Co. KGaA, Weinheim, FRG

4. G. A. Ozin, A. C. Arsenault, L. Cademartiri, *Nanochemistry*: *A Chemical Approach to Nanomaterials*, **2008**, RCSPublishing, 2nd edition, new edition.

5. D. Astruc, *Nanoparticles and Catalysis*, **2008**, Wiley-VCH Verlag GmbH & Co. KGaA, Weinheim.

6. Y. Sun, Y. Xia, *Shape-Controlled Synthesis of Gold and Silver Nanoparticles*, **2002**, Science, *298,* 2176-2178.

7. M.-C. Daniel, D. Astruc, *Gold Nanoparticles: Assembly, Supramolecular Chemistry, Quantum-Size Related Properties and Applications toward Biology, Catalysis and Nanotechnology*, **2004**, Chem. Rev., *104*, 293-346.

8. L. H. Reddy, J. L. Arias, J. Nicolas, P. Couvreur, *Magnetic nanoparticles: design and characterization, toxicity and biocompatibility, pharmaceutical and biomedical applications*, **2012**, Chem. Rev., *112*, 5818-5878.

9. T. L. Thompson, Y. Yates, *Surface science studies of the photoactivation of TiO_2-new photochemical processes*, **2006**, Chem. Rev., *106,* 4428–4453.

10. L. Merhrari ed., *Hybrid Nanocomposites for Nanotechnology: Electronic, Optical, Magnetic nd Biomedical Applications*, **2009**, Springer, New York.

11. R. Costi, A. E. Saunders, U. Banin, *Colloidal hybrid nanostructures: a new type of functional materials*, **2010**, Angew. Chem. Int. Ed., *49,* 4878-4897.

12. L. Sang, Y. Zhao, C. Burda, *TiO_2 Nanoparticles as Functional Building Blocks*, **2014**, Chem. Rev. 11*4,* 9283-9318.

13. S. Pichler, M. Bodnarchuk, M. V. Kovalenko, M. Yarema, G. Springholz, D. V. Talapin, W. Heiss, *Evaluation of ordering in single-component and binary nanocrystal superstructures by analysis of their autocorrelation functions*, **2011**, ACS Nano, *5*, 1703–1712.

14. B. W. Goodfellow, , M. R. Rasch, C. M. Hessel, R. N. Patel, D.-M. Smilgies, B. A. Korgel, *Ordered Structure Rearrangements in Heated Gold Nanocrystal Superlattices***, 2013**, Nano Lett., *13*, 5710-5714.

15. L. Protesescu, A.J. Rossini, D. Kriegner, M. Valla, A. de Kergommeaux, M. Walter, K. V. Kravchyk, M. Nachtegaal, J. Stangl, B. Malaman, P. Reiss, A. Lesage, L. Emsley, C. Copéret, M. Kovalenko et al. *Unraveling the Core–Shell Structure of Ligand-Capped Sn/SnO_x Nanoparticles by Surface-Enhanced Nuclear Magnetic Resonance, Mössbauer, and X-ray Absorption Spectroscopies,* **2014**, ACS Nano, *8*, 2639–2648.

16. H. M. Rietveld, *A Profile Refinement Method for Nuclear and Magnetic Structures*, **1969,** J. Appl. Cryst., *2*, 65-71.

17. R.A. Young Ed. *The Rietveld Method*, IUCr Monographs on Crystallography, **1995**, OUP, Oxford.

18. R. W. Cheary, A. Coelho, *A Fundamental Parameters Approach to X-ray Line-profile Fitting*, **1992**, J. Appl. Cryst., *25*, 109-121.

19. T. W. Woolerton, S. Sheard, E. Reisner, E. Pierce, S. W. Ragsdale, F. A. Armstrong, *Efficient and clean photo-reduction of CO_2 to CO by enzyme-modified TiO_2 nanoparticles using visible light*, **2010**, J. Am. Chem. Soc. *132*, 2132–2133.

20. U. P. Apfel, W. Weigand, *Efficient Activation of the Greenhouse Gas CO_2*, **2011**, Angew. Chem. Int. Ed., *50*, 4262–4264.

21. G. Cernuto, N. Masciocchi, A. Cervellino, G. M. Colonna, A. Guagliardi, *Size and Shape Dependence of the Photocatalytic Activity of TiO_2 Nanocrystals: A Total Scattering Debye Function Study***, 2011**, J. Amer. Chem. Soc., *133*, 3114–3119.

22. P. Scherrer, *Bestimmung der Größe und der inneren Struktur von Kolloidteilchen mittels Röntgenstrahlen*, **1918**, Göttinger Nachrichten Gesell., *2*, 98-100.

23. J.I. Langford, A.J.C. Wilson, *Scherrer after sixty years: A survey and some new results in the determination of crystallite size*, **1978**, J. Appl. Cryst., *11*, 102-113.

24. P.W. Stephens, *Phenomenological model of anisotropic peak broadening in powder diffraction*, **1999**, J. Appl. Cryst., *32*, 281-289.

25. N.C. Popa, D. Balzar, *Size-broadening anisotropy in whole powder pattern fitting, Application to zinc oxide and interpretation of the apparent crystallites in terms of physical models*, **2008**, J. Appl. Cryst., *41*, 615-627.

26. A.A. Coelho, J. Evans, I. Evans, A. Kern, S. Parsons, *The TOPAS symbolic computation system*, Powder Diffr., **2011**, *26*, S22-S25.

27. D. Zanchet, B. D Hall, D. Ugarte, *Structure population in thiol-passivated gold nanoparticles*, **2000**, J. Phys. Chem., *104*, 11013-11018.

28. Z. Kaszkur, *Powder diffraction beyond the Bragg law: study of palladium nanocrystals*, **2000**, J. Appl. Cryst., *33*, 1262-1270.

29. A. Cervellino, C. Giannini, A. Guagliardi, *Determination of nanoparticle structure type, size and strain distribution from X-ray data for monatomic f.c.c.-derived non-crystallographic nano clusters*, **2003**, J. Appl. Cryst., *36*, 1148-1158.

30. F. Niederdraenk, K. Seufert, A. Stahl; R.S. Bhalerao-Panajkar, S. Marathe, S.K. Kulkarni, R.B. Neder, C. Kumpf, *Ensemble modeling of very small ZnO nanoparticles*, **2011**, Phys. Chem. Chem. Phys., *13*, 498–505.

31. A. Longo, L. Sciortino, F. Giannici, A. Martorana, *Crossing the boundary between face-centred cubic and hexagonal close packed: the structure of nanosized cobalt is unraveled by a model accounting for shape, size distribution and stacking faults, allowing simulation of XRD, XANES and EXAFS*, **2014**, J. Appl. Cryst., *47*, 1562–1568.

32. L. Cademartiri, E. Montanari, G. Calestani, A. Migliori, A. Guagliardi, G. A. Ozin, *Size-Dependent Extinction Coefficient of PbS Quantum Dots*, **2006**, J. Am. Chem. Soc., *128*, 10337-10346.

33. I. Moreels, K. Lambert, D. De Muynck, F. Vanhaecke, D. Poelman, J. C. Martins, G. Allan, Z. Hens, *Composition and Size-Dependent Extinction Coefficient of Colloidal PbSe Quantum Dots*, **2014**, ACS Nano, *8***,** 614-622.

34. J. Zhang, J. Gao, E. M. Miller, J. M. Luther, M. C. Beard, *Diffusion-Controlled Synthesis of PbS and PbSe Quantum Dots with in Situ Halide Passivation for Quantum Dot Solar Cells*, **2007**, Chem. Mater., *19***,** 6101-6106.

35. T. Egami, S. J. L. Billinge, *Underneath the Bragg peaks: structural analysis of complex materials,* **2003**, Oxford, Pergamon Press

36. P. Debye, *Zerstreuung von Röntgenstrahlen*, **1915**, Ann. Physik, 46, 809-823.

37. J. Oddershede, T.L. Christiansen, K. Ståhl, *Modelling the X-ray powder diffraction of nitrogen-expanded austenite using the Debye formula*, **2008**, J. Appl. Cryst., *41*, 537-543.

38. G. Cernuto, S. Galli, F. Trudu, G. M. Colonna, N. Masciocchi, A. Cervellino, A. Guagliardi, *Investigating the Amorphous–Crystalline Interplay in SiO_2/TiO_2 Nanocomposites by Total Scattering Methods*, **2011**, Angew Chem. Int. Ed., *50*, 10828–10833.

39. R. Frison, G. Cernuto, A. Cervellino, O. Zaharko, G.M. Colonna, A. Guagliardi, N. Masciocchi, *Magnetite–Maghemite Nanoparticles in the 5–15 nm Range: Correlating the Core–Shell Composition and the Surface Structure to the Magnetic Properties. A Total Scattering Study*, **2013**, Chem. Mater., *25*, 4820–4827.

40. A. Cervellino, C. Giannini, A. Guagliardi, *DEBUSSY: a Debye user system for nanocrystalline materials*, **2010**, J. Appl. Cryst., *43*, 1543-1547.

Chapter 2

Fundamentals of the Debye Function Analysis

2.1 Introduction to Total Scattering Techniques

Chapter 1 focused on the most relevant limitations that make conventional crystallographic techniques unsuitable for characterizing crystals in the size regime of few (or few tens of) nanometers, for which *defects* become a peculiar feature. In particular, it is reported on the large amount of diffuse scattering mostly caused by the lack of a long-range order and by a number of structural defects, which Bragg-based methods [1] are not able to properly model. At variance, methods relying on the Debye equation [2] and on the Pair Distribution Function [3] treat Bragg peak intensity and diffuse scattering (not easily separable in small nanocrystals) on an equal footing, enabling the representation of the whole scattering from the sample. For this reason they are known as Total Scattering Techniques, for which periodicity and order are not a strict requirement. In this chapter, the derivation of the Debye equation, as presented in [4], is reported according to the basics of radiation-matter interaction (in the kinematic approximation) [5, 6] and under some initial simplifying assumptions. The equation will be then specialized to the real case and compared to the Pair Distribution Function. Absorption phenomena will be neglected and treated in the next chapter. The equations will mainly refer to the use of X-rays impinging on the sample, as this kind of radiation has been used in all cases of study here investigated. However, they have a general validity, and may also be applied to other kind of radiations, such as neutrons and electrons. Worth of note, only the *elastic* and *coherent* sample scattering is modeled by the Debye equation. For the elastic scattering, the exchanged energy is zero; this means that the scattered photons have the same energy than the

incoming photons. The coherency of the scattering process implies that there is no phase delay between incoming and outgoing beams.

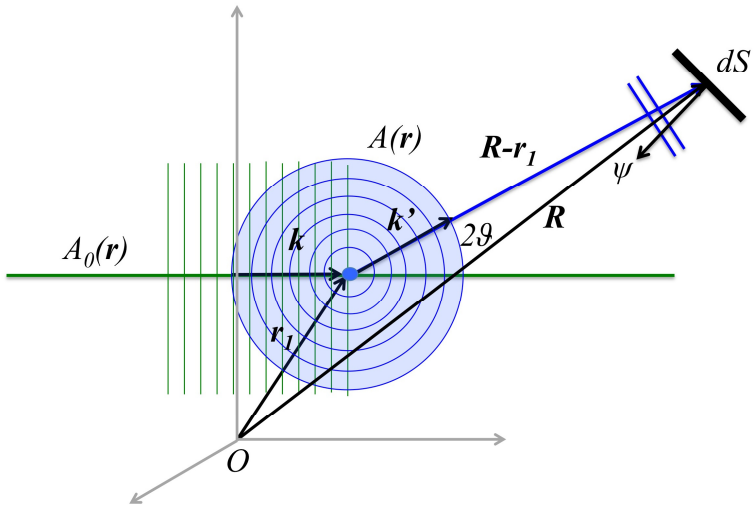

Figure 2.1 Schematics of the scattering process by a single point-like atom

Initially, the ideal condition of a *single point-like atom* is considered, with a plane wave propagating along the direction of the wave vector $\boldsymbol{k}$ and impinging on the atom, as schematized in Figure 2.1. The parallel and uniform incoming beam (of wavelength λ) has an intensity I_0 defined by the number of incident particles (photons) per unit time and unit area. By definition, I_0 also describes the square amplitude of the wave plane that can then be represented by the following equation:

$$A_0(\boldsymbol{r}) = \sqrt{I_0}\, e^{2\pi i \boldsymbol{k}\cdot\boldsymbol{r}} \qquad (1)$$

where $\boldsymbol{r}$ spans the real space, $\boldsymbol{k}$ is the propagation vector of the beam, of $k=1/\lambda$ length, and the exponential term describes the phase factor of the wave plane. The beam is elastically scattered in all directions by the

point-like atom. The elastic scattering by a single atom is quantified by its *elastic cross section* σ, having the dimension of an area. Therefore, the total number of photons scattered in *all directions* is defined by the quantity σI_0. It is important, at this point, considering that the information gained from diffraction experiments is all contained in the angular distribution of the scattered particles. This information is represented by the *differential cross section* $\partial\sigma/\partial\Omega$, a function of the direction out of the target according to which the number of scattered particles per unit time within a small solid angle dΩ around a given direction is $I_0[\partial\sigma/\partial\Omega]d\Omega$, as further schematized in Figure 2.2. In the following, it will be clear that the differential cross section is closely related to the atomic structure of the sample.

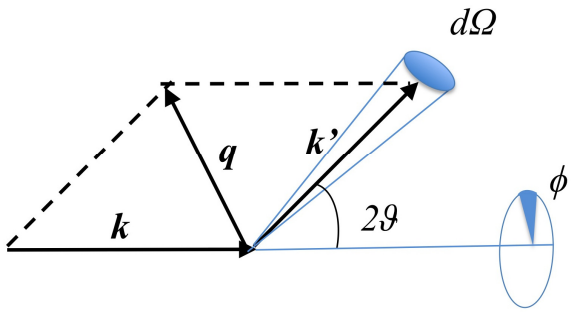

Figure 2.2 Schematics of the solid angle dΩ around a given direction of the scattering beam (***k'***) within which the number of measured particles are confined. The figure also shows the geometrical construction of the scattering vector ***q***.

Coming back to the case of the single point-like atom, located at the position $\boldsymbol{r}_1$ in Figure 2.1, with the detector positioned at the (much longer) distance ***R*** along the direction ***k'***, the scattered radiation is represented by the spherical wave:

$$A(\boldsymbol{r}) = -\sqrt{I_0}\, e^{2\pi i \boldsymbol{k}\cdot\boldsymbol{r_1}} \frac{b}{|\boldsymbol{R}-\boldsymbol{r_1}|} e^{2\pi i \boldsymbol{k'}\cdot|\boldsymbol{R}-\boldsymbol{r_1}|} \qquad (2)$$

the first two terms are amplitude ($\sqrt{I_0}$) and phase ($e^{2\pi i \boldsymbol{k}\cdot\boldsymbol{r_1}}$) of the incident beam at the position $\boldsymbol{r_1}$; b is the atomic scattering length (related to its elastic cross section, $\sigma = 4\pi b^2$); $|\boldsymbol{R}-\boldsymbol{r_1}|$ is the detector–to–sample distance and the last exponential is the phase factor of the scattered beam.[1] Since in a real diffraction experiment $|\boldsymbol{R}-\boldsymbol{r_1}|$ is very large compared to the wavelength, then the scattered beam at the detector can be considered as a plane wave propagating toward of the detector, that is along the vector $\mathbf{k'}$ of Figure 2.1. Its length is $k' = k = 1/\lambda$, as the process is elastic, and its deflection angle is conventionally reported as 2θ (see also Figure 2.2). In order to evaluate the differential cross section, it is necessary obtaining the total scattered intensity by squaring eq. (2):

$$|A(\boldsymbol{r})|^2 = I_0 \frac{b^2}{|\boldsymbol{R}-\boldsymbol{r_1}|^2} \qquad (3)$$

and focussing on what happens at the detector. The scattered photons hit the detector area with an angle ψ with respect to its normal and only on the element dS (see Figure 2.1); its projected area on the wavefront is $dS\cos\psi$ and the solid angle of detection is $d\Omega = dS\cos\psi/|\boldsymbol{R}-\boldsymbol{r_1}|^2$. Therefore, the number of particles measured in the unit time by the detector element is given by:

$$|A(\boldsymbol{r})|^2 dS\cos\psi = I_0 \frac{b^2}{|\boldsymbol{R}-\boldsymbol{r_1}|^2} dS\cos\psi = I_0 b^2 d\Omega \qquad (4)$$

[1] The phase term is conserved – as a factor – after the scattering, as the process is supposed to be coherent. The minus sign, implying a 180 deg phase shift, appears in the case of X-ray-electrons interactions. It does not change the general validity of this derivation.

From this relationship, and considering the previous definition ($I_0[\partial\sigma/\partial\Omega]d\Omega$), the differential cross section $\partial\sigma/\partial\Omega = b^2$ is obtained, which tells us that, in the ideal case of a point-like atom, the number of scattered photons measured at the detector is independent of the scattering angle.

The case of a *multiple (point-like) atoms* sample is now considered. Since absorption effects are neglected (and the σ values are very small), the beam intensity can be considered to be the same on each atom. Equation (2) slightly changes to account for the spherical wave produced by each atom, the amplitudes of which are summed up to obtain the total plane wave incident on the detector:

$$A(\boldsymbol{r}) = -\sqrt{I_0} \sum_{j=1}^{N} \frac{b_j}{|\boldsymbol{R} - \boldsymbol{r}_j|} e^{2\pi i \boldsymbol{k}\cdot\boldsymbol{r}_j} \cdot e^{2\pi i \boldsymbol{k}'\cdot(\boldsymbol{R}-\boldsymbol{r}_j)}$$

$$\simeq -\sqrt{I_0} \frac{e^{2\pi i \boldsymbol{k}'\cdot\boldsymbol{R}}}{|\boldsymbol{R}|} \sum_{j=1}^{N} b_j e^{2\pi i(\boldsymbol{k}-\boldsymbol{k}')\cdot\boldsymbol{r}_j} \qquad (5)$$

In eq. (5) all spherical waves are considered to have approximately the same origin and, therefore, the same distance $|\boldsymbol{R}- \boldsymbol{r}_j|$ from the detector; moreover, due to the position of the detector far away from the sample, all $|\boldsymbol{R}- \boldsymbol{r}_j|$ can be approximated by $|\boldsymbol{R}|$. Worth of note, the dependence of eq. (5) on $\boldsymbol{r}_j$ (in the phase factors) has dramatic effects when squaring the equation to obtain the intensity on the detector element $dS\cos\psi$:

$$|A(\boldsymbol{r})|^2 dS\cos\psi = I_0 \frac{dS\cos\psi}{|R|^2} \left| \sum_{j=1}^{N} b_j e^{2\pi i(\boldsymbol{k}-\boldsymbol{k}')\cdot\boldsymbol{r}_j} \right|^2$$

$$= I_0\, d\Omega \left| \sum_{j=1}^{N} b_j\, e^{2\pi i(\boldsymbol{k}-\boldsymbol{k'})\cdot \boldsymbol{r_j}} \right|^2 \qquad (6)$$

in fact, a differential cross section containing a contribution from the inter-atomic distances is eventually obtained:

$$\frac{d\sigma}{d\Omega} = \frac{|A(\boldsymbol{r})|^2 dS \cos\psi}{I_0\, d\Omega} =$$

$$= \sum_{j=1}^{N} b_j^2 + 2 \sum_{j>i=1}^{N} b_j\, b_i \cos\left(2\pi \boldsymbol{q} \cdot \left(\boldsymbol{r}_j - \boldsymbol{r}_i\right)\right) \qquad (7)$$

In eq. (7) we also introduced the transferred momentum, or scattering vector $\boldsymbol{q} = \boldsymbol{k'} - \boldsymbol{k}$ (see Figure 2.2), the length of which, $q = 2sin\theta/\lambda$ (as derived by simple geometrical considerations), shows the dependency of the scattered intensity on both half the scattering angle (θ) and the beam wavelength (λ). Worth of note, eq. (7) spans both the real and the reciprocal space and tells us that $\partial\sigma/\partial\Omega$ depends on the inter-atomic vectors rather than on the absolute atomic positions within the sample.

On this side, let us consider an ensemble of N point-like atoms positioned at $\boldsymbol{r}_j$ and having scattering lengths b_j, The scattering length density $\rho(\boldsymbol{r})$ describes the distribution of the ensemble

$$\rho(\boldsymbol{r}) = \sum_{j=1}^{N} b_j \delta(\boldsymbol{r} - \boldsymbol{r_j}) \qquad (8)$$

$\delta(\boldsymbol{r})$ is the delta function, *i.e.* a function which is zero everywhere except in the origin and with integral equal to 1. The function $\rho(\boldsymbol{r})d^3\boldsymbol{r}$ measures

the density in the small volume $d^3\boldsymbol{r}$ around $\boldsymbol{r}$ (as schematized in Figure 2.3a).

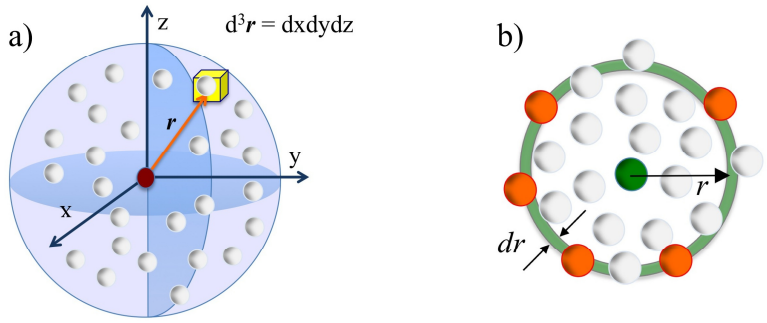

Figure 2.3 a) Schematics of the $\rho(\boldsymbol{r})d^3\boldsymbol{r}$ function measuring the density in the small volume $d^3\boldsymbol{r}$ at the distance $\boldsymbol{r}$ from the central atom. b) pictorial view of the spherical average of the $\rho(r)$ giving the probability of finding an atom at a distance r from a given atom, i.e. a one-dimensional function known as PDF.

By performing its Fourier Transform

$$F(\boldsymbol{q}) = \int d^3\,\boldsymbol{r}\rho(\boldsymbol{r})e^{2\pi i\boldsymbol{q}\cdot\boldsymbol{r}} = \sum_{j=1}^{N} b_j\, e^{2\pi i\boldsymbol{q}\cdot\boldsymbol{r}_j} \qquad (9)$$

and by squaring it

$$|F(\boldsymbol{q})|^2 = \left|\sum_{j=1}^{N} b_j\, e^{2\pi i\boldsymbol{q}\cdot\boldsymbol{r}_j}\right|^2 =$$

$$= \sum_{j=1}^{N} b_j^2 + 2\sum_{j>i=1}^{N} b_j\, b_i\, cos\left(2\pi\boldsymbol{q}\cdot\left(\boldsymbol{r}_j - \boldsymbol{r}_i\right)\right) \qquad (10)$$

the differential cross section derived in eq. (7) is obtained. The Fourier relationship between $\rho(\boldsymbol{r})$ and $|F(\boldsymbol{q})|$ tells us that back Fourier transforming

$|F(\boldsymbol{q})|^2$ (or $\partial\sigma/\partial\Omega$)) allows the density function $\rho(\boldsymbol{r})$ convolved with its inverse $\rho(-\boldsymbol{r})$ to be obtained:

$$\int |F(\boldsymbol{q})|^2 \; e^{-2\pi i \boldsymbol{q}\cdot\boldsymbol{r}} = \; \rho(\boldsymbol{r}) * \rho(-\boldsymbol{r}) \qquad (11)$$

Taking the convolution theorem into account, the Fourier transform of the differential cross section turns to be the *pair correlation function* $G(\boldsymbol{r})$ (also known as Patterson or autocorrelation function), by definition.

2.2 The Debye Scattering Equation

The case of a sample containing *many equal particles* is now considered. The particles are assumed to have different and fully random orientations in space and to be isotropic (in average). This is the classical representation of a polycrystalline material (ideal powder) or of a colloidal suspension of nanoparticles. The total scattering pattern of these systems is obtained by summing up the intensity of the different particles, as derived in the previous paragraph, and by averaging the single particle differential cross section over all orientations in space (*i.e.* over the β, ϕ angles of a polar coordinate system). The interference of waves scattered by different particles can be neglected, as it produces effects only at very small angles (the typical SAXS region), which are not considered here.

The spherical average of $\partial\sigma/\partial\Omega$ is derived by taking the single-particle version from eq. (7) and substituting each term $\cos(2\pi \boldsymbol{q}\cdot\boldsymbol{d}_{ij})$ with the term $\sin(2\pi q d_{ij})/(2\pi q d_{ij})$:

$$\left\langle \frac{\delta\sigma}{\delta\Omega} \right\rangle_{orient.} = \frac{1}{4\pi} \int_0^{2\pi} d\beta \int_0^{\pi} d\phi \sin\phi \frac{d\sigma}{d\Omega}$$

$$= \frac{1}{4\pi} \int_0^{2\pi} d\beta \int_0^{\pi} d\phi \sin\phi \times \left[\sum_{j=1}^{N} b_j^2 + \sum_{j>i=1}^{N} b_j b_i \cos\left(2\pi \boldsymbol{q} \cdot \boldsymbol{d_{ij}}\right) \right]$$

$$= \sum_{j=1}^{N} b_j^2 + \frac{1}{2\pi} \sum_{j>i=1}^{N} b_j b_i \int_0^{2\pi} d\beta \int_{-1}^{1} d(\cos(\phi)) \cos\left(2\pi q d_{ij} \cos(\phi)\right)$$

$$= \sum_{j=1}^{N} b_j^2 + 2 \sum_{j>i=1}^{N} b_j b_i \frac{\sin(2\pi q d_{ij})}{2\pi q d_{ij}} \qquad (12)$$

Eq. (12) is the *Debye scattering equation*, where $d_{ij} = |\boldsymbol{d}_{ij}| = |\boldsymbol{r}_j - \boldsymbol{r}_i|$ is the inter-atomic distance between atoms *i* and *j*.

Eq. (12) has been derived under a number of approximations and simplifying assumptions; some of them do not apply to the case of real scattering particles and are now revised to extend the equation validity to non point-like atoms, also affected by thermal motions and site vacancies. Simple corrections can be introduced in order to take these effects into account.

In fact, when X-rays (and electron beams as well) are used, photons are actually scattered by the atomic electron cloud that extend over a region of a few Å (comparable to the typical radiation wavelength of diffraction studies), which makes the use of constant scattering lengths b_j totally unsuitable. This effect is corrected by substituting b_j with the *(q*-dependent) X-ray atomic *form factors* $f_j(q)$, that are known with great precision, also for ions [7,8]. For electrons, form factors can be calculated

from those available for X-ray and modified by the Mott-Bethe formula [9]. For neutrons, atoms can be really considered as point-like scatterers, since atomic nuclei interact with this kind of particles and they are small enough to make the assumption of a constant scattering length valid [10].

The effect of atomic *thermal motions* is now considered. It is well known that atomic positions in a crystal are equilibrium positions and that atoms oscillate about them with a given frequency and amplitude. The time scale of these oscillations is so short (fs scale) that usual diffraction experiments will capture an averaging over the full arc of atom motions. If the atomic thermal displacement is assumed to be harmonic and uncorrelated, the effect is corrected by introducing the atomic Debye-Waller factor, $T_j(q) = [exp(-2\pi^2 \langle u^2 \rangle q^2)]$, $\langle u^2 \rangle$ being the isotropic mean-square displacement. The $T_j(q)$ Gaussian factor, of decreasing intensity with q, multiplies the atomic form factor in eq. (12). It is worth mentioning that correlated atomic motions, usually referred to as *Thermal Diffuse Scattering* (TDS) [11] can also be at work, although this is a weak effect for X-rays, which can be neglected. However, correcting the TDS is very difficult; anharmonic motions also require other special corrections [12]. The last two affects are not present in the cases of study of this Thesis and will not be considered anymore.

The last simple correction easily treatable in eq. (12) refers to the occurrence of *site occupancy disorders*, which include the cases of either vacancies or atomic species substitutions at the same site. Similarly to the Bragg case, the effect of randomly distributed disorders is accounted for by introducing the occupancy factors, o_j, to define the probability that one atom is actually in its site. It is worth noting that, such a way of correcting site occupancy disorders describes the phenomenon from a statistical

point of view of its effect on the scattered intensity rather than from the point of view of a true physico-chemical model. In fact, in real samples the atomic site is sometimes vacant and sometimes not, while the corrections treat the atomic site in the same way throughout the entire nanoparticle.

All the abovementioned corrections change eq. (12) in the following final Debye formula:

$$\left\langle \frac{\delta\sigma}{\delta\Omega} \right\rangle_{orient.} = \sum_{j=1}^{N} f_j(q)^2 o_j^2 + 2 \sum_{j>i=1}^{N} f_j(q) f_i(q) T_j(q) T_i(q) o_j o_i \frac{\sin(2\pi q d_{ij})}{2\pi q d_{ij}} \qquad (13)$$

The first summation of eq. (13) refers to the zero distances between an atom and itself (called *"self"* term), the second summation refers to the nonzero interatomic distances of pairs of atoms (called *"interference"* term, providing the structural information). Worth of note, the Debye-Waller factors do not apply to the first term, as the atoms self-distance does not change whatever the atomic motion is. Therefore, provided that the set of the interatomic distances of a nanocrystal, or any (even non periodic or disordered) nanoparticle, can be calculated from a (sufficiently approximate) set of structural coordinates, the Debye formula enables the corresponding powder-like total scattering simulation to be reproduced. The added value, compared to standard powder diffraction methods, is that now diffuse scattering enter into the simulation alongside the Bragg intensity, as the entire coherent and elastic scattering over all the q-space is modeled.

However, the elastic and coherent sample scattering is not exactly what is measured by a powder diffraction experiment. Additional components, such as *inelastic* Compton scattering and contributions from the sample holder and from the surrounding, are present and cannot be separated during the data collection process. How they can experimentally be managed within the Total Scattering Techniques and, in particular, within the Debye Function Analysis (DFA), is the subject of the next chapter, where other experimental corrections are also treated.

2.3 Debye Equation *vs* Pair Distribution Function

This paragraph has the aim of highlighting the fundamental relationship between the Debye Equation and the Pair (or Radial) Distribution Function (PDF), which gives the probability of finding an atom at a distance r from a given atom. The PDF is, therefore, conceptually similar to the pair correlation (or Patterson) function. Typically, the latter is obtained by Fourier transforming just the Bragg peak intensities of a crystalline material [the square modulus of $F(\boldsymbol{q})$ sampled at the crystal nodes $\boldsymbol{H}$, $H=(h,k,l)$ being the Miller indices of Bragg reflections] and provide a discrete map of the interatomic vectors. The PDF is instead a continuous (3D or, for isotropic samples, 1D) function obtained via Fourier transform of the total scattering pattern, or, more precisely, of a continuous normalized function of the scattering vector $\boldsymbol{Q}=2\pi\boldsymbol{q}$, the *total scattering structure function* $S(\boldsymbol{Q})$:

$$S(\boldsymbol{Q}) = \frac{I(\boldsymbol{Q})}{N\langle b\rangle^2} - \frac{\langle b^2\rangle - \langle b\rangle^2}{\langle b\rangle^2} \qquad (14)$$

where $I(\boldsymbol{Q})$ is related to the second summation in eq. (7), the angle brackets denote the average scattering length $\langle b^2 \rangle = (\sum b_j^2)/N$ (an average over the atomic species) and the second term has the effect of removing the *"self"* scattering contributions (first summation in eq. 7, which is independent of the atomic arrangement). Eq. (14) follows the notation reported in ref. [13]. With reference to eq. (12), that is the case of isotropic powders, the spherical average $S(Q)$ is obtained as follows:

$$S(Q) = \frac{1}{N\langle b^2 \rangle} \langle \frac{\partial \sigma}{\partial \Omega} \rangle = 1 + \frac{1}{N\langle b^2 \rangle} I(Q) \qquad (15)$$

where $I(Q)$ accounts for the *"interference"* term and, therefore, is related to the pair distribution function.

Several functions are available in the literature, containing almost the same structural information but, according to the definition, different details. Adopting here the definition of $G(r) = 4\pi r[\rho(r) - \rho_0]$, with ρ_0 the atomic density, $G(r)$ can be obtained from the measured pattern, after suitably "cleaning" it of the incoherent components (Compton and extra-sample scattering, described in the next chapter), normalizing it to $S(Q)$ and using the *reduced* scattering function $F(Q)=Q[S(Q) -1]$ to Fourier transform the data to real-space. The PDF [in the form of $G(r)$] is calculated as follows:

$$G(r) = \frac{2}{\pi} \int_{Q_{min}}^{Q^{max}} Q[S(Q) - 1] \sin(Qr) dQ \qquad (16)$$

It has peaks at positions r where pairs of atoms are separated (in the materials) with high probability; positive and negative parts in $G(r)$ correspond to interatomic distance densities, respectively, higher and lower than the average density.

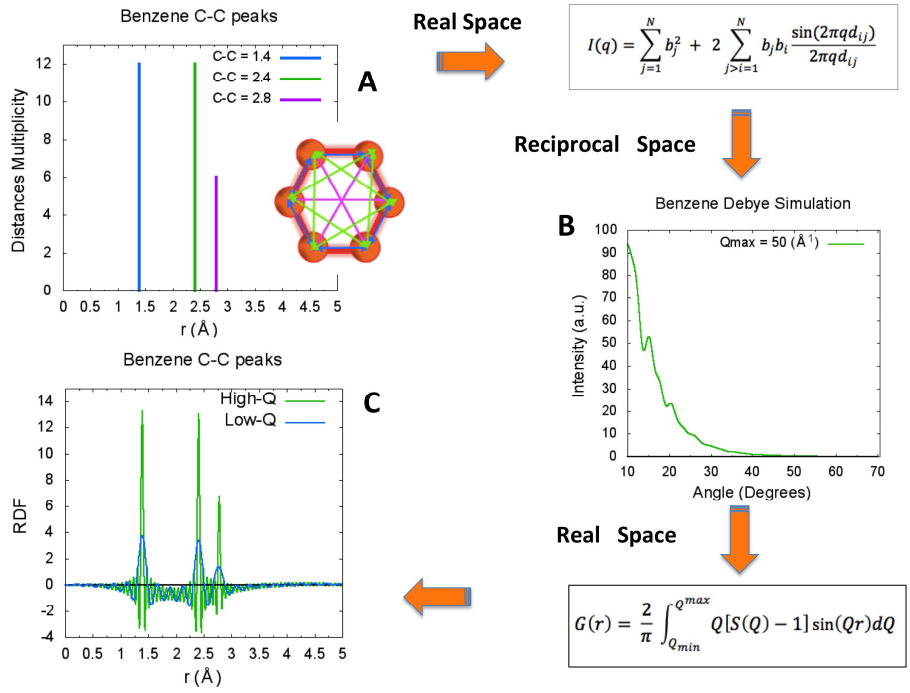

Figure 2.4. Scheme illustrating the complementarity of Debye equation and PDF approach. The benzene molecule is used as a simple example (hydrogen atoms are neglected, as they are rather "invisible" to the X-rays). The histogram in panel A shows the C-C distances: the (shortest) *1,2* at 1.39 Å (blue bar), the *1,3* at 2.4 Å (green) and the *1,4* at 2.8 Å (magenta). In the inset, the same color code marks the distances in the molecules. If used in the Debye equation, each with its own multiplicity (12, 12 and 6, respectively), the pattern simulation shown in panel B is obtained. By sine-Fourier transforming this signal back to the real space, the Radial Distribution Function in panel C is obtained, where peaks corresponding to the C-C distances occur are at the same position than in panel A and same relative intensity.

PDF modeling is typically performed in real space, which is perhaps the most relevant difference compared to DFA (see the scheme in Figure 2.4), with important consequences on both the experimental and modeling side. In fact, to get a good resolution in real space, the scattering pattern for PDF analysis has to be measured over a wide Q-

range, as large as 25 $Å^{-1}$, considering that above 30-50 $Å^{-1}$ (depending on the material) the features in the S(Q) gradually disappear due to atomic thermal motion and/or static disorder. These high Q values are experimentally attained when very high-energy beams (typically > 30 keV) are used. Interestingly for applications to nanomaterials, in high-Q resolution conditions a direct measure of the structural coherence of the sample (i.e. of the diameter of a nanoparticle) is obtained from the amplitude of the oscillations. However, the normalization with respect to the sample cross section that, in case of X-rays ($<f(Q)>^2$) is a decreasing function of Q and becomes very small at high Q, amplifies the weak intensity at this angular region, which need to be collected with very good statistics. Both requirements make synchrotron data highly preferred for PDF analysis. In the next chapter it will be shown that this is presently recommended also for DFA.

References

1. R. A. Young, *The Rietveld Method,* International Union of Crystallography Monographs on Crystallography No. 5, **1993**, Oxford University Press, Oxford.

2. P. Debye, *Zerstreuung von Röntgenstrahlen*, **1915**, Ann. Physik**,** *46*, 809-823.

3. T. Egami, and S. J. L. Billinge, *Underneath the Bragg peaks: structural analysis of complex materials,* **2003**, Pergamon Press, Oxford.

4. A. Cervellino, R. Frison, G. Cernuto, A. Guagliardi, *Debye Function Analysis: Theoretical and Fundamental Aspects,* in *Crystallography for Health and Biosciences*, A. Guagliardi and N. Masciocchi Eds., **2012**, Insubria University Press, Varese, Italy.

5. B. E. Warren, *X-ray Diffraction*, **1990**, 2nd ed., Dover, New York

6. P. Fornasini, *Basics of Matter-Radiation Interaction,* in *Crystallography for Health and Biosciences*, A. Guagliardi and N. Masciocchi Eds., **2012**, Insubria University Press, Varese, Italy

7. D. E. Cullen, J. H. Hubbell, L. Kissel *EPDL97: the Evaluated Photon Data Library, '97 Version Technical Report UCRL-50400*, Vol. 6, Rev. 5, **1997**, Lawrence Livermore National Laboratory, Livermore.

8. D. Waasmaier, A. Kirfel, *New analytical scattering-factor functions for free atoms and ions,* **1995**, Acta Cryst. A, *51*, 416–431.

9. N. F. Mott, *The scattering of electrons by atoms*, **1930,** Proc. R. Soc. Lond. A, *127*, 658–665

10. S. W. Lovesey, *Theory of Neutron Scattering from Condensed Matter: Volume I - Nuclear Scattering*, **1986**, Oxford University Press, Oxford.

11. B. T. M. Willis, in *International tables for crystallography. Vol. B: Reciprocal space (*Ed. by U. Shmueli*)*, **2010,** Kluwer, Dordrecht, Ch. 4.1. Thermal diffuse scattering of X-rays and neutrons, pages 484–491; Second online ed.

12. P. Coppens, in *International tables for crystallography. Vol. B: Reciprocal space (*Ed. by U. Shmueli*)*, **2010,** Kluwer, Dordrecht, Ch. 1.2. The structure factor, pages 10–24; Second online ed.

13. S. J. L. Billinge and T. Egami, *Short-range atomic structure of* $Nd_{2-x}Ce_xCuO_{4-y}$ *determined by real-space refinement of neutron powder diffraction data*, **1993**, Phys. Rev. B, *47,* 14386.

Chapter 3

Experimental and Computational Aspects of the Debye Function Analysis

3.1 Introduction

As stated in the previous chapter, the Debye equation can model only the elastic and coherent sample scattering, from an isotropic collection of (nano)particles. However, independently of the radiation type used in the experiment, several incoherent and inelastic effects are at work, either from the sample (such as incoherent Compton scattering and/or fluorescence effects) or from the environment (such as sample holder and air scattering). These additional contributions to the coherently and elastically intensity scattered by the sample cannot be separated one from each other during the measure. Since they can severely affect the analysis, a strict control is necessary to avoid (when feasible) or to minimize, as much as possible, their effects. Moreover, depending on the X-ray radiation type (synchrotron or laboratory source) and on the instrumental set-up, other corrections may also be needed in order to account for beam polarization and absorption phenomena. These corrections can be applied to the pattern model calculated by the Debye scattering equation or, conversely, to the experimental pattern.

The first part of this chapter is dedicated to briefly describing the most important of these effects and how they have been managed within the Debye function approach here proposed to characterize different classes of nanomaterials. In particular, data collection for DFA makes use of powder diffraction set-ups. The Debye-Scherrer transmission geometry with capillary sample holders (schematically drawn in Figure 3.1) seems to be the most suitable one for extra sample scattering contributions to be taken under control. However, this set-up, unique for colloidal solutions of NPs, typically means a small amount of powder also for dry samples

(smaller than the amount used with the flat-plate sample holder in Bragg-Brentano reflection geometry).

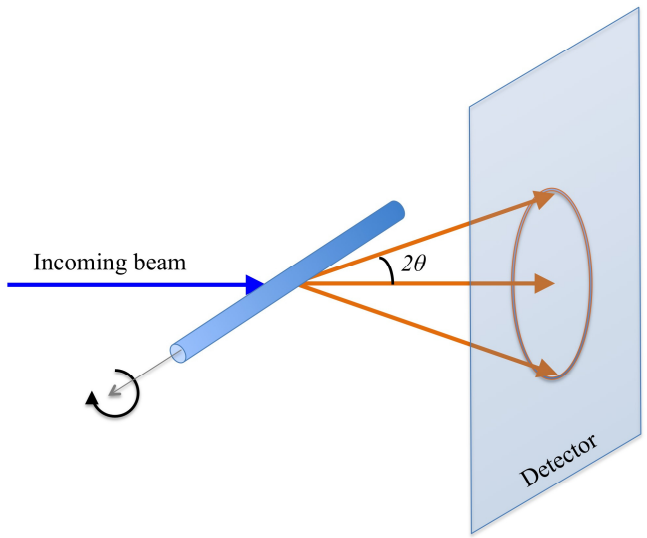

Figure 3.1. Schematics of the Debye-Scherrer transmission geometry with capillary sample holder.

Moreover, high counting statistics and quite high q values (up to 2÷3 $Å^{-1}$ in q or, equivalently, 14÷20 $Å^{-1}$ in Q,) are highly desirable and, considering also the weak scattering power of small nanocrystals, this turns into the need of using a high brilliant source and (depending on the wavelength) of collecting the data over a wide angular range (possibly up to 140 degrees). Standard laboratory equipment is not the best choice, at least presently. At variance, most of the above mentioned requirements are nowadays fulfilled at the powder diffraction beamlines operating at many 3rd generation synchrotron facilities, where the advantage of tunable beam energy has also to be considered. For all the materials investigated

within this Thesis, the data have been measured at the X04SA-MS (Material Science) beamline of the Swiss Light Source (SLS), where a specific protocol for data collection has been set-up, in collaboration with the beamline staff, and a suitable Data Reduction (DR) procedure applied before the DFA. A brief description of the instrumental set-up available at X04SA-MS beamline, of the data collection protocol and the DR process are also included in this section.

The second part of this chapter is devoted to presenting some computational and modeling aspects. The very long calculation times required by the Debye scattering equation, inherent to the fact that the number of distances in the summation increases enormously upon increasing the size of the nanoparticle, has made the use of the equation very limited, even over the last decade, when powerful computational resources have become available. Some tricks to speed up the calculation have been recently proposed in the literature and are here shortly recalled. Finally, all the material characterizations have been performed using the Debussy Suite of programs [1], implementing the DFA according to a suitable modeling strategy, a synthesis of which is also presented.

3.2 Experimental Aspects

This section is organized as follows: the most important experimental effects and corrections to be taken into account during the DFA are briefly described along with the simplest or the most usual way to manage them. They include: Compton scattering, X-ray Fluorescence, Polarization and Lorentz corrections, Absorption corrections. Then, the instrumental set-up available at X04SA-MS beamline, the data collection

protocol developed for DFA, and the reduction procedure applied before performing the DFA, are illustrated.

3.2.1 Experimental effects and corrections in DSE

Compton scattering. When an X-ray photon is scattered by a perfectly free electron, it undergoes a reduction of energy or, alternatively, an increase of its wavelength, to fulfill the conservation laws of energy and linear momentum, as follows:

$$\Delta\lambda = \lambda - \lambda_0 = (h/m_e c)\,(1 - \cos 2\vartheta) = \lambda_c(1 - \cos 2\vartheta) \qquad (1)$$

where λ_c = 0.02426 Å is called the Compton wavelength [2]. As seen in the previous chapter, when scattered by electrons bound to an atom, photons undergo mainly elastic (Thomson) but also inelastic (Compton) scattering. With reference to the Total Scattering approaches, the Compton component (originating from the weakly bound electrons) is generally a weak effect, except when high photon energies are used.

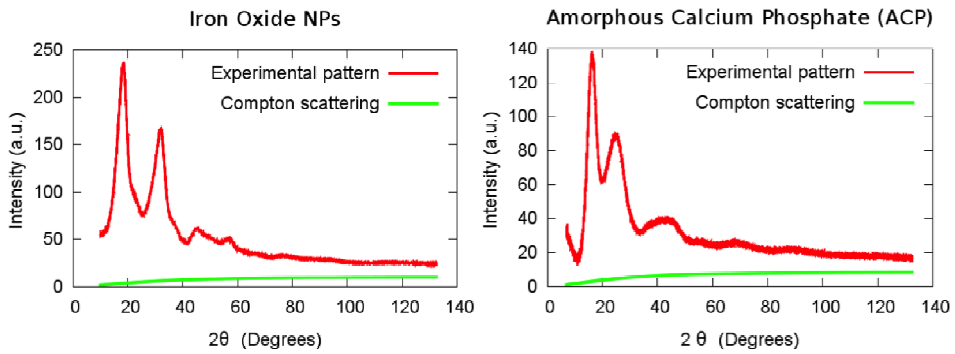

Figure 3.2 Compton scattering (green traces) for some of the samples investigated in this Thesis.

It consists of a (angle-dependent) smooth background term that can be easily calculated from the sample composition and taken into account through analytical formulae [3,4]. Examples are shown in Figure 3.2 for some of the materials studied in this Thesis (data collected with a synchrotron energy beam of 15 keV). Within the PDF approach, this component is typically subtracted from the experimental pattern, while it is treated as an additional modeling term within the DFA approach here adopted.

X-ray Fluorescence. As known, X-ray fluorescence is the phenomenon according to which a radiation is emitted from the sample after that core electrons, removed by the ionizing effect of high-energy photons leaving empty states, relax to the original state. Therefore, depending on the materials composition and on the photon energy, such emission may generate an additional background component strongly disturbing any kind of total scattering analysis. A classical example is the fluorescence of iron oxide nanoparticles when a laboratory source equipped with a Cu target is used. Fluorescence effects are usually managed by resorting specifically devised experimental solutions. For example, laboratory equipment typically work with fixed-wavelength sources and one of the options to avoid measuring these effects is using a crystal analyzer on the diffracted beam, which is feasible only when point detectors are employed. Experiments performed at synchrotron beamlines have the advantage that the photon energy can be suitably tuned taking the sample composition into account, in order to avoid fluorescence emissions. However, the wavelength choice depends also on other experimental requirements, making fluorescence effects sometimes unavoidable. Nevertheless, modern detectors can directly suppress

fluorescent radiation by allowing an appropriate cut-off energy threshold to be set-up, provided that a large enough difference in energy with the incident beam is given. This is also the case of the Mythen 2.0 [5], the detector available at the X04SA-MS beamline.

Polarization Correction. Depending on the polarization state of the incident beam (π or σ polarization, with the electric field perpendicular to, or within, the scattering plane, respectively), the scattering intensity is modulated by a factor $P(2\theta) = 1 + A \cos^2(2\theta)/(1 + A)$, where 1 is the intensity correction required for a beam with π polarization and A is the intensity term related to σ polarization [6, 3]. For fully unpolarized beams from a laboratory source (X-ray sealed-tube or rotating anode), in the case of a non-monochromatic beam, A=1; when a single crystal monochromator with Bragg angle θ_M is used on the incident beam, $A=\cos^2(2\theta_M)$. Synchrotron beams are fully polarized and instruments are built so that the scattering plane is normal to the beam polarization. In these cases, A=0 and, therefore, P=1, when 1D detectors are used.

Lorentz Correction. The Lorentz correction is a factor used for normalizing the integrated intensity to the specimen volume that is actually sampled in reciprocal space, multiplying it by the spherical volume element $4\pi q^2 dq \propto \sin^2\theta \cos\theta \, d\theta \propto \sin(2\theta) \sin(\theta)$ and, eventually, allowing the correct values of the integrated intensity of Bragg peaks to be recovered. The correcting factor is needed only in conventional crystallographic modeling, either in single crystal or powder diffraction methods. Alternatively, for the powder diffraction case, the same correction can be thought as for normalizing the intensity to the fraction of crystallites in diffraction condition and to the sampled portion of the Debye-Scherrer cone. In other words, it is used for obtaining the

sample differential cross section [7]. Therefore, the correction is not necessary when the pattern modeling is obtained according to the Debye scattering equation, as it directly reproduces the differential cross section.

Absorption Corrections. When passing through a sample of thickness *t,* the incoming beam of X-rays or neutrons undergoes an attenuation according to an exponential law (Beer-Lambert):

$$I_T = I_0 \, exp[-\mu(E)t]$$

where μ is the sample *attenuation coefficient*, which depends on its chemical composition and density, and on the photon energy *E.* For X-rays, the attenuation is due to the interaction of the electromagnetic fields with the electronic clouds, through the basic mechanisms of the photoelectron absorption (*i.e.* the photon is absorbed by the atom and its energy is used to excite or ionize the atom) and of the scattering. For a wavelength $\lambda \approx 1$ Å (the typical wavelength for diffraction and structural investigations), the X-ray attenuation is dominated by the photoelectron absorption mechanism. For most of solid materials, the depth at which the X-rays intensity is reduced by a factor 1/*e* (~ 37%) is of the order of few tens of μm (10-40) [8].

As mentioned in the Introduction of this chapter, most of the data used for DFA (either those analyzed in this Thesis or in other cases reported in the literature) are collected at synchrotron beamlines, where the parallel nature of the beam makes the Debye-Scherrer geometry the most appropriate for powder diffraction instrumental set-ups (details can be found in the next paragraph, which focuses on the experimental set-up at the X04SA-MS beamline). Therefore, data collection is carried out in transmission mode and, with reference to the beam energy used for the

cases of study here presented, typically falling in the 15-20 keV range, the absorption phenomena may become very important. However, corrections are not trivial at all, at least for beams within this energy range or even below. It is worth noting that, for DFA and, in general for Total Scattering methods, it is highly desirable working with an experimental pattern related to only the scattering from the sample and free from absorption effects. Therefore, absorption corrections are strictly related to the more general process of data reduction. The procedure adopted for the cases of study considered in this Thesis is illustrated in the next paragraph; here some general aspects are presented. Things become complex mainly because of two factors:

i) The experimental total scattering cross section contains extra sample contributions, such as those from the sample holder (a glass capillary, in all cases here considered) and the environment, which typically have attenuation properties different from that of the sample. These extra sample contributions have to be taken into account, both on the scattering and the absorption side, and must be properly subtracted in order to obtain a reliable determination of the sample-related scattering. In particular, as the sample fills in the capillary (with non negligible wall thickness), the path length effectively travelled by the beam throughout the container, and before and after entering the sample, has to be accounted for, alongside its attenuation coefficient. The same consideration holds for the beam path in the environment.

ii) Though the attenuation coefficient $\mu(E)$ for the various elements for X-ray are tabulated and available, for example, at the US National Institute of Standards and Technology (NIST) website [9], the actual sample attenuation is difficult to be calculated, because the exact

knowledge of the sample composition is often not available and because the attenuation is also affected by the (unknown or only approximately known) powder packing. Therefore, measuring the $\mu(E)d$ quantity for the sample inside the capillary (d being the diameter of the capillary), via transmission (or 'radiographic') measurements, turns to be more accurate. The same quantity for the empty capillary needs to be evaluated, though it is more conveniently calculated from the tabulated values (provided that the glass composition is known).

Once the linear attenuation coefficients are estimated for the sample (μ_S) and for the empty capillary (μ_C), the transmission (or attenuation) corrections $t_S < 1$ and $t_C < 1$ can be achieved by tracing the paths through the sample and the container and by deriving the attenuation of an X-ray following this path (an approach similar to those proposed in refs. [10,11]). The attenuation corrections can be numerically calculated by a ray-tracing approach: $t_S(2\theta)=e^{-\mu_S L_S(P,2\theta)-\mu_C L_C(P,2\theta)}$, $t_C(2\theta)=e^{-\mu_C L_C(P,2\theta)}$ (L_S and L_C being the total beam paths through the powder and the capillary walls], and $t_{CS}(2\theta)$ [obtained as $t_S(2\theta)$ after properly considering the path lengths within the sample and the capillary walls]. Then, absorption correction curves (with their angular dependence) can be calculated for the sample [$a_S \approx N_S/t_S > 1$, N_S being the points falling in the sample region], the capillary in empty conditions [$a_C \approx N_C/t_C > 1$, N_C being the points falling in the capillary walls] and the capillary in filled conditions [$a_{CS} \approx N_C/t_{CS} > 1$].

3.2.2 Data collection strategy at the Material Science beamline X04SA@SLS and data reduction procedure.

The most important features of the Powder Diffraction endstation (http://www.psi.ch/sls/ms/powder-diffraction) of the Material Science beamline X04SA-MS of the Swiss Light Source are here summarized, focussing particularly on the aspects that are relevant for DFA. SLS at the Paul Scherrer Institut is a 3rd-generation synchrotron light source with energy of 2.4 GeV. The MS beamline is one of the first four to be built in 2001 and was served, until 2010, by a wiggler source with access to photon energies as high as 40 keV [12]. A comprehensive upgrade has become operational since 2011, which included the wiggler replacement by a permanent-magnet undulator and completely new optical systems, enabling access to a much higher brilliance of the beam, an energy range of 3-38 keV and a beam flux (at 10 keV) ~ 10^{13} photons/s [13].

Figure 3.3 shows the instrumental set-up of the powder diffractometer, in Debye-Scherrer geometry, with a vertical diffraction plane and three co-axial independent angular degrees of freedom. The inner stage allows the movement of the sample (pictorially represented, in Figure 3.3, by a yellow cylindrical sample holder, typically mounted on a spinner). The other two rotation stages carry independent detector systems, of which, the 1D silicon single-photon counting "microstrip" detector, called MYTHEN 2.0 detector [5], is of high relevance for total scattering techniques and for DFA. It has a modular structure and consists of 24 modules of 1280 Si-sensor elements each, for a total of 30720 channels working in parallel. It subtends a total angle of 120°, which enables data collection over a large angular range within few minutes of few tens of min.

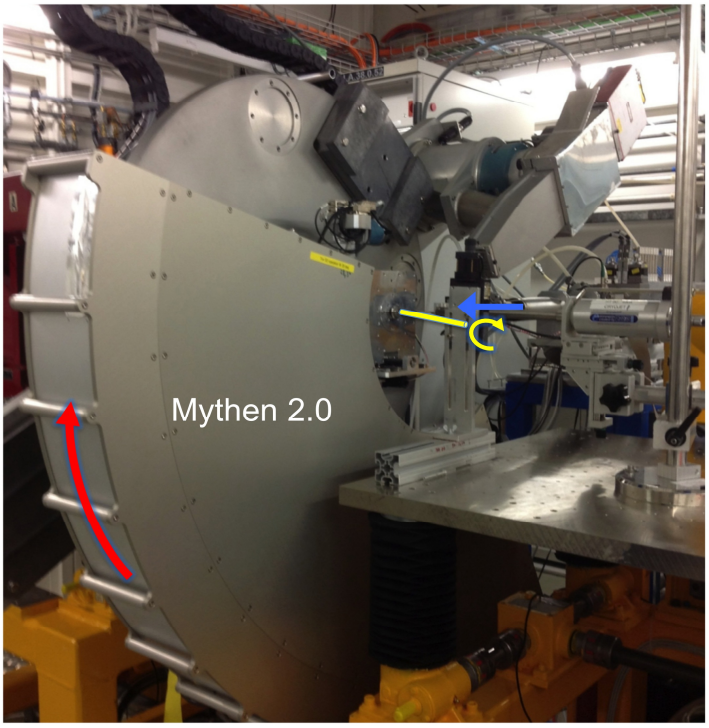

Figure 3.3 Instrumental set-up at the X04SA-MS beamline at SLS. The blue arrow pictorially describes the incoming beam, the yellow arrow the capillary spinning, the red arrow the detector movement.

Each module has a dynamic range of 16 Mcounts, with effectively zero dark noise. The efficiency is more than 85% for X-rays in the range 5–10 keV, but decreases to about 25% at 20 keV (because of the limited thickness of the silicon wafer). Narrow angular gaps of 0.17° between modules (each one subtending an angular range of 4.83°) are covered through multiple acquisitions by moving the detector in different positions (pictorially indicated by the red arrow in Figure 3.3). Additional important features are: *i)* the intrinsic high angular resolution, of 0.0036° (also depending on the long sample-to-detector distance of 760 mm), which allows the instrumental broadening contribution to the experimental pattern to be neglected. This approximation is particularly

acceptable when very broad peaks are measured from nanosized materials and thin capillaries (with diameter well below 1.0 mm) are used; *ii)* thanks to the approximately 1 keV energy resolution, some rejection of unwanted inelastic scattering is possible by properly setting a cut-off energy threshold. This is particularly useful for controlling sample fluorescence contribution.

Data collection and Data Reduction. For all the materials investigated in this work, the data have been collected (at the X04SA-MS beamline) using glass capillary sample holders of known composition (Hilgenberg GmbH 0140) with diameters ranging between 0.3 and 0.5 mm and nominal wall thickness of 0.01 mm. The beam energy was chosen in the range 15-20 keV, depending on the sample. In order to obtain a highly precise determination of the wavelength, diffraction data from an external standard reference material, typically silicon NIST 640c with certified lattice parameters, are collected for each instrumental set-up. For each sample, one transmission and three scattering measurements are carried out (*vide infra*). Before performing the "real" data reduction process, a correction is required to account for the efficiency of the detector elements (this is obtained by exposing all elements to an identical incident intensity and registering the detector response) and a merging of the several patterns acquired at different detector positions is necessary (both operations are achieved by applying a number of programs developed on purpose by the beamline staff).

Data reduction for DFA basically consists of three main steps:

1) Angular corrections due to both capillary displacement (Δx, Δy), in the scattering plane (inducing non-linear shift of the 2θ position), and detector zero-offset ($2\theta_0$);

2) Absorption corrections;

3) Capillary and environment scattering subtraction.

A scheme of the whole procedure, as applied to the materials here investigated, is proposed in Figure 3.4.

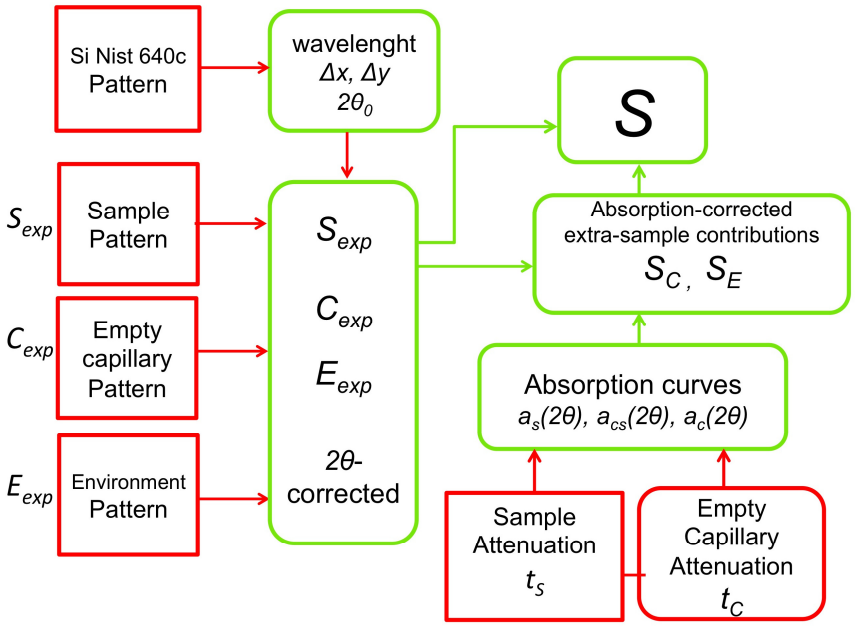

Figure 3.4 Scheme of the Data Reduction procedure.

As far as the angular corrections are concerned, capillary displacements ($\pm\Delta x$, $\pm\Delta y$) from the ideal position is to be intended as for beam displacement from the goniometer center (the capillary is positioned accordingly), which is likely to occur as schematically drawn in Figure 3.5, with reference to a laboratory system in which the *x*-axis runs parallel to the incident X-ray beam, the *xy*-plane coincides with scattering plane

and the *z*-axis runs parallel to the capillary (spinning) axis. The inset also shows possible deviations of the zero-position of the detector ($2\theta_0$).

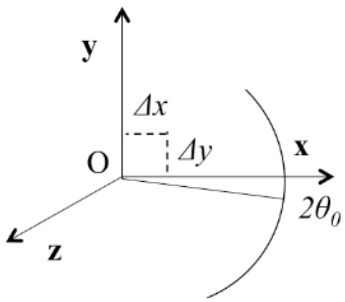

Figure 3.5 Schematics of The inset shows the capillary displacement (Δx, Δy), in the scattering plane and the detector zero-offset ($2\theta_0$)..

These values are usually recovered, simultaneously to the beam wavelength, by least-squares refinement of the pertinent parameters aiming at matching the peak positions of the certified materials. Absolute (Δx, Δy) values are typically estimated in the range from few hundredths to few tenths of mm; while values 2-10 times larger than the angular acquisition step (0.0036°) are typically estimated for the $2\theta_0$ offsets. The inset of Figure 3.6b shows the effects of the angular correction on the 111 and 220 peaks of the standard reference NIST silicon 640c. This correction is subsequently used for upgrading all the 2θ positions of the data collected on the investigated sample in the same experimental conditions.

With reference to the absorption corrections and the subtraction of capillary and environment scattering, from a practical point of view, besides the transmission measurement for estimating the true sample

attenuation coefficient for the specific energy, three additional measurements are necessary in order to acquire the scattering pattern of:

a) the sample within the capillary in the sample environment (S_{exp});

b) the empty capillary in the sample environment (C_{exp});

c) the empty environment (E_{exp}) (or surrounding background).

An example is shown in Figure 3.6a, for one of the samples of iron oxide nanoparticles investigated within this Thesis: the red, green and blue traces are the experimental patterns collected according to points *a)*, *b)* and *c)*, respectively. The inset shows the absorption correction curves (and their angular dependence) as calculated for the sample inside the capillary (a_s) and for the capillary in filled (a_{cs}) and in empty conditions (a_c) (red, green and blue curves, respectively).

The experimental sample pattern collected at point *a)* can be described as the sum of three different contributions ($S_{exp} = S_P + S_C + S_E$):

1) the attenuated scattering pattern from the powder inside the capillary (S_P) ($S_P \cdot a_s$ provides the absorption-corrected pattern required for DFA);

2) the scattering pattern from the container attenuated by the powder inside (S_C). The corresponding absorption-corrected term to be subtracted is obtained from the experimental patterns collected at point *b)* and *c)* as follows:

$$S_C = \left(C_{exp} - E_{exp}\, t_C\right) \frac{a_c}{a_{cs}}$$

where t_C is the attenuation correction calculated for the empty capillary.

3) the scattering pattern from the environment attenuated by both the capillary and the powder (S_E). The corresponding term to be subtracted is obtained from the experimental pattern collected at point *c)* as follows:

$$S_E = E_{exp} t_s$$

where t_S is the attenuation correction measured for the sample inside the capillary.

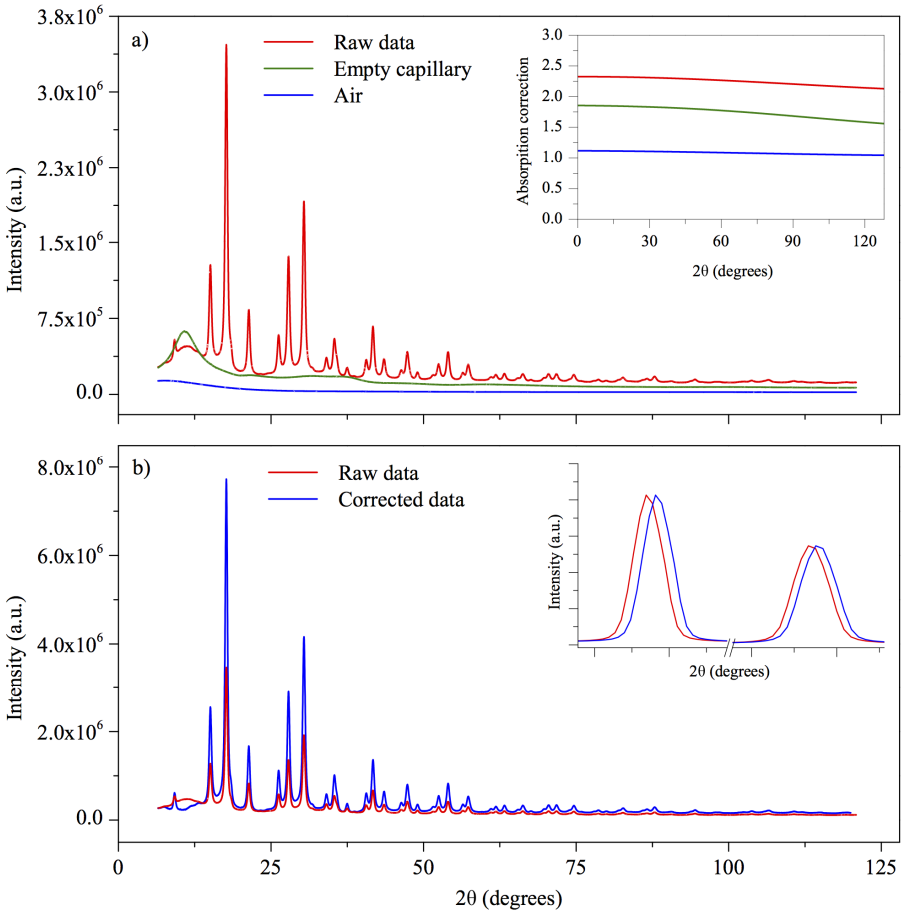

Figure 3.6 a) Scattering patterns, independently measured, of sample (red), empty capillary (green) and environment (blue). Inset: absorption curves for sample (red) and capillary in filled (green) and empty (blue) conditions. b) sample pattern (red) as collected and after data reduction. Inset: angular corrections on the 111 and 200 peaks of reference material Silicon NIST 640c.

The final "corrected and subtracted" sample scattering pattern (*S*) is obtained according to the following formula:

$$S = S_P a_s = (S_{exp} - S_C - S_E) a_s$$
$$= a_s \left[S_{exp} - \left(C_{exp} - E_{exp}\, t_C \right) \frac{a_C}{a_{cs}} - E_{exp} t_s \right]$$

The effects of this data reduction precedure can be seen in Figure 3.6b, where the "angle- and absorption-corrected and subtracted" pattern (red trace) of the same iron oxide NPs sample shown in Figure 3.6a, is compared to the raw data (blue trace).

3.3 Computational Aspects

The DFA relies on an a bottom-up approach, according to which the atomic coordinates of a single nanoparticle (for ideally monodisperse samples) or of a population of NPs (for real samples) must be known (even in an approximate way). Under this condition, DFA is typically carried out through a two-steps strategy: the set of inter-atomic distances is calculated for each NP (in real space) and, then, used in DSE to obtain the model diffraction pattern in reciprocal space. Despite the tremendous potential in the field of Nanoscience and Nanotechnology as a powerful physico-chemical characterization tool, DFA has rarely been used until recently, the most serious limitation being the problem of the DSE computational time. If *D* is the diameter of the nanoparticle, the number of terms to be summed up in the equation very quickly increases with the size and the structural disorder, showing a dependence on D^2 (ordered crystals) up to D^6 (amorphous materials). Advances in modern computers and fast CPUs (excluding the case of parallel computing and Graphical

Processor Units [14]) do not change significantly the picture for practical applications, unless specific tricks are adopted. Some of these are implemented in the Debussy Suite of programs that has been used in this Thesis for characterizing the different classes of nanosized materials. A brief introduction to the speeding up algorithms and the most relevant features of the Suite is presented.

3.3.1 Turning DSE into an efficient computational tool

Considering the two-steps strategy previously mentioned, there are two levels at which computational tricks can be applied, both involving only the "interference" term of DSE: 1) when calculating the set of interatomic distances and 2) when summing them up. Although periodicity and order are not a DSE prerequisite, nevertheless, the existence of any kind of symmetry and regularity within the NP can be used for shortening the list of interatomic distances. Since the distance between atoms *i* and *j* is equal to that between *j* and *i* (*i.e.* the equation is inherently invariant with respect to the symmetry inversion), half the number of terms is to be considered. Furthermore, the translational symmetry in nanocrystals always turns into additional equal scalar distances, further dropping the number to that of distinct non-zero values, each weighed by the appropriate multiplicity. As an effective example, two Au NPs of different size (5 and 50 nm) can be compared in terms of number of atoms (3852 *vs* 3851845) and of distinct non-zero distances (640 *vs* 64000). However, things change a lot, in terms of number of distances, if the two NPs have an amorphous structure (the number of atoms being unchanged): 7.4×10^6 *vs* 7.4×10^{12}. Therefore, a number of interatomic distances 10^2 or 10^6 times larger is obtained, respectively for

the ordered and the disordered case, upon increasing the NP size by a factor 10.

Taking into account the translational symmetry (just in the nanocrystalline case) is not sufficient to make the DSE computationally efficient, particularly for large NPs. In this view, the breakthrough relies on the possibility of using *sampled* distances instead of the original ones. In 1991 Hall and Monot [15] proposed the *binning* of the distances, an operation according to which all distances falling in the interval $k\delta_B \pm \delta_B/2$, with k an integer, are treated as the same distance and approximated with $k\delta_B$. Accordingly, the interference term turns into the sum of *equispaced distances* ($k\delta_B$), each one weighed by its pseudo-multiplicity W_k, carried out over a number of terms M_B equal to the number of bins:

$$C(q)\sum_{k=1}^{M_B} W_k \, sinc\,(2\pi k\delta_B)$$

with $sinc(x) = sin(x)/x$. Such a strategy makes the summation really convenient, from the computational point of view, since M_B grows with the *linear* size (D) of the NP or, equivalently, as $N^{1/3}$. However, it is not free of errors. In fact, it is equivalent to convoluting each distance in real space with a box function of width δ_B. Therefore, the pattern calculated using the set of binned distances needs to be multiplied by the FT of this function [the term $C(q)$] and a quite small binning step δ_B is required to ensure a good accuracy of this simulation, ending up with a compromise solution between a longer computing time (by narrowing δ_B and, then, increasing M_B) and a reduced accuracy.

A step forward in this sense has been obtained by convoluting the distances with a normalized Gaussian function of width $\Delta = \rho\delta_G$ (instead

of a box function) and, then, by sampling them using the step δ_G, as suggested by Cervellino *et al.* in 2006 [16]. It has been demonstrated that an optimal δ_G (producing relative accuracies within 10^{-8}) can be chosen as a function of the wavelength (λ) and of the maximun transferred momentum ($q_{max} = 2\sin\theta_{max}/\lambda$) of the experimental pattern, according to the criterium $\delta_G \leq 0.4/q_{max}$. As an example, for data collected up to $2\theta_{max}$ =160° with λ=0.4 Å, a sampling step $\delta_G \leq 0.08$ Å (giving 12000 sampling points) is enough to correctly reproduce (within the above mentioned approximation) the diffraction pattern of a NP 100 nm in diameter. Gaussian sampling provides $\delta_G >> \delta_B$ (by 1-2 order of magnitudes), with further reduction of the computational time. An additional advantage of using Gaussian sampled or binned distances is the speeding up of the second level of intervention. Indeed, being now distances *equi-spaced*, a fast transform can be used to calculate the DSE. A fast evaluation relies on Chebyshev polynomials of the second kind and their backward recurrence relations, as proposed in [16] and as implemented in the Debussy Suite [1].

3.3.2 DFA implementation in the DebUsSy Suite

The *DebUsSy* Suite of Programs is an open-source project (http://sourceforge.net/projects/debussy) specifically developed to perform the DFA of nanocrystalline materials and nanocomposites. The acronym stands for ***Deb***ye ***Us***er ***Sy***stem, meaning that it has been conceived for enabling any user to deal with its own nanosized materials (within the limits of the available modeling). The main features of the Suite are summarized below.

Fast DSE calculation. Gaussian sampled interatomic distances and a modified DSE are implemented to speed up the calculations, along with many crystal symmetry-related tricks (as briefly presented in the previous paragraph);

Population(s) of Nanocrystals. The occurrence of single-size NPs in a real sample is a rather ideal case, as real materials typically show a distribution of sizes and shapes. For many nanomaterials, monodispersity might play a key role for controlling their advanced properties. According to a commonly accepted definition, monodisperse samples must have a size dispersion $\sigma(D) \leq 0.1 \langle D \rangle$, not exactly matching the concept of a single size; moreover, many other materials do not match the definition, as they show wider size distributions. Therefore, dealing with populations of NCs is a fundamental aspect when modeling engineered or nature-made nanomaterials. In the Debussy Suite, populations of NCs of increasing size can be modeled, either with isotropic or anisotropic shapes. The goal of such a modeling component is extracting the information on the NPs size and shape distributions from the experimental pattern of real systems.

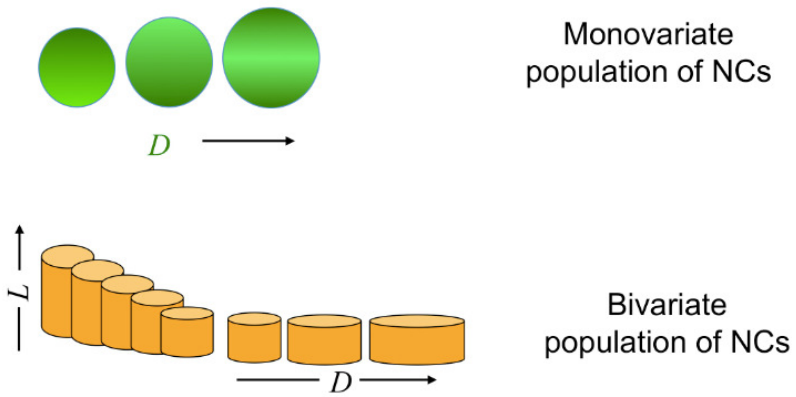

Figure 3.7 Schematics of mono- and bivariate populations of NCs that can be generated by the Debussy Suite.

The two-step strategy. The Debussy generalized strategy follows a two-steps approach: in the **first step**, a mono- (spheres, cubes) or bi-variate (rods and platelets) population of NCs of increasing size and selectable shape, is generated, as schematically shown in Figure 3.7. In the case of anisotropic shapes, NCs are grown according to two independent growth directions, one typically along the crystallographic 3,4,6-fold axis and the other one in the orthogonal plane, where the two growing directions are fixed to be equal by symmetry. The crystallographic unit cell is easily expanded from the asymmetric unit content and used as the NPs building block. For each NP, the set of sampled interatomic distances is, then, calculated and encoded in a suitable database. This step is performed through a suite of programs requiring a minimal input and (in the release 2.0) easily running through a Graphical User Interface [17].

The **second step** is dedicated to performing the DFA of the experimental pattern, using the previously generated database and a number of additional model parameters, which are further optimized by minimizing (through an iterative algorithm) the differences of the pattern model against the experimental data. Global optimization algorithms, such as Simulated Annealing and Simplex [18, 19], are available.

NPs size and shape distributions. The pattern simulation of each NP [$I_n(q)$] from a population of N_T nanoparticles contributes to the total simulated pattern $I_T(q)$ according to a suitable size distribution law (L_n), as follows:

$$I_T(q) = \sum_{n=1}^{N_T} I_n(q)\, L_n$$

With reference to L_n, Debussy uses a lognormal with two (monovariate population of NCs) or five (bivariate population of NCs) adjustable parameters [20], in the form of a discrete size distribution function (according to the discrete generation of NPs): $P(x_n)$, in the monovariate case, where the parameter defining the size $x_n = n\Delta$, n being an integer and Δ a constant increment; $P(x_n, y_m)$, in the bivariate case, with $= (n\Delta_x, m\Delta_y)$, n, m being integers and Δ_x, Δ_y the increments. P describes the fractions of NCs having size x_n with $\Sigma_n P(x_n) = 1$ [or size (x_n,y_m)] with $\Sigma_{n,m} P(x_n,y_m) = 1$]. The corresponding lognormal functions are:

Monovariate population of NCs:

$$P(x_n) = C \cdot \exp[-(\log x_n - \log < x >)^2/(2\sigma^2)]/x_n$$

where C is a normalizing factor (ensuring that $\Sigma_n P(x_n) = 1$) and <x> and σ^2 are the average size and its variance [$<x> = \mu_1$; $\sigma^2 = \mu_2 - \mu_1^2$, $\mu_1 = \Sigma_n x_n P(x_n)$ and $\mu_2 = \Sigma_n x_n^2 P(x_n)$ being the first and second normalized moments of the distribution]. The refinable parameters are <x> and σ (standard deviation). The fractions $P(x_n)$ typically refer to the number fractions (*i.e.* the fraction of the total number of NCs having size x_n). Useful and easily derived are also the mass/volume fractions $P'(x_n) = M_n P(x_n) / \Sigma_n M_n P(x_n)$ giving the fraction of the total mass of NCs having size x_n; here M_n is the mass of the *n-th* NC and the ratio ensures that the sum of fractions is 1.

A graphical example of number-based and mass-based size distributions of a population of TiO_2 spherical NPs is shown in Figure 3.8. It is worth noting that the two distributions (unless in the case of very narrow size dispersion) have different averages and standard deviations; in the example reported in Figure 3.8, the average diameter $<D>_N = 4.0$

nm and σ_N = 2.0 nm, while <D>$_M$ = 7.5 nm and σ_M = 3.3 nm. This aspect is of particular relevance when functional properties have to be correlated to this structural feature and, depending on the investigated property, the most appropriate pair, <D> and σ, should be considered.

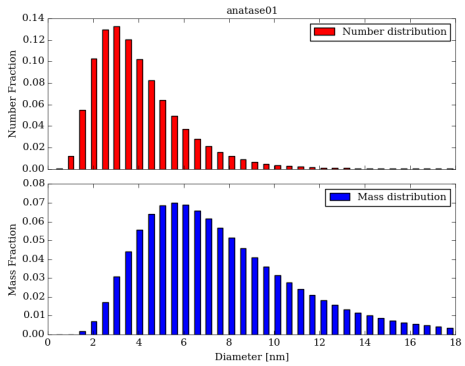

Figure 3.8 Number- and Mass-based size distribution functions for spherical TiO_2 nanoparticles with a size dispersion ~ 0.5 <D>.

Bivariate population of NCs:

A bivariate lognormal is appropriate for anisotropic growth along two directions and is slightly more complex than a pair of lognormals for the two size parameters.

$$P(x_n, y_m) = C \exp\left[-\left(\boldsymbol{L}RDR'\boldsymbol{L}\right)\right]/(x_n y_m)$$

with

$$\boldsymbol{L} = (\log x_n - \log < x >, \log y_m - \log < y >)$$

$$D = \begin{pmatrix} 1/\sigma_x^2 & 0 \\ 0 & 1/\sigma_y^2 \end{pmatrix}; \qquad R = \begin{pmatrix} \cos\phi & -\sin\phi \\ \sin\phi & \cos\phi \end{pmatrix}$$

where C is a normalizing factor (ensuring that $\Sigma_{n,m}\, P(x_n,y_m) = 1$), <x>, σ_x^2 and <y>, σ_y^2 are the average sizes and the projected variances along the

two growth directions [$\langle x \rangle = \mu_{1;x} = \Sigma_{n,m}\ x_n P(x_n,y_m)$; $\langle y \rangle = \mu_{1;y} = \Sigma_{n,m}\ y_m P(x_n,y_m)$; $\sigma_x^2 = \mu_{2;xx} - \mu_{1;x}^2$, $\sigma_y^2 = \mu_{2;yy} - \mu_{1;y}^2$, $\mu_{2:xx} = \Sigma_{n,m}\ x_n^2 P(x_n,y_m)$; $\mu_{2:yy} = \Sigma_{n,m}\ y_m^2 P(x_n,y_m)$; $\mu_{2:xy} = \Sigma_{n,m}\ x_n y_m\ P(x_n,y_m)$ being the first and second normalized moments of the distribution]; and with covariance matrix V and correlation coefficient *c*:

$$V = \begin{pmatrix} \sigma_x^2 & c\sigma_x\sigma_y \\ c\sigma_x\sigma_y & \sigma_y^2 \end{pmatrix}; \qquad c = \frac{\mu_{2;xy} - \mu_{1;x}\mu_{1;y}}{\sigma_x\sigma_y}$$

The correlation coefficient gives information on how much correlated are the two growth modes. In Debussy, refinable parameters are pairs of average size and standard deviation and the correlation angle.

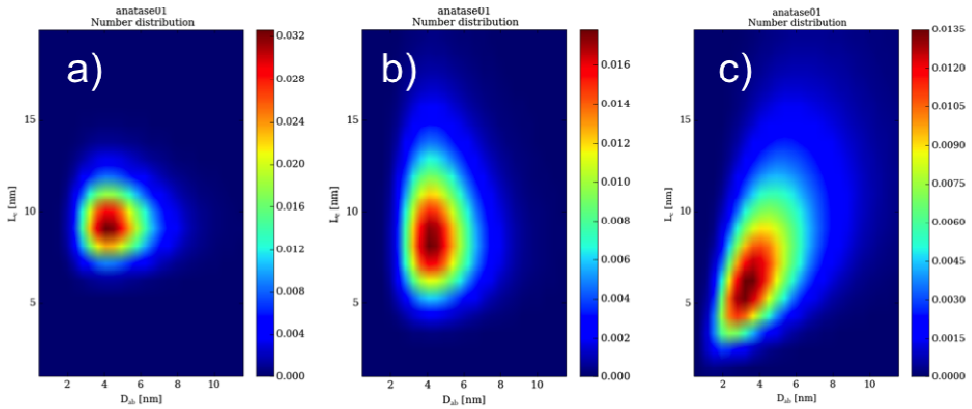

Figure 3.9 2D maps graphically depicting the bivariate lognormal size distributions of populations of NCs of TiO_2 anisotropically grown along two independent directions. The three panels show different parameter combinations of the lognormal function.

Graphical examples of bivariate lognormal size distributions are shown in Figure 3.8 for three different (simulated) combinations of the average sizes along the two growth axes, the size dispersions and the mutual correlation. The functions are represented as 2D maps (the graphical Debussy output) with NPs diameter, *D*, on the horizontal axis

and NPs length, *L,* on the vertical axis; the color scale bars map the number fraction of NPs having sizes (*D, L*). Panel a) depicts a population of NCs having an average diameter of 5.0 nm, an average length of 10.0 nm, similar size dispersions (1.5 nm) along both directions and no correlation between them; panel b) shows a population pretty similar to the previous case, the only difference being the larger size dispersion in the elongation direction (3.0 nm); the third panel shows the effect of a correlation between the two growth directions, the angle being ~60°; the average sizes and the standard deviations along the two directions are slightly different.

The size dependence of structural features. Modeling population of NCs is also of high relevance when taking into account that structural and microstructural properties are likely to change with the NP size. In Debussy such a dependence can be modeled for: *i)* deformation of interatomic distances (uniformly distributed within a single NP). Such a feature allows possible surface contraction or expansion phenomena to be treated; for monometric crystal systems (like in cubic materials), this turns into a modification of the lattice constant; *ii)* site occupancy factors (dealing with a size-variable sample stoichiometry); *iii)* atomic Debye-Waller factors. Details about the modeling will be given in the chapter dedicated to the specific case of study.

*The case of multiple pha*ses. In a very similar way to the case of a population of NCs, the total simulated pattern $I_{T_{PH}}(q)$ when multiple phases occur in the sample, is obtained as follows:

$$I_{T_{PH}}(q) = \sum_{k=1}^{N_{PH}} I_{T_k}(q)\, w_k$$

with N_{PH} the total number of phases, w_k the weight fraction of the k^{th} phase and $\sum_k w_k = 1$. w_k are determined through the refined scale factors of each pattern. Very useful, from this point of view, is the Debussy possibility of including and scaling, as an additional phase component, the experimental pattern of a phase of unknown structure (the typical case of amorphous components), which can therefore be quantified along with the other nanocrystalline phases (provided that the chemical composition is known).

Structural defects: Paracrystallinity and Stacking Faults. Both are very important phenomena which can be found in real materials but among the most difficult to be modeled. DSE seems to be the natural framework for dealing with structural defects and disorders, although in these cases the problem of the long computational time may still become relevant. Definition of the problem and details about the models implemented in Debussy are directly presented and discussed in chapters 6 and 7 treating the pertinent cases of study.

In conclusion, Debussy is a powerful computational tool to characterize nanomaterials via DFA and to extract quantitative information on crystal structure, size and shape of NCs, structural defects and their size-dependence, phase abundance and sample stoichiometry. The materials characterized in this Thesis have largely contributed to improve the models implemented in the Debussy Suite to treat specific sample features. This work has been addressed to preparing a new release of the Suite, which is expected to be ready in 2015.

References

1. A. Cervellino, C. Giannini, A. Guagliardi, *DEBUSSY: a Debye user system for nanocrystalline materials*, **2010**, J. Appl. Cryst, 43, 1543-1547.

2. A.H. Compton, S. K. Allison, *X-rays in theory and experiment*, **1935**, 2nd ed. Van Nostrand.

3. B. E. Warren, *X-ray Diffraction*, **1990**, 2nd ed., Dover, New York.

4. N. G. Alexandropoulos, M. J. Cooper, In *International Tables for Crystallography. Vol. C Mathematical, physical and chemical tables* (Ed. by E. Prince), **2006,** chapter 7.4.3, Compton scattering, 657–661, Kluwer, Dordrecht.

5. A. Bergamaschi, A. Cervellino, R. Dinapoli, F. Gozzo, B. Henrich, I. Johnson, P. Kraft, A. Mozzanica, B. Schmitt, X. Shi. *The MYTHEN detector for X-ray powder diffraction experiments at the Swiss Light Source,* **2010***,* J. Synchr. Rad., *17*, 653-668.

6. H. Lipson, J. I. Langford,H.-C. Hu, In *International tables for crystallography. Vol. C: Mathematical, physical and chemical tables* (Ed. by E. Prince), **2006,** chapter 6.2, Trigonometric intensity factors, 596–598, Kluwer, Dordrecht.

7. E. R. Pike, J. Ladell. *The Lorentz Factor in Powder Diffraction,* **1961,** Acta Cryst., *14*, 53-54.

8. P. Fornasini, *Basics of Matter-Radiation Interaction,* in *Crystallography for Health and Biosciences*, A. Guagliardi & N. Masciocchi Eds., **2012**, Insubria University Press, Varese, Italy

9. National Institute of Standards and Technology, *Physical Reference Data - X-Ray Form Factor, Attenuation, & Scattering Tables,* **2005**, (http://physics.nist.gov/PhysRefData/FFast/html/form.html)

10. H.H. Paalman, C. J. Pings, *Numerical evaluation of X-ray absorption Factors for cylindrical samples and annular samples cells*, **1962,** J. Appl. Phys., *33*, 2635-2639.

11. M. Bowden, M. Ryan, *Absorption correction for cylindrical and annular specimens and their containers or supports*, **2010,** J. Appl. Cryst., *43*, 693-698.

12 . B. D. Patterson et al., *The Material Science beamline at the Swiss Light Source: Design and Realization,* **2005**, Nucl. Instr. Meth. A, *540*, 42-67.

13 . P. R. Willmott et al., *The Material Science beamline upgrade at the Swiss Light Source,* **2013**, J. Synchr. Rad., *20*, 667-682.

14. L. Gelisio, C. L. Azanza Ricardo, M. Leoni, P. Scardi, *Real-space calculation of powder diffraction patterns on graphics processing units,* **2010**, J. Appl. Cryst., *43*, 647-653.

15. B. D. Hall, R. Monot, *Calculating the Debye-Scherrer diffraction pattern for large clusters,* **1991**, Comput. Phys., *5*, 414-417.

16. A. Cervellino, C. Giannini, A. Guagliardi, *On the Efficient Evaluation of Fourier Patterns for Nanoparticles and Clusters,* **2006**, J. Comput. Chem., *27*, 995-1008.

17. A. Cervellino, R. Frison, F. Bertolotti, A. Guagliardi, *DEBUSSY 2.0: a Debye user system for nanocrystalline materials,* **2015**, in preparation.

18. N. Metropolis, A. W. Rosenbluth, M. N. Rosenbluth, A. H. Teller, E. Teller, *Equation of state calculation by fast computing machines,* **1958**, J. Chem. Phys, *21*, 1087-1092.

19. J. A. Nelder, R. Mead, *A Simplex method for function minimization,* **1965**, Comput. J., *27*, 308-313.

20. P. D. Sampson, A. F. Siegel, *The measure of size independent of shape for multivariate lognormal populations,* **1985**, J. Am. Stat. Assoc., *80*, 910-914.

Chapter 4

Iron Oxide Nanoparticles

4.1 Introduction

Over the last two decades, iron oxide NPs (IONPs) have attracted a great deal of attention from both the fundamental knowledge and the application points of view, as they are of interest in many technological (high-density storage media, ferrofluids, electronic devices, catalysis) and biomedical applications [1,2]. In this field, in particular, Magnetite (Fe_3O_4) and Maghemite (γ-Fe_2O_3 or, equivalently, $Fe_{2.67}O_4$) NPs with sizes < 50 nm, show an intriguing super-paramagnetic behavior with appealing use in diagnosis (magnetic resonant imaging, MRI), therapy (hyperthermia, targeted drug-delivery) and theranostic technologies. In the diagnostic case, very small NPs (< 10 nm) with narrow size distribution and controlled composition are of interest. At this small size, super-paramagnetic properties originate from a rather complex interplay of structural, compositional and surface effects, depending on both NP size and oxidation state, which makes the physico-chemical characterization of this materials and the interpretation of their magnetic properties still a challenging task.

From the structural point of view, Magnetite has an inverse spinel structure (*Fd*-3*m*) in which oxygen atoms (Wyckoff position 32*e*) form a closed-packed cubic lattice, Fe^{3+} ions (Wyckoff position 8*a*) are located in the tetrahedral sites and a 1:1 mix of Fe^{2+} and Fe^{3+} ions (Wyckoff position 16*d*) fill the octahedral sites. The easy oxidation of Fe^{2+} in air has multiple (well known but uncontrollable) effects, causing: *i)* the iron diffusion outwards (leaving vacant sites in the crystal lattice); *ii)* the lattice parameter contraction ($a_{Magnetite}$ = 8.3967(3) Å, [3] shrinks to $a_{Maghemite}$ = 8.3457(-) Å, [4]); and *iii)* the formation of non-stoichiometric magnetite-maghemite core-shell NPs ($Fe_{3-\delta}O_4$, δ < 1/3), or of pure

maghemite ($\delta = 1/3$), as a consequence of partial and complete oxidation, respectively. Things are further complicated by the fact that iron vacancies can either be randomly distributed, without any change of the starting crystal space group, or partially/totally ordered; in these cases, the space group transforms into cubic $P4_132$, [5] or tetragonal $P4_12_12$, [6].

As far as the NPs size is concerned, depending on the synthesis route, NPs size distributions can be differently kept under control. Thermal decomposition of organometallic precursors or metal complexes in the presence of surfactants [7-9] is known to enable highly precise control of both size and size distribution through accurate dealing of the reaction temperature and the surfactants concentration. Despite such an advantage, the hydrophobic nature of the NPs surface, the limited amount of the synthesized material and the cost of reactants presently make this synthetic method not particularly viable for biomedical applications. In this view, co-precipitation of Fe^{2+} and Fe^{3+} salts in aqueous media [10,11] at a basic pH remains the most adopted and efficient chemical pathway, though such a method hardly results in very narrow and controllable size distributions.

Regardless of the synthetic method used, very small core-shell magnetite-maghemite NPs are difficult to be fully characterized in terms of size, composition and surface structure, all these features being relevant in addressing the actual magnetic properties. Indeed, a combination of complementary techniques, typically including XRPD (to assess structure and phase purity), TEM (to estimate NPs size distribution) and Mössbauer or other spectroscopies (to estimate sample oxidation state) is commonly used. However, these techniques operate at different sample scales and “see” different sample features. Both XRPD

and Mössbauer spectroscopy provide information that are averaged over the whole irradiated sample volume, though XRPD "sees" only the crystalline fraction. Closeness of peak positions and peak broadening make conventional XRPD rather ineffective in discriminating magnetite and maghemite. Analogously, Mössbauer spectroscopy suffers from serious limitations in accurately quantifying Fe^{2+} and Fe^{3+} when the NPs size is below 20 nm, as super-paramagnetic relaxation phenomena lead to broad and overlapped lines and make the hyperfine structure unresolved [11]. As far as the TEM NPs size estimation is concerned, a limited number of NPs is analyzed (typically 100–300) compared to the amount ($>10^{12}$ NPs) investigated by the other two techniques; moreover, only number-based average sizes are provided, which are rather inappropriate for interpreting mass- or volume-dependent magnetic properties, unless highly monodisperse samples are characterized. This is not the case of the co-precipitated IONPs here investigated.

The work presented in this chapter is the first case of application of DFA to IONPs. The extensive DFA characterization refers to the NPs composition, in terms of stoichiometry and core-shell magnetite-maghemite ratio, their average sizes and their number- and mass-based size distribution, their size-dependent oxidation and their lattice relaxation phenomena. The magnetic properties here measured are discussed and interpreted using the NPs structural and microstructural features provided by DFA. Thanks to the characterization of a large ensemble of samples, a predicting law of size effects on the lattice parameters is derived, within reasonable approximations, and the potential applications to similar systems discussed. As a completing part of this work, a critical study of the current literature reporting on conventional XRPD investigations and

PDF analysis of IONPs is also included and the comparison of the results obtained using Laboratory X-ray data *vs* synchrotron data presented.

Table 4.1. Synoptic collection of all investigated samples. [(1)] a = air, v = vacuum

Sample	Synthesis Conditions				Post-Synthesis (1)	Post-Synthesis (2)	Time Lag from Synthesis to Measures Experim. Conditions	
	[M] Fe(II)	*[M] Fe(III)*	*Solvent and Base*		*T (°C), Time (h),*	*T (°C), Time (h),*	*Days*	*Instrumental set-up*
A1	0.017	0.034	H_2O	NH_3	50, 16, a[1]		16	Syn - 15 keV
A2	0.050	0.100	H_2O	NH_3	50, 16, a		30	Syn - 15 keV
A3	0.050	0.100	H_2O	NH_3	r.t., 16, a		3	Syn - 15 keV
A4	0.050	0.100	H_2O	NH_3	50, 16, v[1]		3	Syn - 15 keV
A5	0.100	0.200	H_2O	NH_3	50, 16, a		9	Syn - 15 keV
A6	0.100	0.200	H_2O	NH_3	50, 16, a	r.t., 2, H_2O_2	2	Syn - 15 keV
A7	0.100	0.200	H_2O	NH_3	50, 16, a	200, 3, a	93	Syn - 15 keV
A8	0.100	0.200	H_2O	NH_3	50, 16, a	200, 16, a	2	Syn - 15 keV
B1	0.005	0.010	H_2O	NH_3	r.t., 2, v		68	Syn - 16 keV
B2	0.050	0.100	H_2O	NH_3	r.t., 2, v		84	Syn - 16 keV
B3	0.100	0.200	H_2O	NH_3	r.t., 2, v		55	Syn - 16 keV
B4	0.250	0.500	H_2O	NH_3	r.t., 2, v		53	Syn - 16 keV
B5	0.250	0.500	H_2O	NH_3	r.t., 2, v	50, 6, a	18	Syn - 16 keV
B6	0.250	0.500	H_2O	NH_3	r.t., 2, v	100, 6, a	17	Syn - 16 keV
B7	0.250	0.500	H_2O	NH_3	r.t., 2, v	150, 6, a	14	Syn - 16 keV
B8	0.250	0.500	H_2O	NH_3	r.t., 2, v	200, 6, a	13	Syn - 16 keV
B9	0.250	0.500	H_2O	NH_3	r.t., 2, v		10	Syn - 16 keV
B10	0.250	0.500	H_2O	NH_3	r.t., 2, v	100, 6, v	10	Syn - 16 keV
B11	0.250	0.500	H_2O	NH_3	r.t., 2, v	200, 6, v	7	Syn - 16 keV
C1	0.365	0.333	H_2O	NH_3	r.t., 16, a		7	Lab, Cu-Kα
C2	0.050	0.000	H_2O	NH_3	r.t., 16, a		1	Lab, Cu-Kα
C3	0.050	0.000	H_2O	NH_3	r.t., 16, a		24	Syn - 16 keV
C4	0.100	0.000	H_2O	NH_3	50, 3, a		13	Syn - 15 keV
C5	0.050	0.000	H_2O	NH_3	r.t., 16, a		7	Syn - 16 keV
C6	0.050	0.000	H_2O	NH_3	r.t., 16, a	100, 1, a	1	Syn - 16 keV
C7	0.050	0.000	H_2O	NH_3	r.t., 16, a	150, 2, a	1	Syn - 16 keV
D1	0.050	0.100	H_2O:EtOH 3:1	NH_3	50, 16, a		143	Syn - 15 keV
D2	0.050	0.100	H_2O:EtOH 1:1	NH_3	50, 16, a		143	Syn - 15 keV
D3	0.050	0.100	H_2O:EtOH 1:3	NH_3	50, 16, a		143	Syn - 15 keV
E1	0.050	0.100	H_2O/CTAB/ 1-Butanol/ 1-Octanol	NH_3	r.t., 16, a		11	Syn - 15 keV
F1	0.400	0.800	HCl 0.5 M	NaOH	r.t., 2, v		83	Syn - 16 keV
G1	--	0.100	H_2O	NH_3	50, 16, a		30	Syn - 15 keV

4.2 Experimentals

A large set of samples was prepared according to suitable modifications of the co-precipitation protocol [10] and under a variety of synthetic conditions, in order to enlarge the ranges of IONPs sizes and oxidation states, which were obtained by tuning: 1) the iron salts molar ratio and concentration (in oxygen-rich or oxygen-free solvent); 2) the post-synthesis temperature treatment and 3) the post-synthesis environment (air or vacuum). Table 4.1 synoptically lists all samples grouped with A to G labels, depending on the synthesis details, which are provided in the Annex 1.

4.2.1 Synchrotron and laboratory X-ray measurements

Synchrotron X-ray scattering data were collected at the X04SA-MS beamline [12,13] of the Swiss Light Source in three distinct experimental sessions, using the experimental set-up described in chapter 3, and 0.3 mm glass capillaries; a partial He beam path allowed the scattering by air to be decreased. The majority of the data sets were measured using the beam energy of 15 keV, the remaining ones using 16 keV, corresponding to 0.82712(4) and 0.77490(3) Å wavelengths, respectively. All the 30 samples underwent the data reduction procedure described in chapter 3, which enabled a total scattering pattern modeling free of any *phenomenological* contribution. Some examples are shown in Figure 4.1.

Laboratory diffraction data were collected overnight, in the 2θ range of 10-100°, with 0.02° steps, on two freshly prepared samples (C1 and C2 of Table 4.1), deposited in the hollow of a quartz zero background sample-holder. A Bruker AXS D8 Advance diffractometer, equipped with Ni-filtered Cu–K$\alpha_{1,2}$ radiation (λ_1 = 1.5406 Å and λ_2 = 1.5434 Å) and a

Lynxeye linear position-sensitive detector (optimized for avoiding, at least partially, Fe fluorescence) was used. The following optics was adopted: primary beam Soller slits (2.3°), fixed divergence slit (0.5°), receiving slit (8 mm). The generator was set at 40 kV and 40 mA.

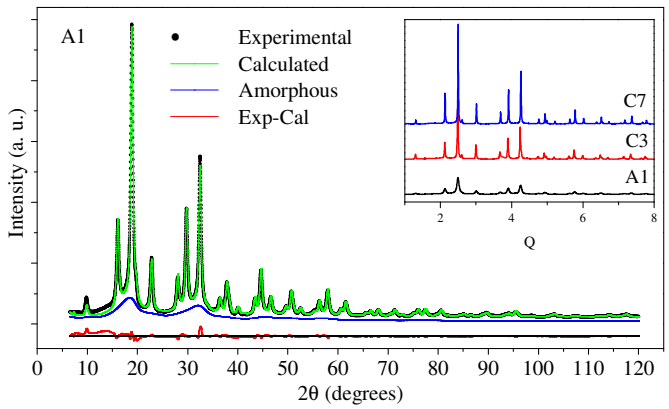

Figure 4.1 DFA best fit of A1 sample. The inset shows some synchrotron X-ray data collected on samples of increasing size (bottom to top).

4.2.2 Magnetic measurements

Magnetization measurements were carried out using a Physical Property Measurement System (PPMS, Quantum Design, San Diego CA, USA). Magnetization (M) versus applied field (H) hysteresis cycles were acquired at 2 and 300 K. Zero-field-cooled (ZFC) and field-cooled (FC) curves were taken in the 2–300 K range, with applied field H = 200 Oe. To acquire ZFC curves, the samples were first cooled, in zero applied field, from r.t. to the base temperature of 2 K, then the field was applied and the magnetization measured while increasing the temperature up to 300 K. Afterward, magnetization was measured on cooling the sample to the base temperature keeping the same applied field (FC).

4.3 Modeling and DFA of magnetic IONPs

The DFA modelling of IONPs was performed, for each sample, by applying the two-stage strategy of the Debussy Suite [14] described in chapter 3. The two main computational steps, in this case, can be summarized in:

1. Generating a discrete population of pure Fe_3O_4 nanocrystals of spherical shape and increasing size, Δr of subsequent spheres being equal to ≈ 0.33 nm; this step ended up with the sampled interatomic distances of each NP;
2. Calculating the pattern simulation, and further adjusting it against the experimental trace, by optimizing:
   a) The NCs size distribution, assuming a lognormal function, the average size ($<D>_N$) and width (σ_N) of which were the refined parameters. Adopting such a function is justified by experimental observations and many theoretical models developed for single-process-driven NP syntheses [15,16];
   b) The size-dependent lattice parameter, using an inverse linear function with two refined parameters (ω, ξ):

$$X_s(n) = \omega + (\omega - \xi)(n_0 + 1/2)[1 - (n_0 + 3/2)/(n + 1/2)]$$

   where n and n_0 indicate cluster shell numbers, $X_s(n_0) = \xi$ and $X_s(n_0+1) = \omega$. Using a single lattice parameter for a core-shell NP is, in this case, an acceptable approximation, thanks to the close similarity of either the end-member lattice values or their bulk moduli, as also confirmed by the lack of evident peak broadening attributable to strain.

c) The size-dependent site occupancy factor (*sof*) of Fe in the octahedral site [Fe(oct)], with three refined parameters (O_0, O_1 and O_L), according to the following law:

$$O(D) = O_1 + (O_0 - O_1) \exp(-D/O_L)$$

where O_0 and O_1 describe the *sof* at the smallest and largest size and O_L the *sof* growth/decay factor.

d) The size-dependent Debye-Waller factor of each atom, according to a three-coefficient law similar to the one used for *sof*.

Parameters optimization was performed through the Simplex method [17]. The best fit for sample A1 is shown in Figure 4.1. The high quality of "clean" data and the total scattering approach enabled an additional amorphous-like component to be detected in most of the samples. Such a component showed a scattering trace very similar to that of the two-line ferrihydrite [18-20], a disordered iron oxy-hydroxide, the structure of which is highly debated. To properly take into account this component in the absence of a reliable structural model, a synthetic sample was prepared (G1), the experimental diffraction pattern of which was found to well behave as a blank curve and was scaled as part of the total pattern model by linear least-squares (the blue trace in Figure 4.1). The integral area under the scaled trace was further used to estimate the mass fraction of this component in each sample (typically in the 15–30 wt % range). Calculation of the G(r) function from the G1 experimental pattern (not shown here) provided a maximum correlation length of ~2.2 nm. Whether such an amorphous phase occurs as an additional external thin layer or as sub-nanometer iron oxo-clusters/disordered oxy-

hydroxides entrapped within the co-precipitated IONPs, cannot be assessed by DFA.

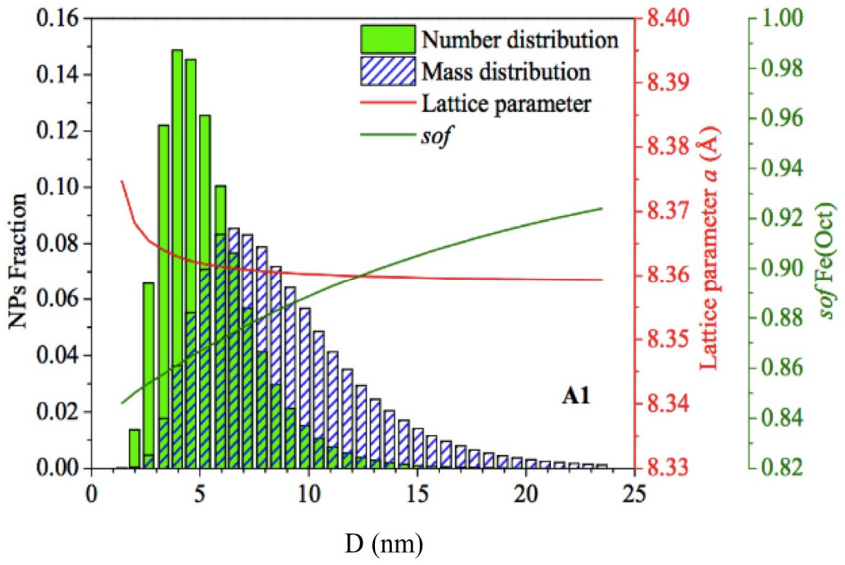

Figure 4.2 Number- and mass-based size distribution for the sample A1. Red and green curves describe the size-dependence of lattice parameter and *sof* of Fe(oct), respectively

DFA results in terms of size and size distribution, lattice parameter and stoichiometry are firstly discussed through the case shown in Figure 4.2 for sample A1. Here, the histograms describe number- and mass-based size distributions, leading to the number-based average diameter $\langle D \rangle_N$ = 5.30 nm and the mass-based one $\langle D \rangle_M$ = 8.54 nm. Average sizes and widths (σ_N and σ_M) of all samples are collected in Table 4.2. In order to provide an simple comparison criterion with the commonly reported (number-based) TEM sizes, as a rule of the thumb, for the IONPs here investigated $\langle D \rangle_M \approx 1.7 \langle D \rangle_N$. The red and green curves in Figure 4.2 describe, respectively, the refined size-dependent lattice parameter and

Fe(oct) *sof*. Interestingly, a lattice expansion upon decreasing the crystal size is indicated by the red curve while, according to the green curve, NPs simultaneously undergo a progressive oxidation, according to which a lattice contraction is expected. This behavior, observed in the majority of the samples possessing average $\langle D \rangle_M$ of ca. 10 nm (*i.e.* 80% of the samples), suggests that the reduced NPs size causes a surface relaxation (significant mainly below 5 nm), from which the observed inflation of the interatomic distances originates. This result, never observed before in IONPs, will be treated in detail later on.

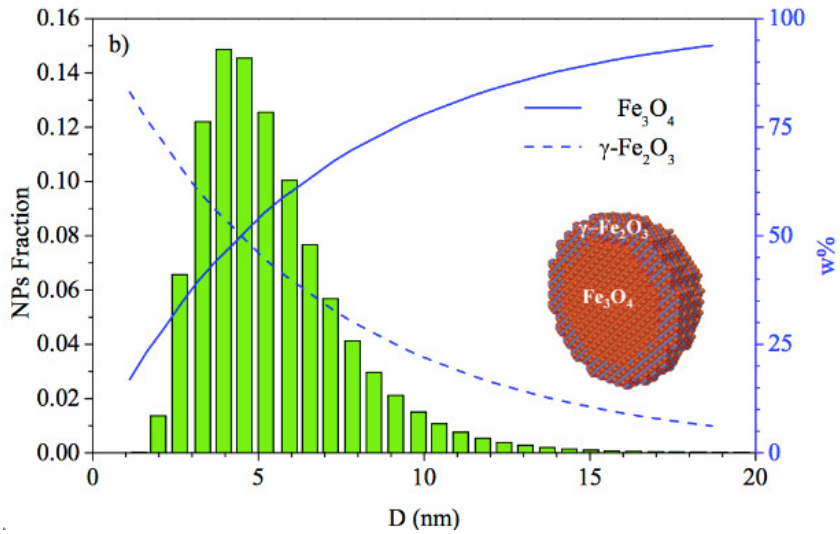

Figure 4.3 Relative variation of the core-shell composition in terms of weight fractions w% of Fe_3O_4 (core) and γ-Fe_2O_3 (shell) (as pictorially shown in the inset) as a function of the NP size.

Adopting the generalized formula $Fe_{3-\delta}O_4$ ($\delta = 0$ for magnetite, $\delta = 0.33$ for maghemite), the refined *sof* of Fe(oct) of each NP can be used to derive its stoichiometry $(3-\delta)$ and, by suitably weighting the contribution of each NP according to the corresponding (number or mass) fraction, the average sample stoichiometry $\langle 3-\delta \rangle$ can be calculated. These values, if

correctly estimated, can play a fundamental role in characterizing small IONPs in terms of core-shell composition, both at the NP and at the sample level. In fact, assuming an idealized core–shell model with a uniformly oxidized shell (therefore neglecting any compositional gradient), the relative weight fractions of magnetite (core) and maghemite (shell) were extracted, as it is depicted in Figure 4.3 for each NP of the sample A1. A first important result is that, differently to what reported elsewhere [11], particles as large as 10 nm may possess a Fe_3O_4 fraction close to 50%, though the average magnetite content in the whole sample is only 27%. The average magnetite fractions are reported for all samples in Table 4.2, alongside the radius of the Fe_3O_4 core (R_{core}) and the thickness of the γ-Fe_2O_3 shell (R_{shell}), also shown in Figure 4.3.

The question, therefore, arises about the accuracy of DFA-derived stoichiometry. The answer can be found in Figure 4.4, where the average cell parameter is plotted *vs* the average stoichiometry of all samples. The stoichiometry spans from pure maghemite [$<3-\delta> = 2.675(4)$) to barely oxidized magnetite ($<3-\delta> = 2.988(6)$].

The very good alignment of the regression (red) line witnesses the reliability of the DFA method to simultaneously determine both highly precise lattice constants and stoichiometry in very small NPs.

The lattice expansion does not influence too much the *average* lattice parameters, as witnessed by the dashed blue line of Figure 4.4, obtained after recalculating the average cell parameter of each sample for a subset of NPs representing the largest size fractions of each distribution (a threshold of 10 nm was applied). The new regression line slightly diverges from the red one at low and medium sample oxidation degrees.

Combined with the size information shown in Figure 4.2, this finding confirms that surface relaxation phenomena are effective for NP populations having a significant (>40%) mass fraction below 10 nm and that, taking such an effect properly into account, a reliable estimation of the IONPs stoichiometry might be obtained from its accurately derived lattice constant.

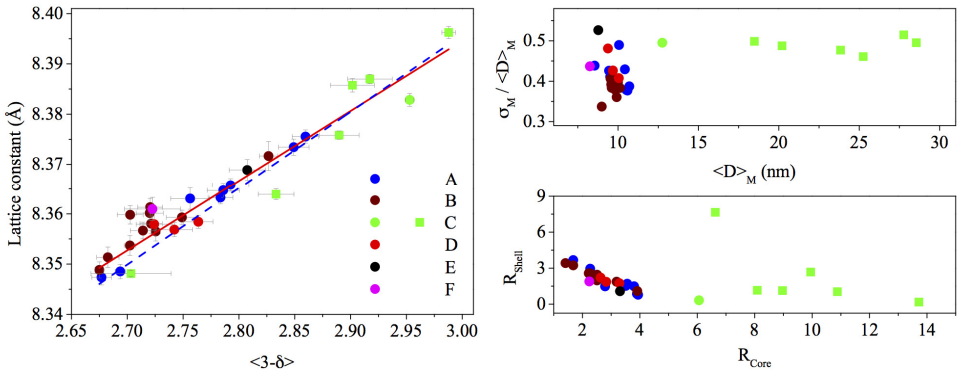

Figure 4.4 Average lattice parameter *vs* average sample stoichiometry <3−δ> and corresponding error bars. Orthogonal regression least-squares provided the straight red line; the dashed blue line is obtained when NPs < 10 nm are neglected (left). Right: (top) NPs average size and size dispersion show a cluster-like distribution, most samples falling in the narrow 8-13 nm range, the remaining in the wider 18-29 nm; (bottom) radius of the oxidized shell *vs* radius of the maghemite core.

Worth of note, while other analytical techniques usually provide the total Fe content, the DFA-based stoichiometry is determined for the nanocrystalline fraction only.

Table 4.2 Synoptic collection of the most relevant DFA results.

Sample	$<D>_N$ [nm]	σ_N [nm]	$<D>_M$ [nm]	σ_M [nm]	$<Cell>_M$ [Å]	$<3-\delta>$	<sof>	Fe_3O_4 w%	R_{core} nm	R_{shell} nm
A1	5.3	2.11	8.54	3.75	8.363(2)	2.76(1)	0.878(9)	27.27	2.79	1.48
A2	5.08	2.51	10.06	4.93	8.363(1)	2.78(1)	0.892(6)	33.33	3.51	1.52
A3	5.7	2.4	9.44	4.02	8.376(1)	2.86(1)	0.930(6)	57.58	3.94	0.78
A4	5.95	2.41	9.52	3.91	8.373(1)	2.85(1)	0.924(7)	54.55	3.9	0.86
A5	7.11	2.65	10.59	3.99	8.366(1)	2.79(2)	0.896(8)	36.36	3.8	1.49
A6	7.05	2.63	10.52	3.98	8.365(1)	2.77(1)	0.893(7)	30.3	3.56	1.7
A7	6.24	2.65	10.43	4.48	8.349(1)	2.694(4)	0.847(2)	7.27	2.27	2.95
A8	7.03	2.69	10.7	4.14	8.347(1)	2.677(9)	0.838(4)	2.12	1.68	3.67
B1	6.55	2.16	8.99	3.03	8.356(2)	2.725(4)	0.863(2)	16.67	2.51	1.98
B2	6.9	2.44	9.92	3.57	8.357(2)	2.71(1)	0.857(6)	12.12	2.51	2.45
B3	6.73	2.53	10.12	3.88	8.359(1)	2.75(1)	0.874(7)	24.24	3.19	1.87
B4	6.39	2.4	9.61	3.68	8.361(2)	2.72(1)	0.860(6)	15.15	2.61	2.2
B5	6.03	2.41	9.54	3.88	8.360(1)	2.72(1)	0.861(6)	15.15	2.59	2.18
B6	6.18	2.43	9.63	3.85	8.354(2)	2.702(5)	0.851(3)	9.7	2.28	2.54
B7	6.6	2.45	9.83	3.72	8.351(2)	2.68(1)	0.841(5)	3.03	1.68	3.23
B8	5.85	2.45	9.66	4.1	8.349(1)	2.675(4)	0.837(2)	1.52	1.41	3.42
B9	6.45	2.52	10	3.97	8.372(3)	2.826(8)	0.913(4)	47.27	3.91	1.09
B10	6.20	2.42	9.61	3.81	8.358(2)	2.72(1)	0.913(4)	15.15	2.61	2.2
B11	6.26	2.4	9.58	3.75	8.360(2)	2.70(1)	0.913(4)	9.09	2.22	2.57
C1	6.49	3.14	12.76	6.32	8.383(1)	2.953(4)	0.976(2)	85.76	6.06	0.32
C2	8.56	6.2	27.77	14.29	8.396(1)	2.988(6)	0.994(3)	96.36	13.72	0.17
C3	10.13	5.07	20.2	9.85	8.386(1)	2.90(2)	0.95(1)	69.7	8.97	1.13
C4	9.14	4.56	18.48	9.22	8.3758(8)	2.89(2)	0.945(6)	66.67	8.09	1.15
C5	11.78	6.05	23.84	11.37	8.3870(9)	2.92(2)	0.96(3)	75.76	10.88	1.04
C6	12.74	6.48	25.25	11.64	8.364(1)	2.83(1)	0.917(8)	48.48	9.95	2.67
C7	9.58	6.69	28.55	14.14	8.3481(6)	2.70(4)	0.85(2)	9.09	6.63	7.65
D1	6.32	2.54	10.05	4.1	8.358(1)	2.76(1)	0.882(7)	27.27	3.29	1.74
D2	5.83	2.46	9.68	4.13	8.358(2)	2.72(2)	0.862(8)	15.15	2.63	2.21
D3	4.89	2.35	9.37	4.51	8.357(1)	2.74(2)	0.871(8)	21.21	2.83	1.86
E1	3.9	2.11	8.77	4.62	8.369(2)	2.81(2)	0.904(8)	42.42	3.31	1.08
F1	4.9	2.08	8.25	3.6	8.361(2)	2.72(2)	0.87(1)	15.15	2.24	1.89

4.4 DFA *vs* magnetic properties

The magnetic properties were investigated on a subset of IONPs; samples showing different oxidation levels [low (C3), medium (B9), and high (B1, B3, B10 and B11)] were selected. The four samples of the B subset also show a rather similar size ($<D>_M \approx 10$ nm). All IONPs exhibit super-paramagnetic behavior both at low and room temperatures. Magnetization (M) versus applied field (H) at 2 and 300 K are shown in Figure 4.5 for the B9 and the C3 samples, possessing an average diameter of 10 nm and 20 nm, respectively (average mass-based values). Both samples, at 2K, exhibit a saturation magnetization (M_s) very close to that of bulk magnetite M_{sB} ~92 emu/g [21]. Samples coercivity (H_C) are in line with the values found for this kind of NPs [22].

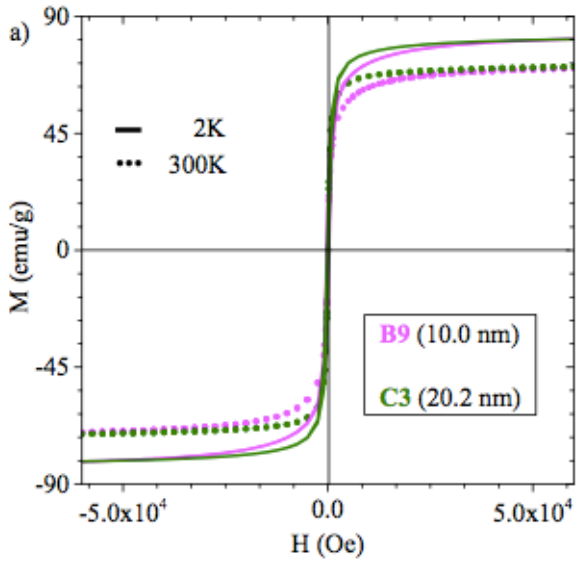

Figure 4.5 Magnetization (M) vs applied field (H) curves for two of the investigated samples: B9 (magenta solid and dotted curves) and C3 (grey solid and dotted curves).

Figure 4.6 shows the temperature dependence (2-300 K) of the magnetization in the ZFC-FC curves, at the applied field H=200 Oe, for samples with variable sizes and size distributions. The blocking temperature T_B (witnessing the transition from the ferromagnetic to the super-paramagnetic behavior) and the broadening of the ZFC curves are strongly affected by the NPs size and their distribution, both increasing with $\langle D \rangle_M$ and σ_M. This implies a broader distribution of energy barriers to magnetic moments reorientation, likely due to large dipole-dipole interactions between particles of larger size.

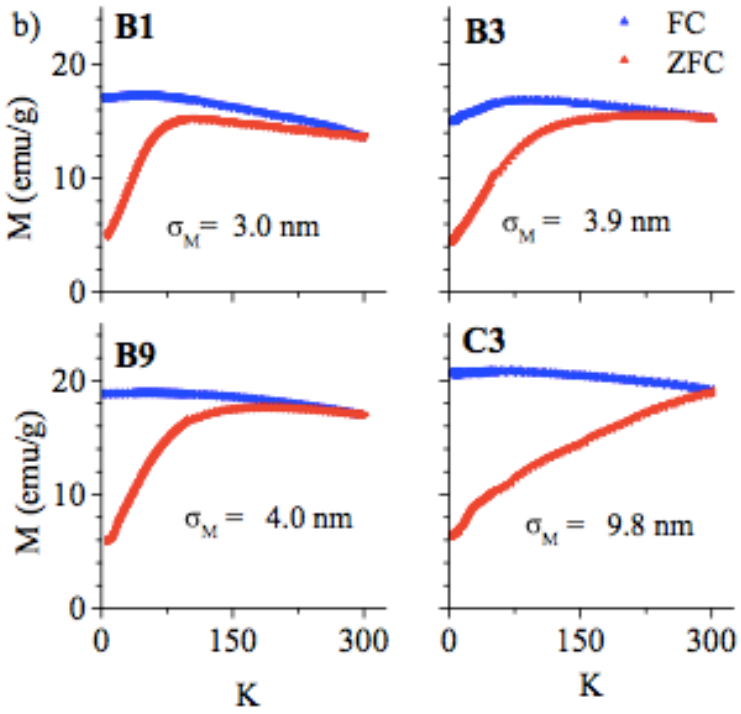

Figure 4.6 Temperature-dependent Magnetization (M) in ZFC (red) and FC (blue) experiments for samples having different size and size distribution.

The most relevant magnetic features are reported in Table 4.3 alongside their DFA-derived average size, width and composition (radius

of the magnetite core and thickness of the maghemite shell). A very interesting test was comparing the DFA-estimated average sizes with the magnetic domain sizes derived, for the same samples, through the Chantrell's equation [23], under the assumption of non-interacting NPs. Assuming a lognormal distribution in which the particles are weighed by considering the fraction of the total magnetic volume having diameters between D and $D + dD$, the center D_V and the width σ of the lognormal function are obtained, through the low field and high field portions of the room temperature magnetization curves, as follows:

$$D_V = \left[\frac{18k_BT}{\pi M_{sB}}\sqrt{\frac{\chi_i}{3M_s}\frac{1}{H_0}}\right]^{\frac{1}{3}}; \qquad \sigma = \frac{1}{3}\left[ln\left(\frac{{}^{3\chi_i}/_{M_s}}{{}^{1}/_{H_0}}\right)\right]^{\frac{1}{2}}$$

where k_B is the Boltzmann constant, T the absolute temperature, M_{sB} and M_s the saturation magnetization of the bulk magnetite and the IONPs, respectively; χ_i is the initial susceptibility calculated at low fields in the region where the dependence of M *vs* H is linear; $1/H_0$ is obtained by extrapolating H at M=0 in the plot of M vs 1/H at high fields, in the region where the dependence is linear.

In order to have values directly comparable to the (mass-based) average sizes provided by the DFA approach, $<D>_{Mag}$ (average diameter) and σ_{Mag} (standard deviation) are obtained as follows:

$$< D >_{Mag} = D_V e^{\sigma^2/2}; \qquad \sigma_{Mag} = < D >_{Mag} \sqrt{e^{\sigma^2} - 1}$$

The values reported in Table 4.3 show a good agreement between R_{core} and $<D>_{Mag}$, with the noticeable exception of the largest NPs sample (C3), likely due to stronger inter-particle interactions.

Table 4.3 Magnetic properties and some relevant DFA structural parameters of selected samples: M_S = Saturation Magnetization; T_B = Blocking Temperature; R_{core}= radius of the Fe_3O_4 core, R_{shell}= thickness of the γ-Fe_2O_3 shell; $<D>_{Mag}$ = magnetic domain size, σ_{Mag} = width of the log-normal size distribution; K_M and K'_M = Magnetic anisotropy constants.

Sample	$<D>_M$, σ_M nm	$<D>_N$, σ_N nm	M_S emu g^{-1} 2-300K	T_B K	2xR_{core} nm	R_{shell} nm	$<D>_{Mag}$, σ_{Mag} nm	K_M; K'_M (10^5 erg cm^{-3})
B1	9.0,3.0	6.5, 2.2	72.2 72.9	67	5.0	2.0	6.5, 2.6	4.4; 9.5
B3	10.1, 3.9	6.7, 2.5	84.0 83.8	100	6.4	1.9	5.9, 2.1	4.2; 8.7
B9	10.0, 4.0	6.4, 2.5	82.2 72.3	93	7.8	1.1	6.5, 2.3	4.0; 8.7
B10	10.0, 4.0	6.2, 2.4	74.5 66.0	131	5.6	2.2	5.6, 2.0	6.3; 8.8
B11	10.0, 4.0	6.3, 2.4	68.2 -	130	4.4	2.6	-	6.4; 8.9
C3	20.2, 9.8	10.1, 5.1	81.0 72.2	300	18.0	1.1	7.3, 2.4	1.3; 4.5

This finding suggests a major role of the magnetite core in determining the sample magnetization, which is further confirmed by the dependence, shown in Figure 4.7, of the saturation magnetization M_s on increasing the thickness of the oxidized shell in samples having similar average size and different R_{core}/R_{shell} ratio. M_s clearly decreases upon increasing the ratio and, very interesting, a linear law is found in B1, B9, and B11 samples exhibiting similar shell thickening at growing *R's* (within each sample population), whereas small deviations towards larger magnetization are observed in samples B3 and B10, showing a steepest oxidation profile, as shown in the bottom left inset of Figure 4.7.

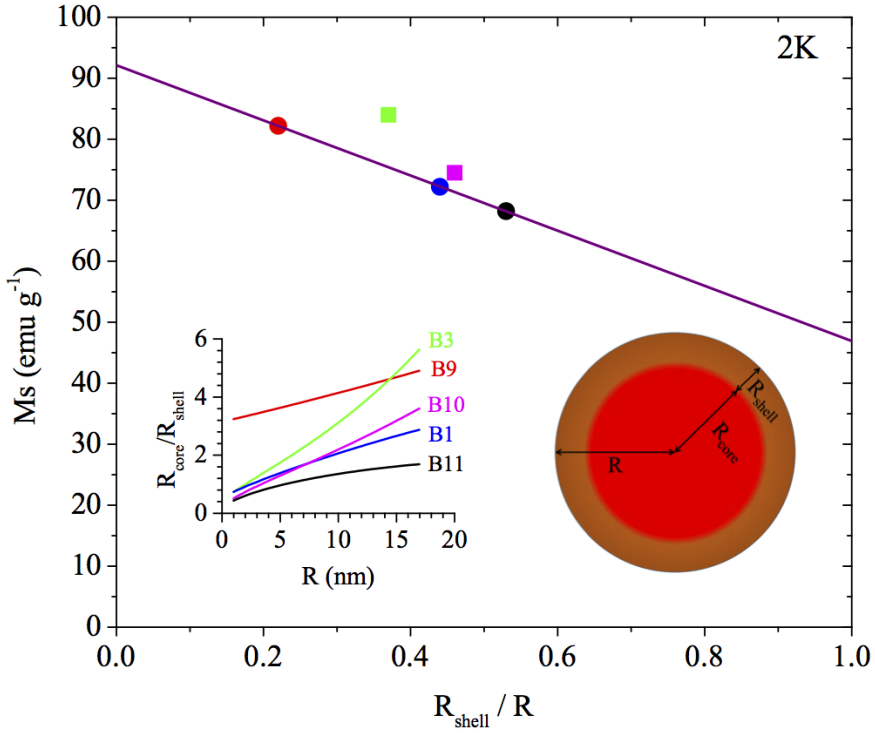

Figure 4.7 Saturation Magnetization (M_s) *vs* R_{shell}/R values in the B subset of samples, which possess a similar average size ($<D>_M \approx 10$ nm) but different R_{core}/R_{shell} ratio (shown in the bottom left inset for all NPs of each samples)

Worth of note, the regression line at $R_{shell} = 0$ (indicating pure Fe_3O_4) matches the saturation magnetization of the bulk magnetite, whereas at $R_{core} = 0$ (pure γ-Fe_2O_3), a value well below the M_s of maghemite (83.5 emu/g) [21] is obtained. Such a result might be caused by a completely oxidized "core" coupled to spin surface disorder, though internal canting effects further lowering the average sample magnetization cannot be excluded [24].

The rather "silent" behavior (from the magnetic point of view) of the external shell may be also explained by some peculiar features of the oxidized maghemite component, related to the appearance of very broad

"superstructure" peaks [5,25] revealing a partial ordering of the Fe ion vacancies, even for samples B1 and B3 (Figure 48a) that underwent r.t. oxidizing conditions.

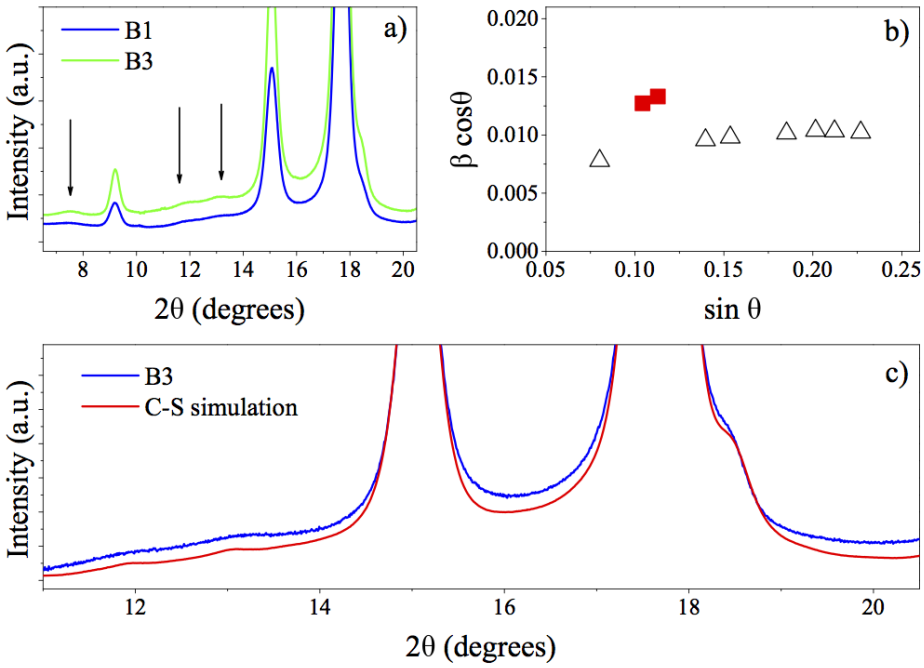

Figure 4.8 (a) Low-angle region of synchrotron data for B1 and B3 samples: the arrows mark the position of very broad peaks (210), (110) and (211) due to Fe ions vacancy ordering at r.t. (b) Integral beadth (β) *vs* angle (θ) in the Williamson-Hall plot for B3 sample: the red points refer to the superstructure peaks; (c) DSE simulation of a core-shell model (red trace) *vs* the experimental data of B3 sample (the red pattern is shifted downward for sake of clarity).

Figure 4.8b shows the widths of these peaks, which are significantly larger than the others and are not accounted for a core-shell model having core radius and shell thickness reported in Table 4.3, the DSE simulation of which provided narrower peaks (Figure 48c). All together, this seems to suggest the occurrence of a fragmented shell, never reported before in IONPs oxidized at r.t., with smaller coherent domains forming a

polycrystalline layer at the NPs surface, which might explain its negligible contribution to the sample magnetization. This point needs further investigation, also considering the NPs surface contribution to the magnetic anisotropy energy [26] (*i.e.* the directional dependence of magnetic properties), depending on the contributions of several terms accounting for magnetocrystalline (K_C), shape (K_{SH}), and surface (K_S) anisotropies and the dipole–dipole interactions between NPs (K_{IN}).

The magnetic anisotropy constant is typically taken as $K_M = 25k_BT_B/V$ [21], a relation valid for a single particle of volume V, or for a collection of NPs within an ideally perfect monodisperse sample. If applied to the samples here investigated, which have relatively broad size distributions, the "unrealistic" values reported in Table 4.3 are obtained. However, an additional advantage of the DFA characterization is the possibility of estimating an "effective" magnetic anisotropy constant K'_M, by modifying the previous relation in order to include the complete mass-based size-distribution of a collection of spherical NPs, [ζ(D), provided by DFA], as follows:

$$K'_M = 25k_B \int 6/\pi\, \zeta(D) T_B(D)/D^3 dD$$

under the hypothesis that the functional dependence of $T_B(D)$ is known. T_B was experimentally found to increase nearly linearly with particle size and in a way very similar to that reported by Park *et al.* [27] for monodisperse magnetic IONPs. Using the same dependence law as in ref. [27], ($\partial T_B/\partial \langle D \rangle_M \approx 24.1$ K nm^{-1}), the K'_M values given in Table 4.3 are obtained, in fair agreement with those reported in ref. [27] for narrowly distributed NPs of similar sizes. Interestingly, K'_M values show a clear inverse trend with the average particle size, witnessing the major

contributions of the K_S term (K_{SH} can be neglected according to the spherical NPs morphology), as can be expected when sizes decrease (and in the absence of surfactant effects [28]).

As for the amorphous component quantified in the 15–30 wt % range, under the hypothesis that it may form an external dead layer, a thickness varying between 0.3 and 1.0 nm was estimated, forming a silent layer further covering the maghemite shell.

4.5 Lattice parameters and iron vancancies: a critical study

During the DFA characterization of IONPs, a relatively large, and unexplained, spread of the lattice parameters, emerged from a deeper survey of the pertinent literature, particularly for maghemite NPs. Therefore, the question arose on the possibility that relatively large fluctuations may derive exclusively from sample features rather than from inaccurate estimates of the lattice parameters, which might easily originate when peaks are broad and necessary angular corrections are not applied.

This point is very important to be clarified when (diffraction-based) average lattice parameters are addressed to deriving reliable estimation of the average sample stoichiometry in non-stoichiometric magnetite-maghemite core-shell NPs, as done in this work and as might be extended to similar compounds. Moreover, differently from the bulk case, where iron vacancies are mainly located at the octahedral site [29], vacancies occurring in both the octahedral and tetrahedral sites of cubic NPs are reported on the basis of Rietveld-based [25] and Pair Distribution Function analyses [30]. This paragraph wants to contribute to clarifying the two aspects, taking the DFA approach point of view into account.

About Lattice Parameters. As far as the accuracy of the IONPs lattice parameter is concerned, for γ-Fe_2O_3, values range from 8.334(2) Å [30] to 8.3457(-) Å [4], whereas the much narrower 8.394(4) - 8.400 (*esd not available*) Å range is attributed to Fe_3O_4 NPs [31,32]. Although very small (perhaps negligible at the microscale), at the nanoscale such variations become important as they are possible indicators of surface effects, as also disclosed by DFA on the IONPs here investigated. Diehm *et al.* [33] have recently reviewed this topic and found that small metal oxide NPs tend (in a nearly systematic manner) to slightly expand (typically, but not exhaustively, in the 0.1-0.4% range) because of negative surface stress (within the frame of the capillary pressure model). Accordingly, for compounds like those here investigated, absolute lattice inaccuracies as large as 0.01 Å might be a serious limitation to the possibility of deriving the sample stoichiometry from the lattice parameter in a reliable way. Worth of note, a cell parameter variation $\Delta a = 0.01$ Å is *smaller* than the difference between Petkov's and Shin's reported parameters (and about one order of magnitude larger than the error presently achievable on small NPs from any standard modern powder diffractometer) and corresponds to an absolute $\Delta(<3-\delta>)$ value of 0.07, which turns into a relative stoichiometry error larger than 20%. In this view, it is also important highlighting that the standard deviations of the IONPs stoichiometry reported in Table 4.2 are in the 0.004 - 0.02 range. Are these differences due to specific sample effects?

To shed light on the question, the DFA results shown in Figure 4.4 have been further compared to those retrieved in the recent paper by Gorski and Scherer [31], correlating the cell values (from laboratory powder diffraction data) to the sample stoichiometry (derived by

independent Mössbauer spectroscopy) of partially oxidized magnetite NPs of $D \approx 20$ nm, as shown in Figure 4.9a (red points and solid red regression line).

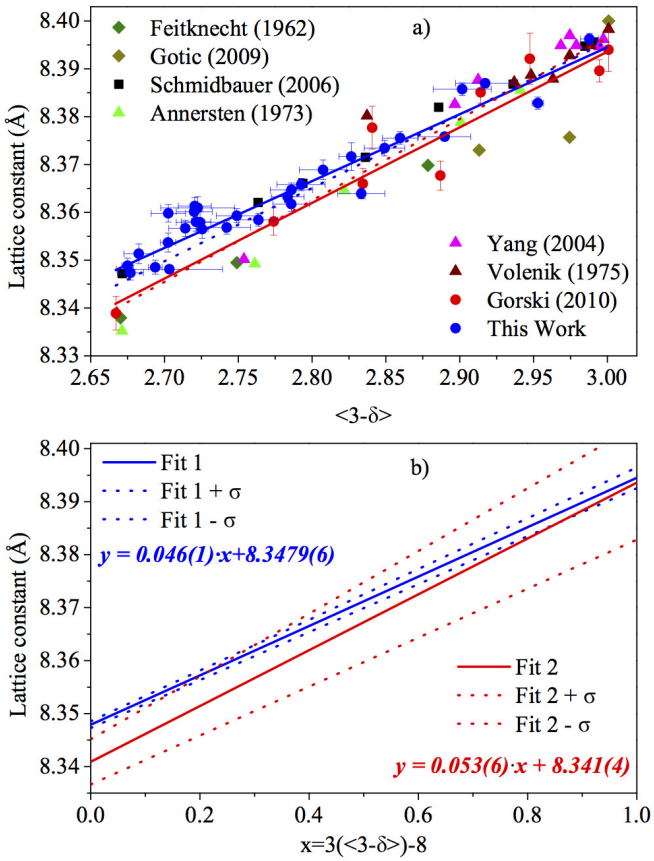

Figure 4.9 (a) Average lattice parameter *vs* average sample stoichiometry <3−δ> and corresponding estimated errors (vertical and horizontal bars, respectively): blue points refer to the samples here investigated, the other points are from Gorski and Scherer [31] and additional samples therein considered. The (solid and dotted) blue orthogonal regression lines are the same described in Figure 4.4 (full set of NPs and only NPs > 10 nm, respectively); solid and dotted red lines refer to NPs from Gorski and the full set of samples therein considered, respectively. (b) Regression (solid) and ±1σ (dotted) lines computed for the full set of NPs of this work (Fit 1, blue lines) and the set of samples from Gorski and Scherer (Fit 2, red lines).

Following the original paper, additional points from other works were also inserted [32,34-38]: the dotted red regression line was then obtained by considering the whole set of points, although most of the newly added points refer to significantly larger particles (micrometer-sized samples or NPs 150-200 nm large). The blue and red lines clearly indicate meaningful cell deviations between the two sets of samples (this work and Gorski's), particularly at low and medium sample oxidation degrees (a $\Delta a \approx 0.01$ Å is measured at $<3\text{-}\delta> = 2.75$), while the tendency to convergence at the largest $<3\text{-}\delta>$ values is observed, likely thanks to the larger size of slightly (or not-at-all) oxidized samples ($<D>$ larger than 15 nm for samples within this work), whose NPs fraction < 5 nm is small or totally absent.

As mentioned before, accuracy and precision of lattice parameters (*i.e.* the estimated standard errors) play an important role, as further discussed taking Figure 4.9b as reference. Here the abscissa is defined as $x = 3(<3\text{-}\delta>)\text{-}8$ ($x = 0$ for pure maghemite, and $x = 1$ for pure magnetite) or, in other words, in the $y = mx + q$ formulation, q is the 100% maghemitic cell and $(m+q)$ is the 100% magnetitic one. Regression ($\pm 1\sigma$) lines from this work and from Gorski's and Scherer's paper are reported as "Fit 1" and "Fit 2", respectively, and the dashed ($\pm 1\sigma$ lines highlight the significance of the small q value changes.

The extrapolated "maghemitic" cells for the samples here investigated range between 8.3479(6) (full set of NPs) and 8.3449(2) (NPs > 10 nm), respectively, well in agreement with the reference value from ref. [4] [8.3457(-) Å]; analogously, the extrapolated "magnetitic" cell of 8.394(1) Å closely matches that from ref. 3 [8.3967(3) Å]. Therefore, a clear linear

trend of the lattice parameter *vs* the sample oxidation degree, *within* the range defined by the two reference cell values, is indicated. As already motivated in the previous paragraph, surface relaxations phenomena can determine small deviations from the reference maghemitic cell, which should be properly accounted for only in the presence of relevant fractions of NPs < 10 nm. Similar effects on the magnetitic cell are likely unexpected since very small NPs having a pure magnetite composition are rather unstable and get easily oxidized.

Much larger *q* value changes are obtained in Fit 2 (red lines), well beyond the parameter precision achievable with modern diffractometers. Moreover, differences larger than those originating from surface relaxation effects are found for magnetite-maghemite NPs with similar oxidation degrees and sizes. Such large deviations, if not resulting from uncorrected experimental effects, in the case of Gorski's NPs might reflect (yet undisclosed) surface NPs *contraction*. Whether this finding originate from the diverse synthetic routes cannot be excluded, however, significant contributions to lattice variations on these causes are unlikely to be expected.

About Fe Vacancies. Until a few years ago, reports on γ-Fe_2O_3 particles (based on diffraction and spectroscopic techniques), systematically attributed the stoichiometric changes to formation of vacancies in the octahedral site. At variance, recent literature on maghemite NPs has pointed out the formation of cation vacancies at both the octahedral and the tetrahedral site. One example is provided by the in situ synchrotron X-ray study of Jørgensen *et al.* [25], in which γ-Fe_2O_3 NPs grown from an amorphous precursor were analysed by the Rietveld method and by the cubic *Fd-3m* structure, indicating that the majority of

the vacancies occur at the tetrahedral site [$sof_{Fe(tet)}$ = 0.865(1)] rather than at the octahedral one [$sof_{Fe(oct)}$ = 0.901(1)]. Interestingly, an unexpected (*hyper*-magnetite-like) lattice parameter of 8.4053(1) Å is also reported for this structure. Another example can be found in Petkov *et al.* [30]. Here both spherical and tetrapod-shaped iron oxide NPs (prepared through thermal decomposition of organometallic precursors in the presence of surfactants) were characterized by PDF analysis. An even smaller *sof's* of both cation sites (well below the δ=1/3 limit) is reported. Stimulated by these results, a new DFA of some samples here investigated was further performed, this time simultaneously refining both Fe sites *sof's* along with the lattice parameter. In order to limit the total number of refined parameters, the isotropic Debye-Waller thermal factors were kept fixed to the values obtained by the previous refinement for all atoms.

Table 4.4 Refined *sof's* of Fe ions at the octahedral [Fe(oct)] and tetrahedral [Fe(tet)] sites (Wyckoff positions are 8*a* and 16*d*, respectively), average lattice parameter ($<a>_M$) and stoichiometry ($<3-\delta>_M$) of samples A1 and A5 (case *a*) are compared to the values obtained by taking the [Fe(tet)] sites fully occupied ($sof_{Fe(tet)}$ = 1) (case *b*). Isotropic Debye-Waller thermal factors in case (*a)* were kept fixed to the values refined in case (*b)*.

Sample	$sof_{Fe(tet)}$	$sof_{Fe(oct)}$	$B_{Fe(tet)}$	$B_{Fe(oct)}$	B_O	$<a>_M$	$<3-\delta>_M$
A1 (*a*)	0.985(7)	0.882(8)	0.452	0.936	0.365	8.362(4)	2.75(2)
A1 (*b*)	1.0	0.893(6)	0.4(1)	0.94(3)	0.36(7)	8.362(1)	2.79(1)
A5 (*a*)	0.976(7)	0.887(6)	0.550	0.938	0.464	8.364(3)	2.75(1)
A5 (*b*)	1.0	0.905(5)	0.550(7)	0.94(1)	0.46(3)	8.364(1)	2.81(1)
γ-Fe_2O_3 [c]	0.865(1)	0.901(1)	1.14(2)	1.14(2)	1.9(5)	8.4053(1)	2.667
γ-Fe_2O_3 [d]	0.90(5)	0.80(5)	-	-	-	8.370(2)	2.5

[c] from Jørgensen *et al.*, 2007; [d] from Petkov *et al.*, 2009

The results are reported in Table 4.4 and compared to the cases in which only the *sof* $_{Fe(oct)}$ was refined. Values from ref. [25] and ref. [30] (spherical case) are also given. DFA modelling clearly indicates a rather modest amount of (randomly distributed) vacancies at the Fe(tet) site, never exceeding (if present at all) 3-4% of the total value. Therefore it seems to confirm that, when small magnetite NPs are oxidized, (most of) the cation diffusion comes from iron removal from the octahedral site.

4.6 Predicting size effects on lattice parameters in IONPs

This paragraph is dedicated to the derivation of a general law from the entire ensemble of NPs (meaning *all* NPs in *all* samples), under the main (acceptable) assumption that their surface conditions are likely to be nearly identical. In this case, and considering that the large number of samples here characterized cover a wide range of sizes and almost the full range of oxidation states x ($x = 3(<3-\delta>)-8 = 0$ for maghemite, and x = 1 for magnetite, as previously reported), the lattice parameter variations due to stoichiometry and to particle size can be usefully combined taking into account the interplay between bulk elastic energy and surface tension [33]. The derivation of the law relies on the following additional assumptions:

1) The magnetite-maghemite system can be considered as an ideal solid solution (*i.e.* with $\Delta H_{mix} = 0$) with small differences between the physical properties of the end members; therefore, a linear dependency of the lattice parameters on stoichiometry, x, can be assumed (as in Vegard's law):

$$a = (1 - x)\, a_{Maghemite} + x\, a_{Magnetite}$$

2) Each nanocrystal behaves as an isotropic medium, which makes the uniform isotropic strain a scalar parameter $\varepsilon = \Delta a/a$. Thus, the NP diameter (D), the surface area (S) and the volume (V) depend on the strain as: $D=D_0(1+\varepsilon)$, $S=S_0(1+\varepsilon)^2$, $V=V_0(1+\varepsilon)^3$, respectively, where D_0, S_0, V_0 are the unstrained quantities and, for a sphere, $S_0= \pi D_0^2$ and $V_0=\pi D_0^3/6$. In these conditions, the surface energy change due to strain (ΔE_s) and the bulk elastic strain energy change (ΔE_b) can be easily derived as:

$$\Delta E_s = \gamma[(1+\varepsilon)^2-1]S_0 = \pi \gamma (2\varepsilon+\varepsilon^2) D_0^2$$

where γ is the surface tension, defined as the quantity of energy needed to create a unit of new surface;

$$\Delta E_b = (9/2) B \varepsilon^2 V_0 = (3/4) \pi B \varepsilon^2 D_0^3$$

where B is the bulk modulus [39], the only elastic constant to be considered in isotropic media. Therefore, the total energy $\Delta E_b + \Delta E_s$ is minimal when

$$\varepsilon = -[4\gamma/(3B)]/\{D_0 + [4\gamma/(3B)]\} \equiv -\Omega / (D_0 + \Omega), \quad \text{where } \Omega = 4\gamma/(3B).$$

3) Ω does not change with respect to x*;* this assumption is largely justified by the similarity of the bulk moduli (B): 186 GPa for magnetite [40] and 203 GPa for maghemite [41]. It is also assumed that B does not change with the (very small) volume change associated to strain.

Since Ω has to be very small compared to D_0, it can safely state that

$$\varepsilon \approx -\Omega/D_0 \quad \text{or equivalently} \quad D = D_0 (1- \Omega/D_0)$$

Thus, stoichiometry and size effects are combined in the following single equation, with a single adjustable parameter (Ω):

$$a = \left[(1-x)a_{Maghemite} + xa_{Magnetite}\right]\left(1 - \frac{\Omega}{D}\right)$$

After extracting the lattice parameter and composition *vs.* particle diameter curves of all samples, and evaluating point-wise standard deviations, all the data were fitted by the previous equation, giving an excellent fit (GoF ≈ 1) and a value of Ω = -2.05(21) 10^{-3} nm, with a rather uniform residual distribution. A graphical representation is given in Figure 4.10 for NP diameters up to 10 nm.

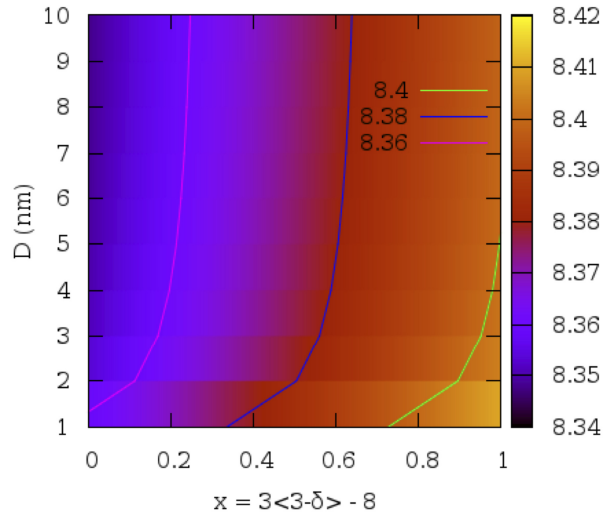

Figure 4.10 2D map of the predicted lattice parameters upon varying the NP stoichiometry and size (up to diameters D ≤ 10 nm).

Worthy of note, this law predicts *an inflation* of the cell parameter upon decreasing the NPs size while keeping constant the oxidation degree. According to ref. [33] this is a common behavior for oxides, meaning that the surface tension must be *negative*.

A similar fit, performed upon assuming a linear dependence of Ω with *x*, did not yield better results, meaning that data of better quality are necessary to detect this subtle effect. The similarity of the two bulk

moduli explains why strain gradients are negligible in the samples here investigated. The magnitude of the surface tension γ for wet-synthesized (and probably ferrihydrite-terminated) magnetite-maghemite NPs can be estimated to be –1.8 to –2.0 eV/nm^2 using either values of the bulk modulus. A generalization to other kinds of surface termination, likely obtained by other synthetic routes/environments, is straightforward as only the value of Ω is supposed to change, depending on the change in γ.

4.7 Synchrotron *vs* laboratory data

In this paragraph the DFA results obtained on parallel measurements using conventional laboratory equipment and synchrotron radiation on the same sample (A2) of the IONPs listed in Table 4.1, are compared. The test was performed using the instrumental set-ups described in paragraph 4.1 and similar experimental conditions for data acquisition. Here, synchrotron data are labeled as S; laboratory data were collected on the pristine material (L#1) and on the same material, stored in the dark, in air and at r.t. for *ca.* 10 months (L#2). In the second case, fine tuning of the detector electronics allowed reduction of the fluorescence level, increasing by at least a factor of five the peak-to-background ratio.

The comparison included the cubic lattice parameter, the sample stoichiometry and the size-distribution analyses. Some limitations, but also some strengthening points, of dealing with conventional powder diffraction data collected on nanocrystalline materials, can be highlighted. Modeling was carried out in a similar way to the one described in paragraph 4.2 and the refined parameters were the same. With reference to the amorphous component, laboratory diffraction patterns were

measured for both L#1 and L#2 experimental conditions and scaled as blank curves in the corresponding refinement processes. S and L#2 final fits are graphically shown in Figure 4.11, whereas the structural and microstructural results for all datasets are reported in Table 4.5.

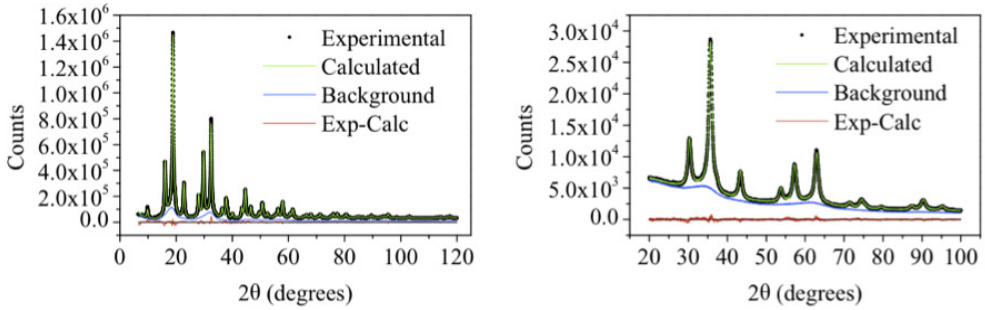

Figure 4.11 Final plot of the DFA best fit obtained on synchrotron (S, λ = 0.826996 Å) (left) and conventional laboratory equipment (L#2 dataset, Cu-Kα radiation) (right).

Table 4.5. Comparison of the structural and microstructural parameters derived by the DFA of the IONP material (see text) from Synchrotron and Laboratory datasets. Note that in the Fe_xO_4 formulation, x = 3 would represent the ideal magnetite, and x = 2.667 the ideal maghemite stoichiometries.

Parameter	Synchrotron	Laboratory	Laboratory
Average $<D>_N$, nm	4.4	5.2	3.9
Average σ_N, nm	2.2	2.3	2.1
Average $<D>_M$, nm	9.0	9.0	8.9
Average σ_M, nm	4.6	4.0	4.7
sof (Fe_{oct})	0.907(5)	0.950(11)	0.946(4)
B_{iso} (Fe_T), Å^2	0.50(2)	0.70(2)	0.94(3)
B_{iso} (Fe_O), Å^2	1.03(3)	0.31(4)	1.99(1)
B_{iso} (O), Å^2	0.48(3)	0.01(1)	0.58(1)
x in Fe_xO_4	2.813(11)	2.900(22)	2.892(8)
R_{wp}, %; GOF	3.78, 3.32	0.29[a], 1.68	2.62, 1.68

[a] This very low value depends on the high fluorescence background, not eliminated by the Ni-filter in the diffracted beam. Better S/N values have indeed been obtained in dataset L#2, by carefully tuning the electronic window of the PSD Lynxeye detector. Accordingly, more statistically significant agreement factors are obtained in the latter case.

The results suggest the following observations:

i) The lattice parameters derived from the S and L#1 experiments are very similar (8.363 and 8.362 Å, respectively), suggesting that they can be estimated with good accuracy also when laboratory equipment are used. However, it must be also taken into account that small misalignments (typically, specimen displacement errors) may induce θ-dependent peak shifts, which are more probable in L, rather than in S data.

ii) The lattice parameter derived from the L#2 experiment is significantly lower (8.349 Å), indicating the nearly complete oxidation of the IONPs, leading to NPs of γ-Fe_2O_3 (*i.e.*, maghemite).

iii) Reasonable agreements are also observed in the size and size distribution derived from the DFA of the *three* datasets. Perhaps surprisingly, the average sizes and widths of the number- and mass-log-normal size distributions match very well, thus giving confidence in the possibility of deriving meaningful microstructural parameters also from conventional laboratory data (as long as the diffraction peaks are not significantly affected by the instrumental broadening). This very important statement witnesses that DFA, working in the measurement (reciprocal) space, does not suffer (to this extent) of a limited Q range, as PDF does.

iv) An important warning should, at variance, accompany the comparison of "structural" features, such as *sof's* and thermal parameters, for the estimation of which L data seem to be much less reliable.

4.8 Conclusions

In this chapter, very small super-paramagnetic IONPs have been investigated by innovative synchrotron (reciprocal-space) X-ray total scattering methods and DFA. Thanks to the advantage of exploiting the information from both Bragg and diffuse scattering, this approach allowed simultaneous determination of accurate lattice parameter and stoichiometry (from which size-dependent core–shell composition in terms of magnetite/maghemite ratios were derived), and full size distributions within a coherent approach. The importance of a robust quantitative characterization deriving mass-based average NPs sizes and size distributions when correlating volume-based magnetic properties has been pointed out.

At the smallest sizes the NPs show surface relaxation. These effects are mostly effective for sizes below 5 nm and can be disentangled from the competing oxidation-driven lattice contraction provided that an accurate data correction for extra-sample contributions and sample displacement is performed.

Based on the particle size distributions of a large series of IONPs samples, a straightforward relationship between the lattice parameter, the Fe oxidation state and the NP size has been established. This law predicts *an inflation* of the cell parameter upon decreasing the NPs size while keeping constant the oxidation degree. Such a behavior is common to many oxides and indicates that the surface tension must be *negative*.

Finally, the DFA approach has been here applied to conventional laboratory equipment data, (mostly) aiming at the extraction of average crystal sizes and of their dispersion. Comparison with the results obtained

from parallel experiments on the very same material, performed at a X04SA-MS beamline, allowed the pitfalls, but also some strength, of this approach, to be highlighted. Needless to say, if a well defined (experimental and computational) protocol, allowing the correct determination of structural and microstructural parameters of nanosized materials, can be devised even by using conventional, widely accessible, laboratory X-ray powder diffractometers, this would give to material scientists new perspectives, and new dimensions, for the characterization of nanocrystalline samples.

References

1. R. Mikami, M. Taguchi, K. Yamada, K. Suzuki, O. Sato, Y. Einaga, *Reversible Photo-Switching of the Magnetization of Iron Oxide Nanoparticles at Room Temperature*, **2004**, Angew. Chem. Int. Ed., *43*, 6135-6139.

2. L. H. Reddy, J. L. Arias, J. Nicolas, P. Couvreur, *Magnetic nanoparticles: design and characterization, toxicity and biocompatibility, pharmaceutical and biomedical applications*, **2012**, Chem. Rev., *112*, 5818-5878.

3. F. Bosi, U. Halenius, H. Skogby, *Crystal chemistry of the magnetite-ulvospinel series*, **2009**, Amer. Miner., *94*, 181-189.

4. H.-S. Shin, *A Study on the Structure of Maghemite (γ-Fe_2O_3). I - Rietveld Analysis of Powder XRD Patterns*, **1988**, J. Korean Ceram. Soc., *35*, 1113-1119.

5. A. N. Shmakov, S. V. Kryukova, S. V. Tsybulya, A. L. Chuvilin, L. P. Solovyeva, *Vacancy Ordering in γ-Fe_2O_3: Synchrotron X-ray Powder Diffraction and High-Resolution Electron Microscopy Studies*, **1995**, J. Appl. Cryst., *28*, 141-145.

.6 C. Greaves, *A powder neutron diffraction investigation of vacancy ordering and cova- lence in y-Fe_2O_3*, **1983**, J. Solid State Chem., *49*, 325-333.

7. T. Hyeon, S. S. Lee, J. Park, Y. Chung, H. B. Na, *Synthesis of highly crystalline and monodisperse maghemite nanocrystallites without a size-selection process*, **2001**, J. Am. Chem. Soc., *123*, 12798-12801.

8. J. Park, K. An, Y. Hwang, J.-G. Park, H.-J. Noh, J.-Y. Kim, J.-H. Park, N.-M.; Hwang, T. Hyeon, *Ultra-large-scale syntheses of monodisperse nanocrystals*, **2004**, Nature Mater., *3*, 891-895.

9. Y.-W. Jun, Y.-M. Huh, J.-S. Choi, J.-G. Lee, H.-T. Song, Sungjun, Sungjun, S. Yoon, K.-S. Kim, J.-S. Shin, J.-S. Suh, J. Cheon, *Nanoscale Size Effect of Magnetic Nanocrystals and Their Utilization for Cancer Diagnosis via Magnetic Resonance Imaging*, **2005**, J. Am. Chem. Soc., *127*, 5732-5733.

10 R. Massart, *Preparation of aqueous magnetic liquids in alkaline and acidic media*, **1981**, IEEE Trans Magn. MAGN, *47*, 1775-1761.

11. J. S. Salazar, L. Perez, O. de Abril, L. T. Phuoc, D. Ihiawakrim, M. Vazquez, J.-M. Greneche, S. Begin-Colin, G. Pourroy, G., *Magnetic Iron Oxide Nanoparticles in 10-40 nm Range: Composition in Terms of Magnetite/Maghemite Ratio and Effect on the Magnetic Properties*, **2011**, Chem. Mater., *23*, 1379-1386.

12 . P. R. Willmott et al., *The Material Science beamline upgrade at the Swiss Light Source,* **2013**, J. Synchrotron Rad., *20*, 667-682.

13. A. Bergamaschi, A. Cervellino, R. Dinapoli, F. Gozzo, B. Henrich, I. Johnson, P. Kraft, A. Mozzanica, B. Schmitt, X. Shi. *The MYTHEN detector for X-ray powder diffraction experiments at the Swiss Light Source,* **2010**, J. Synchr. Rad., *17*, 653-668.

14. A. Cervellino, R. Frison, F. Bertolotti, A. Guagliardi, *DEBUSSY 2.0: a Debye user system for nanocrystalline materials,* **2015**, in preparation.

15. J. Soderlund, L. B. Kiss, G. A. Niklasson, C. G. Granqvist, *Lognormal size distribution in particle growth processes without coagulation*, **1998**, Phys. Rev. Lett., *80*, 2386-2388.

16. L. B. Kiss, J. Soderlund, G. A. Niklasson, C. G. Granqvist, *New approach to the origin of lognormal size distributions of nanoparticles*, **1999**, Phys. Rev. Lett., *10*, 25-28.

17. J. A. Nelder, R. Mead, *A Simplex method for function minimization,* **1965**, Comput. J., *27*, 308-313.

18. A. Manceau, V. A. Drits, *Local structure of Ferrihydrite and Feroxyhite by EXAFS Spectroscopy,* **1993**, Clay Minerals, *28*, 165-184.

19. F. M. Michel, L. Ehm, S. M. Antao, P. L. Lee, P. J. Chupas, G. Liu, D. R. Strongin, M. A. A. Schoonen, B. L Phillips, J. B. Parise, *The Structure of Ferrihydrite, a Nanocrystalline Material,* **2007**, Science, *316*, 1726-1729.

20. A. Manceau, S. Skanthakumar, L. Soderholm, *PDF analysis of ferrihydrite: Critical assessment of the under-constrained akdalaite model,* **2011**, Amer. Miner., *96*, 521-533.

21. B. D. Cullity, *Introduction to Magnetic Materials,* **1972**, Addison-Wesley, New York.

22. C.-R. Lin, R.-K. Chiang, J.-S. Wang, T.-W. Sung, *Magnetic properties of monodisperse iron oxide nanoparticles,* **2006**, J. Appl. Phys., *99*, 08N710.

23. R. W. Chantrell, J. Popplewell, S. W. Charles, *Measurements of Particle Size Distribution Parameters in Ferrofluids,* **1978**, IEEE Trans. Magn. Magn. *14*, 975.

24. P. M. Morales, S. Veintemillas-Verdguer, M. L. Montero, C. J. Cerna, A. Roig, L. Casas, B. Martinez, F. Sandiumenge, *Surface and Internal Spin Canting in γ-Fe_2O_3 Nanoparticles,* **1999**, Chem. Mater., *11*, 3058-3064.

25. J.-E. Jorgensen, L. Mosegaard, L. E. Thomsen, T. R. Jensen, J. C. Hanson, *Formation of γ-Fe_2O_3 Nanoparticles and Vacancy Ordering: An in situ X-ray Powder Diffraction Study,* **2007**, J. Solid State Chem., *180*, 180-185.

26. T. N. Shendruk, R. D. Desautels, B. W. Southern, J. van Lierop, *The effect of surface spin disorder on the magnetism of γ-Fe_2O_3 nanoparticle dispersions,* **2007**, Nanotechnology, *18*, 455704-455706.

27. J. Park, E. Lee, N.-M. Hwang, M. Kang, S.C. Kim, Y. Hwang, J.-G. Park, H.-J. Noh, J.-Y. Kim, J.-H. Park, T. Hyeon, *One-nanometer-scale size-controlled synthesis of monodisperse magnetic iron oxide nanoparticles,* **2005**, Angew. Chem. Int. Ed., *44*, 2872-2877.

28. T. J. Daou, J. M. Grenecȟe, G. Pourroy, S. Buathong A. Derory, C. Ulhaq-Bouillet, B. Donnio, D. Guillon, S. Begin-Colin, *Coupling Agent Effect on Magnetic Properties of Functionalized Magnetite-Based Nanoparticles,* **2008**, Chem. Mater., *20*, 5869-5875.

29. R. J. Armstrong, A. H. Morrish, G. A. Sawatzky, *Mössbauer study of ferric ions in the tetrahedral and octahedral sites of a spinel,* **1966**, Phys. Lett., *23*, 414-416.

30. V. Petkov, P. D. Cozzoli, R. Buonsanti, R. Cingolani, Y. Ren, *Size, shape and internal atomic ordering of nanocrystals by atomic pair distribution functions: a comparative study of γ-Fe_2O_3 nanosized spheres and tetrapods,* **2009**, J. Am. Chem. Soc., *131*, 14264-14266.

31. C. A. Gorski, M. M. Scherer, *Determination of nanoparticulate magnetite stoichiometry by Mössbauer spectroscopy, acidic dissolution, and powder X-ray diffraction: A critical review,* **2010**, Amer. Miner., *95*, 1017-1026.

32. M. Gotic, G. Koscec, S. Music, *Study of the reduction and reoxidation of substoichiometric magnetite,* **2009**, J. Mol. Struct., *924-26*, 347-354.

33. P. M. Diehm, P. Agoston, K. Albe, *Size-dependent lattice expansion in nanoparticles: reality or anomaly?,* **2012**, ChemPhysChem, *44*, 215-220.

34. W. Feitknecht, P. Brunner, H. R. Oswald, *Über den Einfluß der Feuchtigkeit auf die Oxydation von Manganhydroxid durch molekularen Sauerstoff,* **1962**, Z. Anorg. Allg. Chem., *316*, 154-160.

35. H. Annersten, S. S. Hafner, *Valency distribution in synthetic spinels of the series Fe_3O_4- γ-Fe_2O_3,* **1973**, Z. Kristallogr., *137*, 321-340.

36. K. Volenik, M. Seberini, J. Neid, *A Mössbauer and X-ray diffraction study of nonstoichiometry in magnetite,* **1975**, Czech. J. Phys., *25*, 1063-1071.

37. J. B. Yang, X. D. Zhou, W. B. Yelon, W. J. James, Q. Cai, K. V. Gopalakrishnan, S. K. Malik, X. C. Sun, D. E. Nikes, *Magnetic and structural studies of the Verwey transition in $Fe_{3-\delta}O_4$ nanoparticles,* **2004**, J. Appl. Phys., *95*, 7540-7542.

38. E. Schimdbauer, M. Keller, *Magnetic hysteresis properties, Mössbauer spectra and structural data of spherical 250nm particles of solid solutions Fe_3O_4- γ-Fe_2O_3,* **2006**, J. Magn. Magn. Mat., *297*, 107-117.

39. N. W. Ashcroft, N. D. Mermin, *Solid state physics,* Ch. 2 – *The Sommerfeld theory of metals,* **1976,** p. 29–55. Brooks/Cole:Pacific Grove, California, USA.

40. L. W. Finger, R. M. Hazen, A. M. Hofmeister, *High pressure crystal chemistry of spinel ($MgAl_2O_4$) and magnetite (Fe_3O_4): comparisons with silicate spinels,* **1986,** Phys. Chem. Miner.. *13*, 215-220.

41. J. Z. Jiang, J. S. Olsen, L. Gerward, S. Mørup, *Enhanced bulk modulus and transition pressure in γ-Fe_2O_3 nanocrystals*, **1998**, Europhys. Lett., *44*, 620-626.

Chapter 5

Biomimetic Hydroxyapatite Nanoparticles

5.1 Introduction

Organic-inorganic composites assembled by living organisms through complex biomineralization mechanisms typically show hierarchical, sophisticated architectures providing them exceptional functional and adaptive properties. [1] Among these composites, bone is one of the most representative systems in which collagen microfibrils (the organic matrix) act as a template where the deposition of a nanosized and defective hydroxyl calcium phosphate (the mineralized component) takes place. [2] The comprehension of the abovementioned mechanisms, enabling the strict control over the mineral structure, composition, growth and morphology, are still far from being clearly understood. Therefore, there is a great deal of interest for the relevance both on the fundamental knowledge side and as source of inspiration for preparing *biomimetic* materials with advanced biomedical applications (from regenerative medicine and bone tissue engineering to drug delivery). [1,3-5]). In this view, biomimetic apatite NPs (*i.e* very similar in size, shape and composition to the mineral component of bone and teeth), are extensively investigated and used also as model systems, to explore fundamental aspects of the mineralization phenomena.

In bone, tiny crystal platelets of carbonated apatite are thought to grow from an Amorphous Calcium Phosphate (ACP) precursor, the control over crystal morphology being regulated mainly through interaction with collagen fibrils and some acidic non-collagenous proteins [6-9]. The platy shape of the mineral plays an important role in determining the unique functional properties of bone [10,11] and is a key structural feature to be controlled while forming biomimetic apatites.

Interestingly, platelets do not extend normal to the crystallographic *c*-axis, as expected by the hexagonal crystal structure of apatite (space group $P6_3/m$) [12-14] and as pictorially exemplified in Figure 5.1.

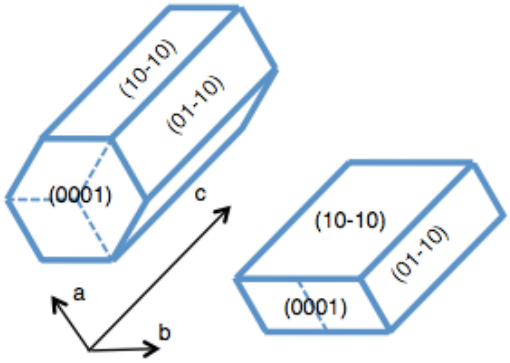

Figure 5.1 Hexagonal (left) and platy (right) morphologies of Ca-deficient hydroxyapatite crystals (later used in the DFA modelling); the platy morphology comes from an independent growth along *a*- and *b*-axes, therefore breaking the hexagonal crystal symmetry. *(h, k, -h-k, l)* indices of the most relevant crystal facets are provided.

Therefore the platy morphology breaks the crystal symmetry through a mechanism that, so far, has remained unclear. Whether or not such morphology is reminiscent of an unstable transient precursor [15,16] (amorphous and/or intermediate, such as the octacalcium phosphate), as already observed in other cases of living organisms secreting mineralized tissues, [17] is still a matter of debate.

ACP is highly unstable and the ACP-to-apatite transformation, which might help in clarifying the origin of platy crystals, has never been directly detected, neither in *in vivo* nor in *in vitro* experiments. Curiously, spherical ACP particles are reported at the early stages of the precipitation process while apatite platelets are observed as the final intrafibrillar mineral phase [6,18]. In this view, the role of small molecules, such as

citrate, has traditionally been neglected. However, things have changed. Organic, low-molecular-weight additives are frequently used nowadays in the synthesis of biomimetic apatites to control the crystal growth within the nanometer size regime [19]. With particular reference to citrate, these molecules might play a broader role than a simple synthetic additive to be used in biomimetic approaches, as recently pointed out by Schmidt-Rohr and co-workers through solid-state NMR studies [20]. According to this study, citrate in bone accounts for about 5.5 weight % of the total organic component (a relatively large amount) and the distance of carboxylate groups in citrate matches that of pairs of neighbouring Ca^{2+} ions at the (10-10) facets of the apatite crystal. These facts cause citrate to be strongly bound to the apatite facets and to block the growth along this direction, thus limiting the platelet thickness. The hypothesis that citrate stabilizes the size and the morphology of bone apatite was further supported by Xie and Nancollas, [21] who highlighted the differences between bone and tooth enamel, where the rod-like crystal morphology of fluoro-apatite may derive from the much lower content of citrate in saliva and the mismatch of carboxylate groups at the crystal surface of fluoro-apatite. However, how, and to what extent, citrate ions influence nucleation and crystal growth in the absence of other organic constituents is difficult to disentangle in biological systems and only rarely explored in synthetic models [22-24].

The work presented in this chapter deals with samples of citrate-bio-inspired apatite NPs prepared at increasing precipitation times to be used as system model and to be investigated by advanced X-ray Total Scattering Techniques [25-27] and Atomic Force Microscopy (AFM). This study took advantage from the use of citrate molecules on two

distinct sides: 1) citrate slows down the transformation rate of ACP-to-apatite, therefore enabling "snapshots" of the NCs structural and morphological changes in time to be isolated; 2) it also allows its unique role in controlling the crystal properties to be investigated *in vitro*. In these conditions, citrate ions are not expected to drive, alone, the crystal morphology to platelets, as the reported distance-matching criterion would apply in the same manner to all six, symmetry equivalent, {10-10} facets of the hexagonal apatite structure [28].

Total Scattering investigations have been addressed to quantitatively characterize nanosized and disordered biomimetic apatite NCs in terms of structure, composition, size and morphology. A (partially) similar approach was applied to engineered bone tissue implants, to simulate X-ray scanning micro-diffraction data [29,30]. In this Thesis, the Debussy Suite was used to carry out the *complete* DFA of the investigated samples; a specific strategy to account for flat apatite NCs was necessary. AFM characterizations allowed the size and shape information on *multi-domain* NPs to be extracted. In this chapter, after illustrating the results of the two complementary techniques, they have been cross-coupled, allowing the amorphous-to-crystal transformation process at molecular scale resolution to be (*ex situ*) reconstructed and a plausible mechanism inducing the platy morphology proposed.

5.2 Experimentals

5.2.1 Materials and synthesis

In order to study the structural, compositional and morphological evolution of apatite nanocrystals in the system model, citrate-controlled

samples were precipitated at 5 min, 4 h and 96 h, following the batch heating synthesis method reported in ref. [22], the main details of which are briefly summarized in Annex 1. Preparations were performed either in the absence or in the deliberate presence of sodium carbonate, CO_3^{2-} being the major phosphate substituent in biological apatites [31,32]. The two groups of samples are here labelled as Ap and cAp, respectively. A sample instantaneously precipitated was also prepared in the presence of sodium carbonate only, providing an amorphous calcium phosphate powder (*vide infra*). Noteworthy, in the absence of citrate ions (a blank run), the reaction proceeded along a completely different pathway, initially leading to the precipitation of octacalcium phosphate (as witnessed by Figure A1.3 of Annex 1).

5.2.2 Synchrotron X-ray Total Scattering measurements

Powder samples were loaded in glass capillaries of 0.5 mm diameter and measured at the X04SA-MS Beamline of the Swiss Light Source of the Paul Scherrer Institut. The beam energy was set at 15 keV and the operational wavelength (λ = 0.82669 Å) precisely determined through a silicon powder standard NIST 640c [a_0 = 0.54311946(92) nm at 22.5°C] (as detailed in chapter 3). Data were collected in the 2-130° 2θ range using the experimental set-up described in chapter 3.

Data reduction for total scattering analysis (also discussed in chapter 3) required independent He/air and capillary scattering traces, as well as empty and sample-loaded capillary transmission coefficients. The reduction procedure eventually provided data subtracted of all extra-sample scattering effects and absorption corrected, [33] enabling a DFA modelling approach, free of any phenomenological component, using the

Debussy Suite. [27] Inelastic (Compton) scattering (strongly visible in all patterns at the beam energy of 15 keV) was calculated and directly added to the Debye pattern model. Figure 5.2 shows the synchrotron X-ray scattering data of Ap (panel A) and cAp (panel B) samples after corrections has been performed. The scattering trace labelled as ACP in Figure 5.2B, refers to the sample instantaneously precipitated in the presence of sodium carbonate. It shows the typical features of an amorphous calcium phosphate and was further characterized through the PDF method [in the form of the reduced G(r)], described above in chapter 2. Elemental and Thermal Analyses of the ACP sample were also performed (following the protocol described in the ref. [24]) to assess the overall *chemical* (not the *phase*) composition.

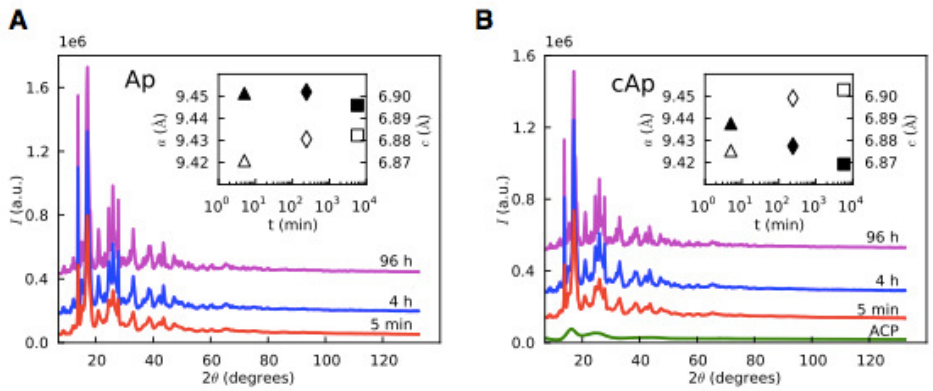

Figure 5.2 Synchrotron X-ray scattering data of Ap (A) and cAp (B) samples at different maturation times (5 min, 4 h, 96 h, vertically offset for the sake of clarity). The ACP sample is instantaneously precipitated (cAp conditions) and shows the typical pattern features of an amorphous material. The two insets show the effects on the lattice parameters of the CO_3^{2-}/PO_4^{3-} substitution; the contraction of the *a*-axis (filled symbols: ▲5min; ♦ 4h; ■ 96h) and the expansion of the *c*-axis (empty symbols: Δ 5min; ◇ 4h; □ 96h) are rather limited in Ap samples and more pronounced in cAp ones.

The statistical agreement index R_{wp} was used to evaluate the match between the experimental and DFA pattern model for each dataset; the Goodness of Fit (GoF) statistical descriptor to measure the quality of the model with respect to the experimental data; GoF = 1 is the expected value for a perfect model; slightly higher values, up to ca. 5-6, are common for synchrotron data with high counting statistics. [34]

For each sample, the cell parameters were derived by the conventional Rietveld method implemented in the program TOPAS-R [35], using symmetrized spherical harmonics to phenomenologically reproduce the anisotropic peak broadening due to the anisotropic crystal shape. Changes in the lattice parameters of biomimetic apatite are known to be largely influenced by ionic substitutions; in the case of the samples here characterized, investigations were mainly addressed to evaluate the effects of the presence of minor amounts of CO_3^{2-} substitutions [31].

5.2.3 AFM measurements

Atomic Force Microscopy (AFM) is a powerful non-invasive tool to measure the size and, particularly, the thickness of samples at nanometer and even sub-nanometer resolution [36]. For the measurements carried out on the apatite NPs here studied, freeze-dried powdered samples were dispersed in ultrapure water and the suspensions were then filtered (0.22 μm, Millipore) to remove the largest aggregates. A drop of the selected slurry was deposited on the (atomically) flat surface of a freshly cleaved mica substrate, and subsequently dried by evaporation overnight at r.t. in a vacuum desiccator.

AFM images were collected with a Nanoscope IIID microscope (Digital Instruments, Veeco, Santa Barbara, USA) in tapping mode by scanning the sample surface in air with silicon probes (NCHV, spring constant of 42 N m^{-1} and resonant frequency of 320 kHz, Veeco Probes, Santa Barbara, USA). For each sample, thickness, width and length were measured on more than 30 single (non-aggregated) nanoparticles. The vertical resolution was better than 0.1 nm, the lateral one better than 10 nm.

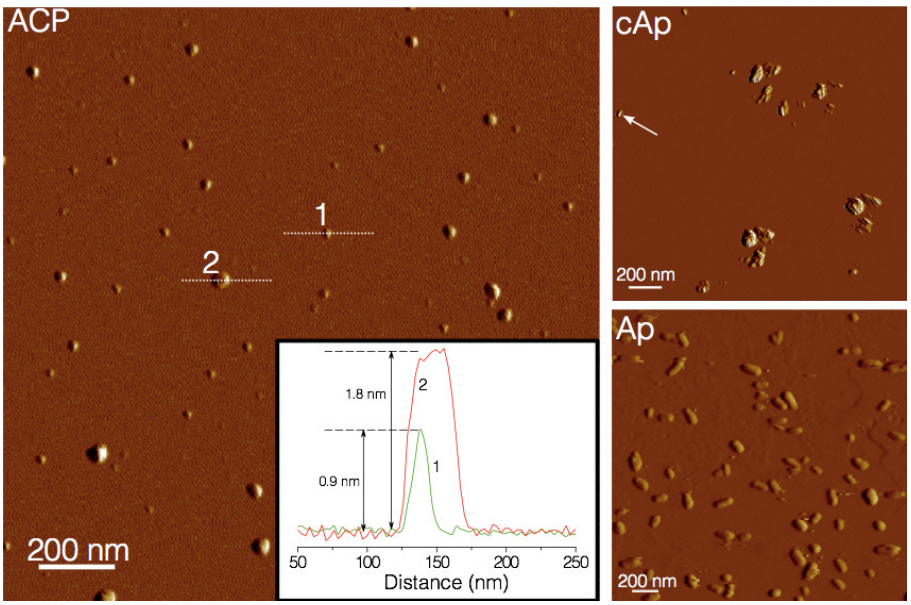

Figure 5.3 AFM images of ACP, Ap 96 h and cAp 96 h samples. The inset shows the *z*-section of ACP NPs 1 and 2, clearly showing the platy morphology. The AFM characterization revealed the NPs platy morphology of all the investigated samples.

5.3 Effects of CO_3^{2-}/PO_4^{3-} substitution on lattice parameters and structural interpretation in carbonated apatite.

The Ap and cAp samples investigated in this study are mainly carbonated apatites of B-type, *i.e.* with CO_3^{2-} substituting PO_4^{3-}, as

confirmed by FTIR spectroscopy [24]. The effects on cell parameters upon sample maturation and the amount of substitution are reported in Table 5.1 and graphically shown in the insets of Figure 5.2. A progressive unit cell *a*-axis contraction and a *c*-axis expansion are observed upon maturation; the maximum relative variations are rather limited in Ap (-0.06%, +0.17%) and more pronounced in cAp samples (-0.20% and +0.40%), in which values up to 8 wt% carbonate inclusion (mimicking the biological case) are detected at high maturation times.

Table 5.1 Cell parameters (Å) [derived by the Rietveld method performed by TOPAS [35] and CO_3^{2-} wt% estimated by Inductively Coupled Plasma (ICP). The wt% of CO_3^{2-} substituting PO_4^{3-} are derived therefrom. Values in the last two columns are taken from ref. [24].

Sample	*a, b*	*c*	$CO_3^{2-}{}_{(ICP)}$	CO_3^{2-} / PO_4^{3-}
Ap 5 min	9.451[a]	6.871	1.5±0.2	4.0
Ap 4 h	9.452	6.881	1.1±0.1	2.9
Ap 96 h	9.446	6.882	1.0±0.3	2.7
cAp 5 min	9.438	6.875	1.5±0.1	4.0
cAp 4 h	9.427	6.899	1.5±0.1	4.1
cAp 96 h	9.419	6.903	2.9±0.1	7.9

[a] The Rietveld-derived cell parameters e.s.d.'s fall near 10^{-4} and are highly unrealistic, being determined mainly using the extremely high synchrotron data counting rates under the assumption of processing data free of systematic errors. Similar concerns have been raised in conventional powder diffraction analysis [34]. Therefore, the reported parameter values have been approximated to more sensible numbers. This is also valid for the Debye-Waller atomic factors reported in Table 5.7.

Considering the changes of lattice parameters, the CO_3^{2-}/PO_4^{3-} substitution suggested an out-of-plane orientation of the vicariant

carbonate anion, that is here explained through the pictorial representation of Figure 5.4.

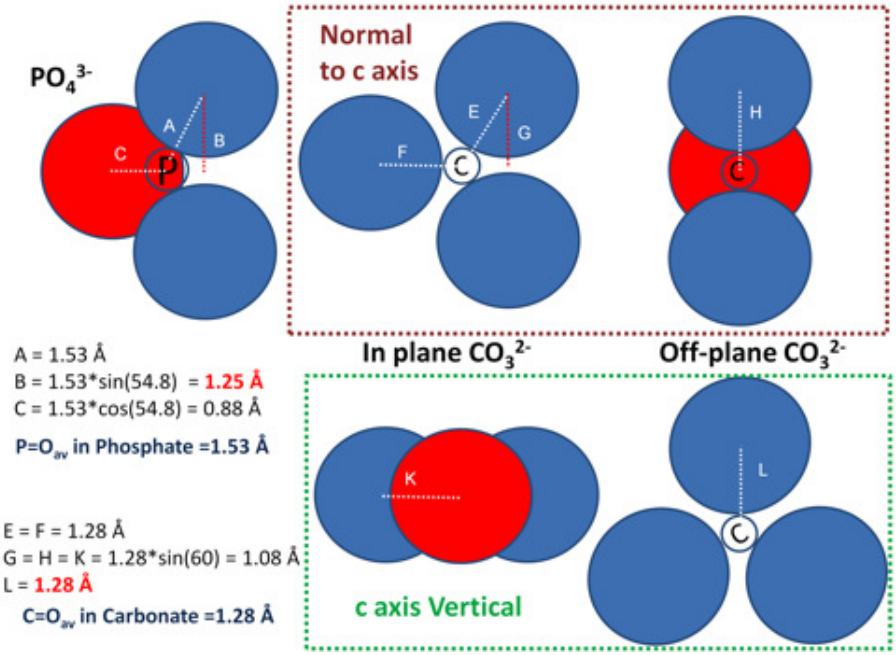

Figure 5.4 Model for out-of-plane orientation of CO_3^{2} ion substituting PO_4^{3-} group in apatite structure, explaining the cell axes behavior, particularly in cAp samples. The red circles refer to out-of-plane oxygen atoms.

The phosphate and the carbonate groups are idealized as a T_d fragment with P=O bond distance of 1.53 Å [37] and as a D_{3h} fragment with C=O of 1.28 Å [38], respectively, of which Figure 5.4 shows the estimate of the steric hindrance. The top section depicts the view down [001], with the P and C atoms lying on the mirror plane of the apatite structure ($P6_3/m$ space group model); the bottom section shows the lateral view along a C_2 symmetry axis of the carbonate group ([001] axis is vertical). For each view, two extreme cases, in-plane and off-plane orientations of the carbonate anions, are illustrated: in the central column,

the carbonate anion *completely* lies on the crystallographic mirror plane, while, in the rightmost part of the panel, the CO_3^{2-} fragment has one C=O vector aligned with [001].

The A-L labels refer to geometrically derived values which, based on literature average P=O and C=O distances, indicate the relative protuberance of the different anions (in ***ab***, and along ***c***). These values are tentatively used to assess their relative steric impact on the observed lattice parameters upon B-type carbonate substitution. Accordingly, shrinking of the *a* and *b* lattice parameters and slight inflation of the *c*-axis in the presence of extra CO_3^{2-} dopants can only be explained by the off-plane orientation of the carbonate anions, as derived from the comparison of the B and K values, highlighted in red in Figure 5.4.

5.4 DFA modelling of apatite platelets

The DFA modelling strategy here applied to characterize Ap and cAp samples, can be summarized in the following steps:

1. The bottom-up approach described in chapter 3 was used to generate a bivariate population of atomistic models of increasing size and hexagonal shape (hex). The crystal structure of a Ca-deficient hydroxyapatite [39] (CDHA) (see Figure 5.5) was adopted and its unit cell used as the building block of hexagonal prisms (as shown in Figure 5.1, left) built up through a layer-by-layer construction and under the assumption of two independent "growth" directions, one along the six-fold symmetry ***c*** axis and the second one in the orthogonal ***ab*** plane, up to 15 nm in ***ab*** and 50 nm along ***c***.

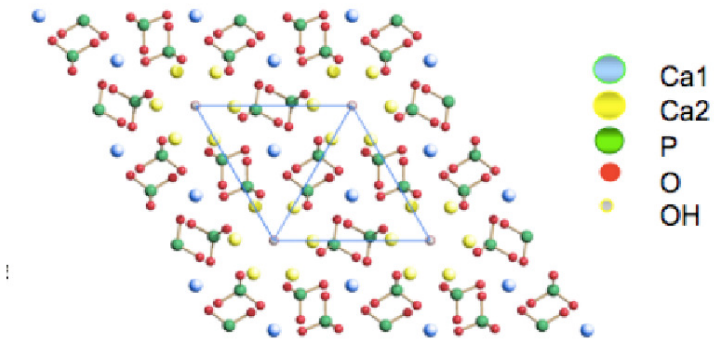

Figure 5.5 Crystal structure of hydroxyapatite, viewed down [001]. Atoms labeled as Ca2 design the so-called ion-channels, running parallel to the crystallographic *c*-axis, where OH^- ions are located.

2. In order to deal with platy CDHA shapes, *bivariate* populations of crystals grown along ***c***, and, in ***ab***, by considering anisotropic parallelogram-shaped bases with fixed 1:2 *a:b* ratio (as shown in Figure 5.1, right), were built (platy NCs). This was the simplest way of managing the platy morphology without introducing a trivariate size distribution function, which in itself is too complex to be extracted from even the best possible diffraction data. This point is explained in deeper detail in the following. The two populations (hex and platy) were then used *together* and constrained to the same NC size distribution and stoichiometry, in a *biphasic* pattern model. When both the hexagonal and platy morphologies were used, the GoF values of model *vs.* experimental patterns were systematically better than the model relying on the hex or platy shapes only. A platy shape population based on a fixed 1:3 *a:b* ratio was also tested but it provided worse (5 min samples) or comparable (4 h and 96 h samples) Gof's with respect to the 1:2 *a:b* ratio case; accordingly, the 1:2 NCs

ensemble was adopted to describe the platy morphology in all samples.

3. The sampled interatomic distances of each nanocrystal for both populations (hex and platy) were computed and stored in suitable databases to be used in the subsequent DFA process.
4. To account for (number- and mass-based) size and shape distributions of the bivariate population of CDHA nanocrystals, the bivariate lognormal function [40] (see chapter 3 for details) was adopted. To best match the pattern models against the experimental patterns, the five parameters of the lognormal distribution (the average/standard deviation pairs of the size distributions along the two growth directions and their correlation angle) were adjusted via the Simplex method. Among the structural parameters, the atomic site occupancy factors (*sof's*) of the two Ca and the hydroxyl O atoms (see Figure 5.5) and all the isotropic atomic Debye–Waller factors were also refined. The phosphate O atoms were constrained to the same value, to limit the number of parameters.
5. The occurrence of an additional amorphous component was detected in all samples and taken into account in the pattern model by scaling (by linear least squares) the experimental pattern of the ACP sample as a blank curve (*no additional background contributions were needed*). Finally, the integral area under the scaled ACP scattering trace was used to derive the ACP mass fraction in each sample.

For each sample, graphical outputs of the best pattern model and of the refined bivariate size distribution 2D map are shown in Figure 5.6 and in Figure 5.7, respectively.

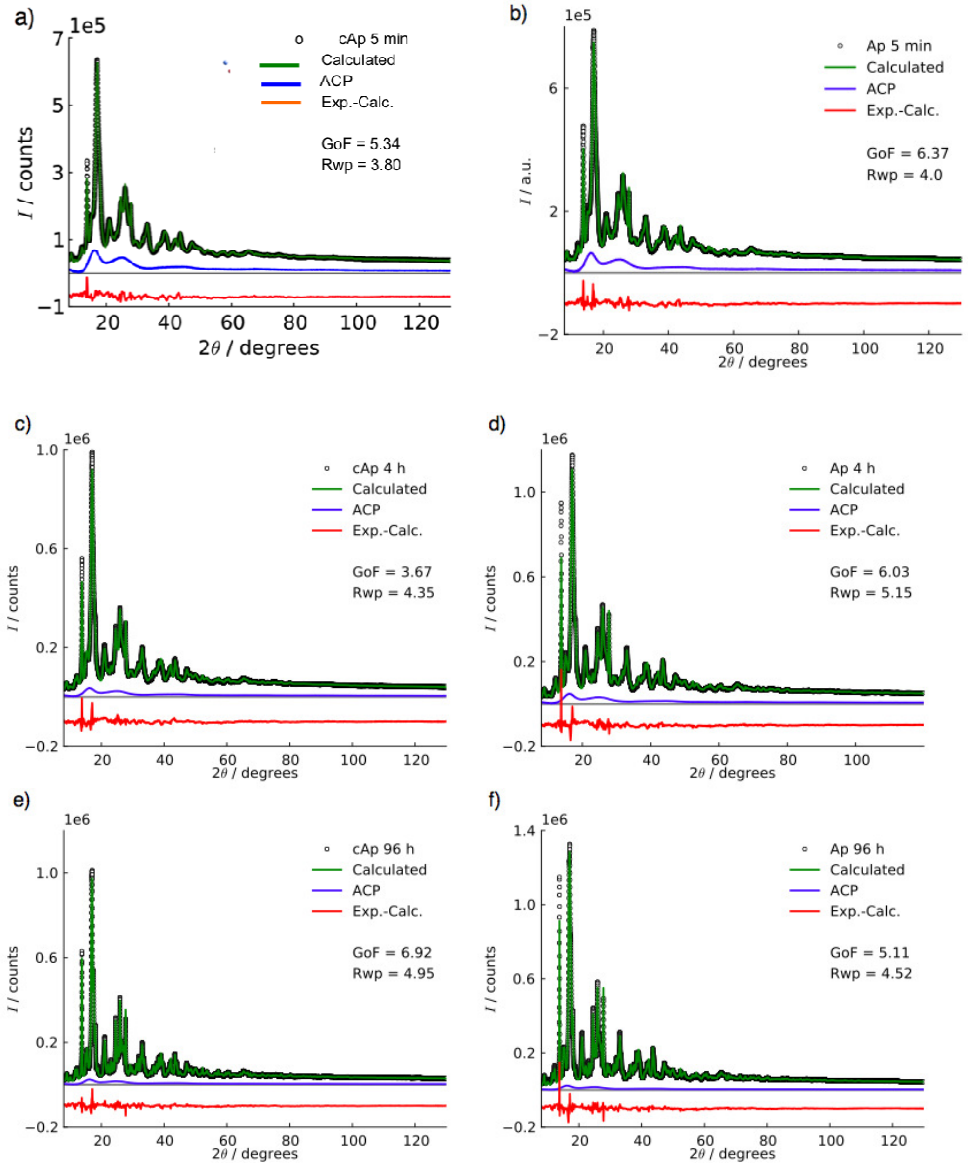

Figure 5.6 Best fit of cAp and Ap samples provided by the DFA approach: experimental powder diffraction pattern (empty circles); total model pattern (green line) with its amorphous component (ACP, blue line); residual between experimental and model patterns (red line, shifted downwards for the sake of clarity). No phenomenological components were used in the model patterns. Downscaling of the amorphous phase upon sample maturation is clearly visible.

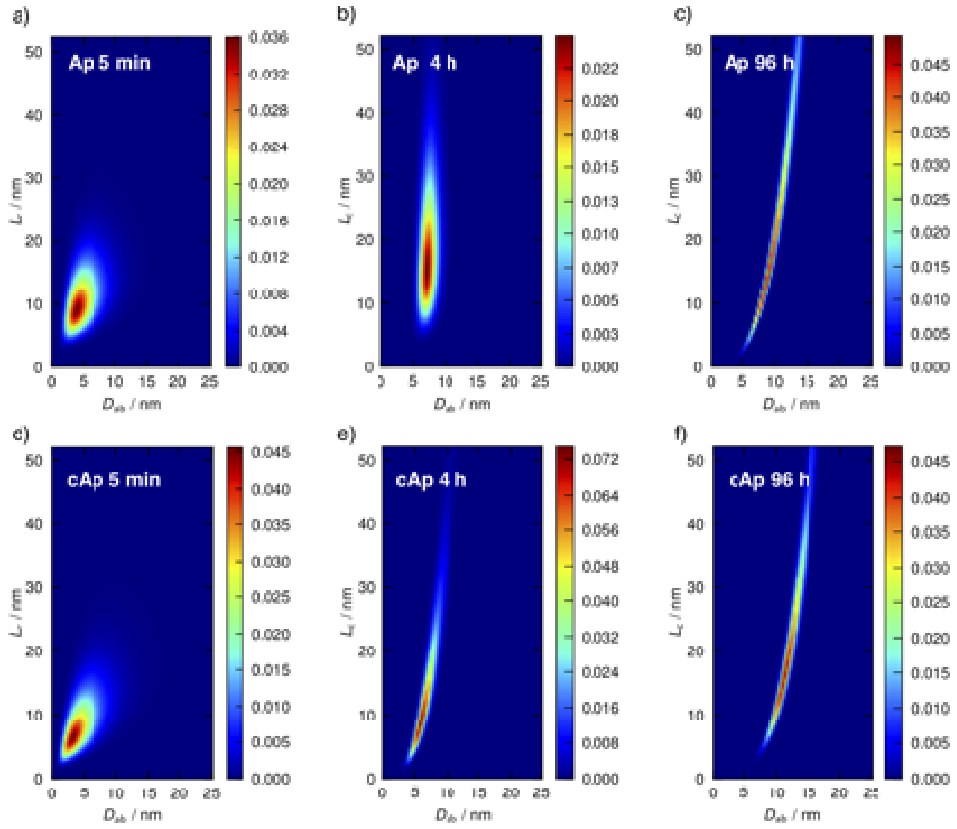

Figure 5.7 Final 2D maps of the bivariate lognormal function modeling the size and the shape distribution of Ap and cAp samples. The horizontal axis refers to the crystal size in the *ab*-plane, given as the diameter (D_{ab}) of the circle of equivalent area, the vertical axis refers to the crystal length along the ***c*** direction (L_c); the relative mass-based frequency of crystals with sizes (D_{ab}, L_c) is represented by a color code, according to the color-coded scale on the right (note the different absolute scale of each map). The correlation between the two growth axes is not negligible at 5 min of maturation time (panels 5.6a and 5.6d) and becomes fairly unimportant in the remaining (more mature) samples.

The way here adopted for dealing with platy apatite shapes makes it possible to extract the shape anisotropy of the *ab*-base (in addition to the anisotropy due to the crystal elongation in the *c*-axis direction) without introducing too many unnecessary parameters. Such anisotropy can be

measured by the ratio (A) between the principal inertia moments (major/minor) of the base shape. For the models here used, A=1 for the hexagonal base, A=6.17 for the platelet base (1:2 *a:b* ratio). Since this measure is linear in the mass fraction, an *effective average base anisotropy* <*A*> was derived through the mass fractions of the two populations, hex and platy (normalized to the total crystalline components), which differ only for the anisotropy of the *ab*-base shape.

Table 5.2 DFA-derived mass fractions (W_T %) of ACP, Hexagonal and Platy CDHA morphologies. The mass fraction of the amorphous component is estimated through the integral area under the scaled ACP scattering trace of each sample, after normalization to electronic units. W_C % values indicate the mass fractions normalized to the content of the two crystalline components, on which the average base anisotropy factor <A> depends.

Sample	ACP / Hex / Platy w_T %	Hex / Platy w_C %	<A>
Ap 5 min	17.8 / 0 / 82.2	0 / 100	6.17
Ap 4 h	11.6 / 38.4 / 50.0	43.4 / 56.6	3.93
Ap 96 h	6.1 / 55.8 / 38.1	59.4 / 40.6	3.10
cAp 5 min	17.6 / 5.9 / 76.5	7.2 / 92.8	5.80
cAp 4 h	10.2 / 29.5 / 60.3	32.8 / 67.2	4.47
cAp 96 h	9.6 / 62.3 / 28.1	68.9 / 31.1	2.61

Accordingly, in the section where the DFA results are discussed, the mass fractions of the two morphologically distinct apatite populations have been used as an indirect indication of the degree of anisotropy in the *ab*-plane, rather than directly referring to the values of the <A> parameter. These values are reported for all samples in Table 5.2; they range from 2.61 (cAp 96 h, 31% of platelets) to 6.17 (Ap 5 min, 100% platelets).

5.5 DFA characterization: structure, composition, size and morphology of biomimetic apatites

According to the DFA method described in the previous section, the synchrotron X-ray scattering data of Ap and cAp samples were processed by considering two bivariate populations of Ca-deficient hydroxyapatite nanocrystals, having hexagonal and platy shapes, respectively, and an additional amorphous phase modelled by suitably scaling the experimental ACP diffraction curve. For each dataset, the DFA provided relevant analytical, structural and microstructural information, specifically on:

1. The relative abundance of ACP and hexagonally/platy shaped CDHA;
2. The bivariate size distribution of CDHA nanocrystals from which the average crystal sizes and shapes and their dispersions were obtained;
3. The site occupancy factors of Ca and hydroxyl O atoms of the apatite structure, from which Ca/P ratios were derived, and the Debye-Waller parameters of all atoms;
4. The surface density of citrate molecules.

Each of these results is hereafter separately described in detail and the most important changes upon sample maturation are pointed out.

Phase abundance. The weight percentage (wt%) of each of the three phases (ACP, hexagonal and platy apatites) in Ap and cAp samples are reported in Table 5.2 and variations at increasing maturation time are also graphically depicted in Figure 5.8. ACP is always a minor component slowly decreasing upon maturation (from 17.8 to 6.1 wt% in Ap, from 17.6 to 9.6 wt% in cAp samples, respectively); platy shapes [varying from 82.2 to 38.1 wt% (Ap) and from 76.6 to 28.1 wt% (cAp)]

represent (nearly) the total crystalline component at 5 min of maturation and tend to decrease upon time, the hexagonal shapes becoming the major crystalline component after 96 h in both Ap (55.8 wt%) and cAp (62.3 wt%) samples.

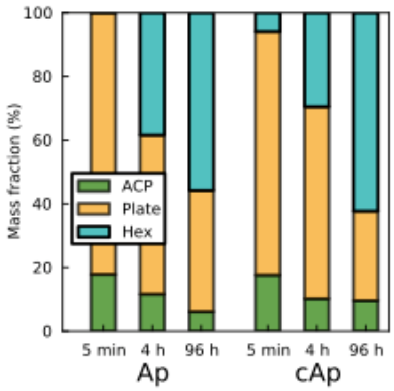

Figure 5.8 Relative abundance of amorphous (ACP) and crystalline apatite phases, having hexagonal or platy shape, as estimated by the DFA method for each Ap and cAp sample at growing maturation time.

Crystal sizes and shapes. As far as the DFA results on the crystal sizes, shapes and their distributions are concerned, by comparing the 2D maps of Figure 5.7 (depicting the refined bivariate size distributions of all samples) at low (5 min) and high (96 h) maturation times, a clear growth of the crystals (and its wide distribution of sizes) along the *c*-axis can be observed, for both the cAp and Ap samples; at variance, a limited growth and a narrow(er) distribution are found in the orthogonal direction (*ab*-plane).

Average (number- and mass-based) crystal sizes and size distributions, derived from the previous maps for both the hexagonal and the platy shapes, are synoptically collected in Table 5.3 and in Table 5.4 and

graphically shown (mass-based values only) in Figure 5.9, where they are given as $<D_{ab}>$, σ_{ab} and $<L_c>$, σ_c in the hex case, as average crystal width (<W>) and thickness (<T>) in the *ab*-plane, in the platy case, the crystal length $<L_c>$ being the same for the two morphologies.

Table 5.3 Bivariate lognormal average sizes ($<D_{ab}>$, $<L_c>$), size distributions (standard deviations σ_{ab}, σ_c) (*nm*), and aspect ratios (AR=$<L_c>/<D_{ab}>$) of hexagonally shaped CDHA nanocrystals. D_{ab} is the diameter of the circle of equivalent area in the ***ab*** base, L_c the length along the ***c*** axis.

Sample	Number Distribution			Mass Distribution		
	$<D_{ab}>$ (σ_{ab})	$<L_c>$ (σ_c)	AR	$<D_{ab}>$	$<L_c>$ (σ_c)	AR
Ap 5 min	3.6 (1.2)	8.4 (3.9)	2.3	4.9 (1.6)	12.1 (5.4)	2.5
Ap 4 h	7.0 (1.0)	16.6 (7.9)	2.4	7.4 (1.0)	21.0 (9.3)	2.8
Ap 96 h	8.5 (1.9)	14.4 (9.6)	1.7	10.5 (1.8)	25.1 (11.9)	2.4
cAp 5	3.2 (1.1)	6.3 (3.1)	2.0	4.5 (1.5)	9.6 (4.6)	2.1
cAp 4 h	5.6 (1.2)	9.0 (5.5)	1.6	6.8 (1.3)	15.0 (7.9)	2.2
cAp 96 h	10.9 (1.7)	16.2 (9.0)	1.5	12.3 (1.7)	24.1 (10.8)	2.0

Table 5.4 Bivariate lognormal average sizes ($<W>$ and $<T>$) and size distributions (standard deviations σ_W, σ_T) (*nm*) of platy shape CDHA nanocrystals. W and T are the width along the ***b*** axis and the thickness of the ***ab*** base, respectively (see inset of Figure 5.9). $<L_c>$ and σ_c values coincide with those reported in Table 5.3.

Sample	Number Distribution		Mass Distribution	
	W (σ_W)	T (σ_T)	W (σ_W)	T (σ_T)
Ap 5 min	4.8 (1.6)	2.1 (0.7)	6.1 (2.1)	2.6 (0.9)
Ap 4 h	8.6 (1.3)	3.7 (0.6)	8.9(1.4)	3.9 (0.6)
Ap 96 h	10.3 (2.6)	4.4 (1.1)	12.4 (2.5)	5.4 (1.1)
cAp 5 min	4.43 (1.49)	1.92 (0.65)	5.66 (2.03)	2.45 (0.88)
cAp 4 h	7.07 (1.63)	2.45(0.70)	8.15 (1.78)	3.53 (0.77)
cAp 96 h	12.90 (2.37)	5.87 (1.03)	14.46 (2.32)	6.26 (1.0)

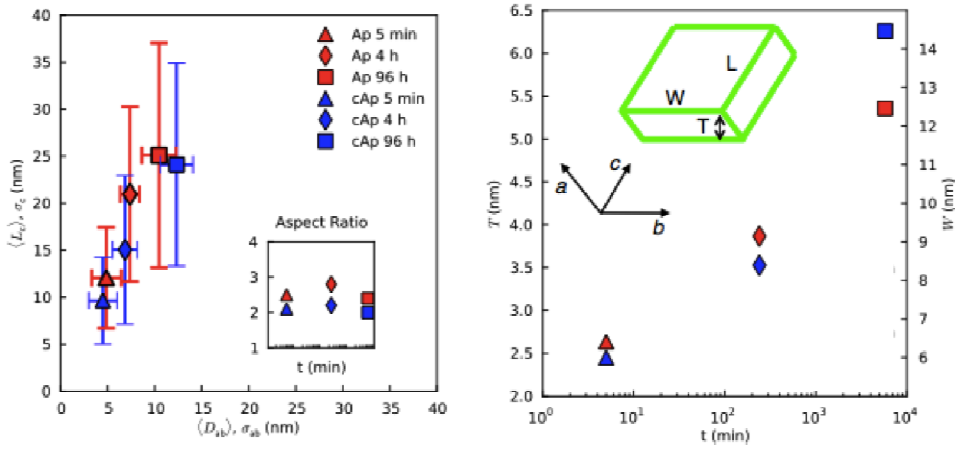

Figure 5.9 Left: Average sizes of hexagonally shapeed apatite crystals at growing maturation time, for Ap and cAp samples. Values are given as crystal length (<L_c, σ_c) and diameter of the circle of equivalent area (<D_{ab}>, σ_{ab}). The inset shows the average aspect ratio. Right: average thickness (T) and width (W) of platy crystals; σ_W, σ_T, not reported for sake of clarity, are available in Table 5.4. The inset shows the assignment of T, W, L to crystal domains and NPs (as seen by AFM) as well.

Upon maturation, crystals of progressively larger sizes along the two (three, for platelets) growth directions are found; in cAp, crystals are systematically smaller and less anisotropic than in Ap, in agreement to what reported in the literature, as the effect of the carbonate substitution [31]; average aspect ratios (<L_c>/<D_{ab}>) are 2.0÷2.2 and 2.4÷2.8 in cAp and Ap samples, respectively.

Citrate coverage. Number-based size distributions have been used in the present study to calculate the (total and lateral) specific surface area (SSA) of each Ap and cAp sample, taking into account both model morphologies. The total surface area (SSA_{Total}) was calculated including {10-10} and {0001} facets, while only {10-10} facets were used for the later surface area ($SSA_{Lateral}$). Combining these values and the amount of

citrate estimated by TGA (taken from ref. [24]), the surface density was evaluated as 1 citrate molecule/(n nm)^2 (*i.e.* using the same formalism proposed in ref. [20] for biological samples). All SSA and n values are reported in Table 5.5. In the investigated samples, the average densities (weighted over the two morphologies) of {10-10} facets are in the range 1.6÷2.0. Worth of note, any *a priori* assumption was used to derive n.

Table 5.5 Citrate molecules w%, from TGA analysis and Specific Surface Area (SSA_{Total} and $SSA_{Lateral}$, m^2g^{-1}) from DFA have been used to derive the citrate surface density n [given as 1 molecule/(n nm)^2] of {10-10} facets in hexagonal and platy crystals.

		Hex crystals			Platy crystals		
Sample	Citrate (w%)	SSA_{Total}	$SSA_{Lateral}$	n	SSA_{Total}	$SSA_{Lateral}$	n
Ap 5 min	5.0	587	490	1.72	586	518	1.77
Ap 4 h	2.4	321	273	1.88	375	332	2.08
Ap 96 h	2.0	228	187	1.71	274	238	1.93
cAp 5 min	5.9	671	542	1.66	646	558	1.69
cAp 4 h	3.3	375	299	1.67	424	361	1.84
cAp 96 h	2.1	193	153	1.51	235	201	1.73

Ca/P ratios. An important structural feature of biomimetic Ca-deficient apatites relies on the Ca/P ratio, a parameter that can strongly affect their dissolution properties [41]. These values have been obtained for Ap and cAp samples by refining the site occupancy factor (*sof*) of the two independent Ca atoms of the apatite structure (see Figure 5.5) and compared to the experimental Ca/P values (available from ref. [24] by ICP-OES). However, this kind of analysis provides a global indicator in

which the likely different Ca/P ratios of amorphous and crystalline components within the same sample cannot be distinguished. The DFA method allows the Ca/P ratio of the *crystalline* apatite to be estimated *independently* of any co-existing ACP fraction. Refined Ca *sof's* and Ca/P ratios derived there from for CDHA crystals only [$Ca/P_{(DFA\text{-}Cr)}$] are reported in Table 5.6 for all samples. Values [$Ca/P_{(DFA\text{-}T)}$] taking the ACP fraction into account were also estimated by adding the (suitably weighted) ICP–OES-determined value for ACP (1.71±0.03) to the previous ones. Table 5.6 also reports the refined *sof* of the hydroxyl O atom, the amount of which may fluctuate as a function of the Ca deficiency and the crystal structure defectiveness [42].

Table 5.6 Site occupancy factor for Ca_1 (Wyckoff's *4f*), Ca_2 (Wyckoff's 6h), and hydroxyl O atoms (Wyckoff's *6h*); $Ca/P_{(DFA\text{-}Cr)}$ ratios are derived by DFA for the crystalline apatite component and $Ca/P_{(DFA\text{-}T)}$ by adding to these values the ICP–OES-determined value for ACP. $Ca/P_{(ICP\text{-}OES)}$ are the ICP–OES-determined Ca/P values (taken from ref. [24]).

Sample	Ca_1	Ca_2	O_{OH}	$Ca/P_{(DFA\text{-}Cr)}$	$Ca/P_{(DFA\text{-}T)}$	$Ca/P_{(ICP\text{-}OES)}$
Ap 5 min	0.937	0.919	0.5	1.54	1.57	1.53(2)
Ap 4 h	0.979	0.892	0.5	1.54	1.56	1.51(2)
Ap 96 h	1.000	0.949	0.46	1.62	1.63	1.54(2)
cAp5 min	0.946	0.914	0.5	1.54	1.57	1.60(2)
cAp 4 h	0.983	0.957	0.44	1.61	1.62	1.60(2)
cAp 96 h	0.993	0.971	0.43	1.63	1.64	1.58(2)

[$Ca/P_{(DFA\text{-}T)}$] values seem to fairly match the ICP-OES-determined Ca/P ratios. Major deviations can be observed in the most mature Ap and cAp samples (96 h), for which more stoichiometric apatite crystals are indicated by DFA. However, this DFA finding is in agreement with self-

healing processes reported in the literature for synthetic apatites at increasing maturation time [41].

Sof's in Table 5.6 refer to values from a size-independent model. Size-dependent *sof*'s have been refined only in the 96 h samples which provided: in cAp, a fairly constant *sof* ~ 0.992 (Ca1), values in the range 0.91÷0.97 for Ca2 and 0.42÷0.44 for O_{OH}, on increasing the crystal size (mainly along the *c*-axis, according to the size distribution map of Figure 2c); in Ap s: *sof* ~ 1.0 (Ca1), 0.92÷0.95 (Ca2) and 0.5 (O_{OH}).

Table 5.7 Isotropic Debye-Waller factors (Å^2) for Ca_1, Ca_2, P, phosphate and hydroxyl O atoms.

Sample	Ca_1	Ca_2	P	O (PO_4)	O (OH)
Ap 5 min	0.86[a]	1.28	1.05	1.13	3.89
Ap 4 h	1.26	0.91	1.12	1.43	2.87
Ap 96 h	1.04	1.11	0.91	1.30	2.46
cAp 5 min	1.01	1.27	1.27	1.13	4.85
cAp 4 h	1.36	1.48	1.31	1.46	4.36
cAp 96 h	1.32	1.14	1.41	1.28	2.77

[a] For the statistical significance of the D-W factors, see note in Table 5.1.

Atomic Debye-Waller factors. (Chemically) plausible values of the (size-independent) isotropic atomic Debye-Waller factor were refined for the investigated samples. The values ranged from 0.9 to 1.5 (Å^2) for Ca, P and phosphate-O atoms, while larger parameters (in the 2.5÷4.8 Å^2 range and decreasing at larger crystal sizes) were found for O_{OH}. All the values are reported in Table 5.7.

5.6 Radial Distribution Function characterization

Aiming at exploring structural similarities between the amorphous phosphate phase and the apatite crystals, the Total Scattering characterization in *real space* of ACP (the instantaneously precipitated material) and of cAp 96 h (the most mature one), was performed. The two corresponding *G(r)'s* functions are compared in Figure 5.10. The first two peaks correspond to the nearest-neighbour P-O (1.5 Å), Ca-O (2.4 Å) and O-O (2.5 Å) inter-atomic distances, respectively. For $r < 5$ Å, peaks indicate a similar local organization around each calcium ion in the two samples.

Figure 5.10 also shows that the particle correlation length in ACP does not extend over 10 Å. This value well matches the (theoretically calculated) radius of Posner's cluster [43] (the purported common building unit of ACP and apatite), as well as the size of experimentally detected calcium phosphate clusters (by Dynamic Light Scattering) [44] and stable pre-nucleation clusters (high-resolution cryo-Transmission Electron Microscopy) [1818] in simulated body fluids, and, to some extent, also the slightly polydisperse ACP NP thicknesses of 1.1±0.5 nm measured by AFM in the present study and described in the next section. Very recently, the nano-sized entities named pre-nucleation clusters in ref. [18], have been identified by the same group of authors as soluble calcium triphosphate complexes which aggregate in solution and, after taking up Ca^{2+} ions, precipitate as ACP, which is described as a fractal of $Ca_2(HPO_4)_3^{2-}$ clusters [45]. Concerning the role of these pre-nucleation (or Posner) clusters, or of the polynuclear complexes, the observations and the results from the present study on the structural and morphological evolution of apatite, and the RDF characterization, seem to be in favour

of a NC growth from a solid precursor in which smaller pre-organized entities progressively grow within the ACP NPs. However, nothing confirming or excluding that these clusters are ion association complexes, can be said.

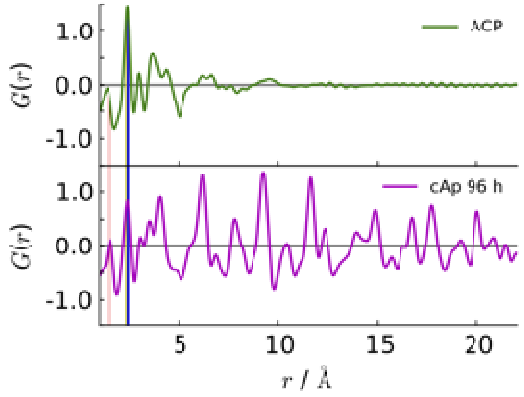

Figure 5.10 Reduced G(*r*) function providing the plot of atomic number density *vs.* atomic distances in ACP (top) and in cAp 96 h (bottom). The first two peaks correspond to the nearest-neighbour P-O (1.5 Å, red vertical bar), Ca-O (2.4 Å, grey vertical bar) and O-O (2.5 Å, blue vertical bar) interatomic distances, respectively. G(*r*) also shows that the ACP correlation length does not extend over 10 Å and, at low *r* values (< 5 Å), peaks indicate a similar local organization around each calcium ion in the two samples.

5.7 AFM characterization of apatite NPs

AFM *ex situ* measurements were carried out on the same samples characterized by the DFA method, as an independent analysis on the size and the morphology evolution of Ap and cAp NPs. Worth of note, AFM resolution cannot "see" the crystalline or amorphous nature of the imaged NPs. The sub-nanometre vertical resolution (better than 0.1 nm) of the AFM images was used, in particular, to obtain reliable values of the NPs thickness. The AFM image of ACP shown in Figure 5.3 and the *z*-section depicted in the inset clearly indicate that they are platelets, the average

sample thickness of 1.1±0.5 nm being much smaller than both the average length and width. The amorphous nature of these particles is witnessed by the synchrotron X-ray scattering pattern and the RDF analysis on samples precipitated under the same conditions. ACP, before and after AFM investigations, remained unchanged; as it was confirmed by X-ray diffraction and Raman spectroscopy (see Figure A1.2 in Annex 1).

Table 5.8 summarizes the dimensions of the NPs as measured by AFM. In all samples, the NPs are platelets increasing their thickness upon maturation time. ACP appears as isometric NPs (in the imaging plane) whereas Ap and cAp are clearly elongated. Their morphological evolution showed opposite trends: Ap NPs increased their width and length; cAp NPs slightly thickened while the other two dimensions progressively reduced. A detailed discussion of these findings is presented in the next section.

Table 5.8 (Number-based) average linear dimensions (nm) and their variances for nanoparticles *imaged* by AFM. Thickness (T_{AFM}), Width (W_{AFM}) and Length (L_{AFM}) are assigned according to Figure 5.9.

Sample [(b)]	$< L_{AFM} >$	$< W_{AFM} >$	$< T_{AFM} >$
ACP	35.5 ± 6.9	34.7 ± 6.5	1.1 ± 0.5
Ap 5 min	53.2 ± 7.4	24.4 ± 3.8	2.5 ± 0.7
Ap 4 h	66.3 ± 22.9	38.9 ± 15.1	6.2 ± 1.1
Ap 96 h	104.1 ± 19.0	56.6 ± 12.2	13.5 ± 4.1
cAp 5 min	80.1 ± 11.6	50.4 ± 10.4	2.8 ± 0.5
cAp 4 h	56.8 ± 13.1	38.0 ± 12.4	4.7 ± 1.6
cAp 96 h	38.9 ± 8.0	28.7 ± 4.2	6.1 ± 2.2

[(b)] The AFM averages are compared in Figure 5.11 to the mass-based values (instead of the number-based ones) derived by DFA. This choice relies on the fact that the mass-based DFA-values are more representative of the whole sample, which is therefore more safely compared to the finest particles analyzed by AFM.

The formation of platy amorphous calcium phosphate NPs is a fairly unusual finding, though not completely new. In fact, other authors by *in situ* AFM have recently reported on ACP (or poorly crystalline apatite) platelets (2.3 nm thick) forming on the surface of calcite crystals through a surface-induced mechanism initiated by the aggregation of clusters and leading to the nucleation and growth of ACP/apatite particles [46]. Interestingly, the process was observed in the presence of citrate that, in low concentration, increased the mineral nucleation rate.

Analogously to these observations, the formation of ACP platelets in the present study might be explained by the action of a template surface favouring the oriented aggregation of calcium phosphate clusters. López-Macipe et al. [2222] already proposed that calcium phosphate heterogeneously nucleates on the surface of sodium citrate crystals grown in the early stages. They suggested that the formation of the template was crucial to obtain apatite particles with nanosized dimensions. In the present study, sub-micrometer-sized $Na_3(cit)\cdot 2H_2O$ and $Na_3(cit)\cdot 5.5H_2O$ crystals were also detected by X-ray diffraction immediately after mixing (see Figure A1.2 of Annex 1) and disappeared very rapidly. This finding suggested that the ACP platelets are formed by the oriented aggregation of clusters adsorbed on the surface of sodium citrate crystals, which later dissolve by sudden pH changes (as shown in Figure A1.1 of Annex 1).

5.8 DFA *vs* AFM: a plausible mechanism forming platelets

This section is dedicated to tentatively interpreting the structural and morphological evolution of the citrate-controlled apatite NPs by cross-coupling the Total Scattering [DFA and G(r)] and the AFM results.

Our AFM analysis shows that tiny platelets form at the earliest stages of precipitation, amorphous in nature (ACP sample), the correlation length of which [*ca.* 1 nm, as measured by the G(r) function] well matches the thicknesses of 1.1±0.5 nm measured by AFM on a sample obtained in the same synthetic conditions. On increasing the maturation time, Ap and cAp appear as thicker but still platy NPs (Figure 5.3 and Table 5.8). On the other side, DFA indicates the formation of apatite nanocrystals after 5 min coexisting with a non-negligible amount of ACP (ca. 18 wt%). At this maturation time, the majority of crystals (more than 90 wt% of the crystal fraction) appear as tiny, platy shaped domains *ca.* 2.5 nm thick, 6.0 nm wide and 9.6 nm long (Figure 5.9). Upon maturation, larger crystals of preferential hexagonal shape (up to 70 wt%) develop while the content of ACP progressively decreases (below 10 wt%). Ap and cAp samples mainly differ in the systematically smaller sizes and the lower aspect ratios of nanocrystals in cAp.

One of the most relevant finding was that, regardless of the chemical environment and the precipitation time, all samples show a broad distribution of crystal lengths (along the *c*-axis) and a narrow distribution of size in the *ab*-plane. Interestingly, the estimated citrate surface density of 1 molecule/(n nm)^2 provided values of n (for the lateral coverage) in the 1.6-2.0 range, which are very close to the value (n~2) reported for avian and bovine bone by Schmidt-Rohr and co-workers [20]. Therefore, both findings (the narrow crystals size distribution normal to the {10-10} facets and the citrate coverage of these facets) are well in agreement with the mechanism, hypothesized in bone mineralization by the previously mentioned authors, of adsorbed citrate stabilizing the apatite crystals thickness. Nonetheless, Schmidt-Rohr and

co-workers do not explain (*they just assume*) the preferential platy shape of crystals found at low maturation times.

Aiming at clarifying this point, the average thickness (T_{DFA}), width (W_{DFA}) and length (L_{DFA}) of *crystal domains* provided by DFA, were then compared to those determined by AFM on whole *single NPs* (T_{AFM}, W_{AFM}, L_{AFM}), disregarding their amorphous or crystalline nature. In doing such a comparison, thickness (T), width (W) and length (L) are assigned to the platelets (either crystal domains or NPs), as in Figure 5.9 (T < W < L,), which also shows the mutual orientation of crystallographic axes and NPs surface. T_{DFA} and W_{DFA} correspond to weighted averages of hexagonal and platy morphologies.

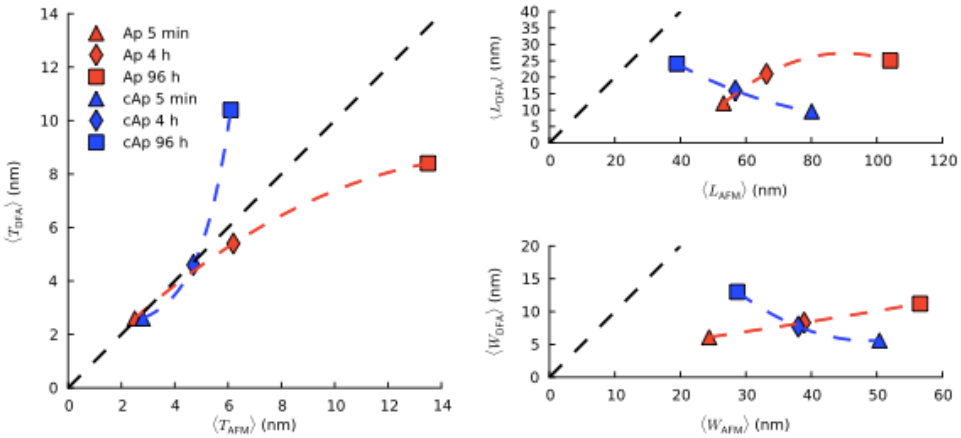

Figure 5.11 Left: average thickness of crystal domains provided by DFA (T_{DFA}) *vs*. average thickness of NPs provided by AFM (T_{AFM}). Right: average length of crystal domains (L_{DFA}) *vs*. average length of NPs (L_{AFM}) (top) and average width of crystal domains (W_{DFA}) *vs*. average width of NPs (W_{AFM}) (bottom).

This comparison is graphically depicted in Figure 5.11. Importantly, crystal thickness systematically matches the NPs thickness ($T_{DFA} \approx T_{AFM}$) until 4 h maturation, while width and length are systematically smaller in crystals than in NPs ($W_{DFA} < W_{AFM}$ and $L_{DFA} < L_{AFM}$). This result implies

that, at low and medium maturation time, NPs *must be* single crystal domains along T_{AFM} and multiple crystal domains along W_{AFM} and L_{AFM}. The coincidence of T_{DFA} and T_{AFM} (the shortest sizes) further indicates that crystals are oriented with their (10-10) plane parallel to the NP surface imaged by AFM (easily caught by comparing platelets of Figure 5.1 and of Figure 5.9). This finding is very important, as it enables the anisotropic growth along the crystallographic *a*- and *b*-axes (breaking the hexagonal symmetry and giving rise to platy crystals) to be inferred. Indeed, due to the finite thickness of the parent amorphous platelets (T_{AFM}) and the further binding of citrate on the surface, the growth is expected to stop in one direction but to freely continue in the other directions within each NP, therefore increasing W_{DFA} and L_{DFA}, as later substantiated.

In order to interpret what happens at longer maturation time and explaining why the crystals and NPs at 96 h do not show similar thickness, many aspects need to be considered. Time-dependent pH variations (Figure A1.1) and the tendency toward dissolution of the smallest crystals (which show, in addition, a lower Ca/P ratio, see Table 5.6) might favour particle aggregation/re-crystallization phenomena [41] and, therefore, new crystals and NPs (having different sizes and shapes) are likely to form. These processes are witnessed by the change towards a preferential hexagonal shape of crystals (according to the DFA findings) and the different way Ap and cAp NPs changed their size and shape (according to the AFM study). Indeed, Ap NPs grew along all three directions (T_{AFM}, W_{AFM} and L_{AFM}) and multiple crystal domains appear even along their thickness. In contrast, cAp NPs slightly thickened while they progressively shrank in W_{AFM} and L_{AFM} (Figure 5.11), T_{DFA} being

1.5 times larger than T_{AFM}, a rather difficult to interpret conundrum. A tentative explanation is hereafter proposed and takes into account that, in DFA, crystal sizes are representative of the entire irradiated sample volume, while AFM analyzes only the finest fraction. Therefore, in the cAp 96 h case, the single NPs might be more selectively made of platy crystals, whose thickness well fits that of NPs (ca. 6 nm, compare values in Table 5.4 and Table 5.8) and accounting for *ca.* 30 wt% of the total crystal fraction. The remaining larger hexagonal crystals are expected to fall into the bigger aggregates. If the same assumption is taken for the youngest samples, results do not change significantly since platy crystals are nearly ubiquitous and the major fraction in the 5 min and 4 h samples.

On the basis of the foregoing results, a plausible mechanism is proposed for the formation of apatite platelets, which is pictorially schematized in Figure 5.12. It relies on the multiple roles citrate ions seem to play for the samples here investigated.

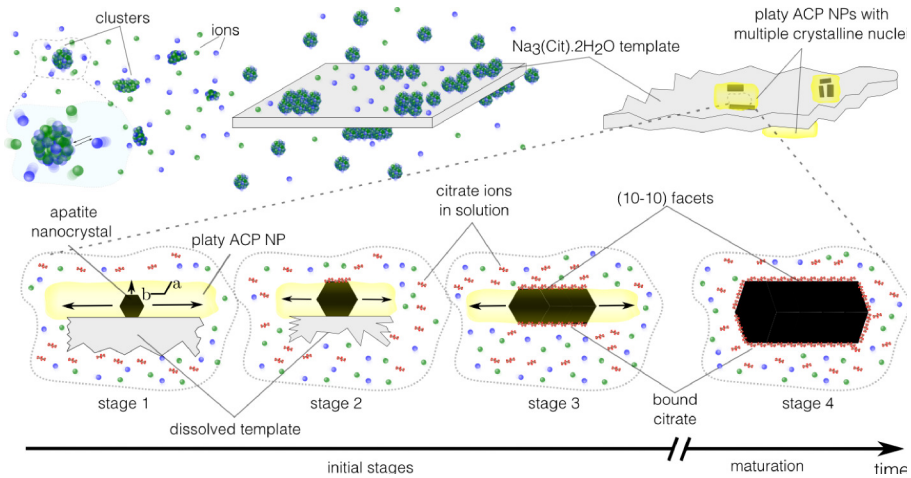

Figure 5.12 Schematics of the mechanism forming crystal platelets during the ACP-to-apatite transformation. A time scale of minutes applies to the initial stages and hours to the maturation process.

The sodium citrate crystals detected at the earliest stages [47] are supposed to act as a template surface which, through adsorption of ionic species (Ca^{2+}, HPO_4^{2-} and OH^-, neglecting the minor ones), might trigger the heterogeneous nucleation process through surface formation of "clusters" that, laterally aggregating, form ACP particles with unusual platy morphology [46]; alternatively, the template surface might adsorb calcium phosphate clusters already formed in solution.

Partial dissolution of the template, due to the drop of pH and the temperature change in the initial stages (Figure A1.1), leads to the formation of $Hcit^{2-}$/cit^{3-} anions, which partially bind to the ACP platelets, slowing down their thickening by inhibiting further ion adsorption and NP aggregation. Apatite crystals start to grow from multiple nuclei *within* each ACP platelet. The hexagonal crystal symmetry drives independent growth of each nucleus along the *c*-axis and isotropically along the *a*- and *b*-axes, in the orthogonal plane until the NP platelet surface is reached. At this point citrate ions [strongly bound to surface Ca^{2+} ions on the free (10-10) crystal facet] stop any further growth in this direction, which anyway continues in the other two (in the presence of as yet untransformed amorphous material) until separately nucleated crystal domains touch each other. Platy crystals of the same thickness as initial ACP platelets are thus formed at low maturation times.

After a few hours this mechanism seems to be still active in controlling the average crystal thickness. However, dissolution, aggregation and recrystallization phenomena start to become effective and hexagonal crystals start to form (or, in other words, the average crystal anisotropy in the *ab*-plane starts to decrease) until they become dominant after 96 h, with the growth of larger (more stoichiometric) apatite crystals.

5.9 Conclusions

In this chapter, Total Scattering Techniques, mostly DFA but also RDF analysis, have been used as a multivalent approach to quantitatively investigate many aspects of interest (structure, stoichiometry, size and morphology) of biomimetic apatites within a coherent framework, showing all the strength and potential of such an approach. Nevertheless, the advantage of jointly use complementary techniques, in this case X-ray scattering (DFA) and microscopic methods (AFM), has allowed the amorphous-to-crystalline transformation process to be disclosed and an appealing plausible mechanism inducing the platy morphology in bio-inspired apatite nanocrystals to be proposed. The role of citrate in driving the formation of platy apatite NCs similar to those formed in bone under the control of acidic non-collagenous proteins, collagen fibrils and, likely, citrate ions, was also pointed out. A similar mechanism might be at work in bone mineralization, where citrate ions might play a broader role than has been depicted to date. Finally, the quantitative picture of the structural, compositional and morphological evolution of citrate-controlled apatite nanoparticles, here presented, can be of great relevance in tuning the properties of this important class of biomaterials for advanced applications.

References

1. F. Nudelman, N.A.J.M. Sommerdijk, *Biomineralization as an Inspiration for Materials Chemistry*, **2012,** Angew. Chem. Int. Ed., *51*, 6582-6596.

2. E. Beniash, *Biominerals-hierarchical nanocomposites: the example of bone*, **2011**, WIREs Nanomed. and Nanobiotechnol., *3*, 47-69.

3. R. Z. LeGeros, *Calcium phosphate-based osteoinductive materials*, **2008**, Chem. Rev., *108,* 4742.

4. H. P. Rim, K. H. Min, H. J. Lee, S. Y. Jeong, S. C. Lee, *pH-Tunable Calcium Phosphate Covered Mesoporous Silica Nanocontainers for Intracellular Controlled Release of Guest Drugs*, **2011**, Angew. Chem. Int. Ed., *50,* 8853-8857.

5. J. Gómez-Morales, M. Iafisco, J. M. Delgado-López, S. Sarda, C. Drouet, *Progress on the preparation of nanocrystalline apatites and surface characterization: overview of fundamental and applied aspects,* **2013,** Progr. Cryst. Growth, *59*, 1-56.

6. J. Mahamid, A. Sharir, L. Addadi, L. S. Weiner, *Amorphous calcium phosphate is a major component of the forming fin bones of zebrafish: Indications for an amorphous precursor phase,* **2008**, Proc. Natl. Acad. Sci. U.S.A., *105*, 12748-12753.

7. J. Mahamid, B. Aichmayer, E. Shimoni, C. Li, S. Siegel, O. Paris, P. Fratzl, S. Weiner, L. Addadi, *Mapping amorphous calcium phosphate transformation into crystalline mineral from the cell to the bone in zebrafish fin rays*, **2010**, Proc. Natl. Acad. Sci. U.S.A., *107*, 6316-67321.

8. F. Nudelman, K. Pieterse, A. George, P. H. H. Bomans, H. Friedrich, L. J. Brylka, P. A. J. Hilbers, G. de With, N. A. J. M. Sommerdijk, *The role of collagene in bone apatite formation in the presence of hydroxyapatite nucleation inhibitors*, **2010,** Nature Mater., *9*, 1004-1009.

9. E. Beniash, *Biominerals-hierarchical nanocomposites: the example of bone*, **2011**, WIREs Nanomed. and Nanobiotechnol., *3*, 47-69.

10. S. J. Eppell, W. Tong, J. L. Katz, L. Kuhn, M. J. Glimcher, *Shape and size of isolated bone mineralites measured using atomic force microscopy*, **2011**, J. Orthop. Res., *19*, 1027-1034.

11. P. Fratzl, H. S. Gupta, E. P. Paschalis, P. Roschger, *Structure and mechanical quality of the collagen-mineral nano-composite in bone*, **2004**, J. Mater. Chem., *14*, 2115-2123.

12. M. I. Kay, R. A. Young, A. S. Posner, *Crystal structure of hydroxyapatite*, **1964,** *Nature*, *204*, 1050-1052.

13. J. C. Elliot, P. E. Mackie, R. A. Young, *Monoclinic hydroxyapatite*, **1973**, *Science*, *180*, 1055-1057.

14. Th. Leventouri, *Synthetic and biological hydroxyapatite: crystal structure questions*, **2006**, Biomaterials, *27*, 3339-3342.

15. N. J. Crane, V. Popescu, M. D. Morris, P. Steenhuis, M. A. Ignelzi Jr., *Raman spectroscopic evidence for octacalcium phosphate and other transient mineral species deposited during intramembranous mineralization*, **2006**, Bone, *39*, 434-442.

16. S. Weiner, *Transient precursor strategy in mineral formation of bone*, **2006**, Bone, *39*, 431-433.

17. Y. Politi, T. Arad, E. Klein, S. Weiner, L. Addadi, *Sea urchin spine calcite forms via a transient amorphous calcium carbonate phase*, **2004**, Science, *306*, 1161-1164.

18. A. Dey, P. H. H. Bomans, F. A. Müller, J. Will, P. M. Frederik, G. de With, N. A. J. M. Sommerdijk, *The role of prenucleation clusters in surface-induced calcium phosphate crystallization*, **2010**, Nature Mater., *9*, 1010-1014.

19. S. V. Dorozhkin, *Nanosized and nanocrystalline calcium orthophosphates*, **2010**, Acta Biomater., *6*, 715-734.

20. Y.-Y. Hu, A. Rawal, K. Schmidt-Rohr. *Strongly bound citrate stabilizes the apatite nanocrystals in bone,* **2010,** Proc. Natl. Acad. Sci. U.S.A., *107*, 22425-22429.

21. B. Xie, G. H. Nancollas, *How to control the size and morphology of apatite nanocrystals in bone*, **2010**, Proc. Natl. Acad. Sci. U.S.A., *107*, 22369-22370.

22. A. López-Macipe, J. Gómez-Morales, R. Rodríguez-Clemente, *Nanosized hydroxyapatite precipitation from homogeneous calcium/citrate/phosphate solutions using microwave and conventional heating*, **1998**, Adv. Mater., *10*, 49-52.

23. Y.-Y- Hu, A. Rawal, T. Prozorov, M. Akinc, S. K. Mallapragada, K. Schmidt-Rohr, *Biomimetic self-sssembling copolymer-hydroxyapatite nanocomposites with the nanocrystal size controlled by citrate*, **2011**, Chem. Mater., *23*, 2481-2490.

24. J. M. Delgado-López, M. Iafisco, I. Rodríguez, M. Prat, J. Gómez-Morales, *Crystallization of bioinspired citrate-functionalized nanoapatite with tailored carbonate content*, **2012**, Acta Biomater., *8*, 3491-3499.

25. T. Egami, S. J. L. Billinge, in *Underneath the Bragg peaks: structural analysis of complex materials*, **2003**, Pergamon Press, Oxford, UK.

26. P. Debye, *Zerstreuung von Röntgenstrahlen*., **1915**, *Ann. Phys., 46*, 809-823.

27]. A. Cervellino, C. Giannini, A. Guagliardi, *Debussy: a Debye user system for nano-crystalline materials*, **2010**, *J. Appl. Cryst*., *43*, 1543-1547.

28. Energy calculations support the preference of citrate binding to {10-10} vs. {0001} facets: M. R. T. Filgueiras, D. Mkhonto, N. H. Leeuw, *Computer simulations on the adsorption of citric acid at hydroxyapatite surfaces*, **2006**, J. Cryst. Growth., *294*, 60-68.

29. A. Guagliardi, A. Cedola, C. Giannini, M. Ladisa, A. Cervellino, A. Sorrentino, S. Lagomarsino, R. Cancedda, M. Mastrogiacomo, *Debye function analysis and 2D imaging of nanoscaled engineered bone,* **2010***,* Biomaterials, *31*, 8289-8298.

30. G. Campi, A. Ricci, A. Guagliardi, C. Giannini, S. Lagomarsino, R. Cancedda, M. Mastrogiacomo, A. Cedola, *Early stage mineralization in tissue engineering mapped by high resolution X-ray microdiffraction,* **2012**, Acta Biomater., *8*, 3411-3418.

31. R. Z. LeGeros, O. R. Trautz, J. P. LeGeros, E. Klein, W. P. Sirra, *Apatite crystallites: effects of carbonate on morphology*, **1967**, Science, *155*, 1409-1411.

32. S. V. Dorozhkin, M. Epple, *Biological and medical significance of calcium phosphates,* **2002***,* Angew. Chem. Int. Ed., *41*, 3130-3146.

33. A. Cervellino, R. Frison, G. Cernuto, A. Guagliardi, in *Crystallography for Health and Biosciences,* N. Masciocchi and A. Guagliardi, Eds., **2012**, Insubria Univ. Press, Varese, Italy.

34. L. B. Mc Cusker, R. B. Von Dreele, D. E. Cox, D. Louër, P. Scardi, *Rietveld refinement guidelines*, **1999**, J. Appl. Cryst., *32*, 36-50.

35. TOPAS-R, V.3.0, **2005**, Bruker AXS,, Karlsruhe, Germany.

36. Y. Gan, *Atomic- and Subnanometer Resolution in Ambient Conditions with Atomic Force Microscope*, **2009**, Surf. Sci. Reports, *64*, 99-121.

37. B. Dickens, L. W. Schroeder, W. E. Brown, *Crystallographic studies of the role of Mg as a stabilizing impurity in β-$Ca_3(PO_4)_2$. The crystal structure of pure β-$Ca_3(PO_4)_2$,* ***1974****,* J. Solid State Chem., *10*, 232-248.

38. T. Pilati, F. Demartin, C. M. Gramaccioli, *Lattice-Dynamical Estimation of Atomic Displacement Parameters in Carbonates: Calcite and Aragonite $CaCO_3$, Dolomite $CaMg(CO_3)_2$ and Magnesite $MgCO_3$,* **1998***,* Acta Crystallogr. B, *54*, 515-523.

39. Th. Leventouri, C. E. Bunaciu, V. Perdikatsis, *Neutron powder diffraction studies of silicon-substituted hydroxyapatite,* **2003**, Biomaterials, *24*, 4205-4211.

40. P. D. Sampson, A. F. Siegel, *The measure of "size" independent of "shape" for multivariate lognormal populations*, **1985**, J. Am. Stat. Assoc., *80*, 910-914.

41. L. Wang, G. H. Nancollas, *Calcium orthophosphates: crystallization and dissolution*, **2008**, Chem. Rev., *108*, 4628-4669.

42. G. Cho, Y. Wu, JL. Ackerman, *Detection of hydroxyl ions in bone mineral by solid-state NMR spectroscopy,* **2003**, Science, *300*, 1123-1127.

43. A. A. Posner, F. Betts, *Synthetic calcium amorphous phosphate and its relation with bone mineral structure*, **1975**, Bone Min. Str., *8*, 273-281.

44. K. Onuma, A. Ito, *Cluster growth model for hydroxyapatite*, **1998**, Chem. Mater.**,** *10*, 3346-3351.

45. W. J. E. M. Habraken, J. Tao, L. J. Brylka, H. Friedrich, L. Bertinetti, A. S. Schenk, A. Verch, V. Dmitrovic, P. H. H. Bomans, P. M. Frederik, J. Laven, P. van der Schoot, B. Aichmayer, G. de With, J. J. DeYoreo, N. A. J. M. Sommerdijk, *Ion-association complexes unite classical and non-classical theories for the biomimetic nucleation of calcium phosphate,* **2013,** Nature Commun., *4*, 1507.

46. L. Wang, E. Ruiz-Agudo, C. V. Putnis, M. Menneken, A. Putnis, *Kinetics of Calcium Phosphate Nucleation and Growth on Calcite: Implications for Predicting the Fate of Dissolved Phosphate Species in Alkaline Soils*, **2012**, Environ. Sci. Technol., *46*, 834-842.

47. According to the data proposed by Gao et al. (J. Gao, C. Xie, Y. Wang, Z. Xu, H. Hao, *Solubility data of trisodium citrate hydrates in aqueous solution and crystal-solution interfacial energy of the pentahydrate,* **2012**, Crys. Res. Tech., *47*, 397-403) the actual concentration values of citrate are well below the supersaturation level at any temperature in the 0:100 °C range; however the occurrence of pH changes and of several complexation equilibria when Ca^{2+} ions are present forces the

precipitation of a small amount of tiny sodium citrate crystals, observed also in blank experiments performed by adding $CaCl_2$ uniquely to *ca.* 0.4 M solution of sodium citrate.

Chapter 6

Defective Coordination Polymers: From Paracrystalline $[Ru(CO)_4]_n$ 1D Polymer to Nanosized Ruthenium Metal

6.1 Introduction

Nanosized 1D molecular metal wires and 1D, 2D superclusters that are assembled through M–M bonds have peculiar geometric and electronic features making them interesting low-dimensional molecular materials for several fields of applications (molecular electronics, nanolithography, catalysis [1-6]). Among these, organometallic polymers containing M-M bonds in the backbone might inherently act as potential precursors to high aspect ratio nanomaterials and ultrathin metal nanowires, thanks to the presence of metal atoms arranged in chains and the relatively inert ligands wrapped around them and provided that the main problem of preventing the aggregation of the metal chains, once organic ligands are removed, is solved [7,8]. Indeed, many extended carbonyl species have been synthesized through the years, [see for example the $HRe(CO)_4$ polymer [9] or the $[Pt_3(CO)_6]_n^{m-}$ stacks of D_{3h} fragments [10]]; however, the tendency of 2nd and 3rd row transition metals to maximizing the metal-to-metal connectivity plays a major role in driving high-nuclearity carbonyl clusters toward a closed, convex, often polyhedral shape [11], making the isolation of 1D species a rare event.

In this view, the long known $[Ru(CO)_4]_n$ polymer [12] features a very anisotropic distribution of metal atoms, within collinear chains of (covalently bonded) ruthenium atoms, making it a promising candidate, as witnessed by the interest in the recent scientific literature. Many papers have addressed the polymer chemical and functional properties [11,13,14] towards the formation of ruthenium nanowires upon controlled thermal degradation [15]. Worthy of note, Ru metal nanoparticles pyrolytically generated at 200 °C from the polymeric precursor [16,17]

show enhanced catalytic activity, *e.g.* in CO oxidation (with reduced conversion temperatures and increased conversion yields), compared to those prepared from Ru salts or Os precursors. These appealing properties are attributed to the presence of *elongated* Ru nanorods (TEM evidence).

"Ruthenium tetracarbonyl" is a cornerstone of modern organometallic chemistry [18]. Its stable and commercial form, the widely known $Ru_3(CO)_{12}$ molecule, normally appears as a cyclic trimer in which ligand-unsupported Ru-Ru bonds generate a triangular cluster of idealized D_{3h} symmetry [19]. At variance, the polymeric $[Ru(CO)_4]_n$ species contains chains of *trans*-D_{4h}-$Ru(CO)_4$ fragments (shown in Figure 6.1) staggered by 45° one to each other, with a Ru-Ru distance of 2.860(1) Å (very close to that found in solid $Ru_3(CO)_{12}$, 2.844(2) Å [20]). Independent solid-state ^{13}C NMR on nanosized $[Ru(bipy)(CO)_2]_n$ polymer ($n \approx 20$) and DFT methods on the pristine $[Ru(CO)_4]_4$ species have confirmed the staggering of chains [21,22]. Therefore, being $[Ru(CO)_4]_4$ a *unique* case of a neutral homoleptic carbonylic polymer where metal atoms are arranged in parallel chains well separated by the ligand shell, it is considered one of the most appropriate candidates for the formation of highly anisotropic Ru metallic nanoparticles, by simple CO desorption.

The renewed interest in its potential nanotechnological properties couples with some intriguing structural and microstructural aspects of $[Ru(CO)_4]_n$ polymer that, nearly two decades after a crystal and molecular model has been proposed (by unconventional structural powder diffraction methods) [23], remain unsolved and leave the interpretation of the structural defectiveness of this compound still unsatisfactory.

This chapter is dedicated to a detailed analysis of the structural defectiveness of the $[Ru(CO)_4]_n$ chain polymer and on its modelling through the DFA approach. The Total Scattering approach enabled a new, previously unforeseen, 2D *paracrystalline* effect to be disclosed. A *paracrystal* is a crystalline species that has a highly distorted lattice with unit cells of variable shape and size, and in which correlation among the different displacement exists. An original way of implementing this structural defect in the DFA approach, *i.e.* including correlated chain displacements, is here presented and its application to X-ray synchrotron data collected on the compound under study is discussed.

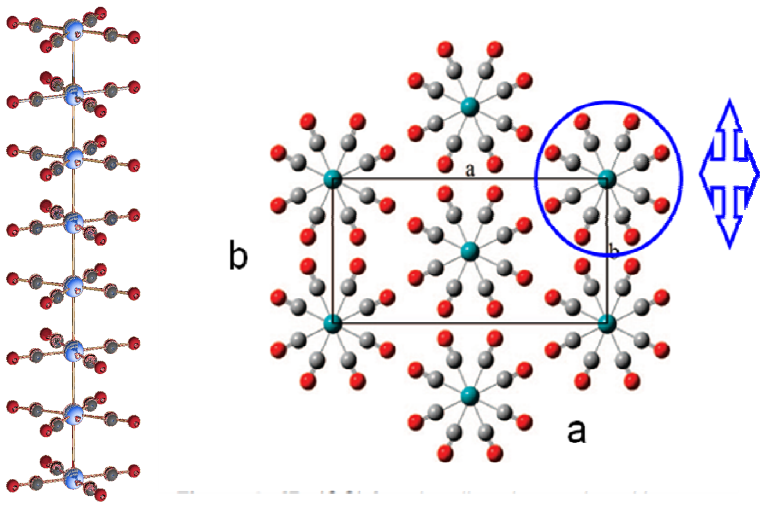

Figure 6.1 Left: a 8-monomers sequence of staggered D_{4h} $Ru(CO)_4$ fragments; right: the pseudohexagonal *Ibam* crystal packing [23] of the polymeric chains in **ab** (viewed down **c**). The arrows refer to the *correlated* shift directions of a paracrystalline model later discussed.

Despite recent advancements (described in chapter 3 [24]) have made it possible extending the application of the DFA approach to the

characterization of a variety of nanosized materials (metals, oxides and chalchogenides and bioceramics, [25-32, however, studies of covalently bound systems by this method have not been reported. Therefore, this is also the first case of application, in the realm of simple organometallic polymers of known *average* structure, allowing otherwise inaccessible structural features to be disclosed.

Moreover, the *in-situ* thermally induced transformation to ruthenium metal nanoparticles was also investigated, aiming at unravelling potential effects of the defects on the formation of nanowires. In this view, surprising results have been obtained.

6.2 Experimentals

6.2.1 Materials

A powdered sample of $[Ru(CO)_4]_n$ was prepared in 4 h following standard literature methods [12,23], using a UV lamp (with an emission peak near 290 nm).

6.2.2 Synchrotron X-ray scattering measurements

Synchrotron X-ray scattering data were collected at the X04SA-MS beamline [33,34] of the Swiss Light Source, at RT on freshly prepared $[Ru(CO)_4]_n$ using the experimental set-up described in chapter 3, a beam energy of 20 keV (λ = 0.620639 Å) and a 0.3 mm ∅ glass capillary. Prior to the DFA modelling, Silicon NIST 640c, air and glass capillary scattering patterns were measured and all the steps of the reduction procedure described in chapter 3 applied to the raw data. The beamline

high angular resolution, without significant instrumental contribution to the peak broadening, played an important role in this case of study.

In a parallel set of experiments, $[Ru(CO)_4]_n$ *in situ* measurements were performed (using the wavelength λ =1.00411 Å), from RT up to 470 K, where transformation to metallic ruthenium was complete, in 5 K steps. Upon cooling back to room temperature, the full diffraction pattern was collected again and used for the characterization of metallic Ru.

Total scattering data analysis was performed using a modified version of the Debussy Suite [35] in which coding of the complex algebra briefly presented in next paragraphs was included. Le Bail and Rietveld refinements (*vide infra*) were performed using the Fundamental Parameter Approach implemented in TOPAS-R [36].

6.3 Facing a complex microstructural problem

The $[Ru(CO)_4]_n$ powder diffraction trace shows some peculiar features, that have been repeatedly observed in different preparations by different groups, also adopting slight modifications of the original synthesis procedure, which are clearly visible in Figure 6.2: the coexistence of a few sharp peaks with very broad ones (wider than 2.0° in laboratory data using Cu-Kα radiation). In the original Rietveld-like [37] structure analysis, with diffracted intensities computed by taking into account Bragg scattering only, such an anisotropic peak broadening was tentatively attributed to lattice strain in the **ab** plane; a *phenomenological* description of the shape and the width of these peaks was adopted and a model able to anisotropically broaden the peaks was applied.

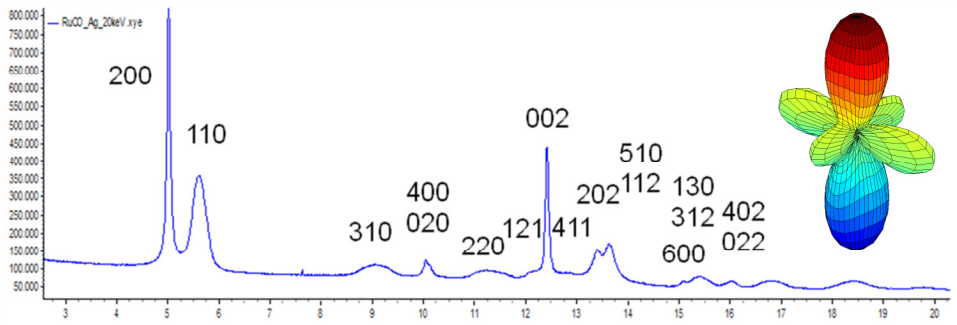

Figure 6.2 Indexed XRPD pattern of $[Ru(CO)_4]_n$, showing very anisotropic peak widths. The inset shows the plot of the isosurface obtained by spherical harmonics representing the *average* crystal shape, resulting in a concave surface with no obvious physical counterpart (the largest lobe lies along the **c** direction).

Aiming at unraveling the complex structural defectiveness behind such experimental observations, the newly collected synchrotron diffraction data (free of instrumental broadening effects) were used for a deeper analysis of the widths of the peaks, following a single-peak fitting procedure. The analysis ended up with very narrow *h00, 0k0* and *00l* peaks, providing microstructural information along **a**, **b** and **c** axes, respectively, and very broad *hk0* peaks ($h,k \neq 0$), related to the off-axes directions. These values were then back transformed into real space to extract information about the (vectorially-spread) *apparent crystal sizes* (*ACS*, determined by estimating the 1/cosθ-dependent Lorentzian size broadening). Interestingly, instead of defining a convex shape, *ACS* nicely fall on a concave 2D plot (Figure 6.3), which would imply questionable star-shaped nanocrystals, with highly protruding beams, 10 times larger in **a** and **b** than along the diagonals. Moreover, a shape of this type was not confirmed by electron microscopy [15].

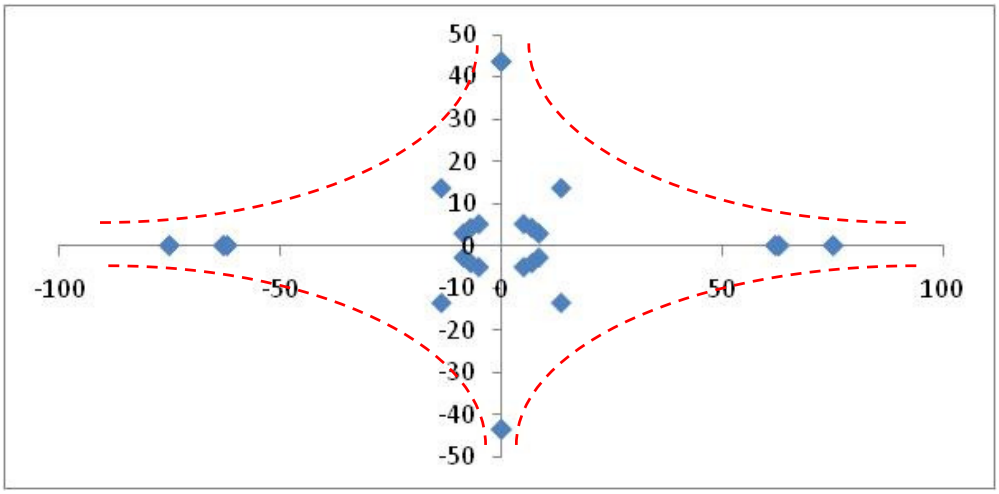

Figure 6.3 Plot of the distribution of the *ACS* values (nm), derived from unconstrained single-peak profile fitting of the *hk0* reflections, drawn in the *xy* real space. The dashed red lines are a guide to the eye.

A full pattern simulation carried out using the (4^{th} order) symmetrized spherical harmonics model of the TOPAS-R program and accounting for *in-plane* and *off-plane* microstructural features, provided apparent *average size* and *shape* of crystals of *mmm* symmetry (inset of Figure 6.2). The *concave* surface shown in the inset speaks for an awkward "perturbation" effect (even if slightly concave Pd nanocubes have been reported [38]). These findings seem to exclude size and shape of the crystal domains as possible causes of the effect observed in the diffraction pattern. In a similar way, if the unusual peak broadening is attributed to strain (with tanθ dependence), no obvious physical counterpart can be devised. These results, eventually suggested the occurrence of a conditional disorder, later attributed to *anisotropic paracrystallinity* of the chains packing in *ab*, as discussed in detail in the following section.

6.4 Including 2D anisotropic paracrystalline effects in the Debye Function Analysis

Recovering the structural defectiveness of $[Ru(CO)_4]_n$ was possible thanks to the intrinsic nature of the DSE [39] of dealing with structural defects in real space and then providing an *exact* modeling, in the reciprocal space, of the whole sample scattering.

Following the seminal work by Hosemann, Bachi and Welberry [40,41], the Debye equation was suitably modified to add anisotropic *paracrystalline* features to the average crystal structure. In order to understand how such a phenomenon of partially correlated shifts can be accounted for within the DSE formalism, some essential algebraic details, based on the Welberry's formalism [41], are also provided in Annex 2.

With specific reference to the case of $[Ru(CO)_4]_n$, *damped* correlations (in real space) between chain axes locations in *ab* were defined and a probabilistic description of the interatomic vectors in that plane was considered. For a better comprehension of the model, the case of 1D displacements in a 2D lattice is firstly considered. According to the algebraic details in A.2.1, the following equation applies:

$$P_a(\boldsymbol{d}) = K_a \exp\left[-\frac{1}{2}\frac{(\boldsymbol{d}-\boldsymbol{d}_0)^2}{2\sigma_a^2\left(1-r_a^{|m|}s_a^{|n|}\right)}\right]$$

where $\boldsymbol{d}$ is the vector separating two chains (in *ab*), r_a and s_a are the so-called *longitudinal* and *transversal* correlation coefficients and *m* and *n* are the location (in lattice units) of the pertinent chain. σ_a^2 is the statistical variance (*i.e.* the amplitude of *uncorrelated* shifts) of the packing periodicity along **a**; σ_a^2 also represents the natural limit of the dispersion

of large interatomic distances (see Figure A.2.1) [40]. A schematic drawing of the geometrical relationships among the different correlation coefficients is shown in Figure 6.4. The left portion of the figure has to be considered in the 1D case. Extension to 2D displacements are easily obtained by adding new r_b, s_b and σ_b terms, where now r_a and s_b are the longitudinal correlation coefficients and s_a and r_b are the transversal ones.

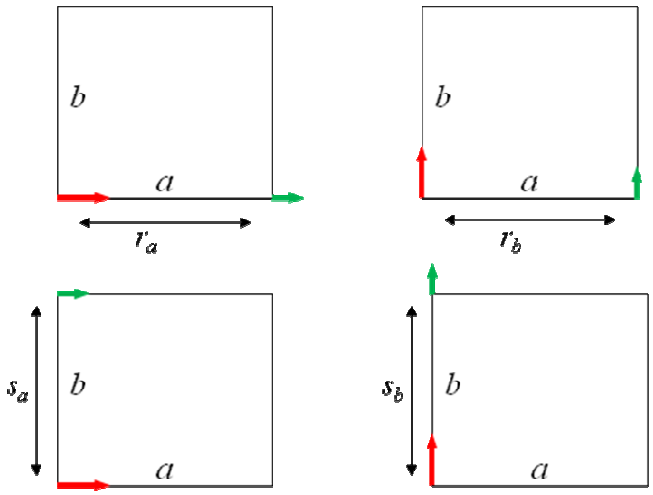

Figure 6.4 Schematic drawing of the geometrical relationships among the different correlation coefficients used in this work. Within each frame, movements depicted by red arrows cause the shifts drawn in green. *Longitudinal* correlation coefficients r_a and s_b describe shifts along the same line of the initial perturbation, while *transversal* ones, represented by the r_b and s_a scalars, describe shifts of the parallel (transversal) rows.

Therefore, the *longitudinal* coefficients describe shifts along the *same* row of the initial perturbation (the horizontal *a* row in the top left box, the vertical *b* row in the bottom right box, respectively) but do not apply to the *parallel* ones; correlated shifts in the parallel rows are indeed described by the *transversal* coefficients. With reference to Figure 6.4, displacements depicted by the red arrows cause the shifts drawn in green.

The equation for 2D displacements becomes:

$$P(\boldsymbol{d}) = K\, exp\left(-\frac{1}{2}\boldsymbol{v}C^{-1}\boldsymbol{v}\right)$$

$$C = \begin{pmatrix} \sigma_a^2 & \sigma_a\sigma_b c_{xy} \\ \sigma_a\sigma_b c_{xy} & \sigma_b^2 \end{pmatrix}; \qquad \boldsymbol{v} = \boldsymbol{d} - \boldsymbol{d_0}$$

In the 1D case, deviation of r_a and s_a from unity represents the loss of correlation for moieties lying, respectively, along *a* and for the laterally displaced ones (for shifts along *a*). In the 2D case, the one that applies to $[Ru(CO)_4]_n$, more complex losses of correlations, combining shifts along *a* and *b*, might be expected. These aspects are elucidated in the next section.

6.5 The paracrystalline DFA modeling of $[Ru(CO)_4]_n$

In order to reproduce the experimentally observed features of $[Ru(CO)_4]_n$ in the pattern simulation, the following model choices were adopted within the DFA approach:

i) a rigid $[Ru(CO)_4]_n$ fragment model of chains with idealized *$P4_2/mmc$* symmetry, and nearest-neighbors distances Ru-C 1.95 Å, C=O 1.15 Å, Ru-Ru 2.86 Å, and angle Ru-C-O 180°;

ii) the I-centered orthorhombic lattice (*Ibam*) of the average crystal structure as in ref. [23] and the polymeric structure defined in *i)* were used to build up prismatic rod-shaped nanocrystals and to calculate the database of sampled interatomic "correlated" distances to be used in the Debussy Suite. A fixed base model in *ab* was applied, the size of which was 50x50 nm^2 (as derived from the *h00* and *0k0* single-peak widths

analysis), whereas the nanorods height varied up to 70 nm along **c**, and a log-normal distribution of heights was assumed, the average size and width of which were subsequently refined;

iii) the paracrystalline correlation coefficients were adjusted by a grid-search approach to the final values: $r_a = 1.00$; $s_a = 0.97$; $r_b = 0.97$; $s_b = 1.00$; $\sigma_a = \sigma_b = 3.0$ Å.

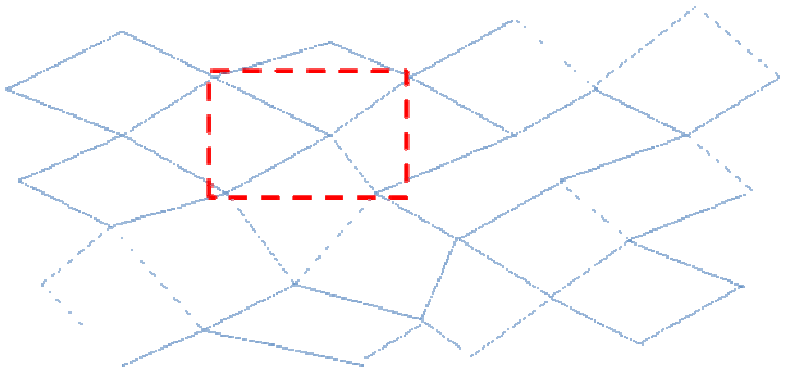

Figure 6.5 A graphically exaggerated *paracrystalline* centered rectangular lattice (dashed red lines), whose displacements from the average periodicity are not random (isotropic strain) nor 100% correlated (ideal crystal).

The first important finding (which will be further discussed) is that deviations from unity are found only for the *transversal* coefficients (s_a and r_b), which are therefore responsible for the large broadening effect of the *hk0* peaks. Although they appear close enough to 1.0 (as it is in a *truly periodic* crystal), their elevation to the $|m|^{th}$, or $|n|^{th}$ power makes the coherence loss at large *d*'s rapidly growing. An easy-to-catch pictorial 2D (exaggerated) representation, in real space, of the *distorted* centered-rectangular lattice of $[Ru(CO)_4]_n$ is given in Figure 6.5, where each node is the projection of one polymeric chain, running along **c**, *i.e.* perpendicularly to the *ab* plane.

A nice graphical 2D representation of the effects in reciprocal space (*hk0* plane) of such deviations is shown in Figure 6.6. Smearing of the intensity and shape modifications for *hk0* nodes with $h \neq 0$ and $k \neq 0$ can be observed. The radial integration of these nodes allows a 1D diffraction pattern to be obtained with very sharp *h00* and *0k0* peaks and rather broad *hk0* ones.

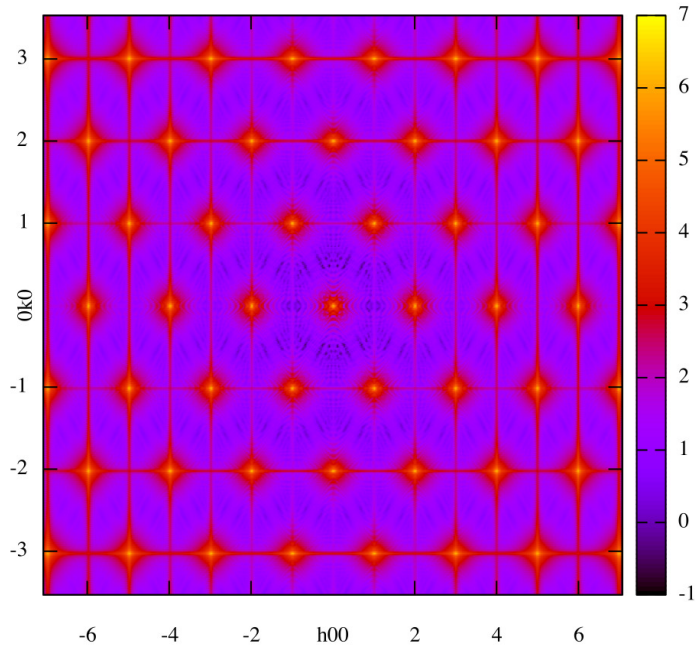

Figure 6.6 2D plot of the intensity distribution in reciprocal space (*hk0* plane, logarithmic scale), calculated by the DSE for an ideal rectangular (centered) paracrystal characterized by the following paracrystalline correlation coefficients: $r_a = 1.00$, $r_b = 0.97$, $s_a = 0.97$, $s_b = 1.00$, $c_{xy} = 0$, $\sigma_x = \sigma_y = 3.0$ Å. Note the shape of the reciprocal lattice nodes, which, after radial integration, give sharp peaks in *h00* and *0k0*, and rather broad traces for *hk0* nodes with $h \neq 0$ and $k \neq 0$.

The DFA paracrystalline approach implemented in the Debussy Suite directly provides the 1D simulation. For $[Ru(CO)_4]_n$ the simulated pattern is shown in Figure 6.6, where it is compared to the experimental

synchrotron trace. The DFA paracrystalline model is able to nicely reproduce the peculiar features of observed peak heights and anisotropic peak widths and shapes. Conventional *profile* agreement factor [42] are $R_p = \Sigma_i |y_{ic}-y_{io}| / \Sigma_i y_{io} = 0.066$, for 570 observed intensity values (y_{io}).

As far as the domain size information is concerned, refined DFA size along **c** gave an average $<L_c>$ value of 44.7 nm and a size distribution 15.4 nm wide. Taking into account the (fixed) edge size of the nanorods base (50 nm), this result indicates that the average domain size in *ab* and along *c* are comparable, therefore witnessing a *nearly isotropic* domain shape of the nanoparticles. Additionally, thermal parameters corresponding to rms vibrational amplitudes of 0.0065 nm (Ru) and 0.0173 nm (C, O) were also refined.

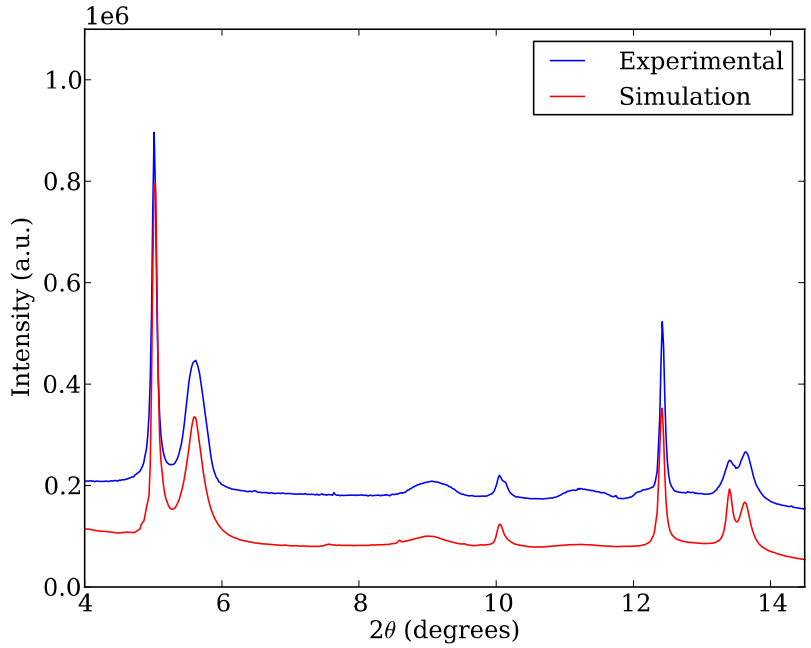

Figure 6.7 Experimental powder diffraction trace for $[Ru(CO)_4]_n$ (blue); DFA simulated trace for the paracrystalline model with the correlations terms quoted in the text (red).

6.6 Chemical interpretation of the paracrystalline $[Ru(CO)_4]_n$ model

The DFA paracrystalline model of $[Ru(CO)_4]_n$ provided *unity* values for the refined longitudinal correlation coefficients, r_a and s_b. With reference to Figure 6.4, this indicates that pushing, or pulling, a $Ru(CO)_4$ chain along *a*, or along *b* (but not diagonally!) induces an analogous shift of the neighbouring chains on the same rows; accordingly, these shifts (being equal in size and direction) do not change the crystal periodicity along the two axes. From the atom-atom interaction point of view, these values are possibly related to the short O···O interactions (3.08 Å) along **a** and, even more evidently, between chains adjacent along **b** (2.81 Å, in the repulsive regime).

At variance, the transversal correlation coefficients, r_b and s_a, though only slightly deviating from unity, are responsible for the large *hk0* peaks broadening, as previously explained. To better interpret this finding, the 2D model depicted in Figure 6.5 is further idealized in Figure 6.8a by a stacking of disks (coins) which schematically describes the collinear Ru chains, each disk representing a *trans*-D_{4h}-$Ru(CO)_4$ fragment, in the case of a perfect (Figure 6.8b) and of an imperfect (Figure 6.8c) stacking. Inspired by the recent work of Macchi *et al.* [43], in which the flexibility of the $Mn_2(CO)_{10}$ molecule was studied under hydrostatic pressures, the hypothesis of *twisted* Ru chains coupling to the imperfect stacking was further explored.

New DFA simulations were performed, in which a (non negligible) bending of the "axial" sequence (very much as in the high pressure phase of the manganese pentacarbonyl dimer) was allowed. Specifically, staggered $Ru(CO)_4$ fragments were allowed to move ca. 0.22 Å off axis

(or, equivalently, the Ru-Ru-Ru angles to change from 180° down to 170°). No relevant differences in the pattern matching were obtained compared to the case of collinear chains (apart from the obvious occurrence of tiny superstructure peaks).

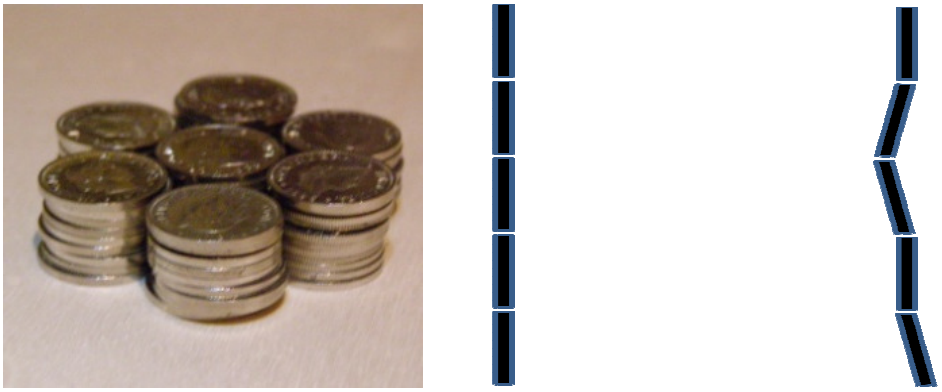

a) b) c)

Figure 6.8 a) Drawing of the packing of flat $Ru(CO)_4$ moieties (idealized by coins) within the (para)crystals. For the perfect (b) and imperfect (c) stacking of linear Ru chains, *see text*. The actual shape and interlocking of the $Ru(CO)_4$ crosses makes the whole average crystal orthorhombic (a/b = 2.0), and not truly hexagonal (a/b = $\sqrt{3}$).

This result suggested that a random chain twisting, as the one shown in Figure 6.8c, if present, (possibly releasing some intramolecular strain) cannot be (easily) detected by diffraction methods. In this view, the hypothesis of a small chain bending was further investigated through the statistical analysis of the X-[$M(CO)_4$]-[$M(CO)_4$]-Y species present in the CSD database, ending up with the following results:

i) X-M-M values as low as 170° are largely represented, with a statistical distribution averaging at 176.8(2.2)°;

ii) staggering of the two $M(CO)_4$ moieties (irrespectively of the actual M, or X, nature and M-M distance), is nearly ubiquitous;

iii) a completely uncorrelated scatterplot between the sets of the X-M-M angles and X-M-M-X torsions is observed, supporting the randomness of the relative disposition of the apical atoms with respect to the M-M axis, and the unlikely presence of ordered *zigzag* or *helical* conformations within the Ru_n chain (which would give rise to weak superstructure peaks, here unobserved). Worthy of note, also the osmium chain present in $Os_5(CO)_{18}(CNBu^t)_2Cl_2$ shows a slight deviation from perfect linearity, with two Os-Os-Os angles of 177° [44].

Further details of the packing disorder were investigated by molecular mechanics, aiming at estimating the relative orientations of the $[Ru(CO)_4]_n$ columns. The packing energy surface of a cluster of seven $[Ru(CO)_4]_n$ chains (see Figure 6.1) was computed using a simple Lennard-Jones potential for the O···O contacts and by perturbing only one column within the cluster through *xy* translation of the inner $Ru(CO)_4$ moieties up to 0.05 nm in each direction.

Interestingly, the columns are found to move more easily along the **b** direction than along **a**, as visible in Figure 6.9 (top), in fairly agreement with the paracrystalline correlation coefficients estimated by DFA model. If the column rotations in the *ab*-plane about the Ru hinges (R_z) are also relaxed, a deep minimum is observed for the 22.5° offset (with respect to the **a** axes) when small *xy* translations are applied, with no significant visible changes in the energy surface (Figure 6.9, bottom).

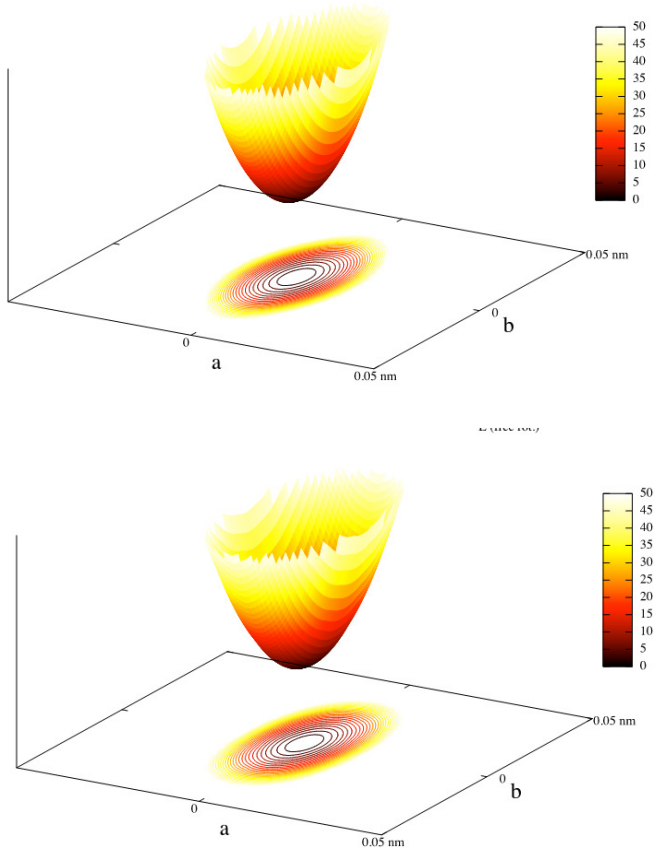

Figure 6.9 Plot of the packing energy surface of a cluster of seven $[Ru(CO)_4]_n$ chains, by perturbing the inner column with xy translations (top) and by adding an additional (free carbonyl rotation) parameter (bottom), with no significant changes between the two surfaces (*graphically indistinguishable*). Energy scale in kJ mol^{-1}.

Plotting the angular variation (°) from this 22.5° "reference value" (obtained by minimizing the potential energy) against the *xy* displacements of the $Ru(CO)_4$ moieties (Figure 6.10), even for a (rather large) 0.05 nm displacement the refined angle is less than 4° off its nominal value. These results witness the near constancy of the $Ru(CO)_4$ orientation, regardless of its actual location, or displacement, in the *xy* plane.

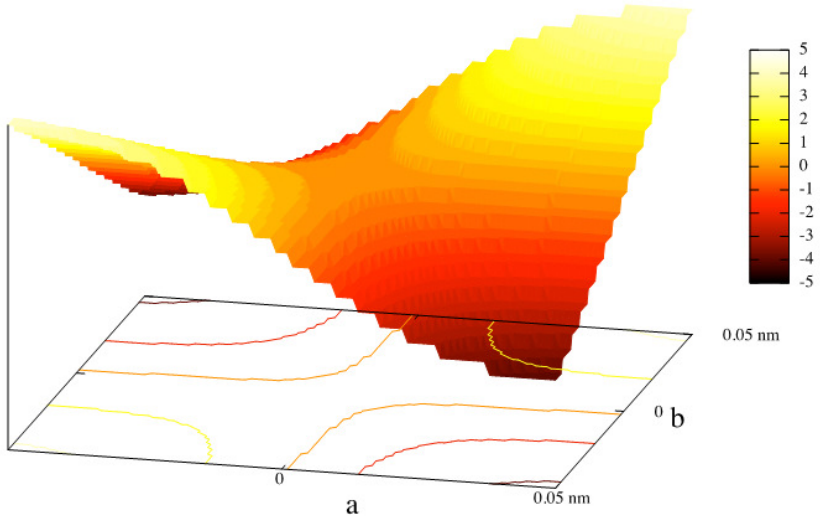

Figure 6.10 Plot of the angular variation (°) from the 22.5° "reference value" showing that the refined angle is less than 4° off its nominal value (vertical scale bar), even a (rather large) 0.05 nm displacement in *xy* is applied to the $Ru(CO)_4$ moieties .

6.7 Thermal evolution study of $[Ru(CO)_4]_n$

The thermal evolution of $[Ru(CO)_4]_n$ was investigated using the conventional (FPA) Rietveld-like approach implemented in TOPAS-R. The 33 diffraction patterns collected in the 30-190 °C temperature range, were used within a parametric whole-pattern refinement providing the lattice parameters relative changes as a function of T, used to calculate the linear thermal expansion coefficients ($\partial \ln x/\partial T$) of $[Ru(CO)_4]_n$ along the three crystallographic axes, as shown in Figure 6.11. The values of 56, 104 and 20 MK^{-1}, for the **a**, **b** and **c** axes, respectively, were obtained. These values indicate a larger thermal expansion suffered by the crystals in the **ab** plane than along **c**, likely due to the swinging motion of the carbonyl groups hinged about the central ruthenium atoms. The combined volumetric value, $\partial \ln V/\partial T$, is nearly 181 MK^{-1}, dominated by the *ab*-

plane component. Interestingly, the conventionally accepted linear thermal expansion coefficient for ruthenium metal [45] is nearly one third of that of $[Ru(CO)_4]_n$ along the **c** axis, witnessing the rather stiff nature of thes Ru-Ru link in this molecular, non-metallic, compound.

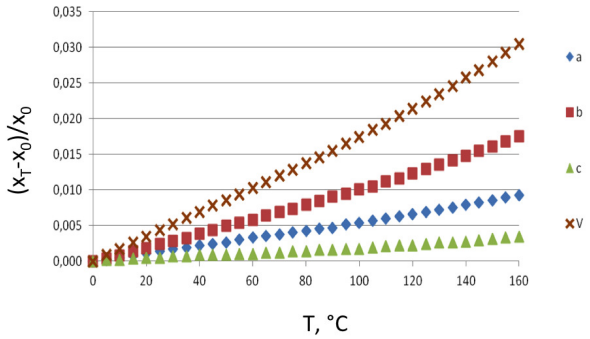

Figure 6.11 Plot of the relative lattice parameter dependence *vs* temperature

The complete transformation of $[Ru(CO)_4]_n$ into the *hcp* Ru metal occurred near 200°C, a temperature significantly higher than those in previous reports [12,15], where the decomposition temperatures of 126°C (under vacuum) or 170 °C are indicated. The higher value observed in experiments performed for the present investigation might be due to the sealed environment (within the glass capillary) and the pressure effects exerted by the freed CO.

The diffraction pattern collected on the *hcp* metallic Ru recovered after cooling to RT was firstly investigated by conventional Rietveld-like analysis, using ideally periodic *hcp* lattice of ruthenium metal and modelling the anisotropic peak broadening by a 8^{th} order spherical harmonics model. The unsatisfactory final fit (R_{wp} 0.072; R_{Bragg} 0.030) highlighted the presence of significant residuals, clearly visible in Figure

6.12, panel A. The differences are compatible with the presence of a (still unknown) cubic phase of Ru (estimated lattice parameter a_0 = 3.86 Å), which suggested, instead, the formation of stacking faults in the ideal *hcp* sequence [46], very much alike the well known paradigmatic case of *hcp* cobalt [47]. Further observation of the systematic broadening of the *h-k≠3N* peaks [48] confirmed this structural hypothesis and pattern simulations (using a specifically developed macro, similar to that proposed by Whitfield *et al*. [49]) provided a (small) growth faulting probability (β) of 0.023(1), well in line with similar values reported on faulted *hcp* metals and alloys.

The presence of stacking faults prevented the DFA of this Ru metal sample, aiming at extracting information on the size and size distribution and at confirming the formation of elongated metal nanoparticles (the Debussy Suite does not – yet - include a model for this kind of defectiveness). However, to obtain an (even) approximated size estimation, the conventional Rietveld-like approach was used considering that, since *00l* peaks are not affected by the presence of faults, a Le Bail, structureless, fit can be applied (see Figure 6.11, panel B), to extract the average domain size in the elongation direction of the expected nanowires. Surprisingly, an average domain size of *only* 5.6 nm was found (nearly one half than that derived in *ab*).

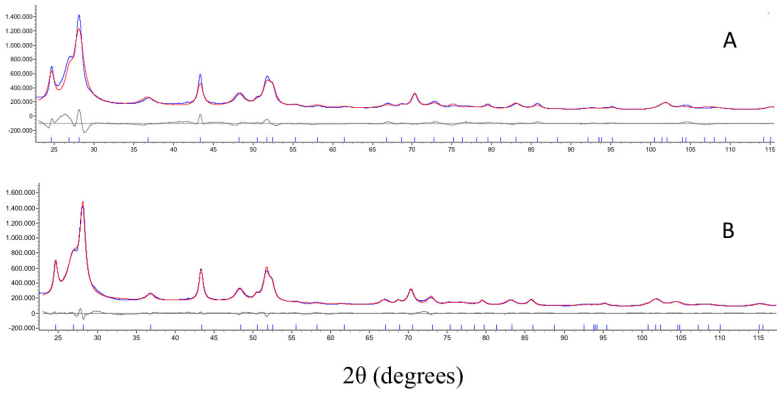

Figure 6.12 Rietveld refinement plots of Ru metal nanoparticles in conventional structural mode (ideally periodic *hcp* lattice of Ru metal is used) (A) and in the structureless (Le Bail) mode (B) with a conditioned broadening of the *h-k≠3N* peaks.

This finding suggests that the polymeric chains, arranged as parallel bundles in the starting $[Ru(CO)_4]_n$ nanoparticles, are broken during the thermal treatment and the metal atoms heavily rearrange in significantly smaller domains. Accordingly, the metallic Ru nanoparticles are neither a single "ordered" phase, nor specifically elongated about one axis. Therefore, the appealing hypothesis that, under pyrolytic conditions, "*the presence of metal-metal bonds allows for retention of the rod-like arrangement of the metal atom chain*" [15] must be dismissed. Worthy of note, alternative ways not using $[Ru(CO)_4]_n$ for preparing high-aspect ratio and catalytically active ruthenium nanorods have been very recently proposed [50].

6.8 Conclusions

The work described in this chapter relied on the development of a specific paracrystalline model, within the more general DFA approach to nanosized materials, and its application to the 1D $[Ru(CO)_4]_n$ species. This work marks a relevant step forward in the history of this *rare* homoleptic metal carbonyl polymer, providing physically sound *quantitative* estimates of unexpected disordering effects, adding "a new dimension" and stereochemical comprehension, after that a convincing structural model was proposed more than 25 years ago and a tentative (semiquantitative) microstructural analysis reported.

As far as the technological interest on this compound is concerned, the thermal desorption of the ligand shell from the polymeric chains of $[Ru(CO)_4]_n$ afforded faulted *hcp* Ru nanoparticles of nearly *isotropic* shape, and *not* elongated metal nanowires, as originally reported. Accordingly, the morphology and the anisotropic structure of the parent organometallic polymer are not maintained in the final product. Reasons different from the high aspect ratio of the metal nanoparticles must be invoked for the observed enhanced catalytic properties.

Finally, on the more methodological side, this work required the development of new analytical expressions and their coding into new computational tools; valid for polymeric $[Ru(CO)_4]_n$, these methods can well be adopted, or adapted, for other "faulted" chain-like structures, where some kind of correlated disorder is present.

References

1. W. R. Caseri, H. D. Chanzy, K. Feldman, M. Fontana, P. Smith, T. A. Tervoort, J. G. P. Goossens, E. W. Meijer, A. P. H. J. Schenning, I. P. Dolbnya, M. G. Debije, M. P. de Haas, J. M. Warman, A. M. van de Craats, R. H. Friend, H. Sirringhaus, N. Stutzmann, *(Hot-)Water-Proof", Semiconducting, Platinum-Based Chain Structures: Processing, Products, and Properties*, **2003**, Adv. Mater., *15*, 125-129.

2. X.-M. Yan, S. Kwon, A. M. Contreras, M. M. Koebel, J. Bokor, G. A. Somorjai, *Fabrication of dense arrays of platinum nanowires on silica, alumina, zirconia and ceria surfaces as 2-D model catalysts*, **2005**, Catal. Lett., *105*, 127-132.

3. F. C. Simeone, C. Albonetti, M. Cavallini, *Progress in micro- and nanopatterning via electrochemical lithography*, **2009**, J.Phys.Chem. C, *113*, 18987–18994.

4. P. Greco, M. Cavallini, P. Stoliar, S. Quiroga, S. Dutta, S. Zacchini, M.C. Iapalucci, V. Morandi, S. Milita, P. G: Merli, F. Biscarini, *Conductive sub-micrometric wires of platinum-carbonyl clusters fabricated by soft-lithography,* **2008,** J. Am. Chem. Soc., *130*, 1177-1182.

5. V. V. Grushin, W. J. Marshall, D. L. Thorn, *A New, Highly Selective Rh(III) Catalytic System for Carboxylation of Arenes via C-H Activation under Mild Conditions,* **2001**, Adv. Synth. Catal., *343*, 161-165.

6. A. Deronzier, in "*Conducting Polymers and Polymer Electrolytes: From Biology to Photovoltaics*". Rubinson, J.F.; Mark, H.B., Jr., **2002**, *ACS Symp. Series*, *832*, 141-153, and references therein.

7. A. Fukuoka, N. Higashimoto, Y. Sakamoto, M. Sasaki, N. Sugimoto, S. Inagaki, Y. Fukushima, M. Ichikawa, *Ship-in-bottle synthesis and catalytic performances of platinum carbonyl clusters, nanowires, and nanoparticles in microporous and mesoporous materials*, **2001**, Catal. Today, *66*, 23-31.

8. S. Zacchini, *Using Metal Carbonyl Clusters To Develop a Molecular Approach towards Metal Nanoparticles,* **2011,** Eur. J. Inorg. Chem., 4125-4145.

9. N. Masciocchi, G. D'Alfonso, L. Garavaglia, A. Sironi, *Complete Structural Characterization by Ab Initio X-Ray Powder Diffraction of [{Re(μ-H)(CO)$_4$}$_n$] and [{Re(μ-H)(CO)$_4$}$_6$], Inorganic Analogues of Polyethylene and Cyclohexane,* **2000,** Angew. Chem., *39*, 4477-4480.

10. C. Femoni, M. C. Iapalucci, G. Longoni, T. Lovato, S. Stagni, S. Zacchini, *Self-assembly of [Pt$_{3n}$(CO)$_{6n}$]$^{2-}$ (n = 4-8) carbonyl clusters: from*

molecules to conducting molecular metal wires, **2010,** Inorg. Chem., *49*, 5992-6004, and references therein.

11. C. Femoni, M. C. Iapalucci, F. Kaswalder, G. Longoni, S. Zacchini, *The Possible Role of Metal Carbonyl Clusters in Nanoscience and Nanotechnologies*, **2006**, Coord. Chem. Rev., *250*, 1580–1604.

12. W. R. Hastings, M. C. Baird, *A new form of ruthenium tetracarbonyl*, **1986,** Inorg. Chem., *25*, 2913-2915.

13. L. Oresmaa, M. A. Moreno, M. Jakonen, S. Suvanto, M. Haukka, *Catalytic activity of linear chain ruthenium carbonyl polymer* $[Ru(CO)_4]_n$ *in 1-hexene*, **2009**, App. Catal. A: Gen., *353*, 113-116.

14. M.-L. Kontkanen, L. Oresmaa, M. A. Moreno, J. Jänis,. E. Laurila and M. Haukka*, One-dimensional metal atom chain* $[Ru(CO)_4]_n$ *as a catalyst precursor - Hydroformylation of 1-hexene using carbon dioxide as a reactant,* **2009,** App. Catal. A: Gen., *365*, 130-134.

15. C. Li, W. K. Leong, *Thermolysis of polymeric* $[Ru(CO)_4]_\infty$ *to metallic ruthenium: molecular shape of the precursor affects the nanoparticle shape,* **2008,** Langmuir, *24*, 12040–12041.

16. C. Li, W. K. Leong, Z. Zhong, Z., *Metallic osmium and ruthenium nanoparticles for CO oxidation*, **2009**, *J.* Organomet. Chem., *694*, 2315-2318.

17. A. D. Pomogailo, A. S. Rozenberg, G. I. Dzhardimalieva, *Thermolysis of metallopolymers and their precursors as a method for the preparation of nanocomposites*, **2011**, Russ. Chem. Rev., *80*, 257-292.

18. M. I. Bruce, C. M. Jensen, N. L. Jones, *Dodecacarbonyltriruthenium,* $Ru_3(CO)_{12}$, **1989**, Inorg. Synth., *26*, 259-261.

19. M. R. Churchill, F. J. Hollander, J. P. Hutchinson, *An accurate redetermination of the structure of triruthenium dodecacarbonyl,* $Ru_3(CO)_{12}$, **1977**, Inorg. Chem., *16*, 2655-2659.

20. C. Slebodnick, J. Zhao, R. Angel, B. E. Hanson, Y. Song, Z. Liu, R. J. Hemley, *High pressure study of* $Ru_3(CO)_{12}$ *by X-ray diffraction, Raman, and infrared spectroscopy,* **2004,** Inorg. Chem., *43*, 5245-5252.

21. G. Gerbaud, J. M. Mouesca, S. Hediger, S. Chardon-Noblat, F. Lafolet, A. Deronzier, M. Bardet, *Structural characterization of metal-metal bonded polymer* $[Ru(L)(CO)_2]_n$ *(L = 2,2'-bipyridine) in the solid state using high-resolution NMR and DFT chemical shift calculations,* **2010,** Phys. Chem. Chem. Phys., *12*, 15428-15435.

22. M. Niskanen, P. Hirva, M. J. Haukka, *Computational DFT Study of Ruthenium Tetracarbonyl Polymer*, **2009,** Chem. Theor. Comput., *5*, 1084-1090.

23. N. Masciocchi, M. Moret, P. Cairati, F. Ragaini, A. Sironi, *Solving simple organometallic structures solely from X-ray powder diffraction data: the case of polymeric [{Ru(CO)$_4$}$_n$],* **1993** J. Chem. Soc. Dalton Trans., 471-475.

24. A. Cervellino, C. Giannini, A. Guagliardi, DEBUSSY: a Debye user system for nanocrystalline materials, **2010,** J. Appl. Crystallogr., *43*, 1543-1552.

25. A. Cervellino, C. Giannini, A. Guagliardi, D. Zanchet, *Quantitative analysis of gold nanoparticles from synchrotron data by means of least-squares techniques,* **2004,** Eur. Phys. J. B, *41*, 485-493.

26. N. Galvez, E. Valero, J. M. Dominguez-Vera, N. Masciocchi, A. Guagliardi, M. Clemente-Leòn, E. Coronado, *Structural and magnetic characterization of Pd nanoparticles encapsulated in apoferritin,* **2010,** Nanotechnology, *21*, 274017.

27. A. Cervellino, C. Giannini, A. Guagliardi, M. Ladisa, *Nanoparticle size distribution estimation by a full-pattern powder diffraction analysis,* **2005,** Phys. Rev. B, *72*, 035412.

28. P. D. Cozzoli, E, Snoeck, M. A. Garcia, C. Giannini, A. Guagliardi, A. Cervellino, F. Gozzo, A. Hernando, K. Achterhold, N. Ciobanu, F. G. Parak, R. Cingolani, L. Manna, *Colloidal synthesis and characterization of tetrapod-shaped magnetic nanocrystals,* **2006,** Nano Lett., *6*, 1966-1972.

29. L. Cademartiri, E. Montanari, G. Calestani, A. Migliori, A. Guagliardi, G. A. Ozin, *Size-dependent extinction coefficients of PbS quantum dots,* **2006,** J. Am. Chem. Soc., *128*, 10337–10346.

30. G. Cernuto, N. Masciocchi, A. Cervellino, G. M. Colonna, A. Guagliardi, *Size and shape dependence of the photocatalytic activity of TiO2 nanocrystals: a total scattering Debye function study,* **2011,** *J*. Am. Chem. Soc., *133*, 3114-3119.

31. G. Cernuto, S. Galli, F. Trudu, G. M. Colonna, N. Masciocchi, A. Cervellino, A. Guagliardi, *Investigating the Amorphous–Crystalline Interplay in SiO_2/TiO_2 Nanocomposites by Total Scattering Methods,* **2011,** Angew. Chem., *50*, 10828-10833.

32. A. Guagliardi, A. Cedola, C. Giannini, M. Ladisa, A. Cervellino, A. Sorrentino, S: Lagomarsino, R. Cancedda, M. Mastrogiacomo, *Debye*

function analysis and 2D imaging of nanoscaled engineered bone, **2010,** Biomaterials, *32*, 8289-8298.

33. P. R. Willmott *et al., The Material Science beamline upgrade at the Swiss Light Source,* **2013**, J. Synchrotron Rad., *20*, 667-682.

34. A. Bergamaschi, A. Cervellino, R. Dinapoli, F. Gozzo, B. Henrich, I. Johnson, P. Kraft, A. Mozzanica, B. Schmitt, X. Shi. *The MYTHEN detector for X-ray powder diffraction experiments at the Swiss Light Source,* **2010,** J. Synchrotron Rad., *17*, 653-668

35. A. Cervellino, C. Giannini, A. Guagliardi*, On the efficient evaluation of Fourier patterns for nanoparticles and clusters,* **2006**, J. Comp. Chem., *27*, 995-1008.

36. TOPAS-R, V.4.0, Bruker AXS, Karlsruhe, Germany.

37. R.A. Young, Ed. "*The Rietveld Method*", **1995**, OUP, Oxford, UK.

38. M. Jin, H. Zhang, Z. Xie, Y. Xia, *Palladium Concave Nanocubes with High-Index Facets and Their Enhanced Catalytic Properties,* **2011,** Angew. Chem., *50*, 7850-7854.

39. A. Guagliardi, A. Cervellino, C. Giannini, C., in "*Diffraction at the Nanoscale. Nanocrystals, Defective & Amorphous Materials*", A. Guagliardi, N. Masciocchi, Eds., **2010**, Insubria University Press, Varese, Italy.

40. R. Hosemann, S.N. Bagchi, *Direct Analysis of Diffraction by Matter*, **1962**, North-Holland Publishing Company, Amsterdam.

41. T.R. Welberry, *Diffuse X-ray scattering and models of disorder*, **2004**, OUP, Oxford, UK.

42. L. B. McCusker, R. B. Von Dreele, D. E. Cox, D. Louër, P. Scardi, *Rietveld refinement guidelines,* **1999**, J. Appl. Crystallogr., *32*, 36-50.

43. P. Macchi, N. Casati, S. R. Evans, F. Gozzo, P. Simoncic, D. Tiana, *An "off-axis" Mn-Mn bond in $Mn_2(CO)_{10}$ at high pressure,* **2014**, Chem. Commun., 12824-12827.

44. F. Jiang, G. P. A. Yap, R. K. Pomeroy*, A Complex with a Linear Chain of Five Osmium Atoms,* **2002**, Organomet., *21*, 773-776.

45. CRC Handbook of Chemistry and Physics, 88th Ed., **2008**, 12-201, CRC Press, Boca Raton, FL.

46. M. Vanden Brink, M. A, Peck, K. L. More, J. D. Hoefelmeyer, *Alkylamine Stabilized Ruthenium Nanocrystals: Faceting and Branching*, **2008**, J. Phys. Chem. C, *112*, 12122-12126.

47. S. V. Cherepanova, O. A. Bulavchenko, S. V. Tsybulya, *Structure of nanocrystalline particles of metallic cobalt formed during the reduction of Co_3O_4 oxide,* **2008,** J. Struct. Chem., *49*, 512-516.

48. R. L. Snyder, J. Fiala, H. J. Bunge, "*Defect and Microstructure Analysis by Diffraction"*, IUCr Monographs on Crystallography, **2000**, OUP.

49. P. S. Whitfield, I. J. Davidson, L. D. Mitchell, S. A. Wilson, S. J. Mills, *Problem solving with the TOPAS macro language: corrections and constraints in simulated annealing and Rietveld refinement*, **2010,** Mater. Sci. Forum, *651*, 11-25.

50. S. G. Peng, J. N. Liu, X. F. Liu, Y. Q. Zhang, J. Zhang, *PVP Stabilized Ruthenium(0) Nanorods as Effective Catalysts in Hydrogen Generation from the Hydrolysis of Sodium Borohydride,* **2011**, Adv. Mater. Res., *197*, 1577-1581, and references therein.

Chapter 7

Defective Molecular Crystals: A Multiple Scale Study of Copper and Silver Nitropyrazolates

7.1 Introduction

In the last two decades, binary metal pyrazolates have attracted a great deal of attention on both the structural side (for their interesting features in terms of connectivities [1,2]) and the functional one (for their appealing luminescent, vapochromic, magnetic, anticorrosive, and even antimicrobial properties [3-10]). Particularly attractive have been the metal polypyrazolates in which long organic spacers are added, as in porous metal-organic frameworks, making this class of highly flexible, thermally and chemically stable compounds, of high relevance in gas storage and separation, in removal and sensing of toxic gases and in drug delivery [11-19].

During their preparation, highly insoluble and intractable solid materials are typically obtained, preventing conventional single crystal structural determination to be performed. In these conditions, when *monophasic* polycrystalline specimens of good crystallinity could be isolated, modern XRPD methods, extensively developed in the course of the last 20 years for *ab initio* structure solution, have allowed many interesting features of these compound to be retrieved [2,20], using conventional powder diffraction equipment. However, more complex structural and microstructural features can take place. This is the case of the two compounds here investigated, Cu(I) and Ag(I) 4-NO_2-pyrazolates, hereafter labeled **1** and **2** respectively; regardless of the synthetic routes followed, they show (reproducibly) very poor diffraction patterns (see Figure 7.1), not easily interpretable by standard XRPD techniques, as some uncommon disordering phenomena disrupt the "ideal" crystal periodicity. Therefore, we found this an appealing problem to be treated via total scattering and DFA approaches [21-23].

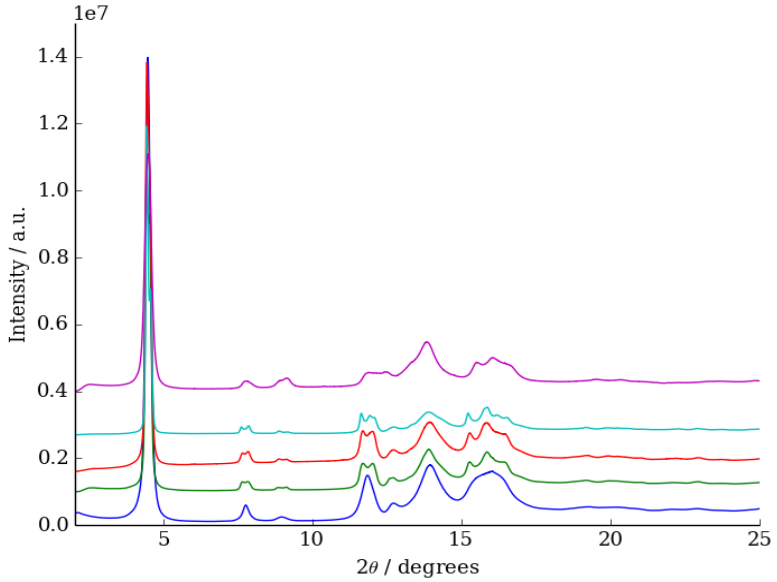

Figure 7.1 Experimental diffraction patterns collected on Ag(I) 4-NO_2-pyrazolate from different synthetic preparations.

Differently from the case presented in chapter 6, for copper and silver nitropyrazolates things were complicated by the lack of an available structural model, which is the essential starting point for further studies on the material defectiveness. For species **1** and **2** this step was accomplished using high-energy synchrotron diffraction data and *ab-initio* XRPD methods complemented by a *phenomenological* approach to peak broadening. The structure determination process is briefly described in this chapter, along with the molecular and (average) crystal structure from which a defective growth mechanism, based on a random faulting within the stacks of trimeric molecules, was inferred [24].

Total scattering techniques, being the most appropriate when dealing with short-range-ordered and defective materials, have been here

applied, both as DFA and as PDF approaches (extensively described in chapter 2 and 3), in order to capture atomic-scale *local* details and to validate the defectiveness model at the atomic and nanometer levels. Such a characterization has been further integrated by a *microscale* analysis obtained from Scanning Electron Microscopy, to address the information on the size and the shape of *multi-domains* particles. Therefore, a multiple scale study was necessary to unravel the highly complex defective growth mechanism of these compounds, which was achieved through the effective combination of conventional XRPD, innovative total scattering techniques and SEM microscopy.

The final part of the chapter, in line with an important aspect of this Thesis, is dedicated to investigating the structure-property relationships, aiming at evaluating the effects of atomic scale defects on the *macroscopic physical properties* of the materials under study [25,26]. In this respect, being the electric properties of high relevance for this class of compounds, the frequency dependent electric behavior (complex AC impedance, and dielectric constant) was measured and compared to that of unfaulted systems of the same class.

Most of the experimental work has been performed on samples of **2** [Ag(I) 4-NO_2-pyrazolate], due to the limited stability of **1** under normal operational conditions.

7.2 Experimentals

Details of the synthesis of Cu(I) and Ag(I) 4-nitropyrazolates are reported in Annex 1. All the alternative synthetic routes described (*i.e.*

using different solvents, concentrations and reaction times) systematically ended up with poorly crystalline materials.

7.2.1 X-ray Total Scattering measurements

Diffraction data were collected in Debye-Scherrer geometry in the 2-120° 2θ range at the X04SA-MS beamline [27,28] of the SLS synchrotron of the Paul Scherrer Institut. Details on the beamline and on the experimental set-up can be found in chapter 3. Powders of **1** and **2** were loaded into 0.3 mm glass capillaries mounted on a rotating (60 rpm) goniometer head. Measurements were performed using a 16 keV radiation [λ = 0.77524(3) Å, after calibration with NIST Standard Reference Material silicon powder 640c] and a He flux on the sample to limit absorption/scattering from air. Angular, angle-dependent intensity corrections, and subtraction of glass capillary and air/He scattering contributions were applied following the data reduction protocol described in chapter 3.

Parallel measurements were also performed in a laboratory instrument, equipped with Ni-filtered Cu-Kα radiation and a 1D position-sensitive detector. While the overall pattern features are confirmed, specimen displacement errors and, for **1**, unavoidable fluorescence effects, suggested to use, for most data analyses, the synchrotron data, even though in this case the advantages of the intrinsic high angular resolution was definitely lost in the extremely broad peaks experimentally observed. Needless to say, for PDF evaluation, only the synchrotron X-ray scattering data were considered. For structure determination and DFA a reduced portion of the synchrotron X-ray diffraction pattern was used.

7.2.2 Scanning Electron Microscopy

SEM images were collected for sample **2** in low vacuum using a FEI XL30 ESEM FEG equipped with an EDAX Quantax 400 and an acceleration voltage of 15.0 kV. Samples were grounded using graphite tapes to prevent charging.

7.2.3 Electric properties measurements

Dielectric constants, and complex AC impedance have been measured, at RT, with an Agilent E4980 LCR Impedance Analyzer. A 20 Hz to 2 MHz frequency sweep at a constant bias of 10 V was used. Changing the bias in the 1 to 15 V range did not alter the obtained results. The measurements were performed on both faulted and reference samples suitably dried and pressed into cylindrical pellets 13 mm wide and with thicknesses in the 0.6–0.8 mm range. Dielectric constants ($\kappa = C_{p(sample)}/C_{p(air)}$) were obtained from experimentally measured capacities C_p (of parallel circuits) for the sample and the air, under the same experimental conditions. DC conductivities (σ_0) were obtained by extrapolating, when possible, the observed AC values to zero frequency using the Universal Dielectric Response model. [29]

7.3 Determining the average crystal structure through a*b-initio* conventional XRPD methods

7.3.1 The a*b-initio* structure solution process

Conventional XRPD *ab initio* structure determination is usually accomplished by performing three main steps [30], aiming at determining: 1) lattice parameters and crystal space group (through peak

search and structureless full profile fitting techniques); 2) atomic coordinates in the asymmetric unit (using direct phasing methods or approaches in real space, such as Simulating Annealing, Genetic Algorithms, semi-exhaustive Grid Search, or others); 3) structure refinement (using the Rietveld method). For the species **1** and **2**, all the steps were performed using the TOPAS-R program [31]. The peak broadening (as clearly visible in Figure 7.1) allowed no more than 12 separated peaks to be used for cell parameters determination that, in combination with the subsequent full profile fitting, provided the estimation of *C*-centered monoclinic cells with a volume (close to 800 $Å^3$) compatible with six $M(C_3H_2N_3O_2)$ (M = Cu, Ag) formula units. Density and symmetry considerations suggested *C*2 as probable space group, later confirmed by successful structure solution.

Two crystallographically independent moieties [$M_{1.5}(C_3H_2N_3O_2)$ and $(C_3H_2N_3O_2)_{0.5}$] with idealized molecular geometries were used to recover the atomic coordinates via Simulated Annealing, allowing for either planar or helical conformations and ending up with the presence of *planar*, trimeric molecules, bisected by the twofold axis aligned with ***b*** and stacked at a short (*ca.* 3.54 Å for M = Cu and 3.50 Å for M = Ag) distance along ***c*** (but not lying normal to it). Rietveld refinements were eventually performed using a phenomenological approach to model anisotropic peak broadening (using both lorentzian and gaussian components) and a Chebyshev polynomial for modeling the background; a single isotropic thermal factor value (B_{iso}) was assigned to all atoms. The best pattern matching is shown in Figure 7.2 and the corresponding average structural model is drawn in Figure 7.3. The most relevant structural information is summarized below.

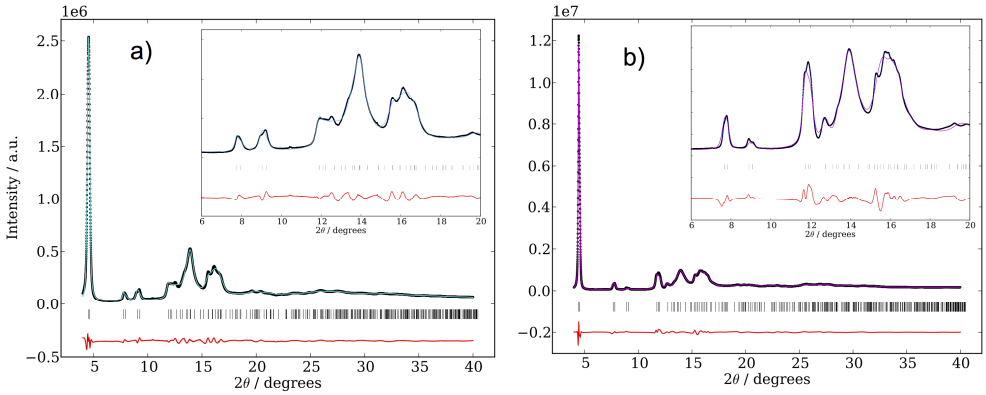

Figure 7.2 Rietveld Refinement plots for **1** (a) and **2** (b) and difference plot (red line) Vertical bars mark reflection position. The insets show the 6≤2θ≤20° regions at a magnified scale.

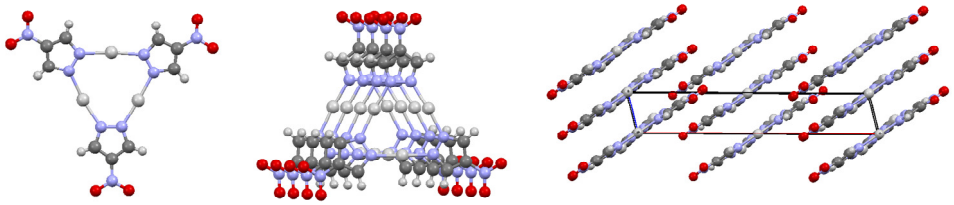

Figure 7.3 (a) Molecular model for the cyclic trimer found in **2** (isomorphous to **1**) and (b) the way it stacks (at a distance of *ca.* 3.5 Å) along the normal to the molecular planes, with a definite (here, horizontal) offset. (c) Crystal packing of **2** viewed down [010], with the molecules, bisected by crystallographic twofold axes, tilted by about 32° from the ***a*** axis (red line, horizontal). The short axis (blue line) is ***c***. At the drawing resolution, the crystal packing and the molecular sketch of **1** and **2** are identical.

Crystal data for **1**: $C_9H_6Cu_3N_9O_6$, fw 526,84 g mol^{-1}, monoclinic, *C*2, a = 19.841(5), b = 11.443(2), c = 3.538(1) Å, β = 104.55(3)°, V = 777.4(3) $Å^3$, Z = 2, ρ = 2.251 g cm^{-3}, F(000) = 516, R_{Bragg} = 0.008, R_p = 0.036 and R_{wp} = 0.044, for 9231 data in the 4-40° (2θ) range, with λ = 0.775276 Å. CCDC No. 982107.

Crystal data for **2**: $C_9H_6Ag_3N_9O_6$, fw 659.81 g mol^{-1}, monoclinic, *C*2, a = 20.242(4), b = 11.600(2), c = 3.509(1) Å, β = 104.71(2)°, V = 797.0(2) $Å^3$, Z = 2, ρ = 2.795 g cm-3, F(000) = 624, R_{Bragg} = 0.015, R_p = 0.044 and R_{wp} = 0.047, for 9231 data in the 4-40° (2θ) range, with λ = 0.775276 Å. CCDC No. 982108.

7.3.2 The average crystal and molecular structures

Crystals of **1** and **2** contain (essentially planar) cyclic trimeric molecules (Figure 7.3*a*) of D_{3h} idealized symmetry (as observed in the majority of Cu(I) and Ag(I) pyrazolates), stacked in columns running along the ***c*** direction. Similar polymeric stacks of planar molecules are also found in other trimeric Cu(I) and Ag(I) pyrazolates [32]. The poor quality of the diffraction traces hampers the derivation of reliable *intra*molecular geometrical parameters involving light atoms, whereas *inter*molecular features are certainly better defined, as they depend on more collective properties of *idealized* molecular models, and on the lattice symmetry and periodicity. Among these, the stacking of parallel molecules [which, bisected by crystallographic twofold axes, lie approximately in the (*-401*) plane], which shows a well defined 3.5 Å separation, typical of π-π aromatic interactions of the graphitic type (Figure 7.3*c*). As depicted in Figure 7.3*b*, the observed stacking occurs through a coherent shift, along one direction, of the trimers, a packing feature highly sensible to faulting and prone to induce crystal defectiveness when the powders of **1**, or **2**, are rapidly precipitated from solution.

The triangular shape of the molecular entities of **1** and **2**, and the presence of strong electron-withdrawing *nitro* groups in their periphery (with large *local* dipoles) generate electron density distributions of non-negligible octupolar character. Not possessing a permanent dipole moment, these molecules, during crystallization, might be less prone to reorientational relaxation, which, for high-performance electro-optical materials, is a detrimental factor favoring antiparallel pairing of dipolar molecules. Thus, if suitable synthetic conditions are found, crystals of **1**

and **2** (optically transparent in the visible spectrum), might show interesting NLO properties.

7.4 Identifying the defectiveness of Ag/Cu nitropyrazolates

As in the case of the ruthenium tetracarbonyl polymer presented in the previous chapter, the powder patterns of both (isomorphous) samples **1** and **2** show an unusual combination of sharp and broad peaks at low angles, accompanied by progressively broader ones. Small, anisotropic coherent domain sizes, lattice strain and/or structural defects, can all cause Bragg peaks to broaden in such an uncommon way, as a consequence of single (local) or cumulative effects. Disentangling the different contributions, when co-present, might become a very complex task, and causes mutual uncertainties in the estimation of the different effects [33].

In this respect, a preliminary (phenomenological) line profile analysis on the (better resolved) low angle peaks, using a pseudo-Voigt description, was performed. The average coherent domain size (D_v, here isotropic) and the root-mean-square strain $\langle\varepsilon^2\rangle^{1/2}$ from the integral breadth (β) of the peaks [$\beta\cos\theta = \lambda K/D_v + 2\langle\varepsilon^2\rangle^{1/2} \sin\theta$] were estimated following the Williamson and Hall approach [34], λ being the wavelength of the diffraction experiment and K a constant depending on the crystal domain shape. Values were found to be *ca.* 67 nm (size) and ~1.2% (strain), the latter parameter being extremely large and unrealistic. Therefore a different approach, based on total scattering techniques, was explored, aiming at interpreting the structural defectiveness at the *atomic level* and at reproducing the observed XRPD pattern features (including the rapid

increase of peak broadening) on the basis of a sound physico-chemical model.

Somehow inspired by the work of Rasika Dias and coworkers [4], who characterized a number of ordered but *differently organized* stacking sequences in several brightly phosphorescent Cu(I) pyrazolates, a faulted structural model featuring a local change in the stacking sequence of the molecular trimers, was conceived. The defective, faulted model of **2** was obtained by stacking the trimers along the *c* axis while using a fault probability parameter *p* (typically, *p* = 10% or 20%), corresponding to mirroring the shift between the centers of mass of the trimers across the normal to the molecular planes, as illustrated in Figure 7.4. This model closely resembles that of aperiodic ZnS polytypes generated by uncontrolled growth kinetics, proposed, using a similar approach, by Palosz et al. [35]).

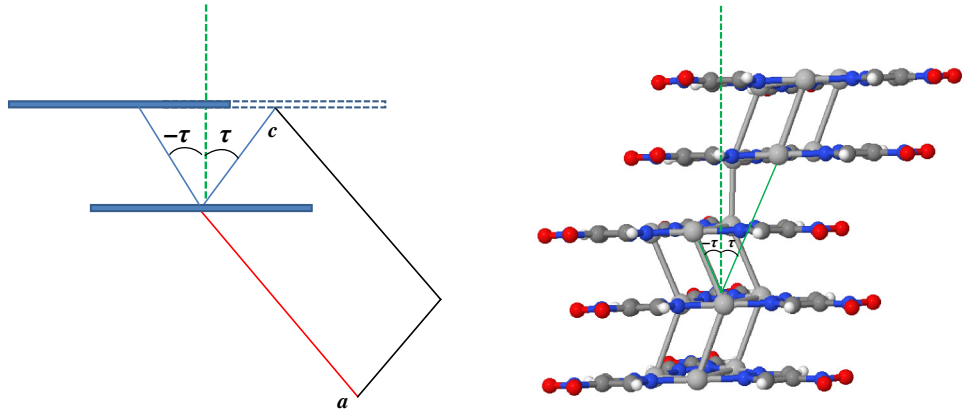

a) b)

Figure 7.4 (a) Schematic representation of the geometric assumptions made in building the faulted models. The blue rods represent the molecular planes of the $Ag(C_3H_2N_3O_2)$ trimers, oriented normally to [*-401*]. The orientation of the unit cell is also reported (viewed down *b*). (b) Stacking of the trimers, defined by a "canting" angle, $\tau = 21.8$ °, occasionally set at *negative* value when a local fault occurs.

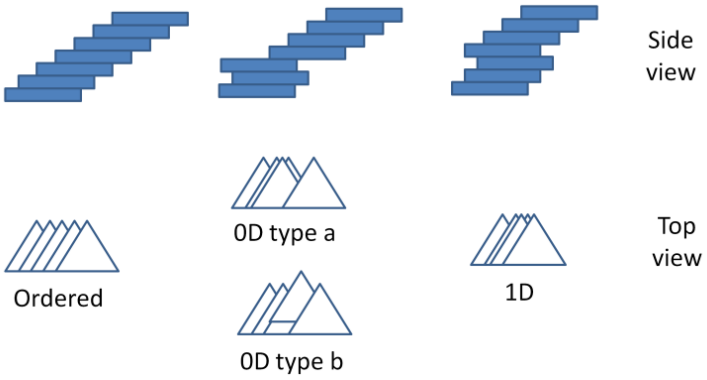

Chart 1. Ordered (left) and faulted sequences of triangles (mimicking the stack, along *c*, of molecules of **2**, as in Figure 3) together with their labeling scheme. Shifts occur with a predefined probability and are uncorrelated in neighboring chains in the lattice.

The defects were (*randomly)* distributed within molecular chains in order to obtain lateral displacements of either a single molecule (as in Figure 7.4b) or a larger segment of the chain. The two cases are labeled as *0D* and *1D* defects, respectively. Different *faulted models* were then tested, as summarized in Chart 1, where the ordered, the *0D* (*a* and *b* types, in which the shift occurs along two different directions) and the *1D* labels are linked to a schematic, pictorial view of the pertinent defect. A combination of *0Da* and *0Db* types was also explored, and referred to as the *0Dab* model. In all cases, the shift within a stack was independent from the shift occurring in the neighboring chains (*uncorrelated faulted models*).

7.5 Modelling the faulted structures within the DFA approach

In order to compare the different faulting models and to identify the most appropriate one on the basis of the best matching with the experimental diffraction pattern of sample **2**, the DFA approach was used

to simulate the XRPD traces of *ordered* and *faulted models* on a number of *nanosized molecular clusters* of variable size and shape [36]. Dealing with highly disordered materials, some computational tricks (in addition to those described in chapter 3) were necessary, in order to obtain the pattern simulations in reasonable computational time.

Aiming at speeding up both the atomic model generation and the sampled interatomic distances calculation steps, particularly while building *large faulted nanocrystals*, locally developed routines were implemented in the Debussy Suite 2.0 and applied either in the *ordered* or the *faulted* case. The additional computational tricks are schematized in Figure 7.5: the lattice nodes within the cluster are firstly generated and the corresponding Cartesian coordinates are stored in a suitable file (Figure 7.5a), then, the interatomic vectors of the trimeric molecular fragment (Figure 7.5b) are combined with the nodes generated in the previous step to obtain the final coordinates of all atoms in the cluster (Figure 7.5c).

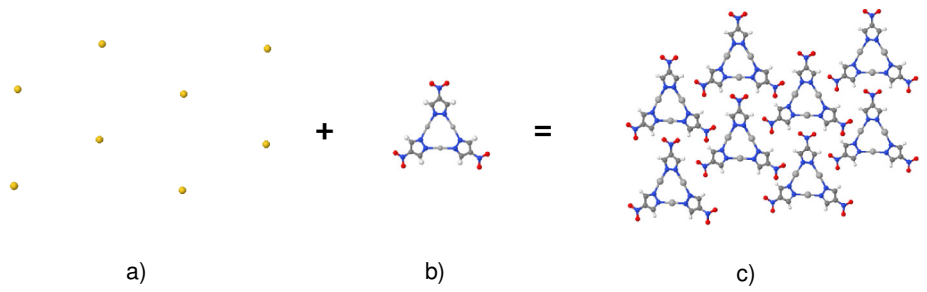

Figure 7.5 Schematic view of the procedure developed to generate faulted clusters and to save computational time: a) cluster nodes generation (here, shown as an ordered, periodic, 2D lattice); b) molecular fragment interatomic vectors generation; c) final atomic cluster model obtained by "dressing" each node in a) with the structural motif shown in b).

As general examples of the required computational times, calculating the sampled interatomic distances for the cluster of 30 x 17 x 3.5 nm^3 (148500 atoms, *vide infra*) took about 40 min CPU time, while 27 h were typically spent for the cluster of 30 x 17 x 10.5 nm^3 (445500 atoms) [both of the *0Dab* type with p = 20%]. Calculations were performed on a HP Server equipped with a 8 GB RAM running under UNIX.

Since the smearing and density of peaks at high angles of the synchrotron data give a nearly featureless curve, Debye simulations were limited to the 3-30° 2θ range and performed for a number of different models, grouped in two main classes:

i) *Ordered clusters*, the average domain size of which, along the three crystallographic directions, were roughly estimated as follows. The detailed analysis of experimentally observed anisotropic peak broadening, revealed the occurrence of narrow(er) peaks for *hk0* reflections, and much broader ones for $l \neq 0$. On attributing such broadening to size-effects *only, platy nanocrystals* of 30–40 nm along *a*, almost half of these values along *b* and in the 3.5–7.0 nm range along *c,* were generated. Simulations for selected nanocrystals having markedly different aspect ratios are shown in Figures 7.6a and a reduced angular region (showing the most important defect-related features) in Figure 7.6b. The agreement factors (R_{wp}) between simulated and experimental patterns, indicated (left panel) that the largest nanocrystal best matches the whole pattern, likely driven by the sharpness of the dominating peak below 5° (2θ). At variance, Figure 7.6b suggested that the smallest size, particularly along *c*, is favoured; this cluster size (30x17x3.5 nm^3) was therefore considered in the following

step. Needless to say, such a choice was also the most advantageous from the computational point of view.

ii) Faulted clusters, according to the formalism illustrated in Chart 1 and with faulting probability set at p = 10% (Figure 7.6c) and p = 10% or 20% (Figure 7.6d, reduced 2θ range). Full pattern simulations of *0Da*, *0Db, 1D* and *0Dab* models (at the p = 10% level) indicated that, within this set of possibilities, the *1D* model can be discarded on the basis of its significantly worse agreement (R_{wp} = 0.64), while the others are nearly comparable to the unfaulted model (R_{wp} = 0.45-0.48). Therefore, the selection of the most probable model was carried out through the systematic evaluation of the agreement factors in the *reduced* angular range (Figure 7.6d). Accordingly, the *0Dab* (p = 20%) model turned to be the best performing in modifying the intensity distribution toward the observed one.

Worthy of note, the occurrence of random faults, *uncorrelated* within each crystal domain, changes the relative peak intensities while the increase of peak width with the scattering angle is only marginally affected. This explains why some peaks are still visible above 20° (2θ) in the simulations of Figures 7.6a,c, and are *not smeared* at large 2θ's, as in the Experimental data set (red trace). In this respect, *correlated* shifts are likely to form in these compounds, since intermolecular contacts are expected to become significantly modified by this kind of faults. This point is later discussed in deeper detail.

The final step of this DFA modelling of a faulted silver nitropyrazolate structure is related to the odd shape of rather broad peaks appearing at 2θ = 12.7° and 2θ = 14.0°, respectively. They correspond to

(*001*) and (*-401*) reflections (*i.e.* the ones at the lowest angles with $l \neq 0$), likely arising from a population of sizes along *c*, which was eventually modelled by weighing the diffraction traces of *0Dab* (p = 20%) nanocrystals of different thickness along *c*, up to 10 nm, the major fraction being represented by 3.5 nm thick platelets. The resulting simulation is shown in the inset of Figure 7.6c.

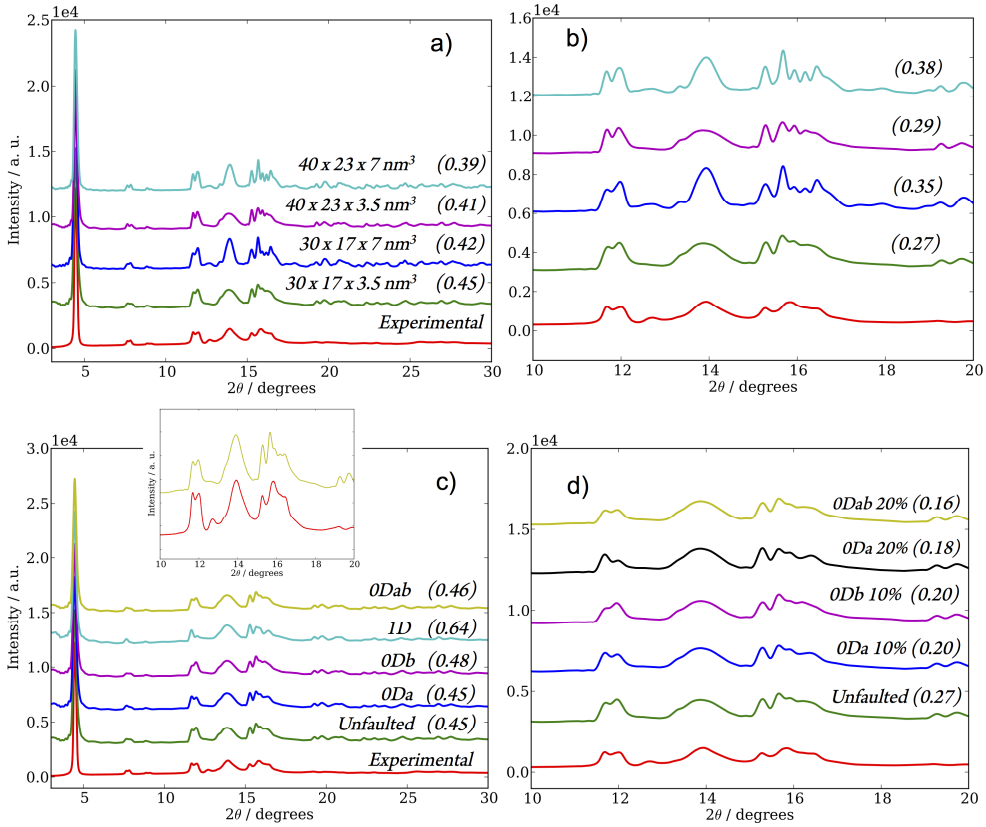

Figure 7.6 a) Comparison of experimental data (bottom red trace) and Debye simulations form ordered clusters of different sizes; conventional weighted profile agreement factors (R_{wp}) are given in parentheses; b) same as a), but with R_{wp} values computed in the $5 \leq 2\theta \leq 20°$ range, on omitting the first, dominating, peak; c) and d) same as a) and b), but with unfaulted and *0Da*, *0Db, 1D* and *0Dab* models of *uncorrelated faults*. In panel c), a probability value p = 10% was used. The inset in c) shows the simulation of the *0Dab* faulted cluster with size 30×17 nm^2 in *ab* and a population of thickness up to 10 nm along *c* (yellow, top trace; R_{wp} = 0.16). In all panels, the red bottom trace refers to the experimental pattern.

7.6 Investigating additional local features by PDF analysis

In order to support the proposed faulted models, the *local structure* of these materials was further investigated through the analysis of the *G*(r) function [37]. The limited Q_{max} value (14 $Å^{-1}$) of the available data and the complexity of the structural problem here investigated (the smallest cluster containing 148500 atoms of five different chemical species) did not allow the fit of the experimental *G(r)*, and the analysis was carried out through the qualitative comparison (shown in Figure 7.7) of three calculated *G(r)*'s, corresponding respectively to the ordered, the 10% and the 20% faulted *0Dab* clusters of 30x17x3.5 nm^3 size (bottom traces) *vs* the experimental *G(r)*'s from two different syntheses of **2** (top).

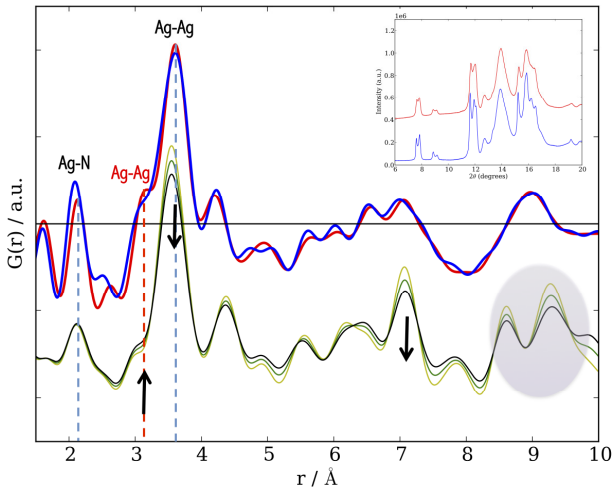

Figure 7.7 Top traces: *G*(r)'s from two different syntheses of sample **2**. The blue curve refers to the sample showing the higher degree of crystallinity (diffraction peaks, in the inset, appear narrower than in the sample corresponding to the red trace). Bottom traces: *G*(r)'s calculated for the ordered and the *0Dab* faulted clusters with p = 10% and p = 20% (yellow, green and black curves, respectively). Peak assignment in the low r region includes the Ag···Ag contacts at 3.05 Å (red label) originating from the lateral sliding of trimers. Arrows indicate the most significant effect on progressively increasing p from 0 to 20% (see text for the shaded area).

The most prominent peak in the *experimental G(r)* refers to *intra*molecular Ag···Ag contacts (ca. 3.51 Å), overlapped with the *inter*molecular ones (3.50 and 3.72 Å). Other intermolecular contacts, are clearly visible at 4.3, 5.6 and 6.1 Å, while the 8.7, 9.1 and 9.3 Å ones all overlap in a broad peak. The Ag-N bonding distance (~ 2.1 Å) clearly appears in the low *r* region. The peak (or shoulder) observed slightly above 3 Å can be attributed to Ag···X (X = C,N,O) distances. However, the slight increase of this shoulder in the *experimental G(r)* of the less crystalline sample (red trace) matches the lateral sliding of the trimers that, in our crude *0Dab* faulted model, gives Ag···Ag contacts at 3.05 Å [38] and is further supported by the effect of augmented faulting in the *calculated G(r)*'s. Consistently, the "regular stacking" peaks at 3.5 and 7.0 Å are lowered upon increasing the defect probability parameter *p* from 0 to 20% (see arrows in Figure 7.7).

Nevertheless, a relevant misfit is observed at distances larger than 8 Å, where a very broad peak occur in the *experimental G(r)* whereas two distinct peaks (shaded area in Figure 7.7) appear in the model *G(r)*'s. This finding is tentatively attributed to the presence of correlated shifts, unaccounted for in the faulted model(s). In this respect, the paracrystalline model described in the previous chapter and available in the Debussy Suite, holds for *orthogonal* crystal systems [36] (*i.e.*, biaxial and orthorhombic cases), whereas a model of correlated shifts in *oblique* systems (required in this case) is still beyond the program capabilities, its implementation requiring a substantial (theoretical and computational) work of high novelty.

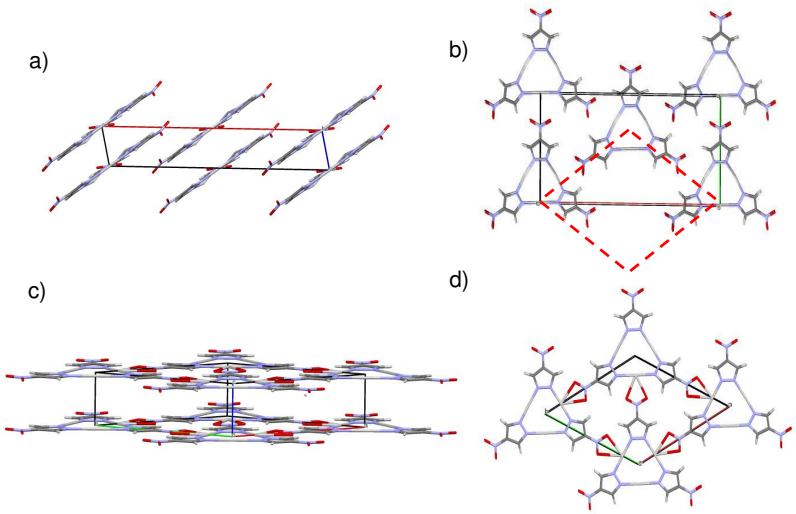

Figure 7.8 Crystal packing of monoclinic (M) species **2**, viewed down **b** (a) and (b) [001] projection, showing a pseudotrigonal symmetry (red dashed lines). In both cases, the horizontal axis is **a**. c) Idealization of a trigonal (T) packing ($a_T = b_T \approx b_M$) with space group *P321* (viewed approximately down [110]) and the [001] projection (d).

In order to (at least indirectly) support the hypothesis of a more complex defectiveness in which correlated lateral displacements of trimers combine with their faulted stacking, a trick was used by taking an *idealized trigonal structural model* (space group *P321*) of $[Ag(4\text{-}NO_2\text{-}pz)]_3$ with lattice parameters $a_T = b_T \approx b_M$, as shown in Figure 7.8, to which a paracrystalline distorsion was applied, using the following correlation coefficients: $r_a = 1.0$, $s_a = 0.995$, $r_b = 0.995$, $s_b = 1.0$; $\sigma_a = \sigma_b =$ 3.5 Å. DFA simulations were then computed for the ordered and the distorted *paracrystalline* models, up to the same Q_{max} of the experimental datasets and the corresponding G(r) curves are compared to the previous ones in Figure 7.9 (bottom traces). The shaded areas highlight the effect of correlated shifts at $r > 8$ Å, in the region where the faulted model

without correlated shifts (in the monoclinic structure) fails in reproducing the features of the experimental *G(r)*.

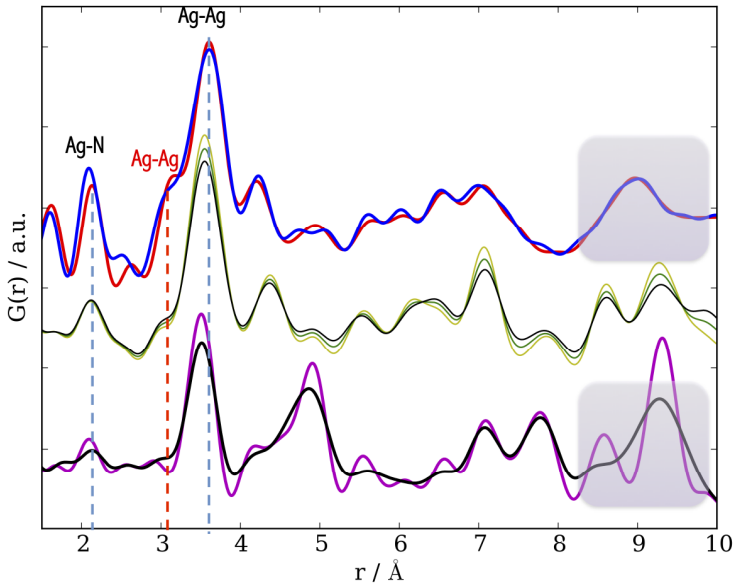

Figure 7.9 Experimental and model *G*(r)'s as reported in Figure 7.7 (top traces) and calculated *G*(r)'s (bottom traces) for the idealized trigonal structure depicted in Figure 7.8c,d: magenta and black curves correspond to the *ordered* and the distorted *paracrystalline* models, respectively. The shaded area highlights the *r* region where the effect of correlated shifts might explain the broad peak observed in the experimental *G*(r) of the (real) monoclinic structure.

7.7 Bending by Faulting: the morphological SEM characterization

Scanning Electron Microscopy measurements allowed reliable information about the morphology of **2** at *micrometric* scale (and, occasionally, at smaller sizes) to be retrieved. SEM images (Figure 7.10) showed *nanofilaments* built by distinct blocks and irregularly stacked along their elongation direction.

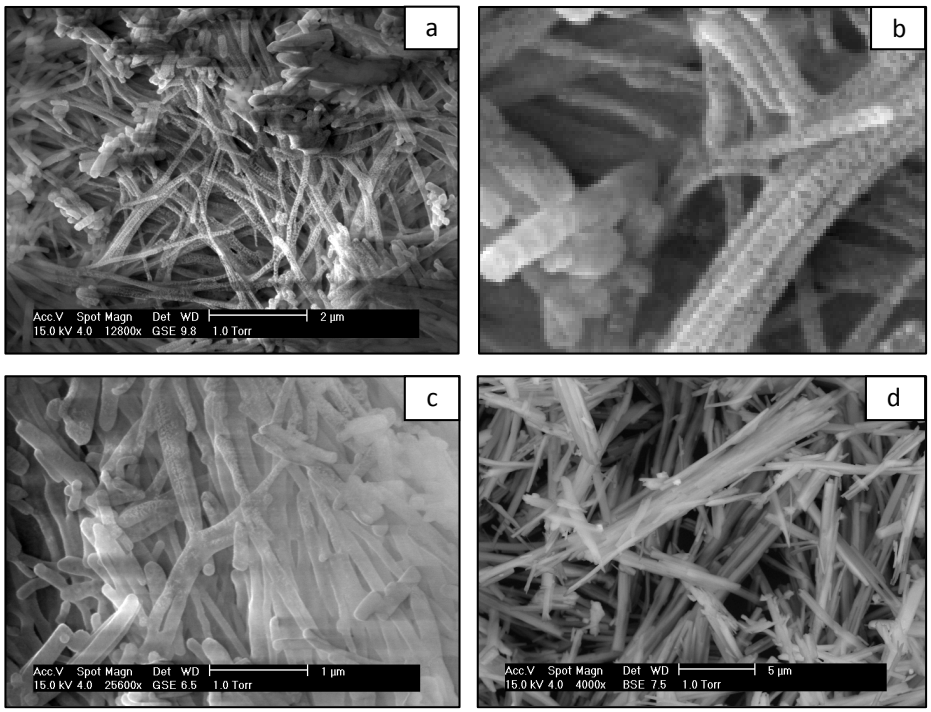

Figure 7.10 (a) SEM images of elongated nanofilaments in sample **2** appearing as the assembly of smaller domains in the magnified (5×) image (b)); in (b) and (c), the presence of a large amount of *bent "crystals"* indirectly confirms the *stacking fault model*, proposed through Total Scattering analysis. For comparison, panel *d* shows regularly shaped crystals from an ordered homologue, trimeric silver pyrazolate $[Ag(pz)]_3$ characterized by higher crystallinity and not possessing any noticeable structural defect.

This unexpected result is apparently in disagreement with the DFA result, suggesting the presence of tiny crystal domains of *platy shape.* However, these filaments appear as polyfragmented rods and show a relevant curvature, their bending being probably the consequence of the presence of several crystalline domains progressively shifted one away from each other. Therefore, this evidence of *bent whiskers* built by *platy*

nanocrystals, can be considered a *microscopical* evidence of the proposed *atomic-scale* models of disorder. Additional SEM images of an *unfaulted* polycrystalline material possessing similar structural features (a polymeric stacking of trimeric silver *pyrazolate* molecules - $[Ag(pz)]_3$ [39]) seem to confirm this hypothesis, as they appears as regular "straight" microcrystals (Figure 7.10d).

7.8 Structure-property relationships: the dielectric behaviour of Ag(I) 4-NO_2-pyrazolate

The potential functional properties of interest for the class of compounds here investigated are many and include also the electric ones. Interestingly, a similar morphology (*bent whiskers*) to the one observed here for silver nitropyrazolates, has been recently extensively studied in the field of semi- and super-conductive oxides to assess the influence of the structural defects on the materials electrical conductivity [40,41]. A similar structure-property study was carried out for the samples here characterized. Therefore, conductivity measurements and dielectric characterization were performed in order to evaluate possible *macroscopical* consequences on these physical properties possibly driven by the structural faults within the molecular stacks. Experimental tests consisted in dielectric and impedance spectroscopic measurements on pressed pellets of four samples: the polycrystalline sample **2**, the already cited crystalline homologue $[Ag(pz)]_3$, [39] a purely organic, hydrogen bonded, solids, *1H*-pyrazole (a zig-zag catameric system) [42] and the *4*-nitro-*1H*-pyrazole (also crystallizing as trimers) [43]. Table 1 summarizes the main results.

Table 1. Electrical characterization of 2, and of its congeners, including the purely organic counterparts. Dielectric constant taken as $\kappa = \kappa_\infty + B\,\omega^{-\nu}$. Electrical conductivity taken as $\sigma(\omega) = \sigma_0 + A\omega^n$ [44].

Compound	κ_∞ at 1MHz	B, ν	σ_0 S m^{-1}	-Log$_{10}$A (A in S m^{-1})	*n*
1H-pyrazole	2.50	28.2, 0.65	2×10^{-8}	9.3	0.44
4- NO_2-1H-pyrazole	2.57	4.5, 0.61	1×10^{-10}	12.7	0.82
$[Ag(pz)]_3$	2.40	0.1, 0.32	$< 10^{-10}$	13.2	0.88
$[Ag(4\text{-}NO_2\text{-}pz)]_3$, **2**	3.02	0.3, 0.26	$< 10^{-10}$	12.9	0.88

1H-pyrazole shows a significant larger *dc* electrical conductivity, σ_0, possibly favored by proton transfer in the *H*-bonded chains (not present in the cyclic organic and metalorganic trimers), which makes it an interesting material for technological applications (*i.e.* reversible batteries, hydrogen and methanol fuel cells, electrochromic displays and windows) [45]. A very low value of 0.44 of *n* in the power law of the universal dielectric response [29] (typically falling in the 0.75-1.00 range, see Figure 7.11a)] witnesses the anomalous behavior of pyrazole; however, though unusual, it is not exceptional (species characterized by a *weak frequency dependence* of the electrical conductivity are known [46]).

As long as *silver pyrazolates* are concerned, the values of σ_0, Log$_{10}$A and *n*, in the three last columns of Table 1 do not allow a distinction between the faulted and the unfaulted systems. Perhaps more interesting is the comparison of the frequency dependence of the dielectric constant (full frequency sweeps in Figure 7.11b) which shows a significant increase of the κ_∞ value for species **2** *vs* $[Ag(pz)]_3$ (3.02 vs 2.40).

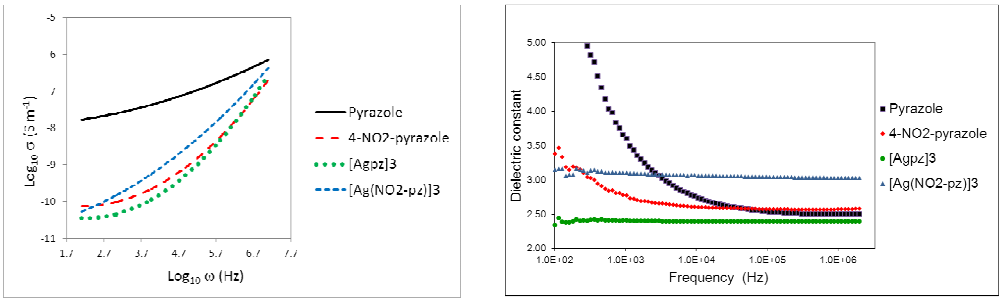

a) b)

Figure 7.11 (a) Frequency ($f = 2\pi\omega$) dependence of ac conductivity (σ) shown as a log-log plot. The curves are parabolic phenomenological fits. (b) Frequency dependence of the dielectric constant (κ *vs* $\log_{10}f$). The anomaly of κ_∞ value for species **2** is discussed in the text.

While it can be easily understood that the presence of a polar nitro group may be taken as responsible for the enhancement of sample dielectric susceptibility, however, the same effect is not found for the *4*-nitropyrazole vs *1H*-pyrazole. Indeed, comparing the *absolute increase* of κ_∞ in the two couples: *1H*-pyrazole/*4*-nitropyrazole ($\Delta\kappa_\infty$= 0.07) and silver pyrazolate/silver-*4*-nitropyrazolate ($\Delta\kappa_\infty$=0.62), the above mentioned enhancement in **2**, can be likely attributed to random or layered inhomogeneities, known to increase the interfacial polarizability in the 10^2-10^6 Hz range [47].

7.9 Conclusions

This chapter has been focused on the multiple scale characterization of silver and copper nitropirazolates, in which a coherent picture of the complex structural defectiveness (faulting and correlated shifts) distorting the regular molecular stacks of the two isomorphic compounds has been drawn. This goal was achieved by combining a non-trivial *ab-initio*

XRPD structural resolution (to derive the *molecular structure* and the *average* packing), with Total Scattering techniques (affording atomic local scale information, quantitative estimates of the faulting probability and microstructure analysis of defective crystal domains) and SEM imaging (providing the *microscale multi-domains* characterization).

The analysis of some *structure-dependent* physical properties of this class of materials, which are expected to behave as diamagnetic insulators, showed the unexpected higher dielectric permittivity of $[Ag(NO_2\text{-}pz)]_3$ in comparison with the unfaulted homologue, here explained as originating by the presence of *structural discontinuities*.

A couple of more general comments were further stimulated by the study here presented: 1) the crucial role that structural disorder can play in tuning relevant physical properties of materials. In this view, coordination compounds, the inherently flexibility of which offers a large variety of possible structural conformations, geometries and network topologies [48], have been emerging as a highly appealing class of materials fostering new promising defects-driven functionalities. 2) the increasing availability of Total Scattering techniques, as a valuable tool for *atomic-scale local* structure determination and *microstructural* characterization, recently resulted in a shift in emphasis towards this kind of materials. This is especially true for the PDF approach [49,50], whereas DFA methods have been rarely used, likely due to their high computational costs that have strongly limited their applications to *molecular crystals.* Some computational tricks have partially overcome this drawback and provided an innovative *defectiveness characterization* through the DFA approach. Accordingly, the cases discussed in this Thesis [the $Ru(CO)_4$ polymer and the Cu(I) and Ag(I) 4-NO_2-pyrazolates] are, as per

December 2014, the only reported extended DFA studies to the covalent species [24,36].

The study of materials that present a limited crystal periodicity, differently affected in the three dimensions by the presence of relatively weak anisotropic interactions, is still a scientific challenge. Some promising advances in this field have been recently proposed using total scattering approaches and Reverse Monte Carlo modeling [51,52]. As anticipated, several theoretical and computational aspects are still unsolved. Therefore, suitably tailored work is also in progress, within this pathway, toward the development of efficient DFA algorithms which would allow the treatment of *correlated paracrystalline disorder* with analytical methods also for *oblique* crystal systems.

References

1. J. Zhang, Y. Zhang, J. Lin, X. Chen X. *Metal Azolate Frameworks: From Crystal Engineering to Functional Materials***, 2012,** Chem. Rev., *112*, 1001–1033.

2. N. Masciocchi, G. A. Ardizzoia, G. L. Monica, A. Maspero, A. Sironi, *The unique formation of a crystal phase containing cyclic oligomers and helical polymers of the same monomeric fragment,* **1998**, Angew. Chem. Int. Ed., *37*, 3366–3369.

3. O. S. Wenger, *Vapochromism in organometallic and coordination complexes: chemical sensors for volatile organic compounds***, 2013,** Chem. Rev., *113*, 3686–3733.

4. H. V. Rasika Dias, H. V. K. Diyabanalage, M. G. Eldabaja, O. Elbjerami, M. A. Rawashdeh-Omary, M. A. S. Omary, *Brightly phosphorescent trinuclear copper(I) complexes of pyrazolates: substituent effects on the supramolecular structure and photophysics,* **2005**, J. Amer. Chem. Soc., *127*, 7489–7501.

5. A. Cingolani, S. Galli, L. Pandolfo, C. Pettinari, N. Masciocchi, A. Sironi, *Sorption-Desorption Behavior of Bispyrazolato-Copper(II) 1D Coordination Polymers*, **2005**, J. Am. Chem. Soc., *127*, 6144–6145.

6. J. C. Vickery, M. M. Olmstead, E. J. Fung, A. L. Balch, *Solvent-Stimulated Luminescence from the Supramolecular Aggregation of a Trinuclear Gold(I) Complex that Displays Extensive Intermolecular Au-Au Interaction,* **1997,** Angew. Chem. Int. Ed., *36*, 1179–1181.

7. A. Bencini, M. Casarin, D. Forrer, L. Franco, F. Garau, N. Masciocchi, L. Pandolfo, C, Pettinari, R. Ruzzi, A. Vittadini, *Magnetic properties and vapochromic reversible guest-induced transformation in a bispyrazolato copper(II) polymer: an experimental and dispersion-corrected density functional theory study,* **2009,** Inorg. Chem., *48*, 4044–4051.

8. K. Babic-Samardzija, C. Lupu, N. Hackerman, A. R. Barron, A. Luttge, *Inhibitive properties and surface morphology of a group of heterocyclic diazoles as inhibitors for acidic iron corrosion***, 2005,** Langmuir, *21*, 12187–12196.

9. K. Nomiya, K. Tsuda, T. Sudob, M. Oda, *Ag(I)-N bond-containing compound showing wide spectra in effective antimicrobial activities: polymeric silver(I) imidazolate,* **1997,** J. Inorg. Biochem., 39–44.

10. A. Tăbăcaru, C. Pettinari, F. Marchetti, C. Di Nicola, K. V. Domasevitch, S. Galli, N. Masciocchi, S. Scuri, I. Grappasonni, M. Cocchioni,

Antibacterial action of 4,4'-bipyrazolyl-based silver(I) coordination polymers embedded in PE disks, **2012,** Inorg. Chem., *51*, 9775–9788.

11. J. Zhang, S. Kitagawa, *Supramolecular Isomerism, Framework Flexibility, Unsaturated Metal Center, and Porous Property of Ag(I)/Cu(I) 3,3‘,5,5‘-Tetrametyl-4,4‘-Bipyrazolate***, 2008,** J. Am. Chem. Soc., *130*, 907–917.

12. V. Colombo, C. Montoro, A. Maspero, G. Palmisano, N. Masciocchi, S. Galli, E. Barea, J. A: R. Navarro, *Tuning the adsorption properties of isoreticular pyrazolate-based metal-organic frameworks through ligand modification,* **2012,** J. Am. Chem. Soc., *134*, 12830–12843.

13. Z. R. Herm, B. M. Wiers, J. A. Mason, J. M. Van Baten, M. R. Hudson, P. Zajdel, C. M. Brown, N. Masciocchi, R. Krishna, J. R. Long, *Separation of Hexane Isomers in a Metal-Organic Framework with Triangular Channels,* **2013,** Science, *340*, 960–964.

14. M. A. Halcrow, *Pyrazoles and pyrazolides-flexible synthons in self-assembly,* **2009,** Dalton Trans., 2059–2073.

15. V. Colombo, S. Galli, H. J. Choi, G. D. Han, A. Maspero, G. Palmisano, N. Masciocchi, J. R. Long, *High thermal and chemical stability in pyrazolate-bridged metal–organic frameworks with exposed metal sites,* **2011,** Chem. Sci., *2*, 1311–1319.

16. M. A. Rawashdeh-Omary, M. D. Rashdan, S. Dharanipathi, O. Elbjeirami, P. Ramesh, H. V. R. Dias, *On/off luminescence vapochromic selective sensing of benzene and its methylated derivatives by a trinuclear silver(I) pyrazolate sensor,* **2011,** Chem. Commun., *47*, 1160–1162.

17. M. A. Rawashdeh-Omary, *Remarkable Alteration of Photophysical Properties of Cyclic Trinuclear Complexes of Monovalent Coinage Metals upon Interactions with Small Organic Molecules***, 2012,** Comm. Inorg. Chem., *33*, 88–101.

18. C. V. Hettiarachchi, M. A. Rawashdeh-Omary, D. Korir, J. Kohistani, M. Yousufuddin, H. V. R. Dias, *Trinuclear Copper(I) and Silver(I) Adducts of 4-Chloro-3,5-bis(trifluoromethyl)pyrazolate and 4-Bromo-3,5-bis(trifluoromethyl) pyrazolate***, 2013,** Inorg. Chem., *52*, 13576–13583.

19. E. Procopio Quartapelle, S. Rojas, N. M. Padial, S. Galli, N. Masciocchi, F. Linares, D. Miguel, J. E. Oltra, J. A. R. Navarro, E. Barea, *Study of the incorporation and release of the non-conventional half-sandwich ruthenium(II) metallodrug RAPTA-C on a robust MOF***, 2011,** Chem. Commun., *47*, 11751–11753.

20. N. Masciocchi, G. A. Ardizzoia, A. Maspero, G. LaMonica, A. Sironi, *Metal Pyrazolato Complexes. Synthesis, Characterization, and X-ray Powder Diffraction Studies of Group 12 Coordination Polymers***, 1999,** Inorg. Chem., *38*, 3657−3664.

21. P. Debye, *Zerstreuung von Röntgenstrahlen***, 1915,** Ann. Phys., *46*, 809−823.

22. T. Egami, S. J. L. Billinge, *Underneath the Bragg Peaks: Structural Analysis of Complex Materials,* **2003***,* Pergamon Press: Oxford, U.K.

23. A. Cervellino, C. Giannini, A. Guagliardi*, On the efficient evaluation of Fourier patterns for nanoparticles and clusters,* **2006**, J. Comp. Chem., *27*, 995-1008.

24. F. Bertolotti, A. Maspero, A. Cervellino, A. Guagliardi, N. Masciocchi, *Bending by Faulting: A Multiple Scale Study of Copper and Silver Nitropyrazolates,* **2014,** Cryst. Growth & Des., *14*, 2913−2922.

25. M. Friák, M. Šob, *Ab initio study of the bcc-hcp transformation in iron,* **2008,** Phys. Rev. B, *77*, 174117-1−174117-7.

26. M. Leoni, R. Di Maggio, S. Polizzi, P. Scardi, *X-ray Diffraction Methodology for the Microstructural Analysis of Nanocrystalline Powders: Application to Cerium Oxide,* **2004,** J. Am. Ceram. Soc., *87*, 1133–1140.

27. P. R. Willmott, D. Meister, S. J. Leake, M. Lange, A. Bergamaschi, M. Böge, M. Calvi, C. Cancellieri, N. Casati, A. Cervellino, Q. Chen, C. David, U. Flechsig, F. Gozzo, B. Henrich, B. Jäggi-Spielmann, B. Jakob, I. Kalichava, P. Karvinen, J. Krempasky, A. Lüdeke, R. Lüscher, S. Maag, C. L. Quitmann, M. Reinle-Schmitt, T. Schmidt, B. Schmitt, A. Streun, I. Vartiainen, M. Vitins, X. Wang, R. Wullschleger, *The Material Science beamline upgrade at the Swiss Light Source,* **2013**, J. Synchrotron Rad., *20*, 667-682.

28. A. Bergamaschi, A. Cervellino, R. Dinapoli, F. Gozzo, B. Henrich, I. Johnson, P. Kraft, A. Mozzanica, B. Schmitt, X. Shi. *The MYTHEN detector for X-ray powder diffraction experiments at the Swiss Light Source,* Journal of Synchrotron Radiation, **2010**, *17*, 653-668

29. A. K. Jonscher, *The 'universal' dielectric response*, **1977**, Nature, *267*, 673 – 679.

30. W.I.F. David, K. Shankland, L.B. McCusker, and Ch. Baerlocher, Eds. *Structure Determination from Powder Diffraction Data*, IUCr Monography on Crystallography 13, **2002**, OUP, Oxford, New York

31. *TOPAS-R*, *V.4.0*; Bruker AXS: Karlsruhe, Germany, **2006**.

32. From a CSD survey on Ag(I)/Cu(I) pyrazolates, *ca.* 70% of the hits of were trimeric structures.

33. B. E. Warren, *X-rays studies of deformed metals*, **1959**, Prog. Metal Phys., *8*, 147–202.

34. G. K. Williamson, W. H. Hall *X-ray line broadening from filed aluminium and wolfram***, 1953,** Acta Metal., *1*, 22–31.

35. B. Palosz, E. Grzanka, S. Gierlotka, S. Stelmakh, S. *Nanocrystals: Breaking limitations of data analysis,* **2010**, Zeit. Kristallogr. *225*, 588–598.

36. A. Cervellino, A. Maspero, N. Masciocchi, A. Guagliardi, *From Paracrystalline $Ru(CO)_4$ 1D Polymer to Nanosized Ruthenium Metal: A Case of Study through Total Scattering Analysis,* **2012,** Cryst. Growth & Des., *12*, 3631–3637.

37. C. A. Young, A. L. Goodwin, *Applications of pair distribution function methods to contemporary problems in materials chemistry***, 2011,** J. Mater. Chem., *21*, 6464 – 6476.

38. This low intermetallic value is not exceptional, since a number of similar species with argentophilic contacts near 3 Å, down to 2.78 Å, are known: L. Koskinen, S. Jääskeläinen, L. Oresmaa, M. Haukka, *Argentophilic interactions in multinuclear Ag complexes of imidazole containing Schiff bases,* **2012,** CrystEngComm., *14,* 3509-3514 and references therein.

39. N. Masciocchi, M. Moret, P. Cairati, A. Sironi, G. A. Ardizzoia, G. La Monica*, The multiphase nature of the Cu(pz) and Ag(pz) (Hpz = pyrazole) systems: selective syntheses and ab-initio XRPD structural characterization of copper(I) and silver(I) pyrazolates,* **1994,** J. Am. Chem. Soc., *116,* 7668-7676.

40. Z. W. Pan, Z. R, Dai, Z. L. Wang, *Nanobelts of semiconducting oxides,* **2001,** Science, *291*, 1947–1949.

41. S. Cagliero, E. Borfecchia, L. Mino, L. Calore, F. Bertolotti, G. Martinez-Criado, L. Operti, A. Agostino, M. Truccato, P. Badica, C. Lamberti, *Insight into non-linearly shaped superconducting whiskers via a synchrotron nano probe***, 2012,** Supercond. Sci. Technol., *25*, 125002-1–125002-7.

42. H. W. W. Ehrlich, *The crystal and molecular structure of pyrazole***, 1960,** Acta Cryst., *13*, 946–952.

43. A. Llamas-Saiz, C. Foces-Foces, F. Cano, P. Jimémez, J. Laynez, W. Meutermans, J. Elguero H. Limbach, E. Aguilar-Parrilla, *The influence of the nitro group on the solid-state structure of 4-nitropyrazoles: the cases*

of pyrazole, 3,5-dimethylpyrazole, 3,5-di-tert-butylpyrazole and 3,5-diphenylpyrazole. I. Static aspects (crystallography and thermodynamics), **1994,** Acta Cryst. B, *50*, 746–762.

44. B. Świątek-Tran, H. Kołodziej, V. Tran, *$Zn(C_3H_3N_2)_2$: a novel diamagnetic insulator,* **2004,** J. Solid State Chem., *177*, 1011–1016.

45. K.-D. Kreuer, A. Fuchs, M. Ise, M. Spaeth, J. Maier, *Imidazole and Pyrazole-based Proton Conducting Polymers and Liquids*, **1998**, Electroch. Acta *43*, 1281–1288.

46. A. Jonscher, M. Frost, *Weakly frequency-dependent electrical conductivity in a chalcogenide glass,* **1976,** Thin Solid Films, *37*, 267–273.

47. K. F. Young, H. P. R. Frederikse, *Compilation of the Static Dielectric Constant of Inorganic Solids*, **1976,** J. Phys. Chem. Ref. Data, *2*, 313-409.

48. A. B. Cairns A. L. Goodwin, *Structural disorder in molecular framework materials,* **2013,** Chem. Soc. Rev., *42*, 4881–4893.

49. V. Petkov, V. Parvanov, D. Tomaliab, D. Swanson, D. Bergstrom, T. Vogt, *3D structure of dendritic and hyper-branched macromolecules by X-ray diffraction*, **2005**, *Solid State Comm.*, *134*, 671–675.

50. A. L Goodwin, M. T. Dove, A. M. Chippindale, S. J. Hibble, A. H. Pohl, A. C. Hannon, *Aperiodicity, structure, and dynamics in $Ni(CN)_2$,* **2009,** Phys. Rev. B, *80*, 054101-1– 054101-7.

51. N. P. Funnell, M. T. Dove, A. L. Goodwin, S. Parsons, M. G. Tucker, *Local structure correlations in plastic cyclohexane - a reverse Monte Carlo study*, **2014,** J. Phys.: Condens. Matter, *25***,** 454204, and references therein.

52. Mc Greevy, R.L.; Pusztai, L. *Reverse Monte Carlo Simulation: A New Technique for the Determination of Disordered Structures,* **1988,** Mol. Simul.*, 1***,** 359-367.

Chapter 8

General Conclusions

The work presented in this Thesis has successfully matched the initial objectives of considering different classes of nanoscaled materials and characterizing them at the atomic and nanometer length scales by innovative and advanced reciprocal-space Total Scattering Techniques.

This Thesis has eventually offered the chance of meeting the world of nanoscience and nanotechnology through a multivalent experience, spanning from the multifaceted aspects of the Debye Function Analysis, covering experimental, computational and modeling issues, to the exciting field of material functionalities, passing through the appealing characterization of their structural and microstructural properties within the coherent framework of the DFA method.

Four classes of materials have been characterized, each of them holding intriguing structural and microstructural features and appealing nanotechnological properties.

Very small **super-paramegnetic iron oxide** NPs, although extensively investigated in the last decades, still represent a challenging system from the physico-chemical characterization point of view, due to the rather complex interplay of structural, compositional and surface effects, which makes the interpretation of their magnetic properties a difficult task. The advantage of the DFA method of exploiting the information from both Bragg and diffuse scattering has allowed the simultaneous determination of accurate lattice parameter, core–shell composition (in terms of magnetite/maghemite ratios) and full size distributions to be retrieved. For the first time, surface relaxation has been detected at the smallest sizes of this kind of NPs and, based on the characterization of a large series of IONPs, a straightforward relationship

between the lattice parameter, the Fe oxidation state and the NP size has been established. Finally, interesting *quantitative* correlations with the NPs magnetic properties and their core-shell structure have been pointed out.

Application of Total Scattering Techniques to biomimetic citrate-controlled **nano-apatites** has allowed DFA to get in contact with the fascinating world of biomineralization, many aspects of interest (structure, stoichiometry, size and morphology) of apatites to be quantitatively investigated as a function of the mineral maturation and the hot topic of the origin of the platy morphology in bone apatite to be explored. By cross-coupling the results of this analysis with AFM characterization, the amorphous-to-crystalline transformation process has been disclosed in the model system and a plausible mechanism inducing the platy morphology in bio-inspired apatite nanocrystals has been proposed. Interestingly, platy apatite NCs similar to those formed in bone under the control of acidic non-collagenous proteins and collagen fibrils are formed in the investigated model system under the driving action of citrate ions, the role of which in bone mineralization might be broader than the role depicted to date.

The high relevant topic of structural disorder and its crucial role in tuning the material properties was the central theme of the other two classes of materials. The development of a specific paracrystalline model, within the more general DFA approach, was successfully applied to the **1D $[Ru(CO)_4]_n$ species**, providing physically sound quantitative estimates of correlated metal chains displacement, while a more complex structural defectiveness, including faulting and correlated shifts, was

found to distort the regular molecular stacks of (isomorphous) **silver and copper nitropyrazolates**.

All the cases of study presented in this Thesis have witnessed that DFA is a highly versatile and promising physico-chemical characterization approach for dealing with complex defective nano-systems.

The materials characterized in this Thesis have largely contributed to improve the method, both on the experimental and the modeling sides. On the experimental side, reliable data acquisition protocol and data reduction procedure have been established at the SLS material science beamline; on the modeling side, the **progressively upgraded Debussy Suite** presently offers a robust tool to extract multiple scales (atomic to nanometer) and quantitative information on: crystal structure, size and shape of NCs, structural defects and their size-dependence, phase abundance and sample stoichiometry.

Integration with complementary techniques, in particular with microscopic methods, may offer an empowered pathway to the important and fascinating realm of nanomaterials, as witnessed by the cases of biomimetic apatites and Cu/Ag nitropyrazolates.

Future perspectives are very encouraging in the (inter-correlated) directions of further development of the method and new, appealing classes of materials to characterize. Progress in the data analysis software and models specialization to novel specific cases are expected to make DFA more and more popular. In this view, the availability of dedicated instrumental set-up for laboratory applications would be a significant step forward.

Annex 1

Details of the Syntheses and Laboratory Experiments

Synthesis of IONPs

***Samples A and B*:** The iron salts solution was prepared dissolving appropriate amounts of $FeCl_2 \cdot 4H_2O$ and $FeCl_3 \cdot 6H_2O$ (with 1:2 Fe(II):Fe(III) molar ratio) in 100 mL of deionized water and stirred for 5 minutes to complete dissolution. Each iron salt solution was added to 100 mL of 1 M NH_3 solution in few minutes.

Samples A: Three different solutions with different iron ions concentration were prepared. Each iron salt solution was added to 100 mL of 1 M NH_3 solution in few minutes. After addition of iron salt solution to the ammonia solution, the suspension was stirred for 5 minutes. The dark precipitate was washed three times with distilled water and three times with acetone, then it was recovered with the aid of a permanent magnet. Different post synthetic treatments, summarized in Table 4.1 of chapter 4, were applied to different batches.

Samples B: Four different solutions with different iron ions concentration were prepared. The deionized water used for the preparation of all solutions was previously deoxygenated by flowing N_2 for 30 minutes, then used in the preparation of the iron salts and ammonia solution. After reactant addition, the suspensions were stirred for 5 min. All reactions were carried out in N_2 atmosphere at r.t. The dark precipitates, after recovery with the aid of a permanent magnet, were washed three times with deionized deoxygenated water and three times with acetone. All samples were dried in vacuum at r.t. for 2 h.

***Samples C*:**

Samples C1 and C2 were prepared dissolving in water ferrous and ferric salts precursors (with 1:1 Fe(II):Fe(III) molar ratio) and stirring them for 5 minutes. The iron salt solution was added to 100 mL of 1 M NH_3 solution in few minutes. The suspensions were maintained in vigorous stirring for 1 h. The precipitates were recovered with the aid of a permanent magnet, and washed with water and acetone. All samples were dried in air at r.t.

Samples C3, C4 and C5 were obtained by precipitation methods using uniquely a $FeCl_2 \cdot 4H_2O$ solution in basic aqueous medium (NH_3 solution, 1 M). The ferrous salt was dissolved in deionized water, the solution was stirred for 5 minutes, and later added to 100 mL of 1 M NH_3 solution. After 1 h, the samples, recovered with the aid of a permanent magnet, were washed with water and acetone. Different post synthetic treatments, summarized in Table 4.1 in Chapter 4, were applied to different batches.

***Samples D*:** 1.00 g of $FeCl_2 \cdot 4H_2O$ and 2.70 g of $FeCl_3 \cdot 6H_2O$ (1:2 Fe(II)/Fe(III) molar ratio) were dissolved in 100 mL of ethanol-water mixture at room temperature (ethanol:water ratios are reported in Table 4.1). Each iron salt solution, stirred for 5 minutes, was added to 100 mL 1 M NH_3 solution in few minutes. After addition, the suspension was stirred for 5 minutes. The dark precipitates, after recovery with the aid of a permanent magnet, were washed three times with deionized water and three times with acetone. All samples were dried at 50 °C overnight.

***Sample E*:** Sample E1 was prepared by the microemulsion method. The reagents, 1.00 g of $FeCl_2 \cdot 4H_2O$ and 2.70 g of $FeCl_3 \cdot 6H_2O$, were mixed in 100 mL of deionized water and stirred to complete salts dissolution, for 5 minutes. 4.00 g of CTAB and 40.00 g of 1-butanol were added into the solution of the $Fe^{2+}$and Fe^{3+} ions. After homogeneization of the solution, 1-octanol (110.00 g) was added in order to form a microemulsion. The mixture was maintained in vigorous stirring for 30 minutes. The magnetic nanoparticles were precipitated by adding dropwise 6.50 mL of ammonia solution (precipitating agent, 29% w/w in water) to the microemulsion under continuous stirring. After 30 minutes, ethanol (40.00 g) was added. The solid sample, after recovery with the aid of a permanent magnet, was subsequently washed with a 1:1 v/v chloroform-ethanol mixture, ethanol and acetone. The powders were then dried in air at r.t.

***Sample F*:** Sample F1 was prepared following the procedure described in the literature [1].

***Sample G*:** 2.70 g of $FeCl_3 \cdot 6H_2O$ were dissolved in 100 mL of water and, after 5 minutes, added to 100 mL 1 M NH_3 solution in few minutes and stirred for 5 minutes after addition. The powders, recovered by centrifugation, were washed three times with distilled water and three times with acetone and dried at 50 °C overnight.

Synthesis of Biomimetic Apatite NPs and Laboratory Experiments

Synthesis of Ap and cAp samples. Calcium chloride dihydrate ($CaCl_2 \cdot 2H_2O$, Bioxtra, ≥ 99,0 % pure), sodium citrate tribasic dihydrate ($Na_3(Cit) \cdot 2H_2O$ where Cit = citrate = $C_6H_5O_7$, ACS reagent, ≥ 99,0 % pure), sodium phosphate dibasic (Na_2HPO_4, ACS reagent, ≥ 99,0 % pure) and sodium carbonate monohydrate ($Na_2CO_3 \cdot H_2O$, ACS reagent, 99.5% pure) were supplied by Sigma-Aldrich. All the solutions were prepared with ultrapure water (0.22 μS, 25 °C, MilliQ©, Millipore). The nanocrystals were obtained by a batch heating method described elsewhere [2].

Briefly, two solutions (1:1 v/v, 200 mL total) of (*i*) 0.1 M $CaCl_2$ + 0.4 M $Na_3(Cit)$ and (*ii*) 0.12 M Na_2HPO_4, + x mM Na_2CO_3 (x = 0 or 100) were mixed at 4 ºC. The pH of the mixture was adjusted with HCl to 8.5. The mixture was then introduced in a 250 mL round-bottom flask, sealed with a glass stopper and immersed in a water bath at 80 °C. The precipitates were then maturated in the mother solution for 5 minutes, 4 hours and 96 hours at 80 °C. An additional experiment with x = 100 mM was carried out by collecting the powder just after immersing the metastable solution in the flask at 80 ºC (time 0). This powder was analyzed by synchrotron X-ray scattering data (see ACP trace in Figure 5.1) and, unwashed, also by laboratory XRPD (Figure A1.2) and Raman spectroscopy (inset of Figure A1.2). Its chemical formula, obtained by TGA and ICP-OES, is $Na_{1.8}Ca_{8.1}(PO_4)_{4.75}(CO_3)_{1.35}(OH)(H_2O)_4$.

A hot-line pH probe (Sentron, Netherlands) immersed in the flask allowed *in situ* measurements of the pH and of the Temperature continuously during the precipitation process (Figure A1.1). After the precipitation, the particles were repeatedly washed with ultrapure water (MilliQ©, Millipore) by centrifugation. Samples to be used for AFM characterization were freeze-dried (LyoQuest, Telstar, Spain) and stored at 4 ºC. Powders obtained without Na_2CO_3 are referred to as Ap, whereas those obtained in the presence of 100 mM Na_2CO_3 are referred to as cAp.

Two samples were synthesized using the same batch heating method in the absence of citrate, maturated for 5 min and 4 h, respectively. Laboratory X-ray powder diffraction patterns revealed a totally different pathway, compared to the case in which citrate ions are used: at 5 min, a sample made of nanosized octacalcium phosphate was obtained; at 4 h, nanosized apatite is found as the major phase together with a minor presence of octacalcium phosphate. The two diffraction patterns were modelled using the Rietveld method implemented in the program TOPAS-R; the best fits are shown in Figure A1.3.

Laboratory XRPD analysis was performed using a Cu Ka radiation (λ= 1.5418 Å) on a PANalytical X'Pert PRO diffractometer equipped with a PIXcel detector operating at 45 kV and 40 mA. XRPD data were collected on the powder precipitated at "time 0" (pristine ACP sample), in the angular range 5-70 degrees, with a 2θ-step of 0.039° (Figure A1.2), and on the two samples synthesized in the absence of citrate, in the angular range 5-140 degrees, with a 2θ-step of 0.013° (Figure A1.3).

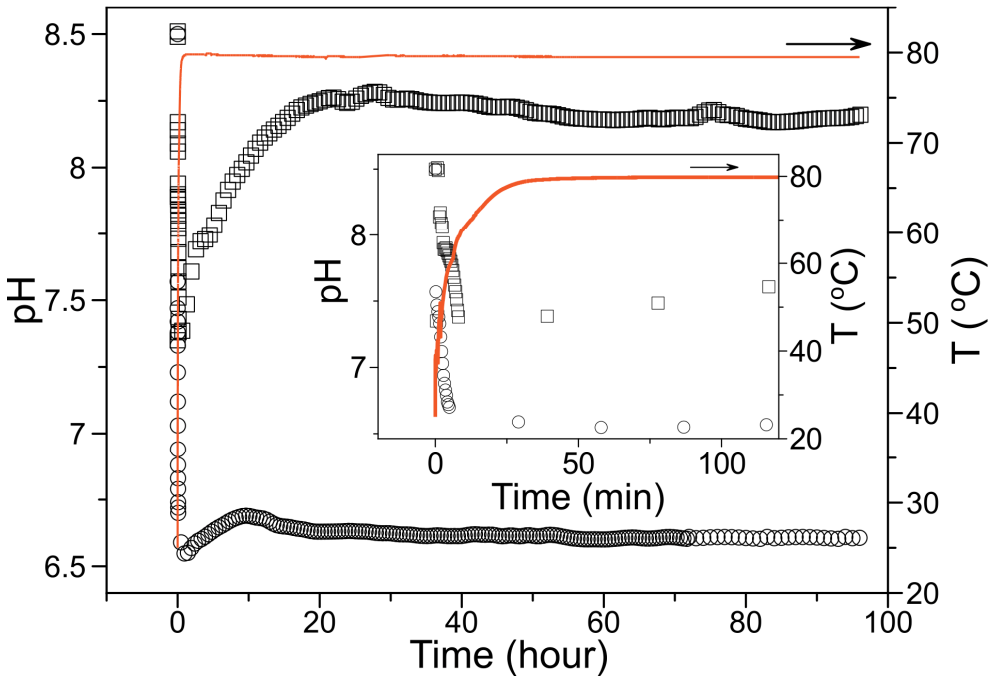

Figure A1.1 Evolution of the pH (□, ○) and Temperature (—) as measured *in-situ* during the precipitation of Ap (○) and cAp (□) NPs. Inset: details of the early stage of the reaction, showing the temperature and pH regimes in which sodium citrate crystals precipitate and progressively dissolve (see text) soon after favoring the formation of ACP platelets, as witnessed by the pH drop.

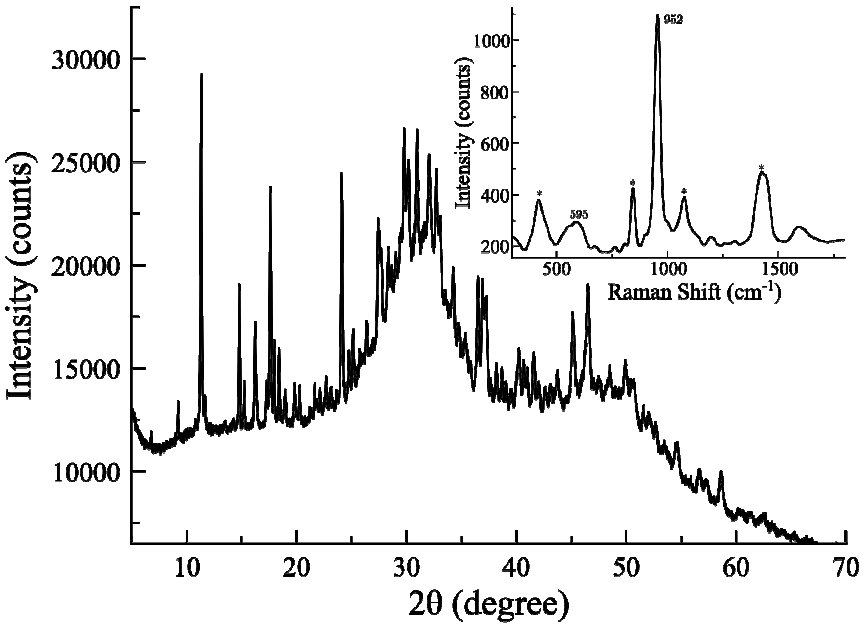

Figure A1.2. X-ray laboratory diffraction pattern of the powder precipitated at 'time 0' (*i.e.* just after mixing calcium and phosphate solutions). It clearly shows the co-presence of ACP and sub-micrometric-sized sodium citrate hydrates [$Na_3(cit)\cdot 2H_2O$, CSD code UMOGAE, and $Na_3(cit)\cdot 5.5H_2O$, CSD code FATTID02], in the 3:1 weight ratio, according to the quantitative analysis performed by the Rietveld method (TOPAS-R); estimated average crystal sizes are 200 and 500 nm, respectively. The Raman spectrum collected on the same sample (using a LabRAM-HR spectrometer with a backscattering geometry, Jobin-Yvon, Horiba, Japan) is shown in the inset. The Raman peaks at *ca.* 595 and 952 cm^{-1} (marked by arrows) are assignable to the bending and asymmetric stretching mode, respectively, of phosphate groups in ACP. [3] The remaining peaks are related to the sodium citrate crystals. [4]

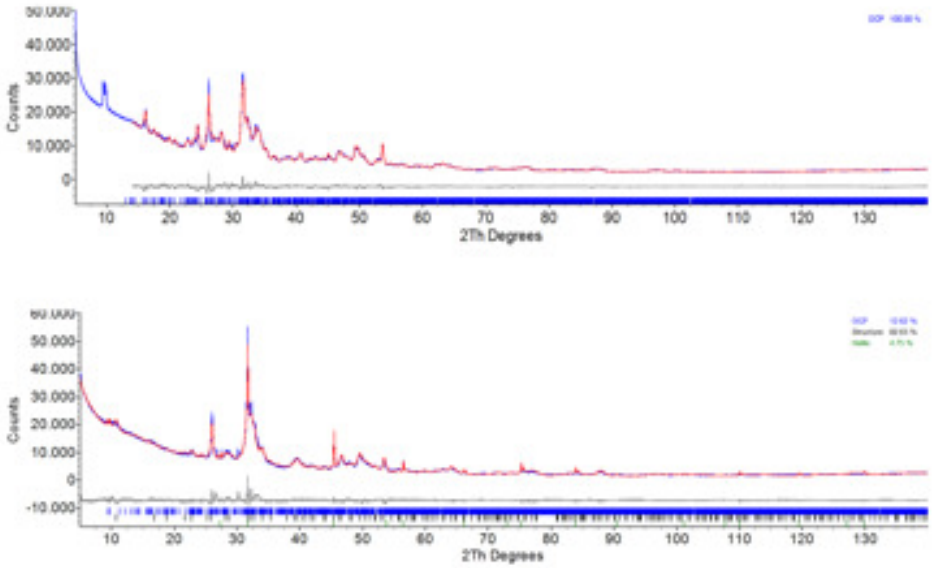

Figure A1.3 X-ray laboratory diffraction patterns of the powders precipitated at 5 min (top) and 4 h (bottom) using the same batch method of the samples here investigated but in the absence of citrate. Best fit obtained by using the Rietveld method as implemented in the program TOPAS-R. [5] Top: Octacalcium Phosphate (ICSD code 27050); Bottom: mixture of apatite (83% wt) and OCP (12% wt). A few very sharp peaks were attributed to contaminant NaCl (5% wt).

Synthesis of Cu(I)/Ag(I) 4-nitropyrazolates

Materials. All chemicals were reagents grade and used as supplied. $CuCl_2$, $AgNO_3$, pyrazole Et_3N, DMF, CH_3CN and NH_3 from Sigma-Aldrich. $[Cu(CH_3CN)_4](BF_4)$ [6] and 4-NO_2-pyrazole [7] were synthesized by literature methods. FT-IR spectra were recorded on nujol mull on a Shimadzu Prestige-21 instrument. Elemental analyses were carried out on a Perkin Elmer CHN Analyzer 2400 Series II.

Synthesis of Cu(I) 4-nitropyrazolate (1). To an acetone solution of 4-nitropyrazole (250 mg, 2.21 mmol) was added $[Cu(CH_3CN)_4](BF_4)$ (695 mg, 2.21 mmol) under nitrogen atmosphere. The colorless solution was stirred for 5 min, and triethylamine (1.5 mL) added dropwise. Immediately a white precipitate formed. The suspension was kept under stirring for 20 min. Then the complex **1** was collected by filtration, washed with acetone and dried under vacuum. Analysis: calc. for $C_3H_2CuN_3O_2$; Mw 175.63, C, 20.52; H, 1.15; N, 23.93%; found: C, 20.15; H, 1.22; N, 23.28%. IR (nujol): 3138(m); 1507(vs); 1424(vs); 1297(vs); 1179(m); 1041(w); 1000(w); 879(m); 820(s);756(s). M.p. 315 °C (dec.). This compound is poorly stable at ambient conditions, since, upon aerial exposure, it turns immediately green, without changing significantly its powder diffraction trace. Thus, we believe that only a minor oxidation of the surface layers occurs.

Synthesis of Ag(I) 4-nitropyrazolate (2). Several modifications of a basic method were tested. Specifically, in each synthesis the previously prepared ligand (4-nitropyrazole) and $AgNO_3$ were dissolved in CH_3CN, DMF (adding alternatively water or ammonia) and water, respectively, at room temperature. After variable reaction times (ranging from 15' to 4h), the white powder of the desired compound is obtained and suitably filtered from solution. (Typical) analysis: calc. for C_3H_2 AgN_3O_2; Mw 219.93, C, 16.38; H, 0.91; N, 19.11%; found: C, 16.45; H, 0.90; N, 18.82%. IR (nujol): 3143(m); 1502(vs); 1419(vs); 1312(s); 1293(vs); 1175(vs); 1031(s);1003(m); 873(s); 819(vs);756(vs). M.p. 335 °C (dec.).

The different preparations, following alternative synthetic routes (*i.e.* using different solvents, concentrations and reaction times), have been performed aiming at obtaining a polycrystalline material with clearly resolved diffraction peaks, amenable to conventional X-ray powder diffraction characterization; unfortunately, no matter what synthetic procedure was followed, no significant improvement of sample crystallinity was attained.

References

1. C. Pereira, A. M. Pereira, C. Fernandes, M. Rocha, Ri. Mendes, M. Paz Fernández-García, A. Guedes, P. B. Tavares, J.-M. Grenèche, J. P. Araújo, C. Freire, **2012**, Chem. Mater., *24*, 1496–1504.
2. J. M. Delgado-López, M. Iafisco, I. Rodríguez, M. Prat, J. Gómez-Morales, **2012**, Acta Biomater., *8*, 3491-3499.
3. G. R. Sauer, W. B. Zunic, J. R. Durig, R. E. Wuthier, **1994**, Calcif. Tissue. Int. *54*, 414-420.
4. G. Socrates*, Infrared and Raman characteristic group frequencies: tables and charts.* **2004**, Wiley, New York, 3rd ed..
5. TOPAS-R (Bruker AXS, V.3.0, Karlsruhe, Germany).
6. G. J. Kubas, B. Monzyk, A. L. Crumbliss, **1979**, Inorg. Synth. *19*, 90–92.
7. R. S. Gross, Z. Guo, B. Dyck, T. Coon, C. Q. Huang, R. F. Lowe, D. Marinkovic, M. Moorjani, J. Nelson, S. Zamani-Kord, D. E. Grigoriadis, S. R. J. Hoare, P. D. Crowe, J. Han Bu, M. Haddach, J. McCarthy, J. Saunders, R. Sullivan, T. Chen, J. P. Williams, **2005**, J. Med. Chem., *48*, 5780–5793.

Annex 2

Algebraic Details

of the 2D Anisotropic Paracrystalline Model

Correlations of random displacements in a 2D lattice

Consider a 2D lattice spanned by the vectors **a**, **b** that, for simplicity, are supposed to be orthogonal along the *x*, *y* axes and with just one atom on each lattice point. Suppose that every atom can be randomly displaced from its average position and that these displacements have normal distribution with variances σ_x^2, σ_y^2 along the coordinate axes.

If the displacements of atoms at different sites are *all* uncorrelated (*i.e.* independent of each other), then the net effect is like a Debye-Waller factor, with diffracted intensities downscaled at higher momentum transfer (higher angle) and peak shapes not affected. In fact, chosen any lattice vector (*m***a**, *n***b**), many pairs of lattice sites separated by (*m***a**, *n***b**) can be found, whose corresponding interatomic vectors will have average (*m***a**, *n***b**) – as in the unperturbed crystal - and variances $2\sigma_x^2$ along *x*, $2\sigma_y^2$ along *y*.

If correlations of random displacements in function of (*m*, *n*) are considered, four correlation parameters r_a, r_b, s_a, s_b [all lying in the (-1, 1) range] are usefully introduced (as proposed by Welberry [1]): r_a describes the correlations of displacements along *x* as a function of separation (*m*) along *x*; s_a describes the correlations of displacements along *x* as a function of separation (*n*) along *y*; r_b and s_b have the corresponding roles with respect to displacements along *y*. Therefore, r_a and s_b describe the *longitudinal* correlations, r_b and s_a the *transverse* correlations. In this case, the variances of the interatomic vectors connecting pairs of atoms at lattice sites separated by (*m***a**, *n***b**) will be $2\sigma_x^2(1-r_a^{|m|}s_a^{|n|})$ along *x* and $2\sigma_y^2(1-r_b^{|m|}s_b^{|n|})$ along *y* (this formalism ensures that correlations are the same regardless of any path on lattice sites).

Supposing now that r_a, r_b, s_a, s_b are all positive and close to 1 (which is a highly reasonable physical assumption), the variances can be recast in a clearer form, if the lattice separation is written as $(D_x, D_y) = (m\mathbf{a}, n\mathbf{b})$; in this case, the *x*-variance goes as:

$$V_x = 2\sigma_x^2\left(1 - exp\left[-\left|\frac{D_x}{a}\right| log\left(\frac{1}{r_a}\right) - \left|\frac{D_y}{b}\right| log\left(\frac{1}{s_a}\right)\right]\right)$$

A similar relationship can be written for the *y*-variance.

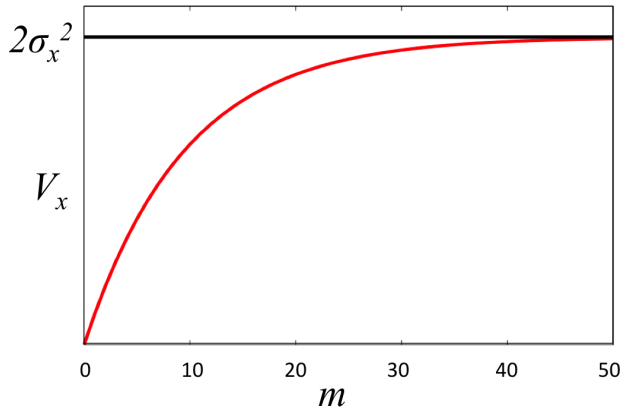

Figure A.2.1 Variance V_x of the inter-atomic vector (red line) as a function of *m* for $D_x = m\mathbf{a}$, $D_y = 0$, and $r_a = 0.97$. The black line is the asymptotic value $2\sigma_x^2$. Horizontal axis is *m*, Vertical axis is V_x (both taken as unitless quantities).

The behavior of this function is simple to be described. For small values of $(|D_x|,|D_y|)$ the variance increases linearly, the slope depending on the direction of (D_x,D_y). For large values of $(|D_x|,|D_y|)$ (*i.e.* at large lattice separations) the variance reaches a limiting value of $2\sigma_x^2$. A graphical example is plotted in Figure 6.4 for $D_y = 0$. Thus, this approach combines the anisotropic dependence of the slope of the variances on the angle in *xy* and the variance of the interatomic vector, which increases linearly with

the vector length, but saturates when a large enough value is reached. This is also the essence of paracrystallinity.

Integrating the paracrystalline model in the DSE formalism

The next step is to account for the *paracrystalline* phenomenon within the DSE formalism, by considering again the interatomic vector (D_x, D_y), its length D and its mutliplicity μ (which is like to say that in the lattice portion used to construct the nanoparticle, μ pairs of sites separated by vector (D_x,D_y) are found).

In the absence of paracrystallinity, the interatomic vector contributes to the scattered intensity with a *sinc* term [sinc(x) =sin(x)/x], as follows :

$$\mu\ sinc\ (2\pi Dq)$$

In the presence of paracrystallinity, a radial variance V_r can be derived [from the above mentioned variances V_x, V_y and the knowledge of the vector (D_x, D_y)] and a Gaussian factor needs to added to the *sinc* term:

$$\mu\ sinc\ (2\pi Dq)\ \exp\ (-2\pi^2 q V_r)$$

able to take into account all effects of anisotropic paracrystallinity. Therefore, the parameters required for describing this effect in a 2D system are the four correlation coefficients r_a, s_a, r_b, s_b and the two limiting variances σ_x^2, σ_y^2. A cross-correlation coefficient c_{xy} 'mixing' the x, y variances can be introduced, which typically lowers the actual point symmetry by distorting the average lattice. For $Ru(CO)_4$ this was

considered to be unnecessary, as symmetry lowering from the orthorhombic *mmm* class was not observed.

Finally, a generalization is needed to the case of pre-organized units (molecule, or any kind of fragment) periodically repeated within the crystal. In the case here treated, this is a 'cross' D_{4h}-$Ru(CO)_4$ fragment, assumed as rigid. Therefore, the interatomic distances relating atoms *within the same unit* are unaffected (zero variance, no Gaussian factor to be applied). For interatomic distances relating atoms belonging to two *different* units, the variances V_x, V_y are firstly evaluated using the distance (D_{0x},D_{0y}) between the centers of mass of the two units; then, for each distance vector (D_x, D_y) between pairs of atoms of the two units, the radial variance V_r is evaluated and the Gaussian factor is applied.

Reference

1. T.R. Welberry, *Diffuse X-ray scattering and models of disorder*, **2004**, OUP, Oxford, UK.

Annex 3

Publications

ARTICLES

From Paracrystalline $Ru(CO)_4$ 1D Polymer to Nanosized Ruthenium Metal: A Case of Study through Total Scattering Analysis

Antonio Cervellino, Angelo Maspero, Norberto Masciocchi* and Antonietta Guagliardi

Crystal Growth & Design, **2012**, *12*, 3631−3637.

Magnetite–Maghemite Nanoparticles in the 5–15 nm Range: Correlating the Core–Shell Composition and the Surface Structure to the Magnetic Properties. A Total Scattering Study

Ruggero Frison, Giuseppe Cernuto, Antonio Cervellino, Oksana Zaharko, Gian Mario Colonna, Antonietta Guagliardi* and Norberto Masciocchi,

Chemistry of Materials, **2013**, *25*, 4820–4827.

Crystal Size, Morphology, and Growth Mechanism in Bio-Inspired Apatite Nanocrystals

José Manuel Delgado-López, Ruggero Frison, Antonio Cervellino, Jaime Gómez-Morales, Antonietta Guagliardi* and Norberto Masciocchi

Advanced Functional Materials, **2014**, *24*, 1090–1099.

Bending by Faulting: A Multiple Scale Study of Copper and Silver Nitropyrazolates

Federica Bertolotti, Angelo Maspero, Antonio Cervellino, Antonietta Guagliardi* and Norberto Masciocchi*

Crystal Growth & Design, **2014**, *14*, 2913−2922.

Lattice parameters and site occupancy factors of magnetite-maghemite core-shell nanoparticles. A critical study

Antonio Cervellino, Ruggero Frison, Giusppe Cernuto, Antonietta Guagliardi* and Norberto Masciocchi

Journal of Applied Crystallography, **2014**, *47*, 1755-1761.

PROCEEDINGS

Testing the Debye Function Approach on a Laboratory X-ray Powder Diffraction Equipment. A Critical Study

Ruggero Frison, Giuseppe Cernuto, Antonio Cervellino, Antonietta Guagliardi* and Norberto Masciocchi

Proceedings of the 13th European Powder Diffraction Conference, EPDIC13, Grenoble, 28-31 October 2012

Powder Diffraction, **2013**, 28, S11-S21.

BOOK CHAPTERS

Debye Function Analysis: Theoretical and Fundamental Aspects

Antonio Cervellino, Ruggero Frison, Giuseppe Cernuto, Antonietta Guagliardi,

in *Crystallography for Health and Biosciences*, A. Guagliardi & N. Masciocchi eds., 2012, IUP, Varese, Italy. ISBN 978-88-95362

Debye Function Analysis of Nanomaterials of Interest for Health and Biosciences

Antonietta Guagliardi, Giuseppe Cernuto, Ruggero Frison, Antonio Cervellino

in *Crystallography for Health and Biosciences*, A. Guagliardi & N. Masciocchi eds., **2012**, IUP, Varese, Italy. ISBN 978-88-95362

Structure and Microstructure of Nanocrystals by the Debye Function Analysis

Antonietta Guagliardi, Antonio Cervellino, Ruggero Frison, Giuseppe Cernuto and Norberto Masciocchi

in *CRC Concise Encyclopedia of Nanotechnology* **2015**, *in press*, Taylor and Francis, ISBN: 9781466580343 | 1466580348

Dissertation submitted in partial satisfaction of the requirements
for the degree of Doctor of Philosophy in Chemistry

Academic Years: 2011-2014

UNIVERSITÀ DEGLI STUDI DELL'INSUBRIA
Dipartimento di Scienza e Alta Tecnologia and To.Sca.Lab - Como